Processing and Manufacturing Mechanics of 3D Woven Composites Influenced by Z-Binder Architecture

A thesis submitted to the University of Manchester for the degree of

Doctor of Philosophy

In the Faculty of Science & Engineering

2022

Kazi Sowrov

Robotics and Textile Composites Group

Department of Materials

School of Natural Sciences

The University of Manchester

Table of Contents

Total Words   **46908**

List of Figures

List of Tables

Abstract

3D woven structures in composite applications are getting increasing attention due to their superior out-of-plane properties and ability to form near-net-shape preforms. However, the in-plane properties of 3D woven composites are often compromised due to manufacturing induced limitations. The through-thickness Z-binder holds the load-bearing warp and weft tows and gives the structural integrity to the 3D woven preforms. This research aims to investigate the role of Z-binder weave architecture and tension on the 3D woven preform and composite mechanical properties. 3D woven structures were developed with four different Z-binder weave architectures: 1x1 plain, 2x1 twill and 2x2 twill with orthogonal binding patterns and an angle interlock (AI) weave. The degree of binder interlacings was deliberately reduced to increase binder float length and reduce the binder waviness. Binders were incorporated in both warp and weft tow directions to alter the directions of the resin channels inside the structures. Two orthogonal structures were manufactured with different binder tensions. Dry preform compressibility and in-plane permeability were measured to explore the effect of binder in preform compaction and resin flow behaviour. Tensile and bending properties were characterised to investigate the role of Z-binder in composite mechanical properties and their failure mechanisms.

Through-thickness binders were found to resist the transverse compaction of the dry preforms. Compressibility was improved by reducing the degree of binder interlacings. Preform permeability was primarily dominated by the resin channels which were created by the Z-binder interlacings. By reducing the frequency of binder interlacings, Z binder crimp % was reduced. This reduction also increased the fibre volume fractions of the composites. Both tensile and bending properties of the composites were primarily dependent on the degree of binder weave interlacings and fibre volume fractions. Angle

interlock weave with minimum crimp % in Z-binder and least number of interlacings resulted in the highest modulus and strength in both tension and bending loads. Composite failure mechanisms were found highly sensitive to the loading directions. Damage modes were significantly distinctive in the binder way and its transverse directions. In both tensile and bending cases, the Z-binders were found the arrest the damage progression and delay the final failure of the composites.

Declaration

No portion of the work referred to in the thesis has been submitted in support of an application for another degree or qualification of this or any other university or other institute of learning.

Copyright Statement

I.   The author of this thesis (including any appendices and/or schedules to this thesis) owns certain copyright or related rights in it (the "Copyright"), and he has given The University of Manchester certain rights to use such Copyright, including for administrative purposes.

II.   Copies of this thesis, either in full or in extracts and whether in hard or electronic copy, may be made only in accordance with the Copyright, Designs and Patents Act 1988 (as amended) and regulations issued under it or, where appropriate, in accordance with licensing agreements which the University has from time to time. This page must form part of any such copies made.

III.   The ownership of certain Copyright, patents, designs, trademarks and other intellectual property (the "Intellectual Property") and any reproductions of copyright works in the thesis, for example, graphs and tables ("Reproductions"), which may be described in this thesis, may not be owned by the author and may be owned by third parties. Such Intellectual Property and Reproductions cannot and must not be made available for use without the prior written permission of the owner(s) of the relevant Intellectual Property and/or Reproductions.

IV.   Further information on the conditions under which disclosure, publication and commercialisation of this thesis, the Copyright and any Intellectual Property and/or Reproductions described in it may take place is available in the University IP Policy (see http://docum ents.manchester.ac.uk/DocuInfo.aspx?DocID=487); in any relevant Thesis restriction declarations deposited in the University Library, The University Library's regulations (see http: //www.manchester.a.c.uk/library/ aboutus / regulations): and in The University's policy on Presentation of Theses.

Acknowledgements

I would like to express my sincere gratitude to my supervisor Professor Prasad Potluri for his valuable guidance and motivation throughout my PhD. Special thanks to my co-supervisor Dr Anura Fernando and other colleagues at our research group who extended their hands to me under different circumstances. In addition, I would like to acknowledge the support I have received from the technical staff of the Robotics and Textile Composites group and the National Composites Certification and Evaluation Facility (NCCEF) at the University of Manchester (UoM). I am also grateful to Professor Philip J. Withers and Dr Billy Koe for their support in X-ray imaging. My sincere gratitude goes to Professor David Lloyd for his constant support in reviewing my final thesis.

I highly appreciate the Commonwealth Scholarship Commission, UK, for providing the financial support for my PhD.

Finally, I would like to extend my gratitude to my family members, friends, my wife, and three lovely children for their love and continuous support throughout my PhD journey.

List of Publications and International Conferences

Parts of this research has been presented at several international conferences, and some publications are in-process of submission.

1. **K. Sowrov**, A. Fernando, V. Koncherry, P. Withers, P. Potluri, "Mechanical Performance and Damage Evaluation of 3D Woven Composites with Warp and Weft Way Binders." **AIAA SciTech 2022** January 3-7, 2022, San Diego, CA, USA; https://doi.org/10.2514/6.2022-1421 (Chapter 7 and Chapter 8).

2. **K. Sowrov**, A. Fernando, V. Koncherry, P. Potluri, "Analysing the Influence of Binder Architectures on Compressibility and Permeability of 3D Woven Preforms with Warp Way and Weft Way Binders." 12th International Conference on Manufacturing of Advanced Composites **(ICMAC 2021),** 20-21, October 2021, Edinburgh, UK; (Chapter 4 and Chapter 5).

3. **K. Sowrov**, A. Fernando, V. Koncherry, P. Potluri "Effect of Binder Weave Architectures on the Tensile Properties of 3D Woven Composites and Their Failure Mechanisms". 24th International Conference on Composite Structures **(ICCS 2021)**, 14-16, June 2021, Portugal; (Chapter 7).

4. **K. Sowrov**, A. Fernando, V. Koncherry, P. Potluri, " Influence of Binder Architectures on 3D Woven Preform Compressibility and Permeability", Textile and Fashion Innovation Congress **(TFIC)**, 15-16 April 2021, UK; (Chapter 4 and Chapter 5).

5. K. Sowrov, A. Fernando, V. Koncherry, P. Withers, P. Potluri, "Mechanical Performance and Damage Evaluation of 3D Woven Composites with Warp and Weft Way Z-Binders." (**Submitted on AIAA Journal**; Dated 19th February, 2022). (Chapter 7 and Chapter 8).

Chapter 1 Introduction

1.1 Background

Textile composites are lightweight, have high modulus and strength, and excellent damage resistance compared to common metallic alloys. They deliver the benefits of through-thickness reinforcement, near net shape preforming and high drapability with easy material handling and most importantly, significant weight reduction [1]. They also offer the ability to tailor the mechanical properties to specific end-uses with high dimensional stability and low thermal expansion properties. All these combinations allow textile composites to replace the metals/alloys in various applications such as aerospace, automotive, marine, medical, sports, and civil infrastructure [2].

Most of the composite materials used so far are in the form of unidirectional (UD) and 2D laminates. These composites have high in-plane mechanical properties. In the thickness directions, these reinforcements are held together by resin only. The UD and 2D composites without through-thickness reinforcement are highly susceptible to through-thickness loading, resulting in poor out-of-plane properties. 3D woven composites, which have Z-binders as through-thickness reinforcements, are becoming more attractive as they offer remedies for these problems, reducing the manufacturing cost and time, offering design flexibility and superior through the thickness properties [3].

Although 3D woven composites offer a wide range of scopes in structural applications, their uses are still limited. There are a few reasons for this. Firstly, the lack of understanding about resin infusion and curing behaviour. The complex geometry of the 3D woven structures presents many challenges during compaction, draping and resin

flow, and composite curing. Another issue with these structures is the z binder undulation, resulting in lower in-plane mechanical properties. The lack of complete understanding regarding the failure mechanisms is probably the most important reason that limits their application. Although extensive attention has been given to exploring these drawbacks in recent days, more analytical and experimental works needs to be carried out to fully understand the nature of these composites for the sake of expanding their uses.

1.2 Problem Definition

In 3D woven preforms, the Z-binders hold the load-bearing warp and weft tows in the through-thickness direction and give the structural coherence of the preforms. At the same time, these binders induce crimp and distortion in the other tows and ultimately influence the preform and composite properties [4]. Despite extensive research on 3D woven composites, specific attention on the Z-binder influences in preform and composite properties is rarely addressed. It is a considerable research gap that needs to be explored.

1.3 Aims and Objectives

This research aims to investigate the effect of Z-binder weave architectures and tension variation on dry preform properties and the mechanical properties of the composites. Dry preforms are subjected to transverse compaction and resin infusion during composite manufacturing. This study will investigate the role of Z-binder parameters on both transverse compressibility and resin permeability of the 3D woven structures. Usually, 3D woven composites have excellent through-thickness mechanical properties, and the role of Z-binders on impact damage properties is well established in the literature. So the current research will focus on the pure bending properties of the 3D woven composites and their failure mechanisms which are rarely addressed in the literature. Along with the flexural properties, the research will also focus on the mechanics of composites during

tensile loading and how the Z-binder parameters play their role in the tensile failure mechanisms.

In order to achieve the research goal, the following objectives are set:

(i)   Manufacturing of 3D woven preforms

3D woven preforms are developed with four different Z-binder weave architectures (1x1 Plain, 2x1 Twill, 2x2 Twill with orthogonal binding pattern and an Angle Interlock structure) while the binders are incorporated in warp fibre directions. These are called warp bound structures. The weave architectures are customised to reduce the degree of interlacings sequentially. Due to sequential decrease of degree of binder interlacings, binder float length is expected to increase and crimp% is expected to decrease. These changes in Z-binders are expected to improve the in-plane mechanical properties of the composites. Necessary modifications on the weft supply system are carried out to develop another set of novel preforms with the same weave architectures. This time the binders are incorporated in the weft fibre direction, and they are termed weft bound structures. The usual practice to manufacture 3D woven preforms is to incorporate Z-binders in the warp yarn directions. However, the incorporation of binders in weft yarn directions will reduce a manufacturing step eliminating Z-binder winding process as well as give the justification of the impact of Z-binders on directional loading of composites and their failure mechanisms. Another set of preforms is developed, varying the binder tensions. The warp tension unit is modified to variate the binder tension.

(ii)   **Analysing the transverse compaction behaviour of the dry preforms**

Warp and weft bound preforms are subjected to cyclic compaction to investigate the influence of degree of binder interlacings on transverse compaction. Changes in preform thickness and fibre volume fraction against compaction load are systematically explored. The compressibility of these preforms is also measured.

(iii)   **Permeability study of these preforms**

A permeability measurement setup is developed to analyse the preform permeability. In-plane permeability of warp and weft bound preforms are measured. The permeability value is correlated to the binder degree of interlacings to see the impact of resin channels on preform permeability. X-ray micro CT images are used to explain the fibre directional influences on resin flow.

(iv)   **Manufacturing the 3D woven composites and analysing their geometrical properties**

3D woven composites are manufactured using a customised vacuum infusion method. These composites' overall fibre volume fraction is measured along with directional fibre volume fraction and void content. The crimp % of Z-binders in different weaves are also measured using microscopic images.

(v)   **Characterising the tensile properties and tensile failure mechanisms of these 3D woven composite laminates**

Tensile properties of warp bound and weft bound composites are characterised to investigate the influence of Z-binder weave architecture on in-plane tension. Tension is applied both in warp way and weft way to analyse the loading directional sensitivity of the composites. To explain the failure

mechanism, Digital Image Correlation (DIC), online video monitoring and image analysis of the post failed samples are carried out.

(vi)   **Characterising the flexural properties and flexural failure mechanisms of these 3D woven composite laminates**

Flexural properties of warp bound and weft bound composites are characterised to investigate the influence of Z-binder weave architecture on bending. The four-point bending principle is used instead of three-point bending as the former applies pure bending on the specimens. Load is applied both in warp and weft ways to analyse the composites' loading directional sensitivity. To explain the failure mechanism, online video monitoring during test progression, X-ray micro CT of the pre-loaded samples and image analysis of the post failed samples are carried out.

1.4 Thesis Outline

After the introduction in Chapter 1, Chapter 2 contains a literature review. The literature chapter is presented in six sections. The first section highlights the different topics to be reviewed in the chapter. The second section presents the general definition of 3D woven structures, their manufacturing processes and the current and potential applications of 3D woven composites. Section three discusses the response of 3D woven dry preforms under transverse compaction loading. Resin flow behaviour of 3D woven preforms is discussed in section four. General definitions of permeability and its measurement methods are also discussed in this section. Previous research investigating the mechanical performance of 3D composites is discussed in section five. Finally, this chapter concludes by highlighting the key findings from the literature study and commenting on the justification of the current research methodology.

Chapter 3 details the manufacturing process of the different 3D woven preforms considered in this research. A brief description of the weaving machine and modification of its different parts to manufacture preforms with warp way binders and weft way binders are also discussed. The warp tension unit modification is discussed to highlight the manufacturing process of 3D woven preforms with different binder tensions. All the preform specifications are detailed in this chapter.

In chapter 4, the compaction behaviour of these preforms is investigated. This chapter detailed the experimental setup, presented compaction results and analysed the effect of binder weave architectures on compressibility.

Chapter 5 then discusses the characterisation procedure to measure the in-plane permeability of these preforms. The development of a permeability measurement tool is also discussed there. The chapter discusses the permeability results of these preforms and the possible explanations for their variations.

A short chapter (Chapter 6) is dedicated to discuss the composite manufacturing process and the geometrical properties of these composites.

Chapter 7 discusses the experimental procedure to characterise the in-plane tensile properties of 3D woven composites. The effect of Z-binder weave architectures and binder tensions on tensile properties and their failure mechanisms are discussed in detail in this chapter. The chapter also details the uses of different techniques, including DIC and online video monitoring, to track stress concentrations and damage propagation.

Chapter 8 continues to investigate the composite behaviour in flexural loading. The effect of z-binder weave architectures and binder tensions on bending properties and their failure mechanisms are discussed. Four-point bending tests, carried out to characterise

the bending behaviour, are described. The damage mechanisms are explained, using results from online video monitoring during tests and X-ray micro CT on pre-loaded samples.

Finally, the key findings of this research are summarised in Chapter 9, followed by recommendations for future works.

Chapter 2 Literature Review

The literature chapter is divided into several sections. Section 1 presents the general definition of 3D woven structures, their technological development, current and future potential applications of 3D woven composites. Responses of 3D woven dry preforms under transverse compaction are discussed in section 2. Resin flow behaviour through these 3D woven dry preforms is discussed in section 3. In-plane and through-thickness mechanical properties of 3D woven composites and their failure mechanisms are discussed in section 4. Key findings from the literature review are presented in the final section of this chapter. The justification of the current research based on the literature review is also discussed in that sub-section.

2.1 3D Weaving, Technology and Applications

This section presents a brief discussion on the various types of 3D woven structures and their manufacturing technology and applications of their composites.

2.1.1 General Definition

The 3D woven structures consist of warp, weft, and binder yarns in X, Y, and Z directions. The warp and weft yarns stay in layers perpendicular to each other, whereas the binder goes inside those layers in a predefined Z- directional way so that it gives cohesion to the whole fabric structure. Fig. 2. 1 shows a schematic of developing a 3D woven orthogonal structure.
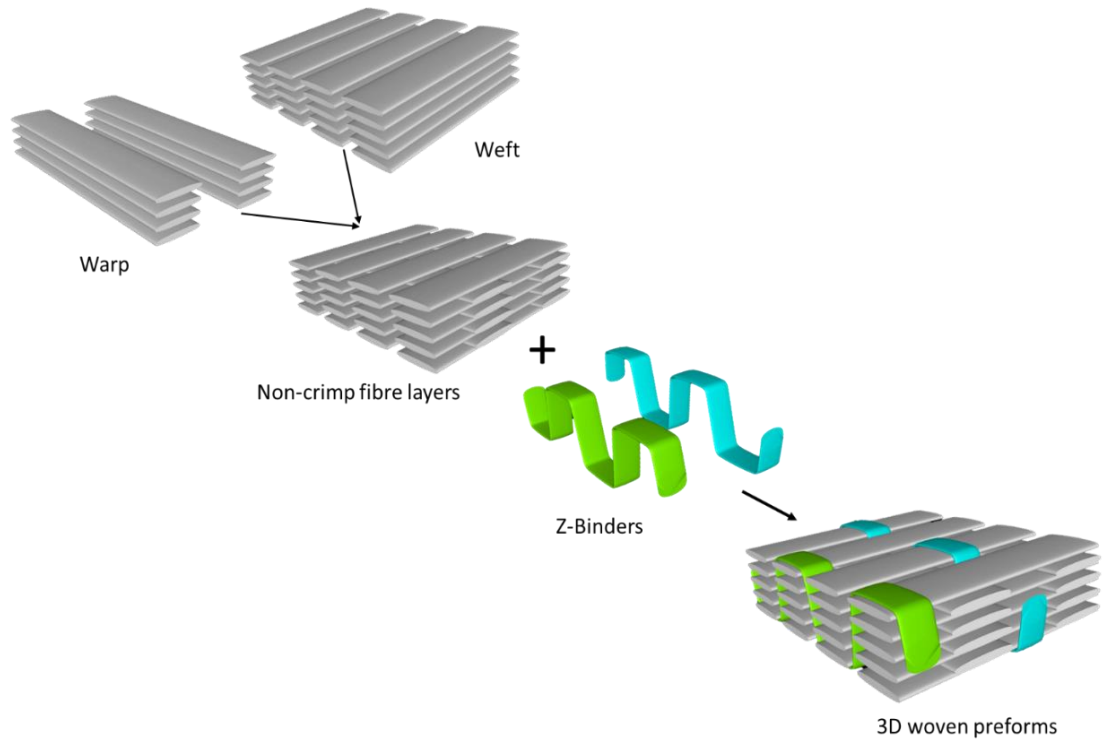
Fig. 2. 1 Development of a 3D woven structure

Two geometrical parameters distinguish the 3D woven structures – (a) angle type of binder and (b) penetration depth of the binder through the thickness of the preforms [5]. Combining these two parameters, a general classification of the 3D woven fabrics is proposed by F. Boussu et al. [6]. This classification is mentioned below (see

Fig. 2. 2).

(i) Orthogonal through-the-thickness (O/T): In this type of structure (figure a), the binder goes through all the thickness of the preform from one surface to other surfaces. Due to structural integrity, this structure is the most stable.

(ii) Orthogonal layer-to-layer (O/L): In this type of structure (figure b), the binder follows the perpendicular route to bind the other yarns but does not bind all the way to thickness; rather, it binds a specific number of layers. However, the binder collectively binds the whole thickness of the preform.
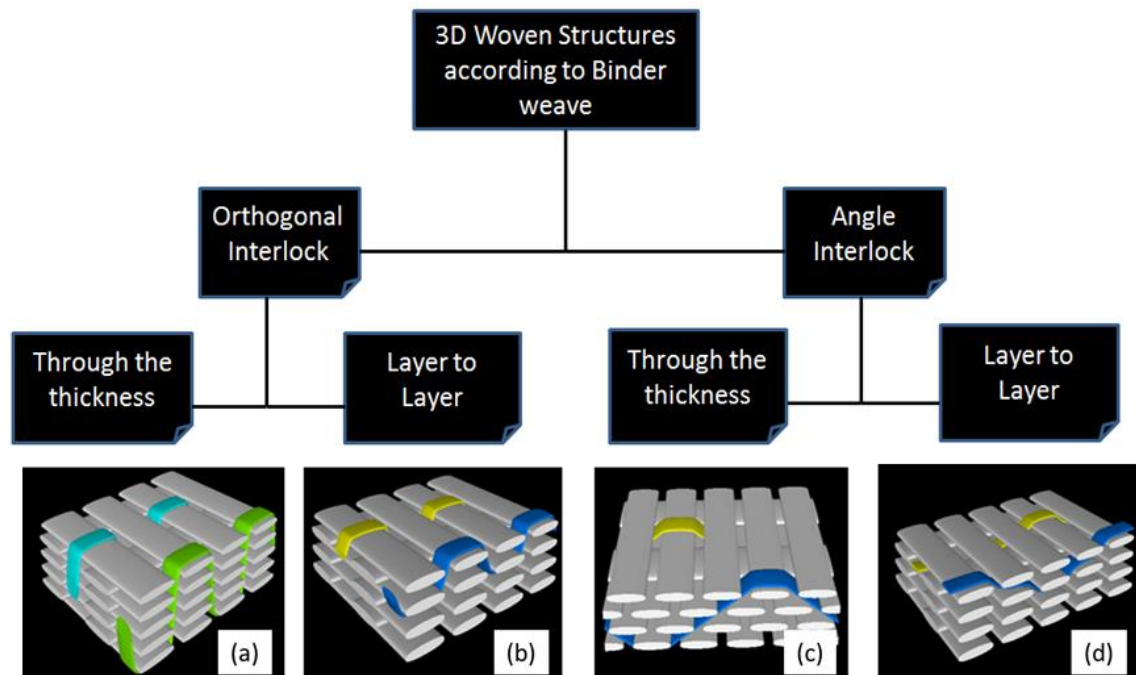
Fig. 2. 2 TexGen models of the various 3D woven structures: (a) Orthogonal through-the-thickness (O/T) (b) Orthogonal layer-to-layer (O/L) (c) Angle Interlock through-the-thickness (A/T) (d) Angle Interlock layer-to-layer (A/L)

(iii) Angle interlock through-the-thickness (A/T): In angle interlock, through the thickness structures (figure c), the binder goes through all the thickness of the preform from one surface to other surfaces, maintaining a lower binding angle. Generally, they have larger weave repeats compared to the orthogonal structures.

(iv) Angle interlock layer-to-layer (A/L): In this type of structure (figure d), the binder follows an angled route to bind the other yarns but does not bind all the way through the thickness; rather, it binds a specific number of layers. Likewise, O/L, the binder collectively binds the whole thickness of the preforms.

2.1.2 3D Weaving Technology

The conventional weaving technique has been used to produce 2D woven fabrics for hundreds of years. This traditional means of weaving involves three basic functions, namely shedding, picking and beating-up [7]. Shedding is making a gap between the warp layers, picking is inserting the weft or filler into the warp layer gaps, and beating-up is to make the structure more compact by pushing the newly inserted weft closer to the previous one (Fig. 2. 3). The cohesion of the woven structure is obtained by the interlacing of the warp and weft yarns.

a) Shedding   b) Filling (weft) Insertion   c) Beat-up
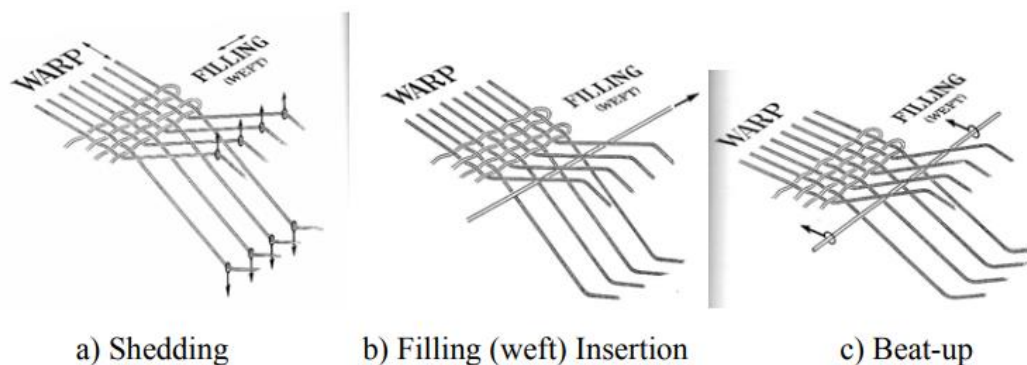
Fig. 2. 3 Basic functions of weaving: (a) shedding (b) picking (c) beating-up [7]

In 3D weaving, there is an additional set of yarns (z-binder) along with warp and weft yarns which offers more challenges to weave them together. There are mainly two ways of manufacturing 3D woven preforms- modifications of the conventional 2D loom and the fully integrated, special purpose 3D loom [8].

Perhaps the most commonly used method to manufacture 3D woven preforms is to use a modified conventional 2D loom. These modifications can be carried out in any section of the weaving machine, including but not limited to warp let-off unit, warp tensioning, shedding, weft insertion, beat-up, and preform take-up [9]. Rudov-Clark et al. used a warp beam unit instead of a creel unit to reduce the cost of preform manufacturing [10]. Chou and Cheng used a multi-warp weaving method to weave 3D orthogonal and angle

interlock preforms [11]. Patel et al. added a warp tension control unit to the existing warp creel unit to remove any tension variations among the warp layers [12]. They also modified the weft insertion unit to reduce the filamentation of the weft yarns.

However, manufacturing 3D fabrics using the 2D weaving principle has some drawbacks. When the high-performance fibres are woven in these modified looms, they are prone to damage in the form of fibre filamentation and breakages because of the repeated vertical movement to form the warp sheds. A few published pieces of research have reported the severity of fibre damage in composites properties [9], [13]. Another problem associated with this technique is the induced waviness (crimp) in the load-bearing tows, which is detrimental to the ultimate composite properties. Crimp is generated when the tows are interlacing with each other. Addressing these two critical issues, 3TEX has done a benchmark modification to the traditional 2D weaving machines for manufacturing 3D fabrics with reduced crimp and least fibre damage [14]. In this modified loom, warp movement is reduced by using multilayer shedding principles. Only the Z directional binder yarns move on each weaving cycle (see Fig. 2. 4). Hence this process reduces the chances of fibre damage as well.
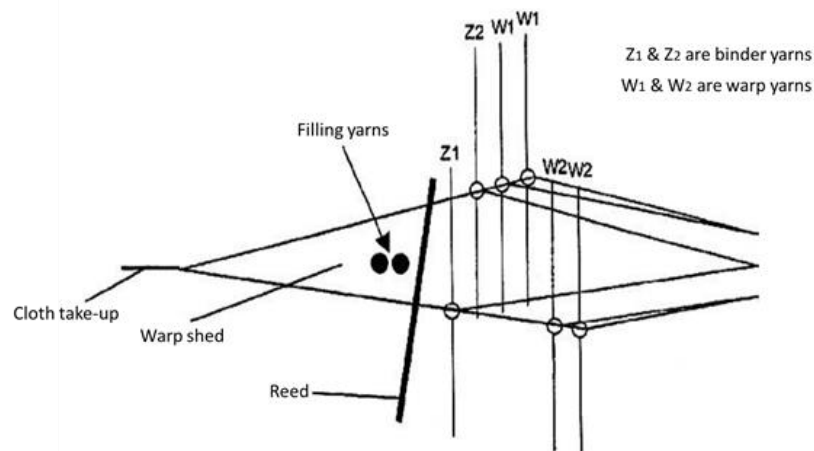
Fig. 2. 4 Warp arrangement for multilayer weaving on the 2D weaving machine [14].

Fully integrated 3D weaving techniques are developed to manufacture 3D woven preforms with non-crimp load-bearing tows with the least fibre damages. Fukuta et al. [15] disclosed a method and apparatus for manufacturing 3D woven preforms where warp, weft and binders are mutually in orthogonal position to each other. Multiple wefts are inserted simultaneously by using a stack of picking plates that are vertically spaced. Z yarns are inserted from below and above the weft layers (see Fig. 2. 5). The manufactured preforms are limited in rectangular or square block cross-sections and thickness.
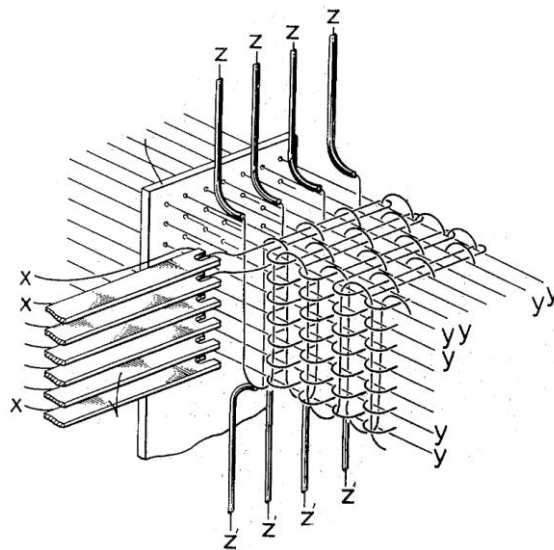
Fig. 2. 5 Schematics of 3D weaving by Fukuta et al. [15].

Mohamed and Zhang [16] have developed a novel weaving machine with multiple weft insertions simultaneously. This machine produces a unit of non-crimp multi-layered fabric at every weaving cycle. This method removed the involvement of building–up of the yarn layers as the warps are arranged in several layers, and wefts are inserted in multiple layers simultaneously (see Fig. 2. 6). As a result, a thick, non-crimp multi-layered preform is developed in each cycle of weaving. Up to ten wefts can be inserted at a time, which increases the productivity of the 3D woven preforms. The preforms

37

developed by this weaving have no internal crimp in the directional warp and weft yarns as there is no interlacing among those yarns. The yarns can also be kept in straight condition. Moreover, as only the binder moves in this weaving, the probability of tow/yarn damage is greatly reduced. However, this novel technique is limited only to orthogonal type structures. It possible to produce complex near-net shaped structures like 'I',' T',' Π',' H' etc. using this weaving machine.
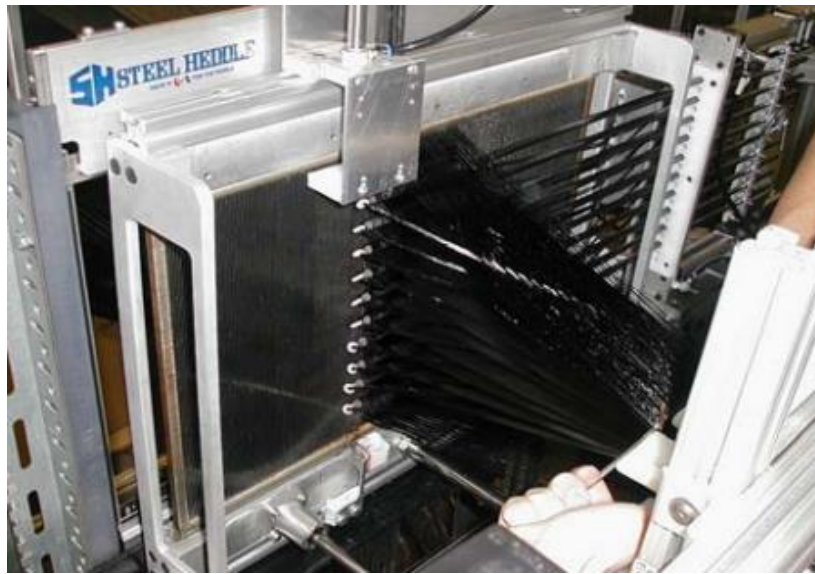
Fig. 2. 6 Simultaneous insertion of multiple fillers in 3TEX non-crimp weaving machine [15].

Potluri et al. [17] have developed another novel technique that allows flexibility in binder architectures [see Fig. 2. 7 (a)]. This novel machine can manufacture all the common 3D weaves architectures such as orthogonal, angle interlock in both through-the-thickness and layer to the layer binding pattern. This machine allows to insert twenty two wefts at every weaving cycle simultaneously. This machine is also able to produce preforms of various thicknesses as well as near-net-shape preforms (see Fig. 2. 7 (b)) [18].
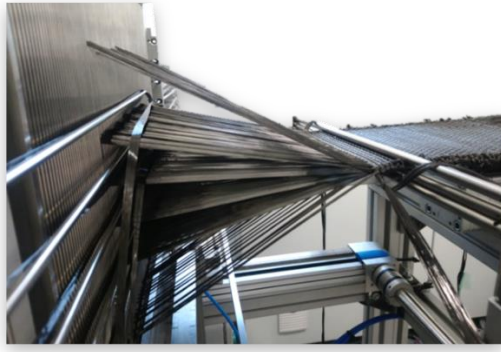
<div align="center">(a)</div>
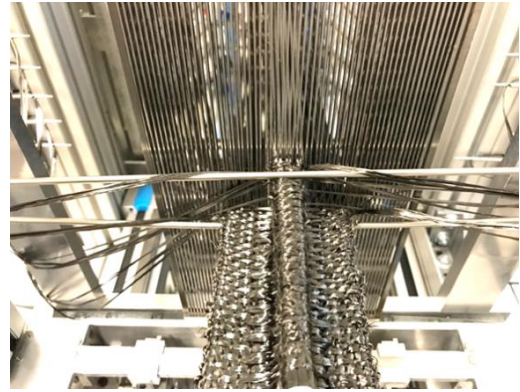
<div align="center">(b)</div>

Fig. 2. 7 (a) Multi-weft insertion loom developed by Potluri et al. [17] (b) T-shaped

preform developed on loom [18]

2.1.3 3D Weave Software

3D woven preforms are primarily developed as reinforcements of structural composites.

A number of software packages have been developed to generate the models of 3D woven

preforms and analyse their behaviour under different loading conditions. TEXCAD is

designed to calculate the elastic properties of the composites numerically as well as to

predict the progressive damage inside the composites during loading [19]. Weave

Engineer®, a software developed by TexEng [20] is dedicated for the computer aided

design and manufacture (CAD/CAM) of 3D woven textiles with both solid and hollow

architectures [21], [22]. WISETEX [23] and TexGen [24], [25] are developed based on

micromechanical models and calculate the elastic stiffness of the composites. It is

important to note that TexGen is open-source software, and all the 3D woven models

shown in this thesis were developed using this particular software.

2.1.4 Applications of 3D Woven Composites

The scope of 3D woven composites in industrial applications is ever-increasing, thanks

to their excellent structural properties. The first 3D woven composite is reported to have

been developed by AVCO in the 1970s to replace the metal alloys in aircraft brakes. In 1983 a carbon-carbon sandwich composite was used in some parts of the scramjet engine of a hypersonic missile [26]. Mouritz et al. [3] mentioned applications of 3D woven composites in the aerospace sector as rocket motors, nozzles, fasteners, and T and X shaped elements for joining fuselage to the frame structures.

From the geometric structural point of view, applications of 3D woven composites depend on the 3D weave architectures. Orthogonal 3D woven composites were used in the LEAP engine in the A320neo and Boeing 737-Max as fan blades and engine casings (see Fig. 2. 8) to improve the damage tolerance [27].

Fan Blades made of 3D woven composites

Fan case made of woven composites

3D woven composite vanes
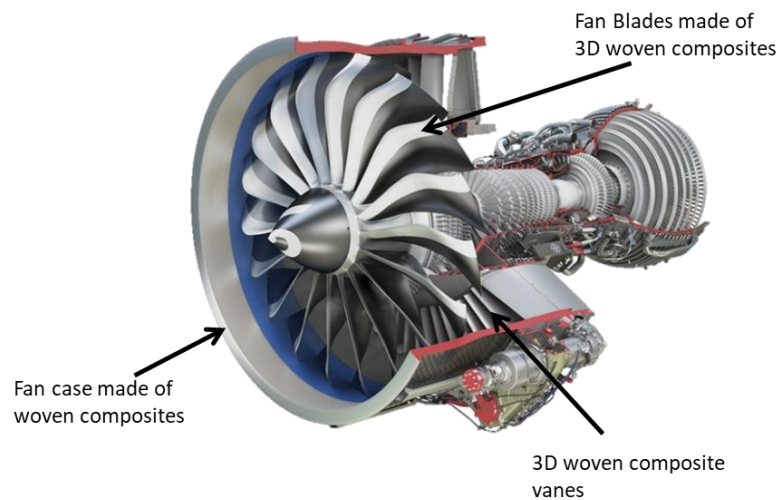
Fig. 2. 8 LEAP engine parts equipped with 3D woven composites [27].

The General Electric (GE) Company developed airframe components and fan casings for the next generation aero engine. They used a combination of multiaxial orthogonal 3D weave with 2D weaves [28]. The structure offered a high weight reduction (about 450kg). Orthogonal structures were also used in the engine fan blades in Boeing 787 and Airbus A350 [29]. Mohamed and Wetzel [30] reported the use of orthogonal weaves in wind turbine rotor blades. They have integrated $\prod$ joints to I-beams to connect the spar cap and the shear web to improve the damage property by resisting delamination. Sharp et al. also

reported the use of orthogonal weaves in rotor blades [31]. Orthogonal structures are also used in thermal applications. Hemrick reported the use of carbon fibre orthogonal 3D woven structures in the heat exchangers for vehicle radiators [32]. NASA has recently used 3D orthogonal woven composites for thermal protection and pyro-shock resistance in the Orion test vehicle (see Fig. 2. 9) [33].

Fig. 2. 9 Quartz fibre 3D woven composite used by NASA for Orion test vehicle [29].

Angle interlock and layer to layer structures are reported to have been used in high load applications [34]. These structures have been used in curved beams, brackets and T joints successfully [35]. High-strength steel has been replaced by LTL reinforced composites in the automotive industries [36]. AI and LTL architectures were also reported to have been used in truss beams with integral off-axis stiffeners, which eliminated the need for fasteners and bonds for joint applications [37]. 3D woven structures are also reported to have been used in civil [2], ballistic [38] and biomedical [39] applications.

2.2 Compaction Behaviour of Woven Structures

The dry fibre structures are compacted up to a certain pressure level during moulding in the composite manufacturing processes. This compaction affects the tow dimensions and resin channel geometry, i.e. the microstructure of the preform, and determines resin

impregnation and fibre volume fraction, which ultimately affect the mechanical properties of the composites [40], [41].

In 3D woven preforms, the Z binders hold the almost crimp-free layers of warp and weft tows together, following a path in the thickness direction and giving the structure coherence. As a result, this binder influences the preform properties and composite properties. A few compaction models of 2D woven fabrics and their multilayer structures are presented below from previous research. The compaction behaviour of 3D woven structures is discussed accordingly.

To understand compaction behaviour, extensive research has been carried out on different types of woven structures [42]–[51]. A summarised literature on the compaction of woven structures is reported by Hu [42]. Van Wyk [43] is considered the first to report a model of bending units under compression load. This research comes out with an inverse cubic relationship between the applied pressure and the volume change. The considered bending units were the elements of fibres from fibre to fibre contact areas. A new model was developed by Harwood et al. [44] considering the compression of the yarns. They modified Van Wyk's model by considering the yarn as a closed pack of fibres. Gutowski [45] proposed a similar model to Van Wyk. However, he explained the elastic deformation of carbon fibre bundles, and the compaction of the fibre bundle was ascribed to the bending of the curved filaments.

Using Van Wyk's model, De Jong et al. [46] described the pressure thickness curve of a wool woven fabric. They showed that it is not possible to explain the compaction behaviour of woven structures with a single mathematical function under all pressure ranges. Matsudaira and Qin [47] explained the microstructural changes of woven structures in compression. They proposed a pressure thickness curve having three distinct

regimes (see Fig. 2. 10). The exponentially related pressure-thickness curve is connected to two linear relationships at the beginning and the ending.
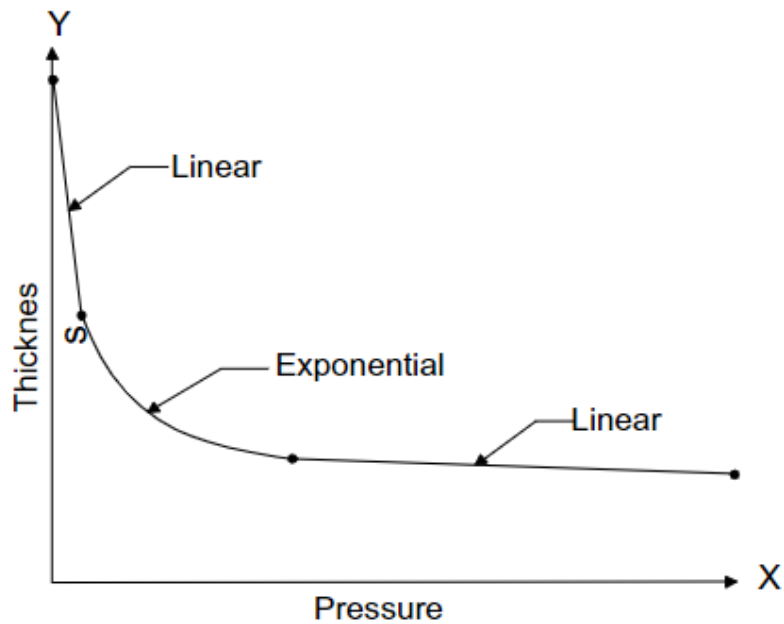
Fig. 2. 10 A typical pressure thickness curve proposed by Matsudaira and Qin [47].

The woven fabric compaction model proposed by Chen et al. [48] describes that the initial mode of compaction is due to the reduction of pore gaps among the fibres and yarns. The last stage is due to the bending deformation of yarns.

Potluri et al. [49] detailed the structural changes during the compression with the following schematic diagram in Fig. 2. 11.
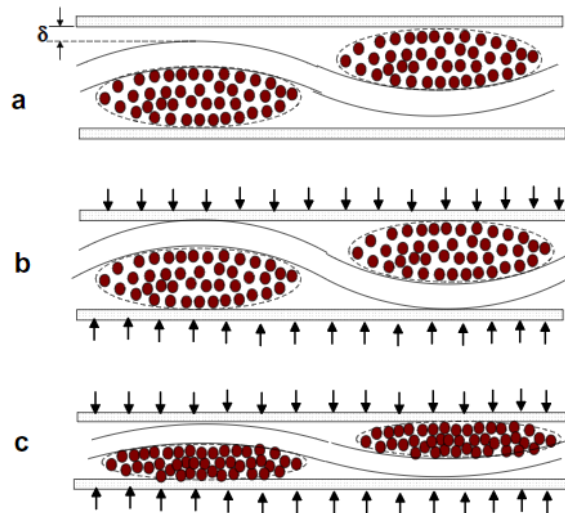
Fig. 2. 11 Stages of fabric compaction (see texts below) [49].

According to their model, fabric goes through three different stages when compressed between two parallel plates. The stages are mentioned below-

(a) The first stage is crimp balancing. At this stage, the small gaps between the warp and weft are reduced to almost zero, which increases the curvature of one set of yarns and decreases the curvature of the other.

(b) In the second stage, further compression leads to the crossing yarn flattening, resulting in the reduction in crimp of that yarn.

(c) At the final stage, the compressional load flattens the yarns until the fibres/filaments come into contact.

Several researchers have studied the compaction behaviour of multilayer fabrics [50]–[52]. Saunders et al. [52] studied the compaction behaviour of plain-woven fabric with 20 ply stacking. They concluded that the compression of such multilayers of fabrics shows three different modes. In the first mode, the nesting of yarn layers happens, which brings the fabric layers close to each other. In the second phase, the thickness of individual plies was reduced by the reduction of yarn crimp amplitude, and in the third mode, the

fibres inside the deformed yarns are also deformed and compressed. A similar conclusion is drawn by Potluri et al. [49] for the multilayer woven structures.

 Chen et al. [50] identified the main contributing factors that lead to the compaction of the multilayer woven structures. These factors are shown below in Fig. 2. 12. Their micromechanical model also showed that the plain weaves encounter the least deformation compared to twill and satin weaves. This smaller deformation is because of the highest ratio of curved parts to straight parts in the weave structures, resulting in more resistance to compression.
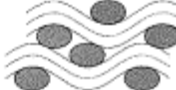
Fig. 2. 12 Compaction factors in multilayer woven structures [50].

The compaction behaviour of 3D woven preforms is expected to differ from the 2D woven preforms due to their complex internal structures caused by the through-thickness binders. However, only a few pieces of research have been found that explore the compaction behaviour of 3D woven structures [53]–[59]. Parnas et al. [53] reported that the compressibility of some undisclosed 3D woven structures is lower than random mats. Endruwiet and Long [54] investigated the compressibility of different 3D woven preforms. They considered two angle interlock structures and an orthogonal preform.

They carried out quasi-static compaction at single and cyclic loading at a force of 10kN. They have found that the orthogonal preform shows the least compressibility because there is no offset between the identical layers of yarns/tows. The main compression is due to the compaction of the fibres bundles. The binder yarns offer more stiffness and prevent bending of the weft bundles, leading to lower compressibility. They also remarked that the binder yarn show high compaction and deformed the weft bundles at a high compression load. The binders buckled under high compression, which affects the geometry of voids.

Mahadik et al. [55] investigated the compression behaviour of two layer-to-layer preforms with different binder interlacement sequences and at different levels of compaction. They used X-ray micro-CT to capture the internal geometry of these structures at increased compaction levels. They found that the major initial changes in the structures are due to the nesting of weft yarns between the interlacing points by the binders. Further compaction modes include closing the gaps between warp and weft yarns/tows and straightening the single tows.

Vernet and Trochu [56] reported the compaction behaviour of five angle interlock structures with different warp-weft ratios. They identified that tow flattening and bending are the primary compaction phenomenon. The compaction behaviour of a 3D orthogonal structure with a 5/1 binder weave was investigated by Stewart et al. [57]. They reported that a limited nesting was formed on the weft tows close to the binder crossing areas. They also mentioned that the angular binder path allowed more compaction in the thickness direction. Swery et al. [58] and Alhussein et al. [59] reported that multiple cyclic compactions resulted in permanent deformations within the preform structures, due to the changes in the tow geometries. They also found that the less vertical binder path in layer

to layer preforms allows more compaction than the orthogonal structures where the binders are far more vertical.

2.3 Resin Permeability of 3D Woven Preforms

A general discussion on the resin permeability through the textile preforms and measurement procedure for in-plane permeability is included in this section. The effect of preform parameters, especially the Z-binder's role on permeability, is also presented.

2.3.1 Permeability Definitions

Permeability is the property of a porous medium that explains how easily a fluid flows through the material. This property varies in all three dimensions of the preforms, i.e. X, Y and Z directions.

Permeability is measured in two conditions-dry preform condition and wet preform state. When the flow is measured in resin filling-in condition of the dry preform, it is called unsaturated or transient permeability. It is measured by tracking the flow front with respect to time. Saturated or steady-state permeability is measured when the preform is wetted, and the flow stabilises. Generally, by sensing the pressure drop, saturated permeability is measured.

Permeability is also measured in the preform's in-plane and out-of-plane directions. Generally, only the in-plane permeability is measured for those materials with a minimum thickness. For a material with a considerable thickness, the out-of-plane or through-the-thickness permeability needs to be measured. The permeability can be measured using both unidirectional (1D) and radial flow (2D).

In unidirectional flow, also known as channel /rectilinear flow, the resin is allowed to flow from one end of the preform to the other with the help of infusion pressure. Both unsaturated (transient) and saturated (steady-state) permeability can be measured by following the channel flow method. In the case of unsaturated permeability, the flow front progression is monitored when the cavity is being filled. In the latter case, permeability is measured by the pressure drop between two selected points when the preform is filled with the resin. A schematic figure is shown below to illustrate the methods (see Fig. 2. 13).

(a)   (b)
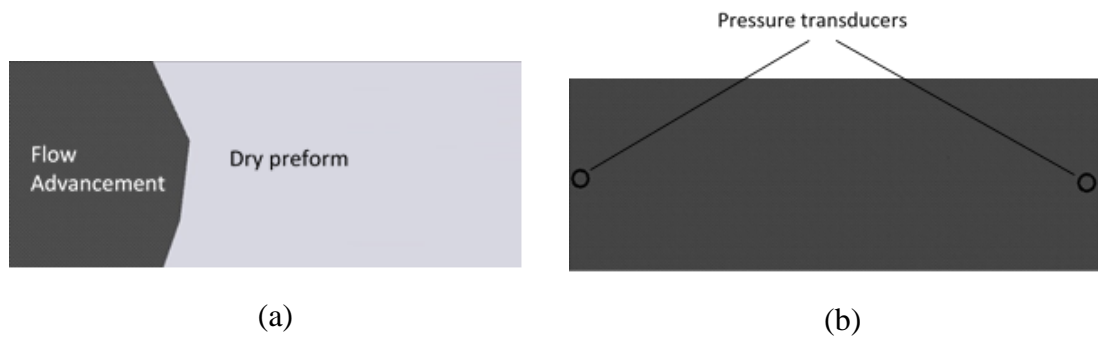
Fig. 2. 13 Schematic of the channel flow permeability measurement: (a) Transient flow or unsaturated flow, (b) Steady-state flow or saturated flow.

For orthotropic preforms, it is required to perform three experiments with the preform at 0°, 90° and 45° directions, to determine the principal permeability. Weitzenbock et al. [60] proposed the following model (see Fig. 2. 14) for yielding effective permeability tensors (K_I, K_{II}, K_{III}) in those directions. In those directions, these effective permeability tensors are used to calculate the principal permeability values, K_1 and K_2.
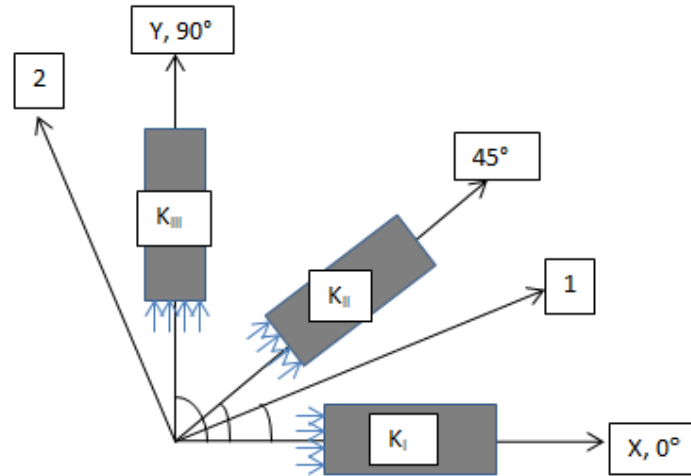
Fig. 2. 14 Measurement of principal permeability in two dimensions [55].

The radial flow method, also referred to as 2D permeability, is measured by injecting the resin from the transverse direction of the preform at a particular position, usually from the centre position. When the actual flow occurs through the preform, the resin follows a radial pattern. The shape of the radial flow depends upon the nature of the preform. The flow will follow a circular shape (Fig. 2. 15) for the isotropic medium. For the orthotropic medium, it develops through an elliptical shape (Fig. 2. 15).
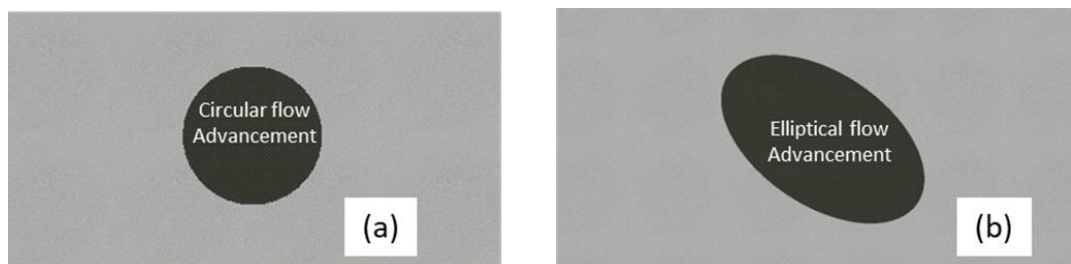
Fig. 2. 15 Radial flow permeability: (a) Isotropic preform and (b) Orthotropic preform.

Like the channel flow method, permeability is also measured on both unsaturated (dry) and saturated (steady-state) states in the radial flow method. Permeability values are

obtained by tracking the progression of the flow front on the unsaturated method and using the pressure drop for the saturated flow.

The most advantageous feature of the radial flow method is that, the permeability values of both X and Y axes can be measured in the same experiment. This is because the principal directions coincide with the major and minor axes of the elliptical flow front [61], [62].

When the permeability is measured through the thickness/out-of-plane direction of the preform, it is termed as 3D permeability or through the thickness permeability. In general, when the preform thickness is minimal, this is neglected in permeability measurement. However, for 3D preforms, it is necessary to measure the out of plane permeability to understand the complete impregnation of that preform. Due to difficulty in front flow tracking in the thickness direction, in most cases, the 3D permeability is measured in saturated conditions using the pressure drop.

2.3.2 Flow Analysis

The principal permeability (i.e. permeability in the warp and weft directions) can be measured only if the effective permeability values are obtained. The effective permeability is the scaler value of the flow front tensors in three different directions- warp (0°), weft (90°) and off-axis (45°).

Linear flow method

Vernet et al. in their benchmark work [63] and in the guidelines provided by Alms et al. [64], the whole technique to measure the effective and principal permeability using the linear flow method is documented. In this technique, the preform needs to be cut in three directions from the fabric sample. The cutting orientations are shown in Fig. 2. 16.
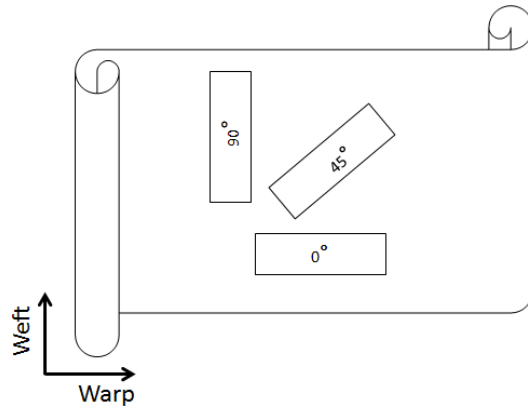
Fig. 2. 16 Cutting directions of the preforms from bulk.

(a)   (b)
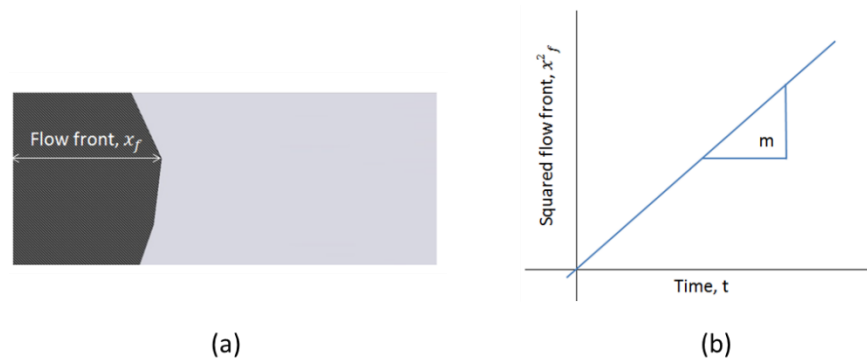
Fig. 2. 17 (a) Flow front progression, (b) Slope measurement in the squared front flow

method (schematic) [64].

The permeability is measured using the following equation based on Darcy's linear constant pressure infusion law.

$$K_i = \frac{x_{f,i}^2 \varnothing \mu}{2 \Delta P t_i} \quad \dots\dots\dots\dots\dots\dots\dots \quad (2.1)$$

Where X_f is the flow front position [see Fig. 2. 17 (a)], $\varnothing$= porosity of the preform, μ is the viscosity of the resin, ΔP denotes pressure difference, and t is the time in seconds. In the equation, $\frac{x_{f,i}^2}{t_i}$ is replaced with the slope (m) of the trend line mentioned earlier [see Fig. 2. 17 (b)]. So the effective permeability equation becomes

$$K_i = \frac{\emptyset \mu}{2\Delta P} m \quad \ldots\ldots\ldots\ldots\ldots\ldots \quad (2.2)$$

Here i = I, II and III for effective permeability in 0°at 90° and 45° directions.

The fibre volume fraction is measured with the following formula

$$V_f = \frac{A_w N_L}{\rho_f h} \quad \ldots\ldots\ldots\ldots\ldots \quad (2.3)$$

Where A_w is the areal density, N_L is the number of layers, ρ_f is the fibre density, and h is the thickness of the preforms. From the volume fraction, porosity is calculated using the following formula

$$\emptyset = 1 - V_f \quad \ldots\ldots\ldots\ldots\ldots\ldots \quad (2.4)$$

With the effective permeability tensors, the principal permeability is calculated using the following equations

$$k_1 = k_I \frac{A-D}{A-(\frac{D}{\cos(2\theta)})} \quad \ldots\ldots\ldots\ldots\ldots\ldots \quad (2.5)$$

$$k_2 = k_{III} \frac{A+D}{A+(\frac{D}{\cos(2\theta)})} \quad \ldots\ldots\ldots\ldots\ldots\ldots \quad (2.6)$$

Where A= $(K_I+K_{III})/2$, D= $(K_I-K_{III})/2$ and Θ is the angle of rotation. The following formula calculates the angle of rotation

$$\theta = \frac{1}{2}\tan^{-1}(\frac{A}{D} - \frac{A^2-D^2}{K_{II}D}) \quad \ldots\ldots\ldots\ldots\ldots\ldots \quad (2.7)$$

The resin race tracking (where the flow develops unevenly epsecially in the longtitudinal sides of the prefoms) is one of the concerning issues in the linear flow method. So the race track is measured with the following equation.

$$R = (\sum_{i=1}^{n} x_{f,i} - x_{n,i})/(n.L) \quad \text{............................} \quad (2.8)$$

Radial Flow Method

The resin is injected from a central gate in the radial flow method. For the orthotropic material, the flow is an elliptical shape. A single experiment can measure the effective permeability tensor in all three directions in this method. Weitzenbock et al. have documented this technique in their works [61], [62]. The permeability tensors in three different directions in radial flow are shown in the following Fig. 2. 18.
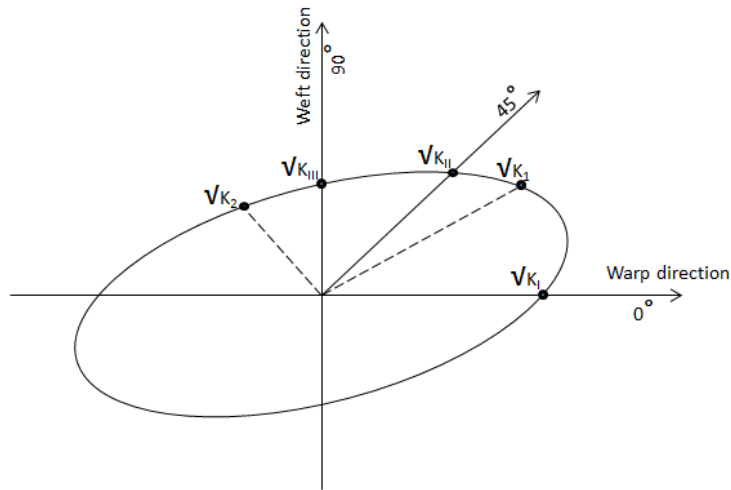
Fig. 2. 18 Effective permeability tensor in radial flow method [61].

Here in this method, the principal permeability is measured using the following equations

$$k_1 = k_I \frac{A-D}{A-(\frac{D}{\cos(2\theta)})} C \quad \text{.............................} \quad (2.9)$$

$$k_2 = k_{III} \frac{A+D}{A+(\frac{D}{\cos(2\theta)})} C \quad \text{..............................} \quad (2.10)$$

Where A= $(K_I+K_{III})/2$ and D= $(K_I-K_{III})/2$ and C is a constant calculated from preform porosity (Ø), resin viscosity (μ) and infusion pressure (P) with the following formula

$$C = \frac{\text{Ø}\mu}{4\Delta P} \quad \text{...............................} \quad (2.11)$$

The angle of rotation, Θ is calculated using the formula mentioned in the linear flow measurement method.

The effective permeability is calculated by the following formula.

$$K_i = \frac{N_i}{t_i} \quad \ldots\ldots\ldots\ldots\ldots\ldots\ldots\ldots\ldots\ldots \quad (2.12)$$

Here i = I, II and III for effective permeability at 0°,90° and 45° direction, respectively. Also,

$$N_i = r_{f,i}^2 [\, 2\ln(r_{f,i}/r_{0,i}) - 1] + r_{0,i}^2 \quad \ldots\ldots\ldots\ldots\ldots\ldots\ldots\ldots \quad (2.13)$$

The radii are defined as $r_{f,i} = \sqrt{x_{f,i}^2 + y_{f,i}^2}$ and $r_{0,i} = \sqrt{x_{0,i}^2 + y_{0,i}^2}$

Where $(x_{f,i}, y_{f,i})$ and $(x_{0,i}, y_{0,i})$ are the coordinates of the flow front (f) and inlet (0) of the physical system.

2.3.3 Permeability of 3D Woven Structures

Although extensive research has been carried out to measure the permeability and resin flow behaviour of unidirectional (UD) and 2D fibre reinforcements [65]–[75], only a few works have been reported related to the 3D woven structures [54], [59], [76]–[80].

Endruweit et al. [54] have studied three selected 3D carbon fibre preforms to investigate the influence of Z binder on in-plane and through the thickness permeability. They used two angle interlock structures and one orthogonal structure preform for their investigation. They reported that the binders create resin channels, enhancing the resin flow for the orthogonal structures. At low fibre volume fractions, the impact of these resin channels is highly dominant, resulting in significant differences between the warp and weft way permeability values. The flow is more uniform at high fibre volume fractions

in the two principal directions. The in-plane permeability was measured using the unsaturated radial flow method.

Vernet and Trochu [76] studied the permeability of five 3D interlock fabrics with different tow densities and weave patterns. They used the unsaturated unidirectional flow method to measure the in-plane permeability. Their study found that microscopic pores have a significant impact on permeability value. Another interesting conclusion from their study is the independence of permeability values from pore sizes. It is reported that as long as the total volume of the pores in a structure remains the same, the permeability values will also be the same as long as the resin viscocity does not change.

Umer et al. [77] studied the permeability of three different 3D woven preforms: orthogonal, angle interlock and layer to layer structures. They reported that the orthogonal and angle interlock structures have more in-plane permeability than the layer to layer structures. To explain this phenomenon, they used X-ray CT scan images. They have found more and larger mesoscopic gaps around the Z binder for the orthogonal and angle interlock structures, allowing the resin to flow more easily. The permeability of the layer-to-layer structure was lower due to the smaller and fewer gaps between the layers.

A similar observation was also reported by Alhussein et al. [59]. Their study reported that the larger gaps around the z binders reduced significantly with the compaction pressure, resulting in lower in-plane and through-the-thickness permeability. Ali et al. [78] used a hybrid experimental and numerical approach to determine the in-plane permeability of a 3D orthogonal structure. They found that the size of the resin channels and the shape of the binder yarns play a vital role in determining the in-plane permeability values of 3D woven structures. They also reported that the Z-binder substantially obstructs in-plane resin flow, reducing the permeability value in that direction. Stig et al. [79] studied the

permeability of an angle interlock structure with two structural variables - tow crimp and fibre volume fraction. They found that the fibre volume fraction is the one that significantly affect the permeability values. They also concluded that the tow crimp variation has minimal impact on the resin flow behaviour.

The 3D permeability of each sub-layer depends on the yarn permeability, inter yarn gap permeability and the areal coverage of the fabric. Xiao et al. [80] correlated the fabric permeability with yarn permeability and equivalent gap permeability. They found that the equivalent gap permeability is more dominant in the through-thickness direction.

2.4 Mechanical Properties of 3D Woven Composites

Due to the Z binder, 3D woven composites exhibit superior out-of-plane properties by preventing damage growth with a compromise in the in-plane properties. This subsection discusses the in-plane and through-thickness mechanical properties of 3D woven composites and their failure mechanisms.

2.4.1 Out-of-Plane Mechanical Properties

3D woven composites have been investigated by researchers for their superior impact damage tolerance. For aerospace applications, the 3D composites are impact tested with a wide range of impact velocities from low (<10m/s), to high (>50m/s), and to ballistic (~900m/s) [34]. Many researchers [81]–[86] have impacted the 3D woven composites with low to high impact velocity to evaluate their resistance to hail and bird strikes during flight, dropping of tools during the maintenance or kick-up of debris during taxi. Ballistic impact resistance was investigated using high-velocity bullets to understand their response in military aircraft and armoured applications [87].

Impact damage tolerance of orthogonal 3D woven structures was found as much as twice as similar 2D woven structures [83], [88]. In both cases, the Z-binder is found to delay the damage mechanism and improve the damage tolerance. It is also concluded that the impact properties can further be enhanced by improving Z binder parameters [88].

To investigate the influence of binder fibre volume fraction on composite properties, Gerlach et al. [89] studied two angle interlock 3D woven composites with binder fibre volume fractions of 3% and 6%. They found that the binder content considerably influences the matrix delamination. With more Z binder content in the structure, the delamination resistance increases.

To investigate the role of Z- binder in delamination resistance, Guenon et al. [90] studied composites with 1% through the thickness Z binders. They found that even this small amount of z binders improve the fracture resistance more than ten times in the out-of-plane direction and 25% in the in-plane direction compared to the counterpart 2D laminates. The biggest amount of fracture resistance is reported by Arendts et al. [84]; they added 8% Z-binder and found that the delamination resistance increased by more than 20 times compared to the 2D laminates.

 An explanation for the improved delamination resistance of the 3D woven composites is given by Mouritz et al. [91]. The study concluded that the high delamination resistance is due to the debonding of fibre to the resin, bridging and pull-out of the Z-binders and crack branching (see Fig. 2. 19).
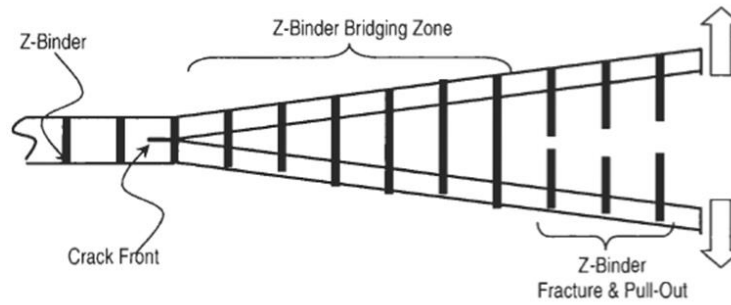
Fig. 2. 19 Schematic of mode-I delamination cracking in 3D woven composite [91]

Tanazawa et al. [92] reported improvement in delamination toughness by making the Z binder path slacker. They decreased the binder tension for slackening the binder path. This slackening of the z binder resulted in longer effective stretching and pull-out length, which made the bridging zone larger. Umer et al. [93] investigated the effect of weave architecture on damage tolerance of the 3D woven composites. They studied the common 3D weave architectures: orthogonal, angle interlock, and layer-to-layer. Damage tolerance of the composites was studied using two different impact energy, 25J and 40J. They found that due to the coherent nature of the orthogonal preform, the damage is very limited with small delamination adjacent to the impact location on the top surface. In contrast, a significant level of fibre fracture & delamination resulting in severe damage was found for the angle interlock and layer-to-layer laminates. Potluri et al. [94] reported that a structural modification of layer to layer composites improved the impact damage significantly. They used two additional yarn layers on top and bottom surfaces of the preforms, which delayed the failure mechanisms in impact loading.

Luo et al. [95] reported that the impact damage mechanisms of 3D orthogonal composites were due to matrix cracking, fibre breakage, and fibre pull-out. Seltzer et al. [96] used X-ray CT to explain this higher energy absorption by the 3D structures. They found that the higher energy absorption was due to delamination resistance offered by the Z- binders.

The binder dissipated the energy to different damage mechanisms, including tow splitting, out-of-plane shear and extensive tow rupture.

Bending properties of 3D woven composites have been reported in several research works. Bending properties and failure mechanisms are reported to be highly influenced by the preform weave architectures. Most importantly, the through-thickness binders were found to resist the growth of delamination cracks [89], [97]–[102]. Dai et al. [98] investigated the bending behaviour of 3D woven composites with orthogonal and angle interlock structures under three-point bending tests. They found that the angle interlock structure with an angled binder path exhibited more stiffness and strength than the orthogonal weaves. They also reported that the dominant failure mode was tow-matrix delamination. A similar finding is also addressed by Umer et al. when they conducted three-point bending tests on orthogonal, angle interlock, and layer to layer composites [97]. Kuo et al. found that introducing through-thickness Z binders is an effective method to arrest the delamination [99]. Gerlach et al. reported that the binder density controls the delamination length [89]. Jin et al. investigated the fatigue responses of 3D angle-interlock glass/ polyester woven composites under three-point bending. They concluded that the main failure modes are a combination of crack propagation and tow rupture [100]. Zhang et al. reported that the ultimate bending failure combines kinking, cracking in matrix and fibres, intra-ply delamination, and fibre bundle rupture under three-point loading [103].

2.4.2 In-Plane Mechanical Properties

Due to the through-thickness Z-binder, the 3D woven composites have superior out of plane properties when compared to the equivalent 2D laminates. However, their in-plane

mechanical properties are often compromised due to manufacturing induced defects such as undulation in load bearing tows and fibre filamentation [104].

One of the major factors for lower tensile properties is the waviness and crimp of the Z-binders and other load-bearing tows. J.P.Quinn et al. [105] reported a Z binder crimp of about 19%, reduced the tensile modulus and strength by more than 11% and 50%, respectively. The binders pinch the other load-bearing tows at interlacings and thus induce crimp on these load-bearing tows as well (see Fig. 2. 20). As a result of the crimp and waviness in load-bearing yarns, the ultimate tensile properties are reduced [4].
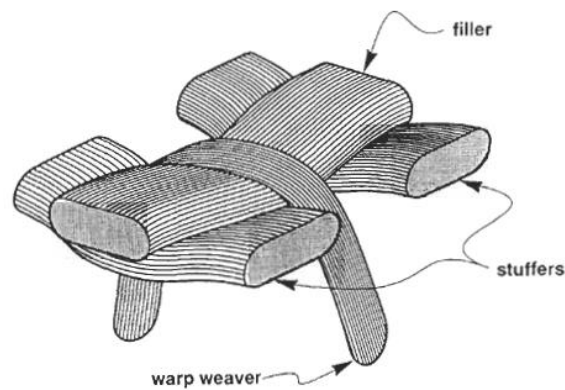
Fig. 2. 20 Schematic view of tow pinching by binder producing distortion and crimp [4].

Stig et al. [106], [107] studied three orthogonal composites with different warp crimps. They found that the least crimped composite resulted with improved tensile modulus. Bogetti et al. [108] reported that strength reduction is extremely sensitive to ply waviness. Callus et al. used an orthogonal and two angle interlock (normal layered and offset layered) preforms to examine the influence of binder weaves on the tensile properties of 3D woven composites. They reported that the offset layered interlock structure, due to having less waviness, performs better in tensile loading [109]. Dai et al. [98] focused on four orthogonal and two angle interlock woven composites with different binder weave patterns. They found the least wavy architectures showed the most enhanced tensile properties and thus concluded that the tensile properties of 3D woven composites could

be improved by minimising the waviness of the load-bearing yarns [98]. Saleh et al. [110] studied the effect of Z binder architectures on laminate geometrical properties and tensile properties. They considered three different architectures of 3D woven composites having distinct binder weaves (ORT, AI and LTL). The study reported that the tensile properties are highly sensitive to the loading direction. It also suggested that the tensile properties are dominated by the directional fibre volume fraction [110].

Another challenge in 3D woven composites is the fibre/tow damage during weaving. Warp tows and Z-binders are extremely susceptible to breakage due to frequent movement during shed formation. A major cause of damage is due to two types of abrasion: fibre-to-fibre abrasion and fibre-to-machine component abrasion [10], [13], [111], [112]. Lee et al. showed that E-glass fibre loses about 30% of its strength after weaving due to extreme breakage and filamentation of the tows. This reduction contributed to the 20% strength reduction in the ultimate composite [13].

Dhiman et al. [113] reported that the higher squashed area at the interlacement points led to reduced tensile properties. They studied two orthogonal composites with 6K and 3K binders. They found that the composite with a 6K binder has much wider crossing points and significantly lower tensile strength. Leong et al. [114] modified the binder path from a quasi-sine wave to a quasi-square wave (see Fig. 2. 21), where they managed to reduce the resin-rich areas in composites. They showed that, due to this modification, tensile strengths were improved.
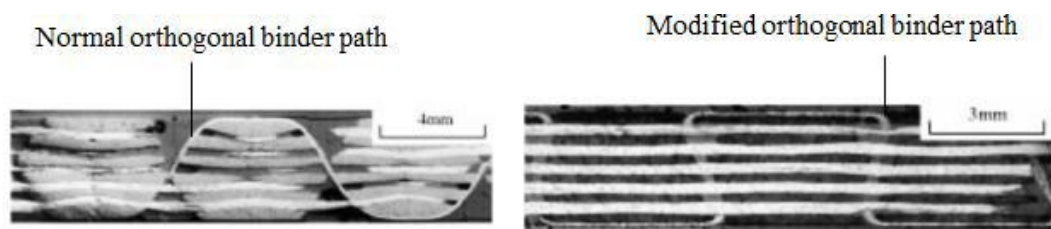
Fig. 2. 21 Different binder path orientation used by Leong et al. [114]

The effect of binder in the tensile failure of 3D woven composites has also been studied repeatedly. Early investigation by Cox et al. reported that the dominant failure modes were fibre pull-out and tow rupture, when they loaded orthogonal and layer to layer composites in tension [4], [115]. Binders cause stress concentrations and create a weak point in the 3D woven laminates which then initiates the cracks in the composites and ultimately leads to final failure. Castaneda et al. studied the tensile response of an orthogonal composite loaded in both warp and weft directions to understand the influence of Z binder in tensile properties and failure mechanisms [116]. They used a combination of DIC, AE and X-ray tomography to correlate the failure mechanisms. They concluded that the dominant failure mechanisms involved surface tow debonding, surface tow transverse cracking and inner tow debonding. They also suggested that, even though these binders cause the out-of-plane deformations, they still assist these composites in transverse directional reinforcement. Lomov et al. identified the binder interlacement points as the damage initiators, which then progressed orthogonal to the loading directions [117]. The composites finally failed when the load-bearing tows were fully ruptured. A recent study also showed that the strain localisations are highly dependent on weave architectures and these strain locales are the damage initiators [118]. A recent investigation by Sawrov et al. [119] reported that the damage mechanisms are highly sensitive to the loading directions. In the binder way loading, matrix cracking is the dominant initial failure, whereas, in the orthogonal direction to the binders, tow-matrix debonding is the major failure type.

Compressive properties of 3D woven composites are also found to be highly affected by the waviness of the binder and load-bearing tows. Y. Mahadik & S.R. Hallett [120] reported that the high crimp in the Z-binder reduces the compressive strength even if the load-bearing yarns are comparatively crimp free. They used X-ray CT scans to show that

the failure is initiated from the highly crimped area, leading to further stuffer failures. Johnson et al. [121] reported that the preform with the layer to layer weave, which has lower stuffer waviness than the angle interlock, exhibits higher compressive strength. Wang et al. [122] reported that compression failure is due to the local yarn buckling and kink bands formation. He also reported that the through-thickness Z-binder decreases the failure zone's delamination possibility and size. Cox et al. [115], [123] have explained that composite failure in compression is caused by kinking of the load-bearing yarns. Kuo et al. [124] explained that there are two primary failure modes for 3D woven composites in compressive loading. The first one is the microscopic fracture band which consist of fibre kink bands in axial fibres and matrix cracking in the transverse directions. The other one is the mini-scopic band, which consists of tow ruptures. They reported that although the microscopic bands are more intensive and are responsible for the initial damage due to the fibre misalignment and local stress concentrations, the ultimate failure is caused by the mini-scopic failure, which is dominated by the reinforcement weave architectures. Farley et al. [125] reported that the successive penetration of the Z-binder creates loops on the surface of the outer layer. These loops are the cause of kink. With the removal of these loops, an increment in the compressive strength by 7-35% was found.

Warren et al. [126] and Dai et al. [98] studied the effect of weave architectures on the compressive properties. In the earlier case, it was found that the orthogonal composites outperform the layer to layer composites, and in the second study, an angle interlock composite was found to outperform orthogonal performs. In both cases, it is reported that the maximum compressive properties are recorded for the least crimped structures.

2.5 Key Findings from the Literature & Justification for this Research

2.5.1 Key Findings

From the literature review, the following key findings can be noted.

(i)   3D weaving offers the versatility to develop 3D reinforcements for various applications. Highly complex structures with near-net-shape preforms can be conveniently developed by using this manufacturing technique. Yet the development of 3D woven preforms has been limited due to the manufacturing induced defects and limited availability of integrated 3D weaving machines.

(ii)   Both compressibility and resin permeability of 3D woven are preforms are weave architecture-dependent. Transverse compaction of the preforms is often resisted by the Z-binders resulting in less compressibility in orthogonal structures. Resin permeability is primarily driven by the resin channels created by the Z-binder path.

(iii)   The excellent delamination resistance and superior impact damage properties of 3D woven composites are due to through-thickness reinforcement offered by the Z-binders. Due to the presence of through-thickness binders, the failure mechanisms of these composites are complex and consist of several failure modes.

(iv)   The in-plane properties of 3D woven composites are often lower compared to the UD and 2D woven composites. This is due to the undulation and waviness of the binders and other load-bearing tows. A common conclusion drawn from the tensile and compressive response of these composites is that the in-plane properties can be improved by reducing the waviness of the structural yarns.

2.5.2 Justification for this Research

In most cases, the characterisation focused either on dry preform properties or composite mechanical properties. The current research focused on a comprehensive characterisation where the role of Z-binder is investigated for both preform and composite mechanical properties.

Although extensive research has been carried out on 3D woven composites and the interest is continuously increasing, in most cases, the concentration is focused on commercially available common structures, namely orthogonal, layer to layer and angle interlock structures. These are structurally so different that it is very difficult to correlate the impact of z-binders among these structures. So the current research concentrates on developing such preforms where the variation of Z binders can be strongly correlated. Considering this, four 3D woven preforms were developed where the degree of interlacings was sequentially reduced to decrease the binder crimp.

Another novelty of this research is the development of weft bound performs by altering the binder incorporation direction. This binder path alteration will be useful for explaining and justifying the impact of resin channels and binder crimp on resin permeability and mechanical properties of the composites and their failure mechanisms.

Another point is that only reinforcement architectures were taken into consideration in most previous research. Binder tension, which can strongly impact the preform and composite properties, was rarely considered for characterisation. The current research also considered this parameter of 3D woven structures.

Chapter 3 Manufacturing of 3D Woven Preforms

3.1 Introduction

This chapter gives a brief discussion on warp bound and weft bound 3D woven structures. The manufacturing process of the 3D woven preforms is detailed with the description of the weaving machine and preform designs. The method of manufacturing 3D woven preforms with different tow tensions is also discussed.

3.2 Description of the Weaving Machine

3D woven preforms can be manufactured by using a variety of automated looms starting from conventional shuttle looms [127] to modern shuttleless looms [128]–[130] and specially designed weaving machines [15], [16], [131]. Some of the important criteria for selecting the weaving machine are the scope of preform structural design variety and the high degree of automation. Jacquard shedding because of specialised harness control system, offers the scope of the highest design versatility. On the other hand, modern shuttleless looms offer a high degree of automation which reduces the manufacturing costs of process inspection and increases the design repeatability and quality of the product [7].

A Dornier loom with jacquard shedding mechanism and rigid rapier weft insertion systems is used for manufacturing the intended 3D woven preforms with different binder weaves and tensions. The loom was previously modified for weaving the carbon fibre. The machine is shown in Fig. 3.1. The integrated weaving setup can be broadly divided into three sets of units: warp passage units and weft passage units and the weaving zone.
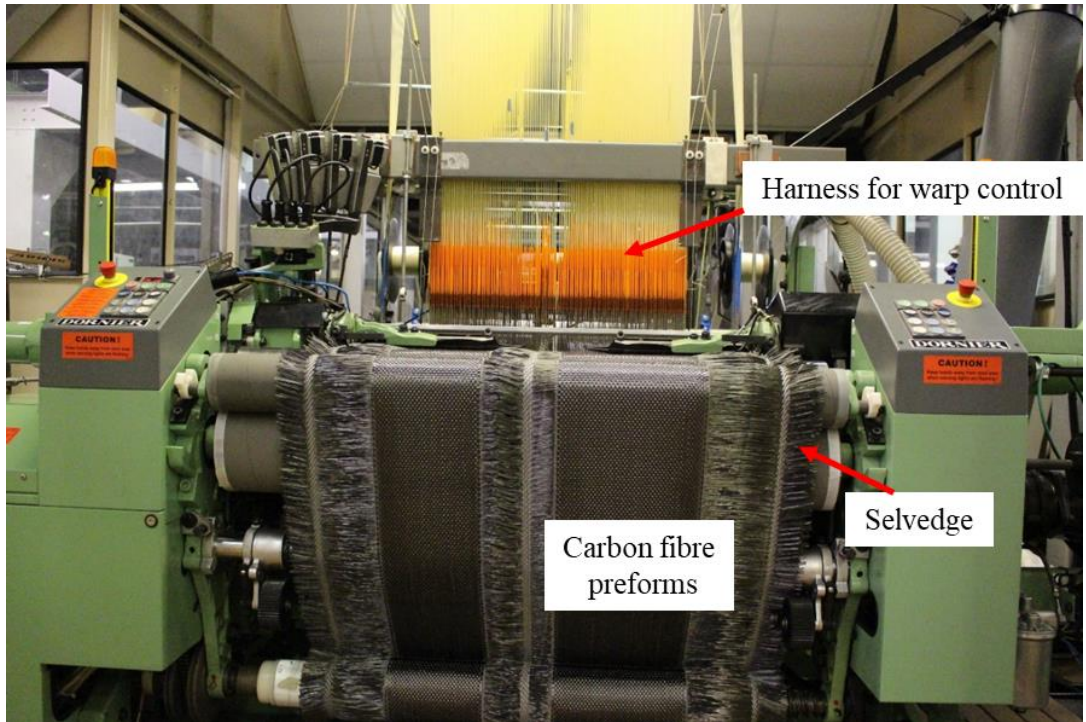
Fig. 3.1 Dornier loom with jacquard mounting

3.2.1 Warp Passage Unit

The schematic diagrams of warp passage units is shown in Fig. 3. 2.
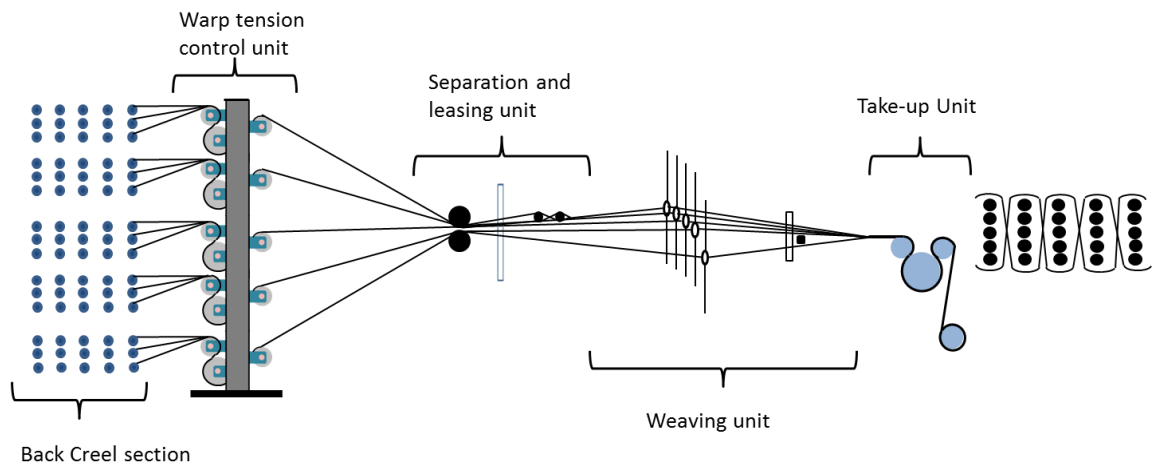
Fig. 3. 2 Schematic of the weaving machine setup (warp passage diagram).

The warp supply system or warp passage of this current loom consists of the following units.

(a) Warp creel unit

(b) Warp tension control unit

(c) Warp separation and leasing unit

The functions of different units of this weaving machine are briefly described as follows:

Warp creel section

Generally, there are two types of warp delivery systems in the conventional looms – (i) warp creel and (ii) warp beam. In the case of high-performance stiff fibres like carbon, glass etc., it is essential to prevent fibre filamentation. In this system, the warp packages are mounted on the creel and delivered to the machine (see Fig. 3. 3). The warp delivered from individual packages on the creel is less prone to fibre damage due to less processing.

The warp creel consists of 15 rows and four columns of warp tow bobbins, including the binder tows. Metal bobbin holders covered with rubber tubing were used for holding the bobbins. On each of the bobbin holders, two bobbins were mounted in such a way so that the yarn unwinding is done in opposite directions to each other, and circlip clips were used to hold them. Eight hundred forty warp bobbins were used in this weaving process, including the binders. A Herzog USP 300 single-end winder was used to rewind the warp bobbins from the virgin carbon fibre package.
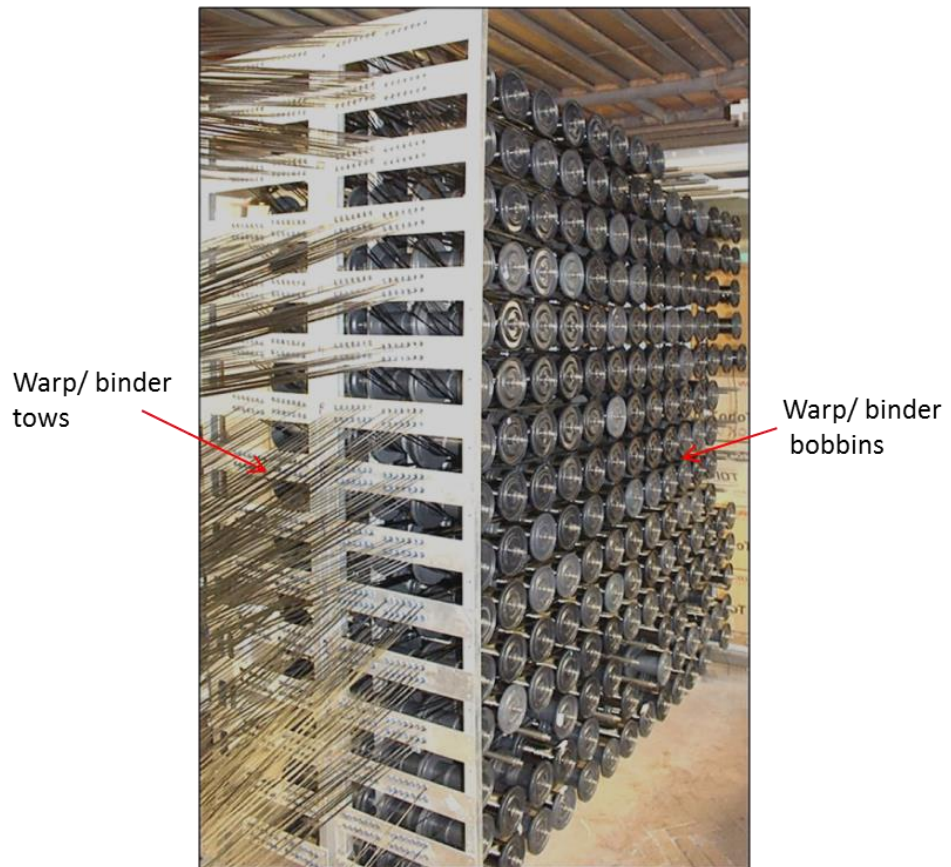
Fig. 3. 3 Warp creel used in the current research

Warp tension control unit

A system consisting of three rollers is used to control the tension of each warp and binder

(see Fig. 3. 4). The consisted rollers are:

(i)   Heavy stainless steel nip roller

(ii)   Rubber coated roller

(iii)   Lightweight free rotating roller.
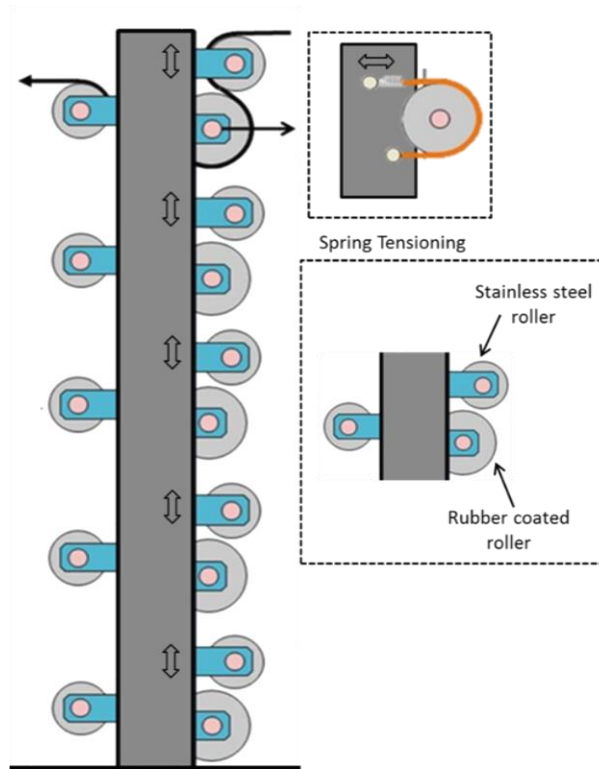
Fig. 3. 4 Schematic of the warp tension control unit.

In this roller system, three types of adjustments are available to control the warp and binder tension as described below.

(a) The vertical directional movement of the nip roller from the rubber-coated roller offers the difference in the warps' wrapping angle, hence a variation in tension.

(b) The rubber-coated roller is designed with flanges on both ends with a housing of tensioning belts and spring assembly to control the rotational movement of this roller. By changing the position of the tensioning belts, tension on this roller can be adjusted to required level.

(c) The third way to control the warp tension is the lightweight free roller's vertical and horizontal movement. Again, it will variate the wrapping angle of the tows on the rubber-coated roller.
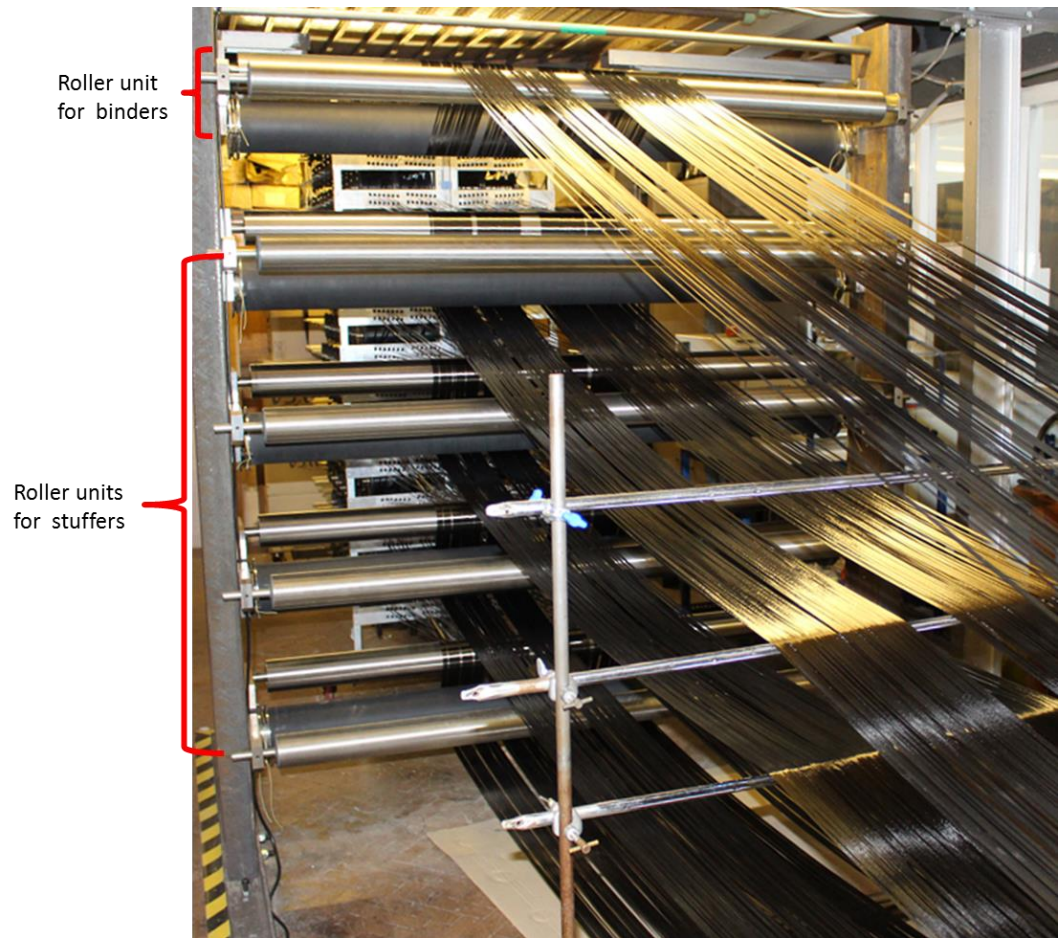
Fig. 3. 5 Warp tension control roller units in the weaving setup

Among these roller systems, the top one was reserved for the binder yarns for the sake of ease in roller adjustments, and the rest four was for the four warp layers (see Fig. 3. 5).

Warp Separation and Leasing Unit

A back reed was used to separate the warp yarns and reduce the possibility of fibre damage. To keep the warp yarns straight, each of the units of four warp yarns were drawn through each dent of a back reed (see Fig. 3. 6).
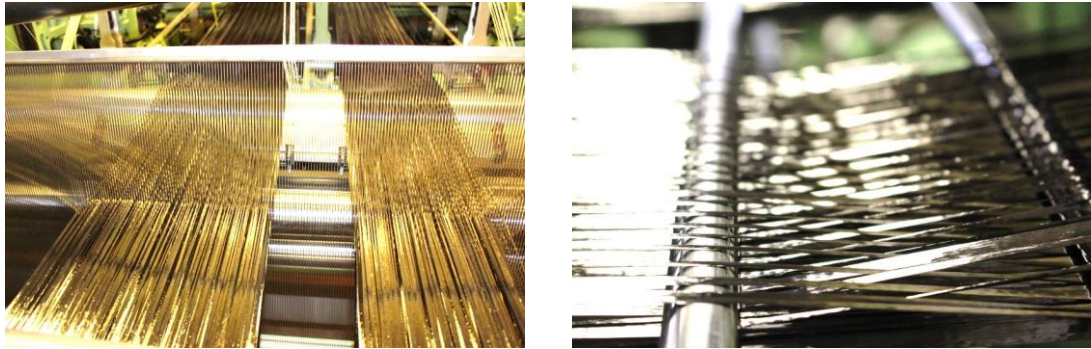
Fig. 3. 6 Back reed (left) & leasing rods (right) for warp unit separation

In the warp bound structures, only the Z-binders move up and down to make the interlacement. So they are more prone to damage during each movement. To reduce the probability of the binder fibre damage, leasing was done for the binder layer using two lease rods (see Fig. 3. 6).

3.2.2 Weft Insertion Unit

The weft insertion unit consists of several elements: weft tensioner, guide, weft detector, weft selector, weft cutter and rapier heads. A schematic diagram of the weft insertion unit is shown in Fig. 3. 7.
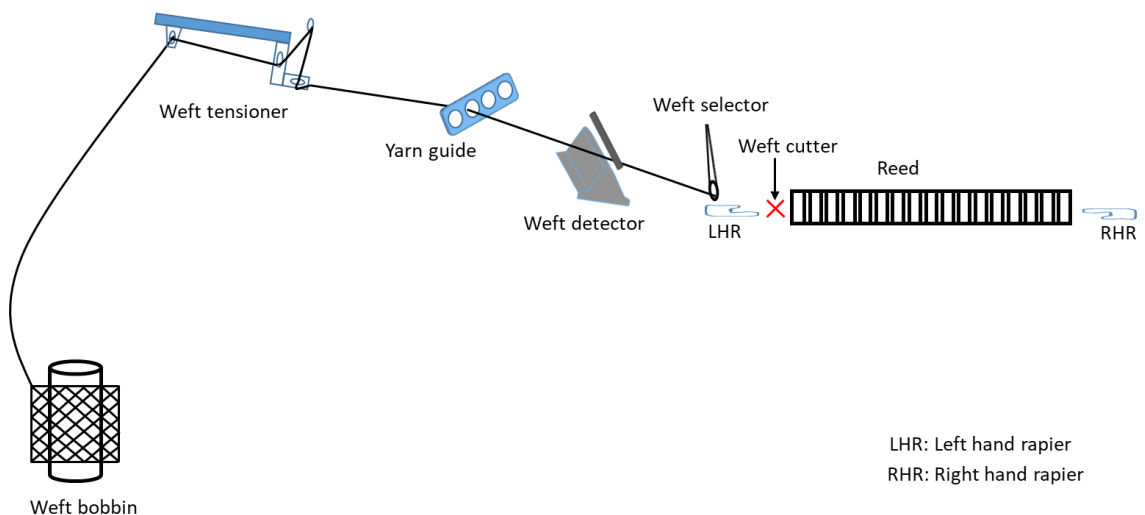
Fig. 3. 7 Schematic of the weft insertion unit.

A weft detector is used to indicate any breakage of weft yarns during the picking process. In case of any weft breakage, the weft detector stops the machine to prevent any weft missing fault in the final preform. The weft tensioner ensures that the wefts are kept in uniform tension throughout the weft insertion process. Weft tow is fed to the left-hand rapier (LHR) through the weft selector, which is then transferred to the right-hand rapier (RHR) to complete the weft insertion process. The cutter on the left-hand rapier side cuts the weft tow when the weft transfer is completed. Weft insertion process and weft transferring systems are shown in Fig. 3. 8 and Fig. 3. 9.
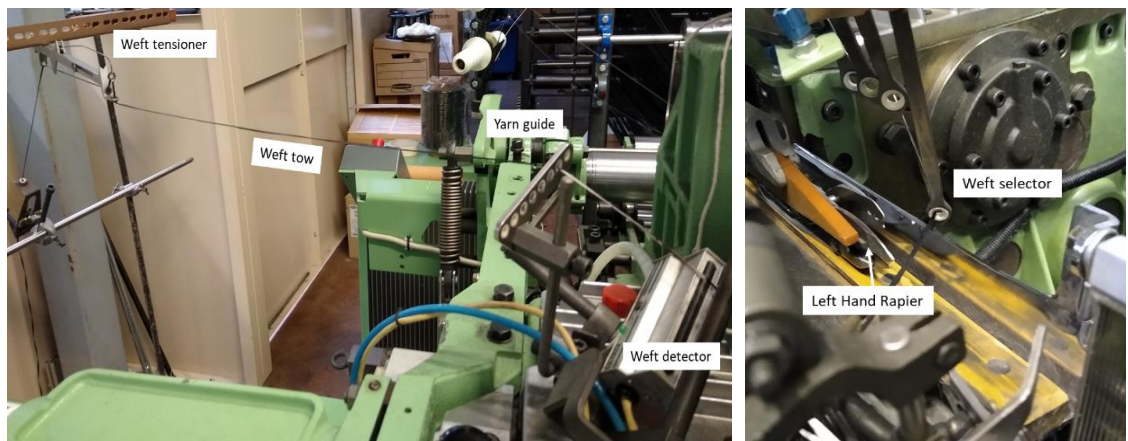
Fig. 3. 8 Weft feeding system to the rapiers.
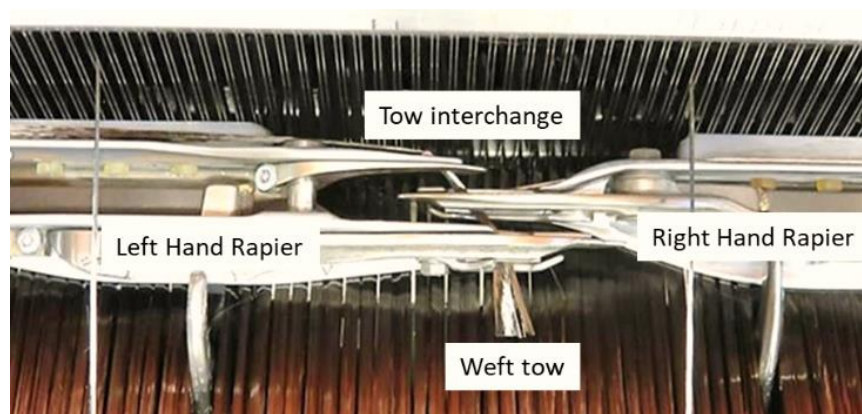
Fig. 3. 9 Weft transferring process

3.2.3. Weaving and Take-Up Unit

In the weaving unit, the three primary weaving motions, i.e. shedding, picking, and beating-up, are carried out to complete the weaving cycles (see Fig. 3. 10).
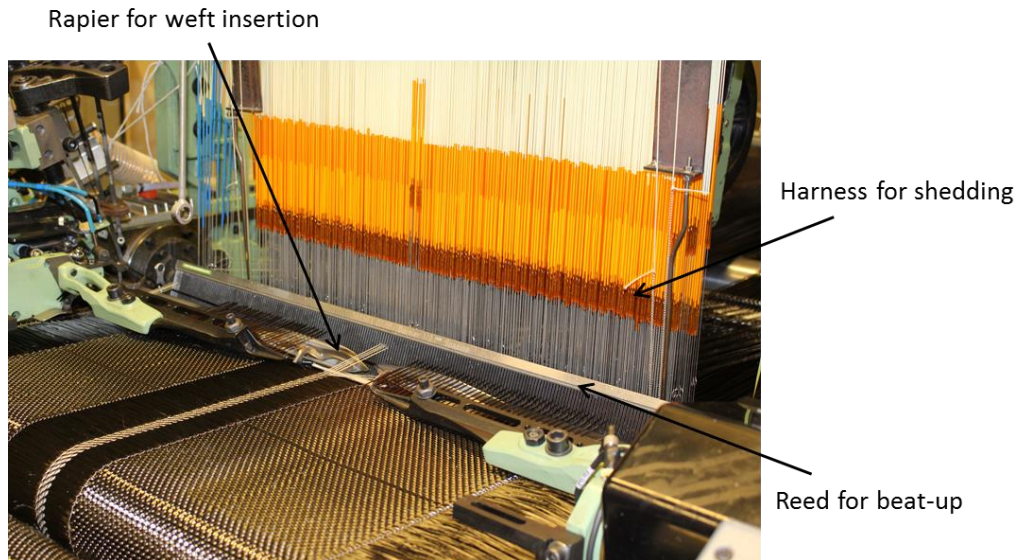
Fig. 3. 10 The weaving section

The shedding mechanism was controlled using a Staubli CX880 jacquard system with 1808 hooks for harness control. The jacquard shedding enables to produce all the variations of the intended designs needed for this research without any other changes in the loom setup. A double rigid rapier system were used to insert the weft yarns into the sheds. Weft sensors were used to stop the machine in case of weft breakage or weft missing. For the beating-up, a specially designed reed was used with two different dent thicknesses to reduce the friction between the warps and binders. The wider dent is used for warp tows and the narrower dent is used for the binders (see Fig. 3. 11). The take-up unit consists of one take-up roller two guide rollers and one cloth roller. The take-up controls the pick spacing and the warp let-off from the back creel.
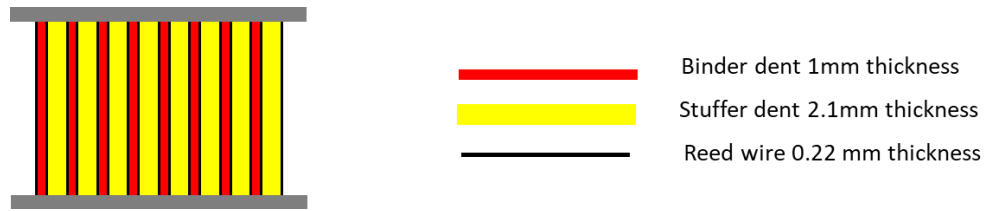
Fig. 3. 11 Schematic of the especially designed reed for this research

3.3 Manufacturing of Warp Bound Preforms

In the warp bound structures, the Z-binder is incorporated into the warp and weft tows from the warp yarn/tow direction. It is the conventional way of binder incorporation and is most widely used in developing 3D woven structures.

3.3.1 Warp Bound Structures

The preforms were developed with four different binder weave architectures. The considered weave architectures were 1x1 plain, 2x1 twill and 2x2 twill with orthogonal binding pattern and an angle interlock weave. These preforms are designed considering the degree of interlacings of the binders. The interlacing positions are deliberately changed to create more floating in the Z-binder tows to reduce the binder waviness. The detailed specifications of the preforms are given in Table 3. 1.

Table 3. 1 Specifications of the warp bound preforms

Preforms	Tow density/cm			Tow linear density (K)			Layers		GSM	No of interlacings /100cm^2
	Warp	Weft	Binder	Warp	Weft	Binder	Warp	Weft		
1x1 Plain	11.28	12.5	2.82	12	12	6	4	5	2043	705
2x1 Twill	11.28	12.5	2.82	12	12	6	4	5	2033	470
2x2 Twill	11.28	12.5	2.82	12	12	6	4	5	2029	353
Angle Interlock	11.28	12.5	2.82	12	12	6	4	5	2019	235

All the preforms were made with four warp layer and five weft layers of carbon tows. For warp and weft tows 12K Torayca T700SC 50C untwisted yarn was used. For the binder

6K tows were used from the same group of fibres. All the yarns had 1% size content by weight. The binder and warp ratio was maintained as 1:1 in which after every binder one unit of warp tow was inserted. The specified tow density was chosen so that warp and weft directional fibre volume fractions become almost equal. When the Z-binder contributions were combined to the warp yarns, their directional fibre volume fractions became almost the same as the weft directional fibre volume fractions.

The first orthogonal preform is designed with a 1x1 plain binder weave structure where the binders are interlacing each other after every weft units consisting of five weft tows. The binders move over and down to the weft tows alternatively to make the interlacement and hold the whole structure. The 3D geometrical model of the structure with the weave plan is shown Fig. 3. 12.
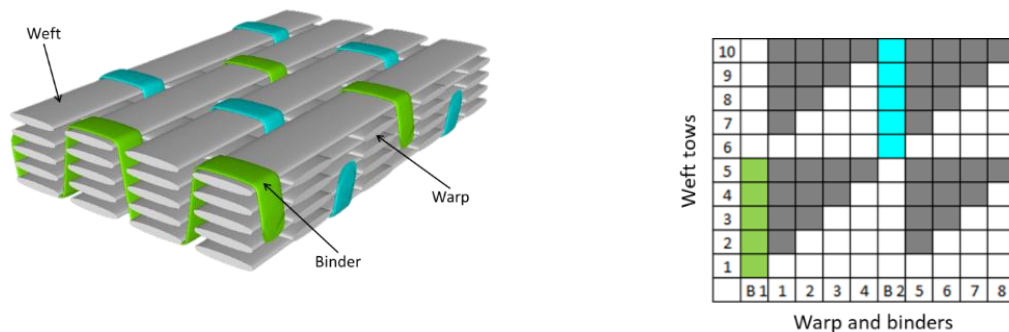
Fig. 3. 12 A 3D model of the 1x1 Plain orthogonal structure with weave plan. (Coloured tows represent binders.)

There are generally two methods of stacking the warp and weft tows in a 3D woven preform: (a) drop-down method and (b) pull-up method. In the drop-down method, all the warp yarns are positioned in the top shed position and with the insertion of every weft yarn, warps are dropped down one by one. When all the warps are dropped from the top shed position to the bottom shed position, the binders interchange their respective

positions causing the interlacing. On the other side, in the pull-off method, all the warps are set on the bottom shed position and they are pulled- up one by one with the insertion of wefts. In the pull-up method, extreme tows were breaking frequently. This is probably because of the surface abrasion of the tows to the metallic headle eyes. During pulling-up, additional pull up tension with the abrasion may have led to this severe breakage which needs a separate investigation. On the other hand, drop-down method offered significantly less fibre filamentation. As a result, drop-down method was used to develop all the preforms in this particular research.

Apart from the 1x1 plain orthogonal preform, three more warp bound structures were manufactured for this research which are shown below in Fig. 3. 13, Fig. 3. 14 and Fig. 3. 15.
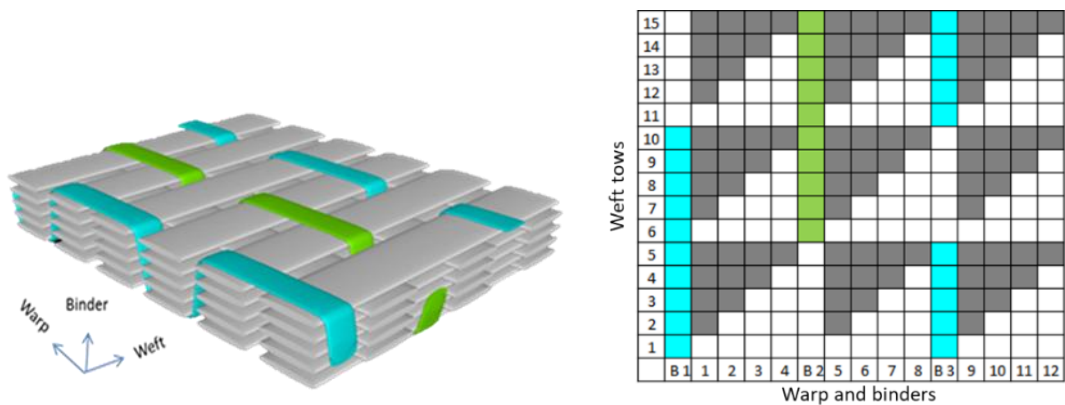
Fig. 3. 13 A 3D model of the 2x1 Twill orthogonal structure with weave plan.
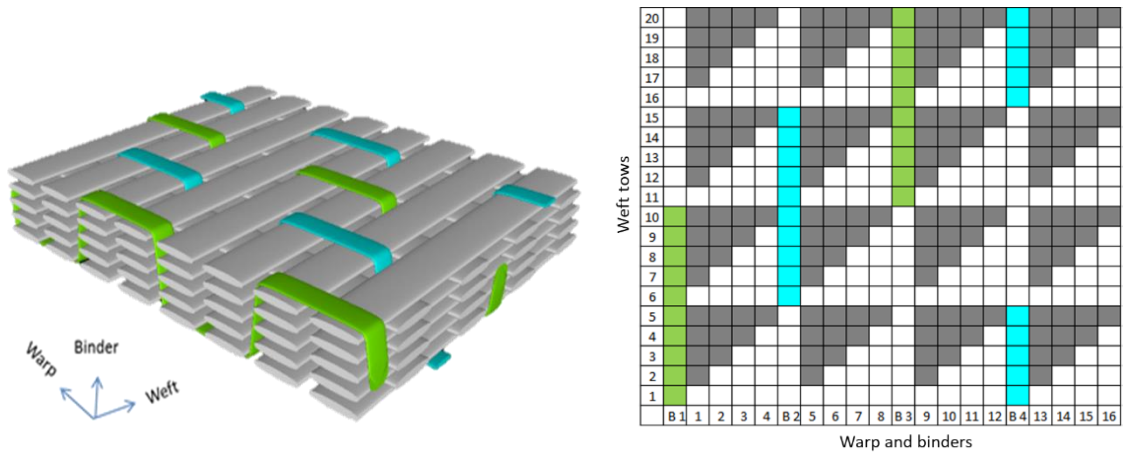
Fig. 3. 14 A 3D model of the 2x2 Twill orthogonal structure with weave plan.
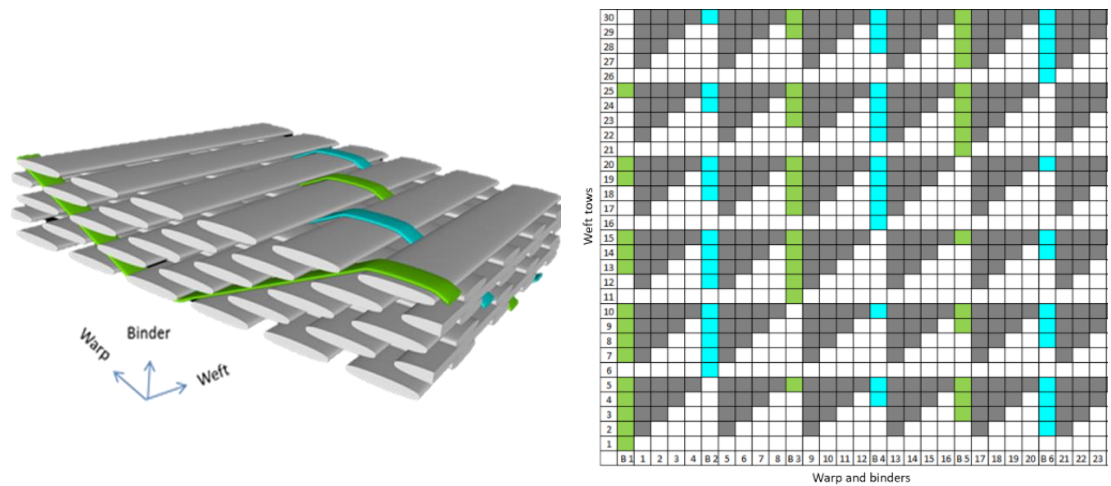
Fig. 3. 15 A 3D model of the Angel Interlock (AI) structure with weave plan.

In the twill structures, the binders move one step right and one step up, giving more floating to the tows. In 2x1 twill, the binder interlaces the weft tows in every two units and then one unit where as in 2x2 twill, the binder interlaces the weft tows in every two units together. The z-binder follows an angular path in the angle interlock weave to move from one surface of the preform to another surface. Due to this angular movement it creates minimum crossings with the weft yarns. The degree of interlacings were calculated based on the density of warp and weft and the crossing pattern of Z-binder based on the weave architecture.

3.4 Manufacturing of Weft Bound Preforms

In the weft bound preforms, the Z-binder is incorporated from the weft yarn direction. Additional weft supply system is needed to accommodate the weft way binder.

3.4.1 Method of Weft Way Binder Incorporation

A simple modification was done to the current setup of the Dornier loom to manufacture weft bound preforms. In the weft bound preforms, an additional weft supply system is needed which works as the weft binder along with the weft stuffer tows. Hence in the modified system, another yarn bobbin was added to the weft supply system as well as another weft tensioner. For this additional weft binder, an additional weft selector was activated through loom programming. A schematic of the modified loom setup is shown in Fig. 3. 16 along with the actual setup in the loom (see Fig. 3. 17).
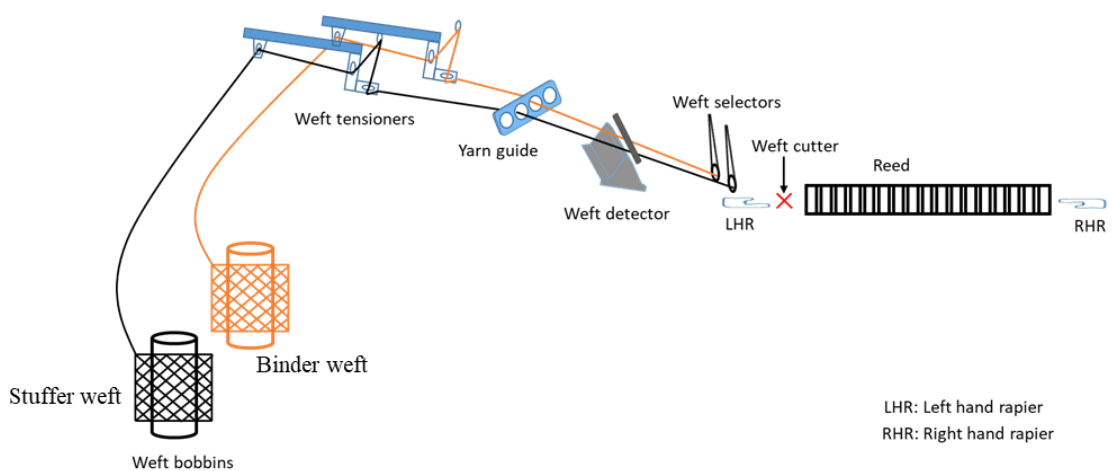
Fig. 3. 16 Schematic diagram of weft binder insertion facility (coloured one represents weft way binder tow)
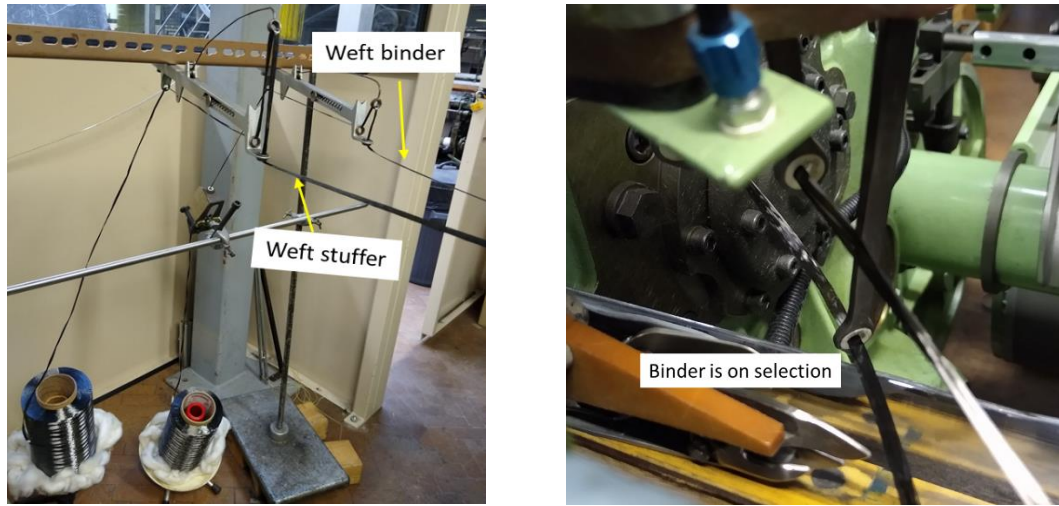
Fig. 3. 17 Addition of weft binder supply (left) and activation of additional weft selector (right)

3.4.2. Weft Bound Structures

Like the warp bound preforms, weft bound preforms were also developed with four weave architectures- 1x1 plain, 2x1 twill and 2x2 twill with orthogonal binding pattern and an angle interlock weave. The detailed specifications of the weft bound preforms are given in Table 3. 2.

Table 3. 2 Specifications of the weft bound preforms

Preforms	Tow density/cm			Tow linear density (K)			Layers		GSM	No of interlacings /100cm²
	Warp	Weft	Binder	Warp	Weft	Binder	Warp	Weft	M	
1x1 Plain	11.28	6	2	12	12	6	4	3	1470	564
2x1 Twill	11.28	6	2	12	12	6	4	3	1467	376
2x2 Twill	11.28	6	2	12	12	6	4	3	1467	282
Angle Interlock (AI)	11.28	6	2	12	12	6	4	3	1465	188

In 3D woven structures, the binder way stuffer tow layers always need to be one layer less to the other directional tows to perform the interlacings. In this research it was decided to keep the warp directional specifications same for both warp and weft bound

structures for comparative analysis. As a result, number of weft layers was reduced from five to three. Also, to accommodate the binders in weft way, weft yarn density was also reduced. However, the carbon fibres linear density (Tex) were same for both warp and weft bound preforms.

3D models of weft bound preforms showing their interlacement pattern and their weave plans are shown in Fig. 3. 18, Fig. 3. 19, Fig. 3. 20 and Fig. 3. 21 for the four weaves.
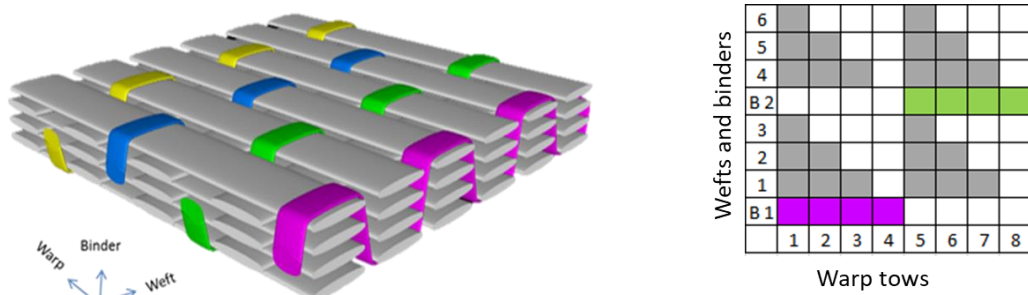
Fig. 3. 18 3D model of the 1x1 Plain orthogonal weft bound structure with weave plan.
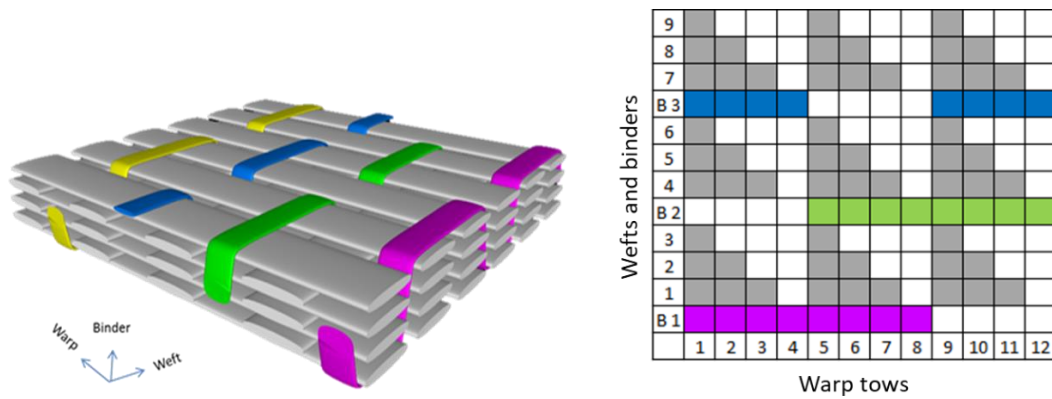
Fig. 3. 19 3D model of the 2x1 Twill orthogonal weft bound structure with weave plan.
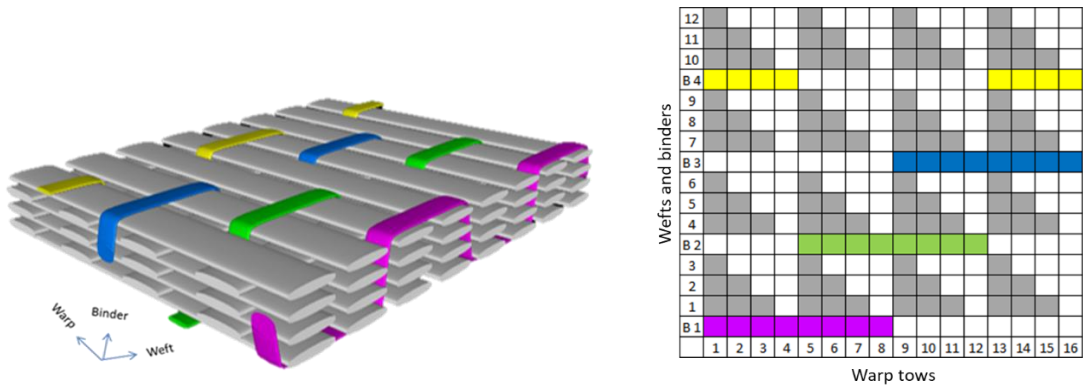
Fig. 3. 20 3D model of the 2x2 Twill orthogonal weft bound structure with weave plan.
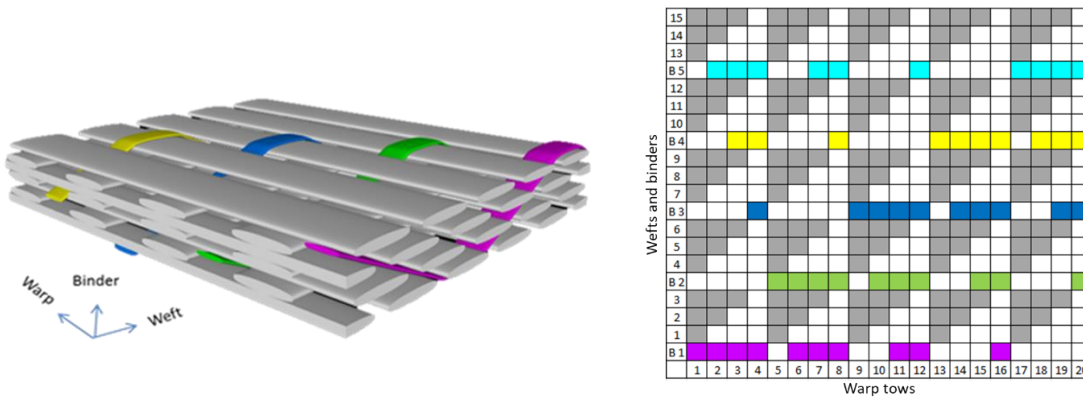
Fig. 3. 21 3D model of the Angel Interlock (AI) weft bound structure with weave plan.

3.5 Preforms Manufactured with Binder Tension Variation

The multiple warp and weft layers in the 3D preform structures are held by the through-thickness Z-binder yarns. These binder tows make interlacement with the warps/wefts. During these interlacements, the binder induces crimp on the load-bearing tows [123]. Again, the yarn tension affects the crimp of the yarn [12] which ultimately affects the mechanical properties of the composites [107]. In this research the binder tension variation is taken as an investigation parameter. The effect of binder tension on the preform and composite mechanical properties is investigated.

Warp bound orthogonal preform with 1x1 binder weave structure is considered for two level of binder tensions named as nominal tension (NT) and another one is higher tension

(HT) than the nominal one. The structures have no other differences except the variations in the binder tensions.

3.5.1 Method of Controlling Binder Tension

The binder tension was controlled from the warp/binder tension control unit which is discussed previously (in section 3.2.1 Warp Passage Unit). In this control unit, there are three rollers and their position can be moved also the rotational movement of the main rubber-coated roller can be controlled through spring loading.

To increase the tension from the nominal one, the front free roller is moved upwards and left. As a result, the tows find more angle of wrap with the main roller and thus give more tension to the binder.
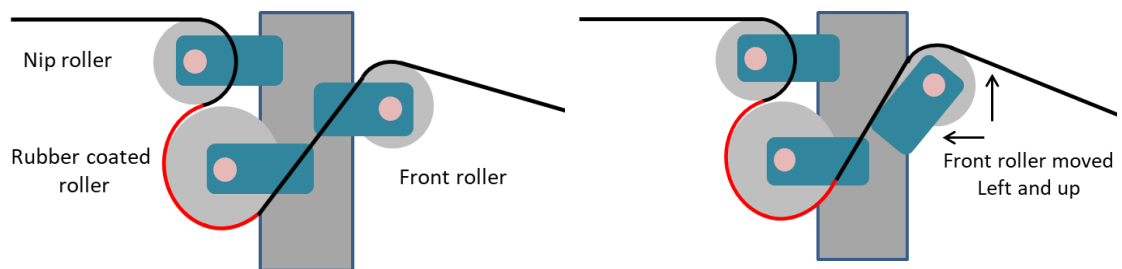
Fig. 3. 22 Schematic of the binder tension controlling system

In the above schematic figure (see Fig. 3. 22), the red lines represent the tow wrapping length on the rubber-coated roller. For higher tension this length was increased by moving the front free rotating roller in left and upward direction. As a result it gives more tow wrapping angle with the rubber roller. The following table (Table 3. 3) shows the wrapping angle of the two set up.

Table 3. 3 Tow wrapping angle for the two setup

Preform structure	Nominal Tension (NT)	Higher Tension (HT)
Angle of wrap	175°±6°	219°±4°

3.5.2 Measurement of Binder Tension

The dynamic tension of binders with both of the roller setup is measured with a SAUTER FH-50 Force Gauge. Individual tow tension was measured with random sampling from the binder tows. The tension measurement setup is developed with the tension meter and two free guided rollers. Free rollers were used so that they do not impart any additional tension on the binder tows. The tension measurement setup is shown in Fig. 3. 23 and Fig. 3. 24.
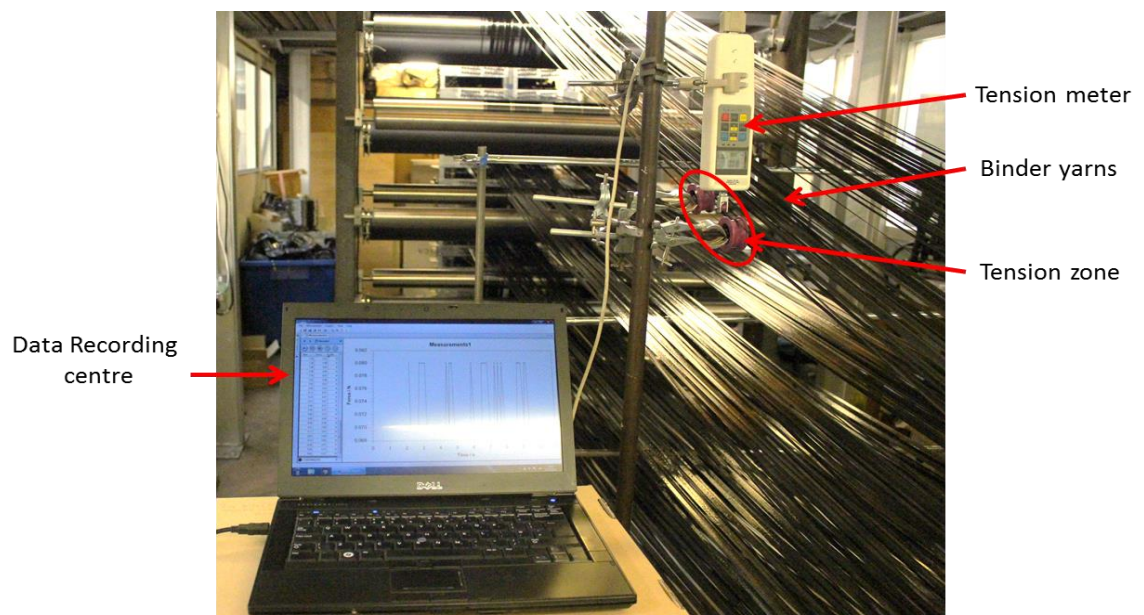
Fig. 3. 23 Binder tension measurement setup.
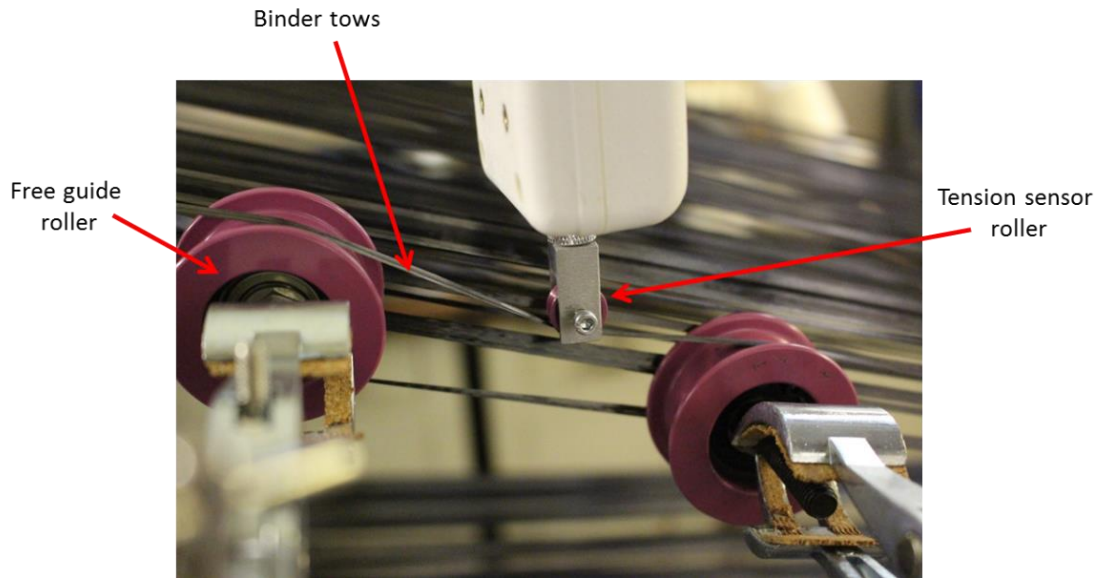
Fig. 3. 24 Tension measurement zone.

The dynamic tension of the binders was measured when the loom was in running state and the tension data were recorded against time. The data recorded for at least 60 seconds for each of the binders. The average tow tension for the two setup is given in Table 3. 4.

Table 3. 4 Single tow dynamic tension for the two setup

Preform structures	Nominal tension (NT)	Higher tension (HT)
Dynamic tension (cN)	55±7	80±11

3.5.3 Preform Structures

Surface structures of the two preforms with different binder tensions were captured using a Keyence VHX-5000 optical microscope with 3D stitching technique to reveal the dimensions of the interlacing points. They are shown below in Fig. 3. 25.
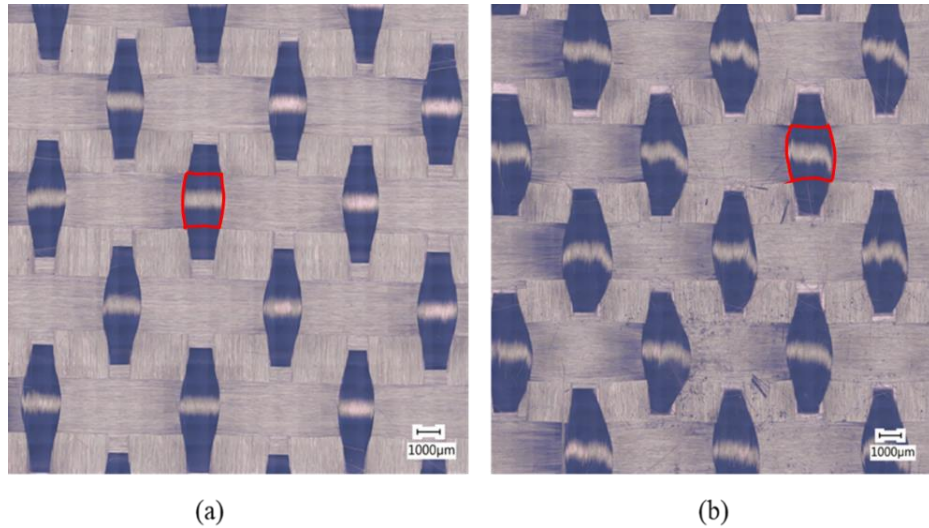
Fig. 3. 25 Surfaces of the 3D woven orthogonal preform (1x1 Plain weave) with different binder tension (a) Nominal Tension (NT), (b) Higher Tension (HT). **(**Red marked areas represents the interlacing squashing areas).

The surface pictures of the two structures show that with the higher tension, the binders are more spread than the other one. So in this state, the binders will produce more squashing area with the weft yarns. The interlacement squashing area is further calculated using imageJ software. The results (see Table 3. 5) show that in high tension state the binders are far more spread (approximately 25% more) compared to the nominal tension state.

Table 3. 5 Interlacement squashing areas of the orthogonal structures with different binder tensions.

Preform structures	Nominal tension (NT)	Higher tension (HT)
Squashing area (mm^2)	0.15±0.003	0.19±0.004

3.5 Concluding Remarks

3D woven preforms were manufactured considering two binder parameters: binder weave architectures and binder tension. Warp bound, and weft bound preforms were developed

with four different binder weave structures. The considered weave architectures were 1x1 plain, 2x1 twill and 2x2 twill with orthogonal structures and an angle interlock weave structure. The weave structures were chosen to reduce the degree of binder interlacings sequentially, which directly affect the crimp percentages of the binders. Weft bound preforms with same binder weave architectures were developed by modifying the existing weft supply system. Another set of 3D woven preforms was developed where the Z-binder tension was varied. The warp tension unit was modified to variate the binder tension. Two orthogonal preforms were developed with 1x1 plain weave, where the binders were drawn in two different tensions. They were named nominal tension (NT) structures and high tension (HT) structures. The interlacement squashing areas of the two structures show that the binders in higher tension (HT) structure are more spread than in nominal tension (NT) which may affect the dry preform and composite mechanical properties of that particular structure.

Chapter 4 Compressibility of 3D Woven Preforms

4.1 Background

During composite manufacturing, dry fibre structures are compacted up to a certain pressure level during moulding. This compaction affects the tow dimensions and the resin channel geometry, i.e., the microstructure of the preform. It determines resin impregnation and fibre volume fraction which ultimately affects the mechanical properties of the composites.

In 3D woven preform, the Z binders hold the almost non-crimp layers of warp and weft yarns following a path in the thickness direction and give the structure coherence. As a result, this binder influences the preform properties and, ultimately, the composite properties. This chapter will analyse the effect of z binder weave structure and tension on the dry 3D woven preforms compressibility.

Extensive research work has been carried out to understand the compaction behaviour of woven reinforcements which mainly focus on 2D woven structures [40], [42], [43], [48]–[52], [132]. Due to the through-thickness z binders, compaction mechanisms of 3D woven preforms differ from the stacked 2D woven structures. However, only a few studies concentrated on the 3D woven preforms [53], [54], [58], [120], [133].

Parnas et al. [53] reported that the compressibility of the 3D woven structures is lower than the random mats. Endruwiet and Long [54] have investigated the compressibility of different 3D woven preforms and concluded that the compaction mechanisms highly depend on the preform internal architectures. They have found that the orthogonal preform shows the least compressibility because there is no offset between the identical layers of yarns/tows. The binder yarns offer more stiffness and prevent bending of the

weft bundles, leading to lower compressibility. However, in the angle interlock structures, bundle cross-sections are significantly deformed and lead to high compressibility due to offsetting the yarns and angular binder path. Khan and Umer [133] reported that multiple cyclic compactions resulted in permanent deformations within the preform structures due to the changes in the tow geometries. They also found that the less vertical binder path in layer to layer preforms allows more compaction than the orthogonal structures where the binders are far more vertical.

In order to understand the role of Z binder parameters on the compaction behaviour of 3D woven preforms, transverse compactions tests are carried out. This chapter details the characterisation method for this particular study. Two critical parameters- binder weave architectures and binder tension were considered. Preform specifications are detailed in Chapter 3. Warp bound, and weft bound preforms with four different binder weave architectures are compacted in multiple cyclic loading to explore the role of binder weave architectures on compaction behaviour. Two other preforms with different binder tensions are tested to understand the effect of binder tension on the compressibility of 3D woven preforms. Findings of the compaction tests are presented in terms of changes in preform thickness, compressibility and fibre volume fractions against compaction load. At the end of the chapter, the main concluding remarks are summarised.

4.2 Mechanical Testing

The transverse compaction tests of the 3D woven dry fibre preforms made with different binder parameters were carried out by using the Instron 5969 Universal testing machine (Fig. 4. 1) with a load cell of 10kN. In this machine, the compaction zone is made of two circular metal plates, each having a diameter of 80mm. The sample size is kept 100mm X 100mm to cover the total area of compaction plates. The cyclic compaction tests were

performed for each type of sample understand the compaction behaviour of the 3D woven preforms and their internal geometry changes during compaction.

The samples were placed in between the metal plates, and the quasi-static compression was carried out with a constant speed of 1 mm/min until the load reached 10kN (20bar/2000KPa). A 2N preload was applied at the beginning so that the initial thickness of the preforms was perfectly recorded [12].

For each category of structures, three specimens were subjected to compression loading. To investigate the potential differences of compaction in subsequent cycles, five loading cycles were carried out. After the first loading cycle, the metal plates were moved to their original positions until the initial 2N load was found. And then the second cycle started. In the same way, each preform was subjected to five cycles of compactions and the load-displacement curves were recorded.

A recent benchmark work on preform compactions led by Yong et al. has identified two main variables responsible for data scattering- machine compliance and the accuracy of initial thickness measurements [134]. Both of these issues were addressed during the compaction tests. Before starting the compression test, the compliance curve was generated by pressing the metal plates together at 1mm/min speed without any sample. Load versus cross-head displacement curve was generated and recorded. This process was repeated a few times until a stable compliance curve was found. This compliance curve was imported to the main data domain to accurately generate the load-displacement curves for the preforms. To measure the initial thickness, cross-head displacements were used following Patel et al. [12] by applying a 2N preload.

Fig. 4. 1 Instron set-up for compressibility test (left) and the compaction zone (right).

Different composite manufacturing processes impart different levels of compaction pressures on the preforms; for example, in vacuum bag infusion, one bar pressure is applied whereas, in low-pressure RTM, this ranges from 10-20 bars [135]. So, before studying the compressibility of preforms with different binder structures, it is essential to know about the effect of compaction pressure on the preform compressibility.

In this research, compression tests are carried out in three steps. In the first step, the effect of compaction pressure on the compressibility of the orthogonal preform is investigated. In the second step, the effect of the z binder weave structures is explored, and finally, the influence of binder tensions on the preform compressibility is studied.

4.3 Results and Discussion

4.3.1 Effect of Compaction Pressure on Compressibility

To explore the effect of compaction pressure on the 3D woven preforms, a range of pressures (100KPa, 500KPa, 1000KPa and 2000KPa) were applied with cyclic loading (five cycles) on the orthogonal preform with the 1x1 plain binder weave (warp bound).
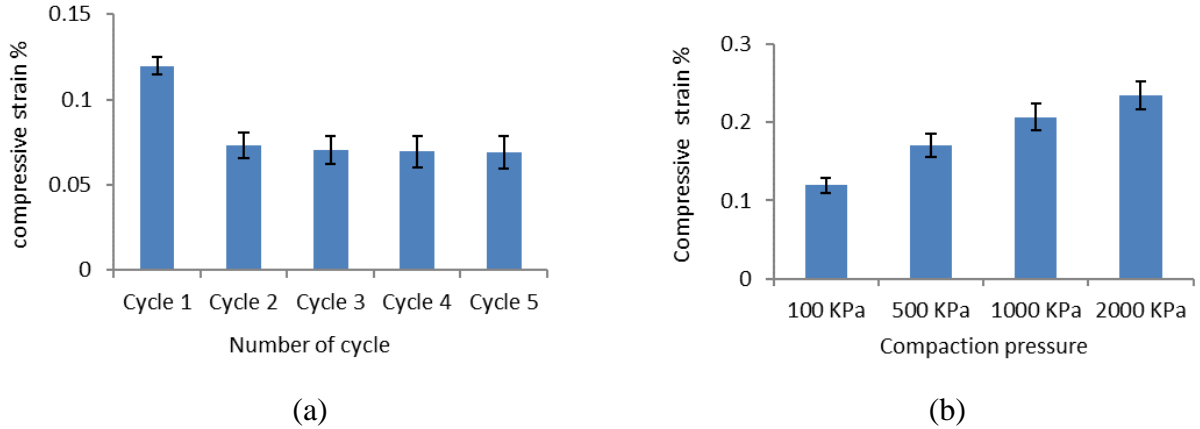
Fig. 4. 2(a) Compressive strain in cyclic load with 100KPa pressure and (b) compressive strain with different compaction pressure.

From the bar charts, it is clear that the maximum compaction is in the first cycle of compressive loading (Fig. 4. 2). As mentioned earlier, the primary compaction in 3D woven structures is due to the compaction on the fibre bundles in which the filaments are reordered. At the first cycle of compressive pressures, the fibres are permanently reordered; as a result, it gives maximum strain. In the subsequent cycles, it is seen that the compressive strains are almost equal. Endruwiet and Long [54] mentioned that this effect is due to the elastic behaviour of the preforms.

The compressive strain increases with the compaction pressure, which is very understandable. With more pressure, the filament reordering occurs in a more stable way. This may reduce the gaps between the fibres. As a result, the compressive strain increases with the compaction pressure.

A summarised bar chart (Fig. 4. 3) on the compressive strain in different loading cycles at different compressive pressures justifies the above statements.
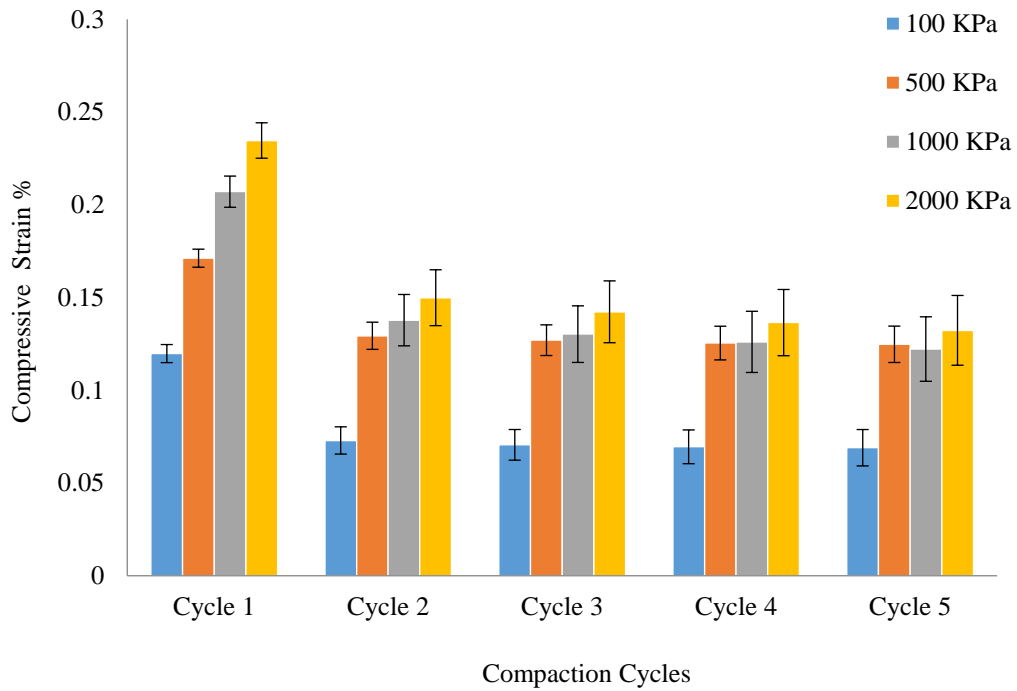
Fig. 4. 3 Compressive behaviour of the orthogonal preform with different compaction pressures under cyclic loading.

4.3.2 Effect of Binder Weave Structure on Compressibility

Representative pressure-thickness curves for both warp bound and weft bound preforms with different binder weave architectures are shown in Fig. 4. 4 and Fig. 4. 5. Three samples of each type of preforms were subjected to the compressive pressure with five cyclic loadings until the load reached ~2000KPa (20 bar).

From Fig. 4. 4 and Fig. 4. 5, it is clearly evident that the preform thickness continues to decrease with an increase in compaction pressure, which followed the similar trend of thickness-pressure curves reported in the literature [12]. However, the major changes in the preform thicknesses were found to occur during the first cycle of loading for all the preforms. In the subsequent cycles, these changes are less significant. This phenomenon suggests that a form of permanent reordering of the fibres bundles within the preform structure happened during the first cycle. Closer observations reveal that the maximum

reduction in thickness happened within the pressure range of ~ 100KPa (1 bar), which represents the vacuum infusion process. However, even at maximum compaction (i.e. 2000KPa), the curves still show nonzero slopes, where it still have the scope of more compaction with increased levels of pressure which supports the findings from Ali et.al.[78]. So more compaction pressure is needed for the ultimate permanent reordering of the fibre bundles.
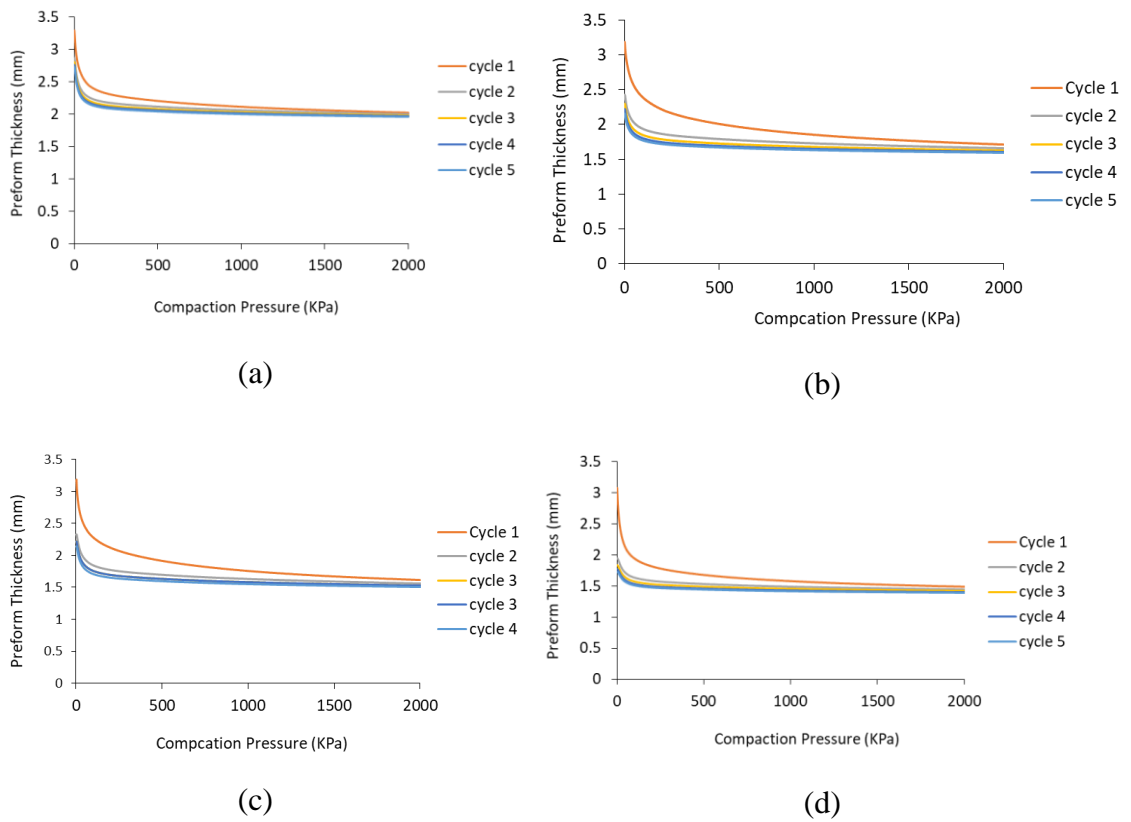
Fig. 4. 4 Pressure thickness curve for the warp bound preforms: (a) 1x1 Plain, (b) 2x1 Twill, (c) 2x2 Twill, (d) Angle Interlock (AI)
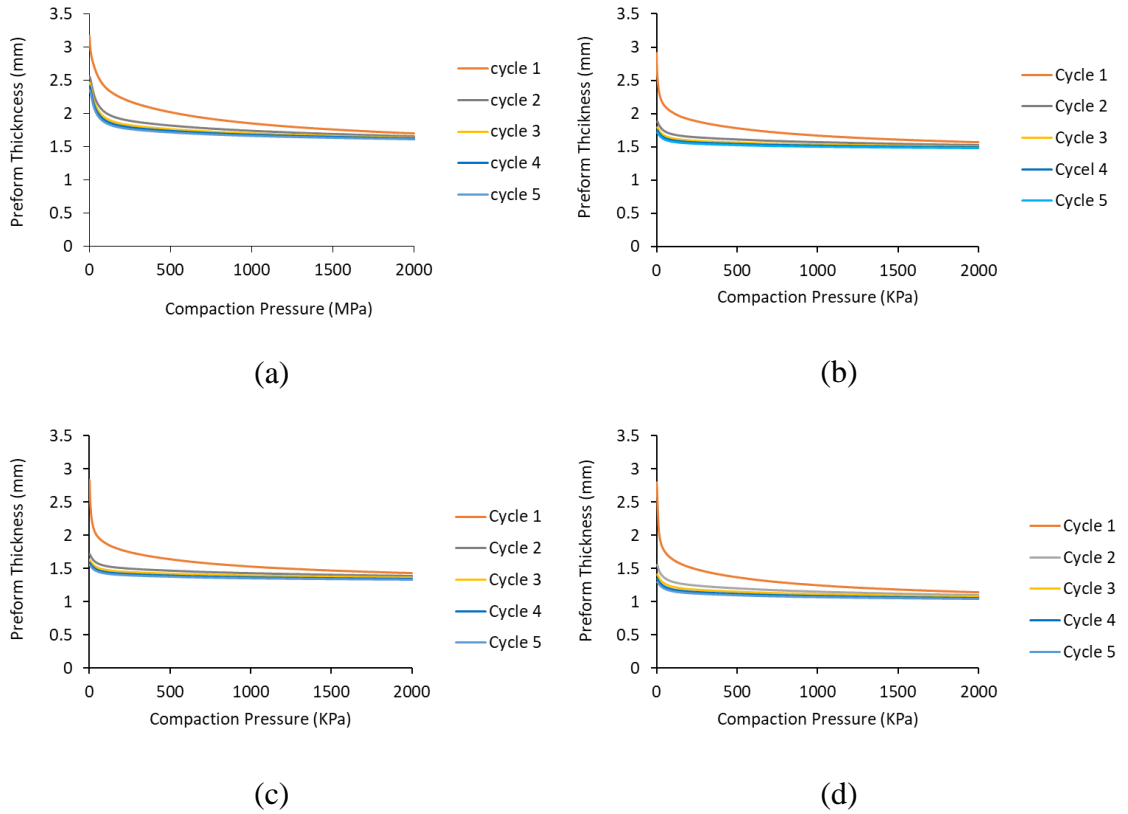
Fig. 4. 5 Pressure thickness curve for the weft bound preforms: (a) 1x1 Plain, (b) 2x1 Twill, (c) 2x2 Twill, (d) Angle Interlock (AI)

To compare the effect of binder weave architectures on the compaction behaviour of the 3D woven preforms, a quantitative approach was adopted [54]. Compressibility (k), which is a factor of change in preform thickness over compaction pressure considering preform initial thickness, was calculated for each of the samples.

$$k = -\frac{1}{h_0}\frac{\Delta h}{P} \dots\dots\dots\dots\dots\dots\dots\dots\dots\dots \text{(4.1)}$$

Where h_0 indicates the initial height of the preform at the start of the load cycle (i.e. 2N load), and Δh is the change in thickness during compression at pressure P.

Compressibility values for the preforms at 100KPa are plotted as a function of compaction cycles at Fig. 4. 6 for the warp bound preforms and at Fig. 4. 7 for the weft bound preforms. In both cases, the values are found fairly representative as the variance among

the samples were found within 6% [Appendix I (a) and Appendix I (b)], indicating high
repeatability of those experimental results.
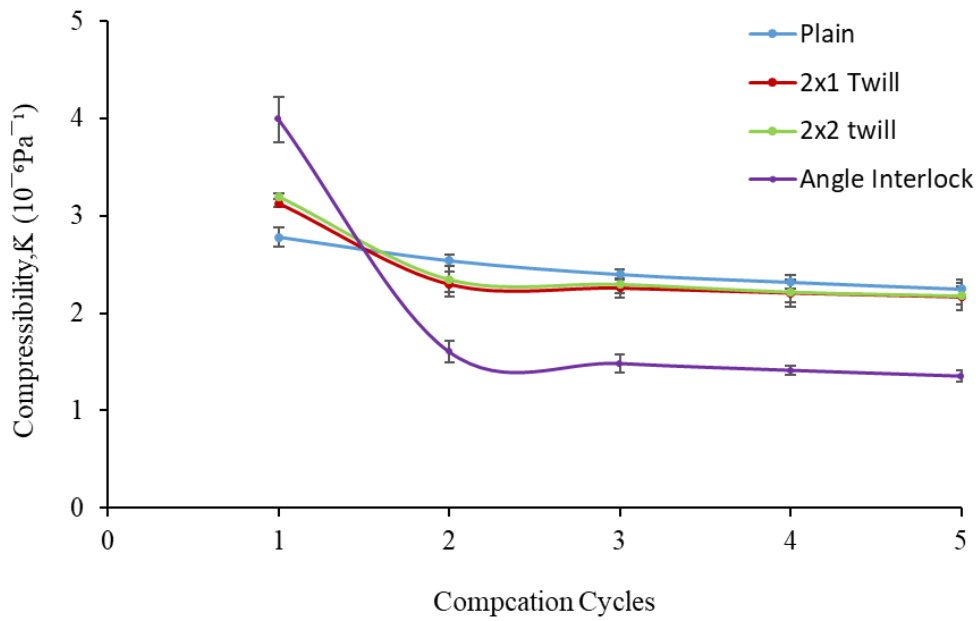
Fig. 4. 6 Compressibility as a function of the number of compression cycles: warp
bound preforms with different binder weaves.
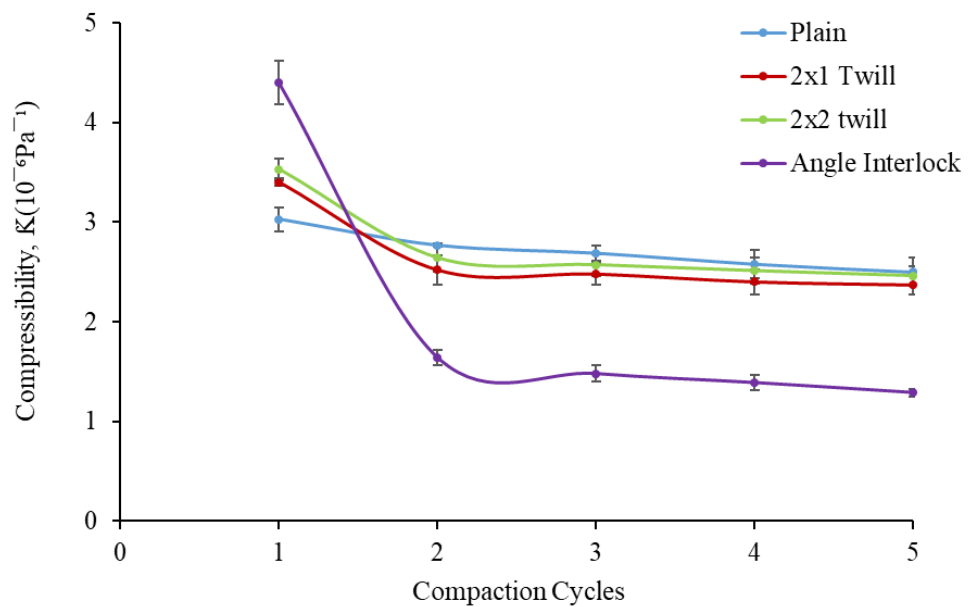
Fig. 4. 7 Compressibility as a function of the number of compression cycles: weft bound
preforms with different binder weaves.

Dry preform compactions are found highly related to the binder weave architectures from the compressibility-compaction cycle plots. During the first loading cycle, preforms with 1x1 plain binder weave have the lowest compressibility, which has improved for 2x1 twill and 2x2 twill weaves. The angle interlock (AI) has the highest compressibility among all these preforms. This change in the compressibility is directly related to the binder weaves as all other parameters in those structures were kept the same. For better illustration, binder way cross-sectional images of the warp bound preforms were generated using the TexGen software. TexGen images (Fig. 4. 8) show that the 1x1 plain weave has the highest degree of binder interlacings ($705/100cm^2$), sequentially reduced to 2x1 twill ($470/100cm^2$), 2x2 twill ($353/100cm^2$) and the angle Interlock has the lowest ($235/100cm^2$) . The actual number of the interlacement points per $100cm^2$ are also recorded in Chapter 3 (section 3.3.1 Warp Bound Structures).

(a)

(b)

(c)

(d)
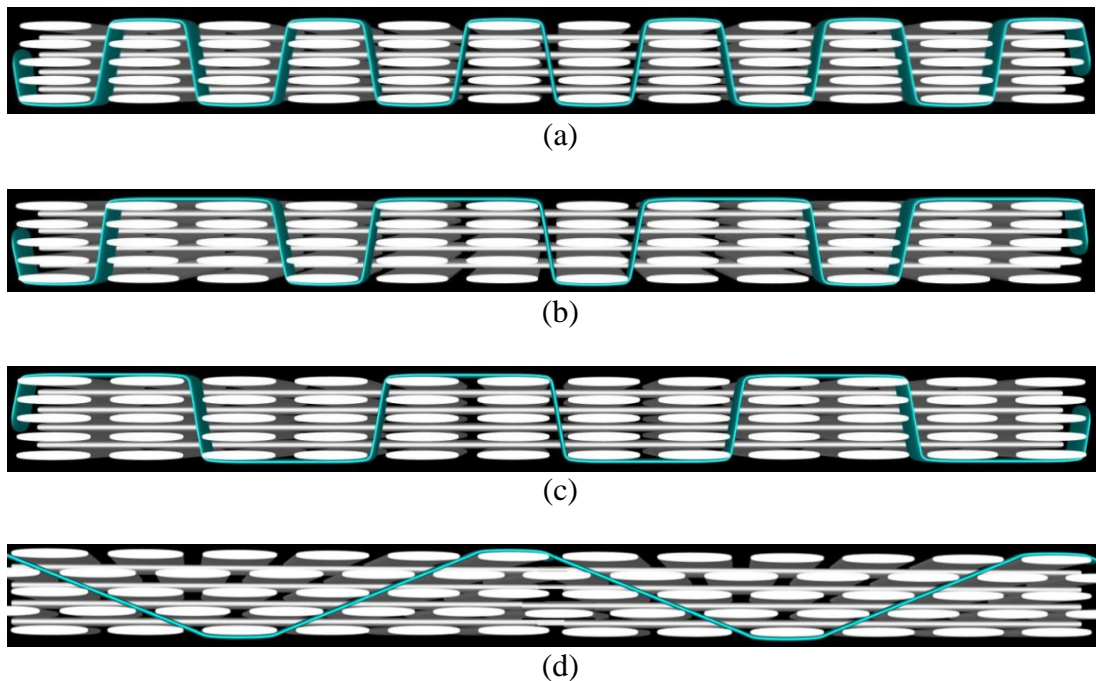
Fig. 4. 8 Binder way cross-sectional view (TexGen models) of the warp bound 3D woven preforms: (a) 1x1 Plain, (b) 2x1 Twill, (c) 2x2 Twill and (d) Angle Interlock.

In 1x1 plain weave, there are more binder yarns in between the weft yarns i.e. most interlacings (705/100cm^2). As a result, these binders prevent the stacked weft yarns to come closer to each other. Therefore, the major compaction phenomena are gap reduction between the tows and fibre flattening. These frequent binders may offer additional stiffness upon compaction and reduce the bending of weft fibres on the surface resulting in lower compressibility [54]. For the twill weaves, the presence of binders in between the weft yarns/tows are reduced gradually (470/100cm^2 and 353/100cm^2 respectively for 2x1 Twill and 2x2 Twill). This reduction assists the adjacent weft yarns to merge and form nesting between the yarn layers. This addition of nesting to fibre gap reduction and fibre flattening results in higher compaction in twill weaves. Chen et. al. [50] also explains the higher compressibility for the twill weaves due to nesting in multilayer structures. These compaction behaviours are even more prominent in angle interlock structures due to the lowest degree of interlacings (235/100cm^2) and angular binder path. This minimum interlacings with angular binder path led to the permanent deformation of the preform structures [59]. As a result, angle interlock structures have the highest compressibility among all the weaves during the first loading cycle.

The next observation is the reverse compaction behaviour of these preforms after the first cycles. The angle interlock weave has the lowest compressibility from the second to the fifth cycle. In contrast, the 1x1 plain weave has the highest values. All the orthogonal weaves (i.e. 1x1 plain, 2x1 twill and 2x2 twill) show a similar level of compactions after the first cycles. The least changes in the compressibility levels of 1x1 plain weave from first to the subsequent cycles suggests more relaxation of the structures during the unloading process due to the frequent binder positioning within the preform structure. A similar observation is also reported by Endruwiet and Long [54]. An intermediate level of compactions for the 2x1 twill and 2x2 twill weaves suggests some forms of permanent

deformations due to nesting and tow flattening. However, binders still assist in relaxation during the unloading process due to the orthogonal binding patterns. A significant drop in the compressibility in the angle interlock structures after the first cycles indicate that the fibres are permanently deformed due to a high degree of nesting.

To better understand this particular behaviour, geometrical architectures of 1x1 plain and angle interlock weaves were revealed in two stages. Composites were made out of these structures by impregnating the dry preforms using resin hardener mixing manually (manual infusion) and vacuum bag infusion method with 1 bar vacuum pressure (Fig. 4. 9). On the manual infusion method, the preform is dipped into the degassed resin-hardener mixing and then left for 24 hours for curing at room temperature. This process does not apply any additional pressure as a result named as without pressure infusion as well [12]. The details of resin and hardener specifications are given in Chapter 6. The vacuum bag infusion method is explained in Chapter 6.

(a)   (b)
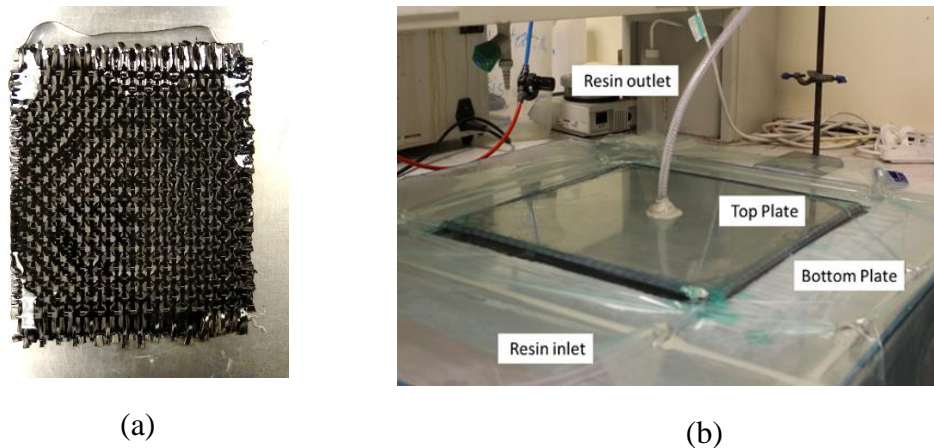
Fig. 4. 9 Composite manufacturing: (a) mannual infusion, (b) vacuum bag infusion

Tow architectures were analysed using a Keyence VHX-5000 optical microscope (details in section 6.3.1) to explore the impact of compaction pressure (1 bar) on preform structural reformation.
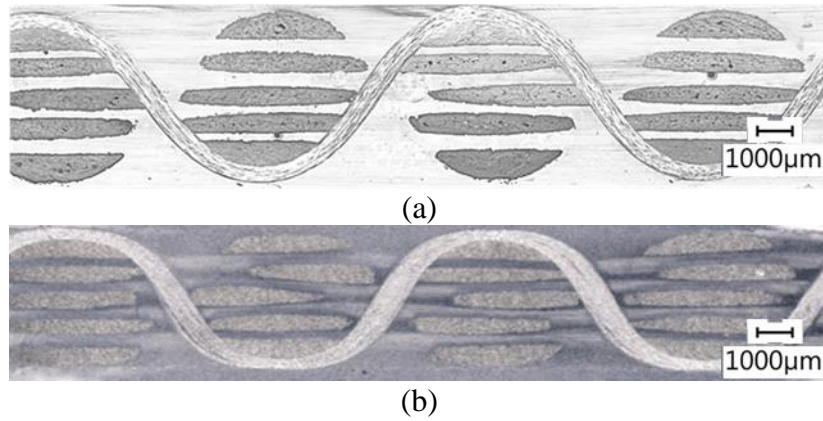
Fig. 4. 10 Binder way architecture of 1x1 Plain weave: (a) Without pressure,

(b) With 1 bar pressure
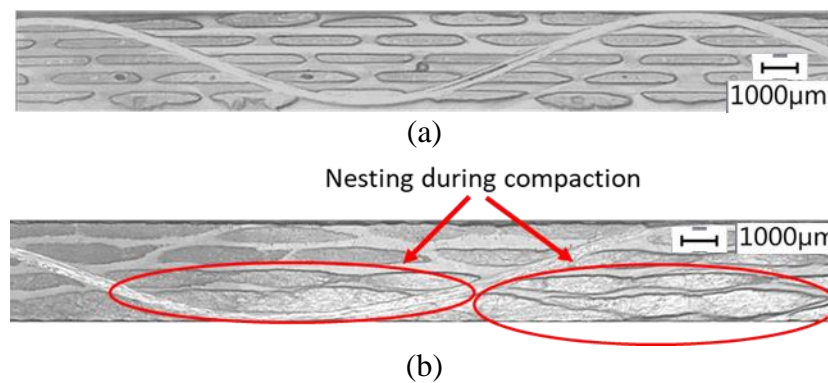
Fig. 4. 11 Binder way architecture of Angle Interlock (AI) weave: (a) without pressure,

(b) with 1 bar pressure

The images (Fig. 4. 10 and Fig. 4. 11) show that there is almost no nesting in plain weave at 1 bar pressure. In contrast, in angle interlock, significant levels of nesting are observed. The angular binder path allows the fibres to come closer on compaction and form the nesting.

Pressure-thickness curves from the compaction tests are a reliable source for predicting the fibre volume fraction of the composites [136]. FVF was calculated using the cyclic pressure thickness curves to predict the maximum fibre volume fraction. The volume fraction of the preforms at every compression state was calculated with the following formula.

$$V_f = \frac{m}{\rho A h} \quad \text{...........................} \ (4.2)$$

Where *m* is the specimen mass, *A* is the specimen area, ρ is the density of the used carbon fibre (ρ =1.80X10^3 kg/m^3), which is taken from the material data sheet [137] and h is the perform thickness which is recorded at every stage of compaction. FVF-compaction pressure curves are shown in Fig. 4. 12 for the warp bound preforms and Fig. 4. 13 for the weft bound preforms.
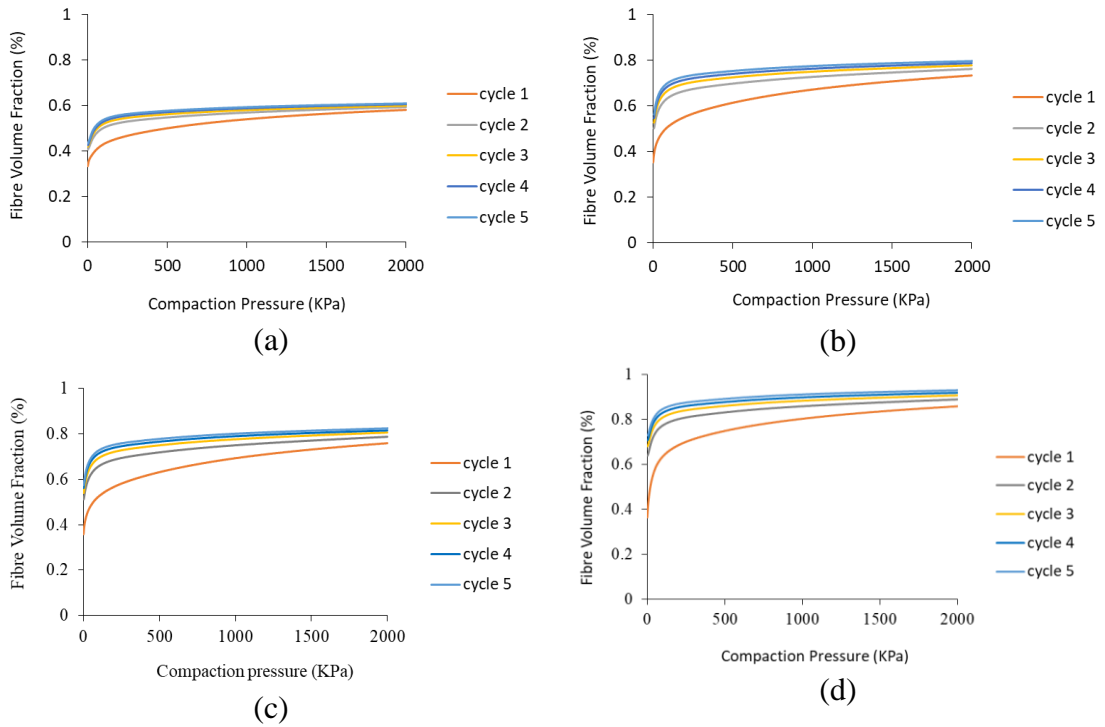
Fig. 4. 12 Pressure-FVF curves for the warp bound preforms: (a) 1x1 Plain, (b) 2x1 Twill, (c) 2x2 Twill, (d) Angle Interlock (AI)
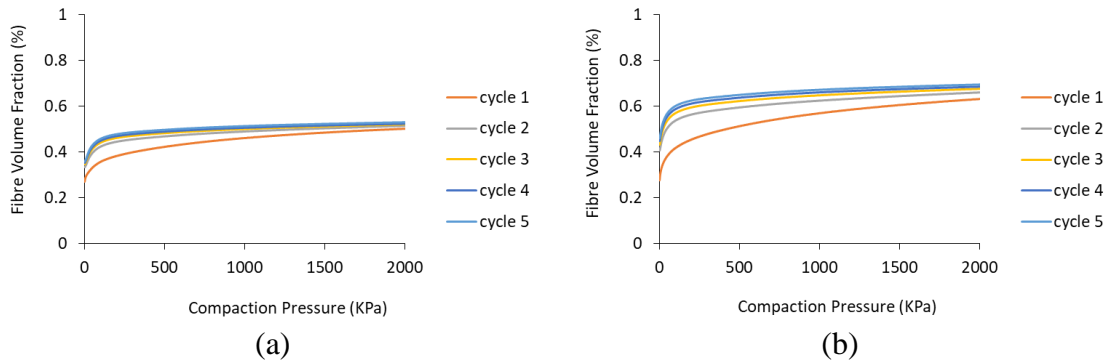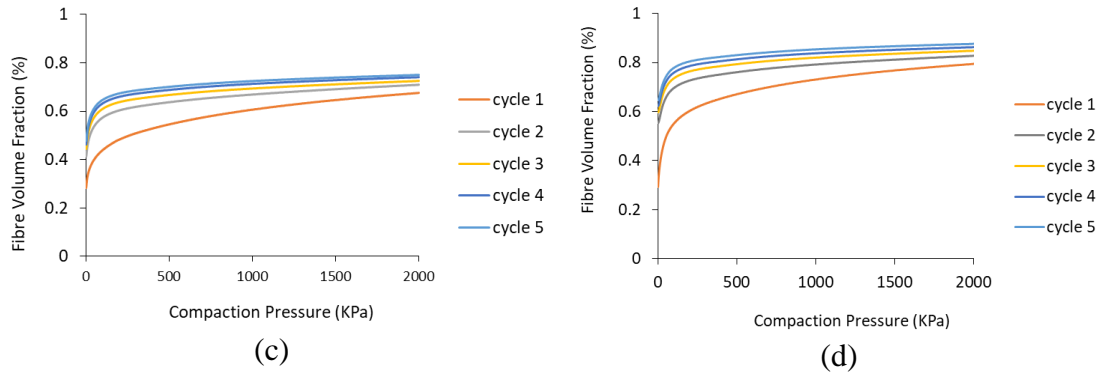
Fig. 4. 13 Pressure-FVF curves for the weft bound preforms: (a) 1x1 Plain, (b) 2x1 Twill, (c) 2x2 Twill, (d) Angle Interlock (AI)

Most significant changes in the fibre volume fractions occur during the first cycles because of the more compactions in that particular cycle. From the second to the fifth cycle, this is less significant. However, in both cases, it is seen that, after every compaction cycle, there are some forms of permanent deformations in the preforms, which allow to get higher fibre volume fraction in the subsequent cycles [59]. As a result, the maximum FVF for all the weaves were obtained at the final cycle.

The graphs also show that the 1x1 plain weave has the least FVF among the four weaves, which is increased for the 2x1 twill and 2x2 twill weaved preforms. Angle interlock weave has the highest among them in both warp bound and weft bound preforms. This is so due to the compaction nature of the preforms, as discussed earlier.

4.3.3 Effect of Binder Tensions on Compressibility

To investigate the effect of binder tensions on preform compressibility, the compressive test is carried out for the samples with different binder tensions. Three specimens of each category are tested, and the pressure-thickness, pressure-fibre volume fraction graphs are plotted (see Fig. 4. 14 and Fig. 4. 15). Also, the compressibility values at 1 bar pressure on each cycle are plotted in Fig. 4. 16 .
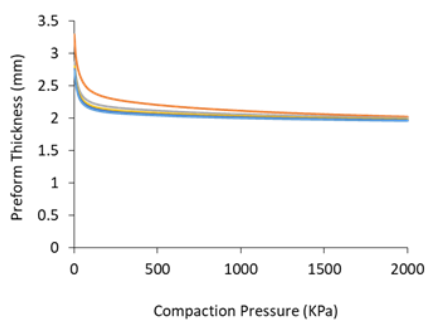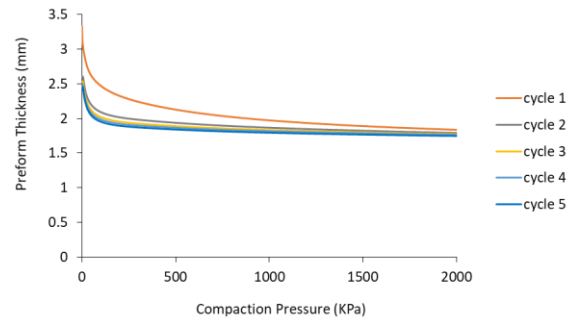
(a)   (b)

Fig. 4. 14 Pressure- thickness curves for preform with binder tension variation: (a)

Nominal tension, (b) Higher tension.
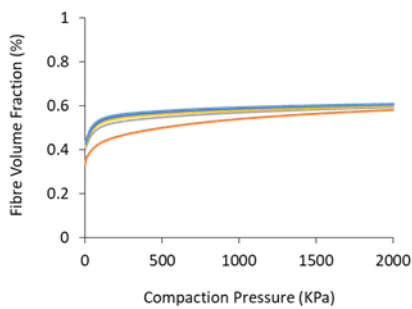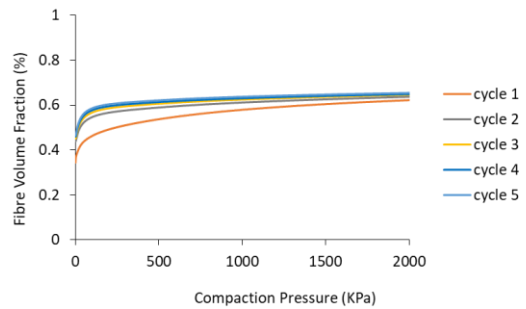
(a)   (b)

Fig. 4. 15 Pressure-fibre volume fraction (FVF) curves for the preform with binder

tension variation: (a) Nominal tension, (b) Higher tension.

No significant difference in the compaction behaviour in terms of changes in thickness

(Fig. 4. 14) or volume fraction (Fig. 4. 15) is noticed for the two preforms with different

binder tension. However, singificant difference in the compressibility values is observed

between the two structures which varies from 13.0%-19% depending on the compaction

cycles.
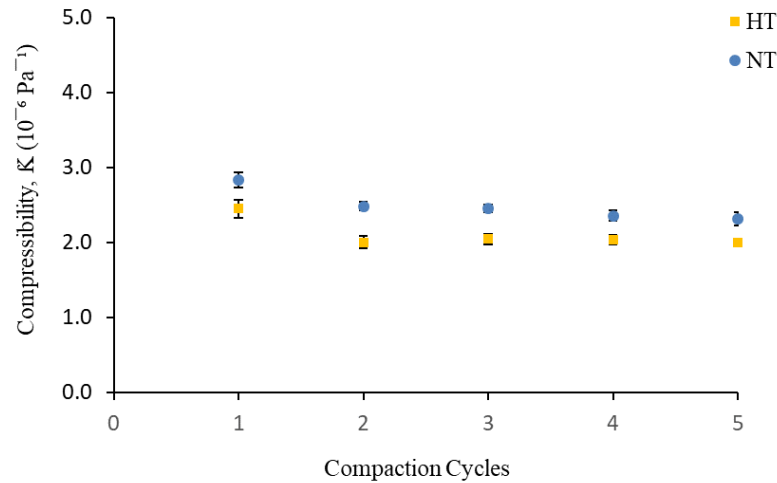
Fig. 4. 16 Compressibility of the orthogonal preform with two different binder tensions.

In the preform with higher binder tension, the binder compresses the surface yarns and reduces the gaps between the tows during manufacturing. The binder way cross-sectional image (see Fig. 6. 7) of the two structures also indicates these effects. As a result of this pre-compaction by higher tension of the binders, this preform has lower compressibility than the other structure.

4.4 Conclusion

The compaction behaviour of the 3D woven preforms with different binder weave structures and tension is studied. The transverse compression of the preforms is studied up to the pressure range of 2000KPa (20 bar), which covers a wide range of composite manufacturing processes, including vacuum infusion (VI), vacuum-assisted resin transfer moulding (VARTM), autoclave, resin transfer moulding (RTM) etc. Preform compressibility was measured from the thickness-pressure curve. The fibre volume fractions were also predicted at different compaction levels.

It was observed that the major changes in the preform thicknesses occurred during the first cycle of loading for all the preforms. In the subsequent cycles, these changes are less

significant, suggesting that the internal fibre structures were reordered during the first cycles. However, the magnitude of this reordering highly depends on the binder weave architectures. 1x1 plain weave has the least compressibility due to more binder crossings in their structures. These frequent binders prevent the preform on compression. With the reduction of the binder crossing points, compressibility was increased for 2x1 twill and 2x2 twill. Angle interlock (AI) weave, due to the angular binder path and least number of interlacings, compressed more, yielding the highest compressibility in the first cycle. However, in the subsequent cycles, the compaction behaviour is almost opposite to the first cycle, where angle interlock weave has the least compressibility, and orthogonal weaves have high compressibility.

Regarding fibre volume fraction (FVF), it was observed that the maximum FVF is obtained after multiple loading cycles. After every compaction cycle, there are some forms of permanent deformations in the preforms, which allow to get higher fibre volume fraction in the subsequent cycles. Angle interlock weave due to highest compressibility yielded highest fibre volume fractions among all the weaves.

There was no significant difference in the compaction behaviour of preforms manufactured with various binder tensions. However, a less significant difference in compressibility indicates that the preform with higher binder tension was pre-compacted during the manufacturing process.

Chapter 5 In-Plane Permeability of 3D Woven Prefoms

5.1 Background

This chapter discusses the influence of Z binder architectures on the resin flow behaviour of 3D woven preforms. A permeability measurement set-up is developed to measure in-plane permeability and is detailed in the second section. Flow analysis method is explained in the third section. Resin parameters are discussed in section four. Permeability results are discussed in fifth section of this chapter. The chapter finishes with some concluding remarks.

5.2 Development of Permeability Measurement Setup

The permeability of textile preforms can be measured in both linear and radial flow techniques. Each of the techniques can use both saturated flow and unsaturated flow methods. However, significant differences are reported in the permeability values resulting from these techniques [138]–[142]. About 50% differences in the permeability values are reported between the saturated and unsaturated permeability measurement methods, and about 15% difference was found for parallel and radial flow methods [138]. Gebart et al. [141] reported a minor difference between these methods, whereas Hammond et al. [142] reported no difference between the saturated and unsaturated unidirectional flow method. According to Lundstrom et al., minimum data scattering and best repeatability are found in the unsaturated permeability measurement technique [143], [144].

Again, between the parallel and radial flow methods, the latter one offers more data reliability as all three permeability tensors can be obtained from a single experiment [61]. This method also eliminated the issue of race-tracking, which can significantly affect the

results of permeability measurements [145]. In addition, three separate experiments need to be carried out for the parallel/linear flow method to obtain permeability tensors in 0°, 45° and 90° axes. Considering both aspects, the current research opted to measure resin permeability of 3D woven preforms in radial flow technique using unsaturated flow method.

In permeability measurement, the flow front is needed to be tracked. To track the flow front, researchers have taken many initiatives. Modi et al. [146] presented a summary of the flow sensing technology in permeability measurement by different investigators and tabulated the advantages and disadvantages of these technologies. Skordos et al. [147] used dielectric to sense the flow front. Time Domain Reflectometry (TDR) sensors were used by Dominauskas et al. [148] for online flow sensing. Kang et al. [149] used still photos to track the front flow. Pressure transducers to measure the pressure drops and hence sense the flow front has been used by several investigators [145], [150]–[152]. Optical fibre sensors [153]–[156] as well as SMART Weave conductive sensors [157]–[160] has been used by some other investigators. Modi et al. used the web camera for front flow visualisation. However, the most common technique is to use the digital camera [161]–[166] for front flow tracking. Using a digital camera for the front flow tracking is easy and simple, but it requires at least one side of the mould to be transparent. Grimsley et al. [165] and Sayre & Loos [166] have used a transparent vacuum bag on the top side for front flow tracking. D. Nielsen et al. in their all works [162]–[164] used the CCD camera and Plexiglas for front flow tracking. They also used dark green food colour for more clear flow front detection.

As a part of the current research, a permeability measurement tool was developed to measure resin in-plane permeability with a cavity controlling system. This mould

thickness controlling system is adopted by segmenting the top plate in two parts-inner part and the outer part. This novel designing of the top plate allows a vertical movement of the inner part which ultimately control the thickness of the preforms and determine the FVF of the composites as well. The system is developed based on the radial flow technique. The flow front is tracked through the flow visualisation technique. A schematic figure of the system is shown below in Fig. 5. 1.
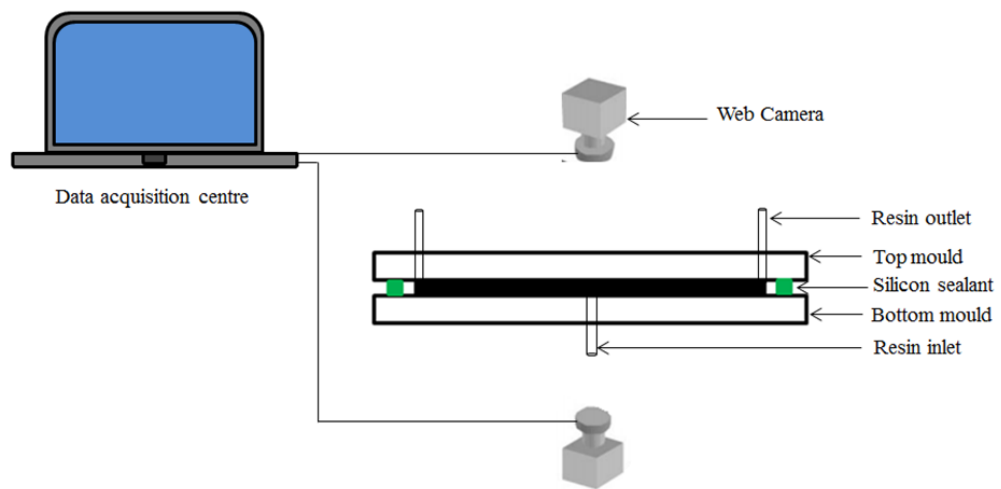
Fig. 5. 1 Schematic view of the flow front tracking and data acquisition system.

The permeability measurement setup includes the two Perspex plates with the dimension of 400mm X 400mm X 20mm, two HD web cameras (Logitech Pro C920) -top (1) and bottom (2), arrangements for appropriate lighting (2X21W, 230V adjustable desk light from RS components), a pressure gauge to check the sealing, a laptop for flow front data acquisition and aluminium supporting frame. A silicone rubber sealant sheet (3mm thickness) is used between the top and bottom moulds to create the sealing. G-clamps were used to ensure the proper sealing by clamping pressure. Spacer bars were used to control the cavity thickness. The resin inlet system is set in the centre of the bottom mould, and the outlet is set on the two sides of the top mould. The pressure gauge is attached to check the proper sealing of the two moulds. The whole set-up is shown in Fig. 5. 2.
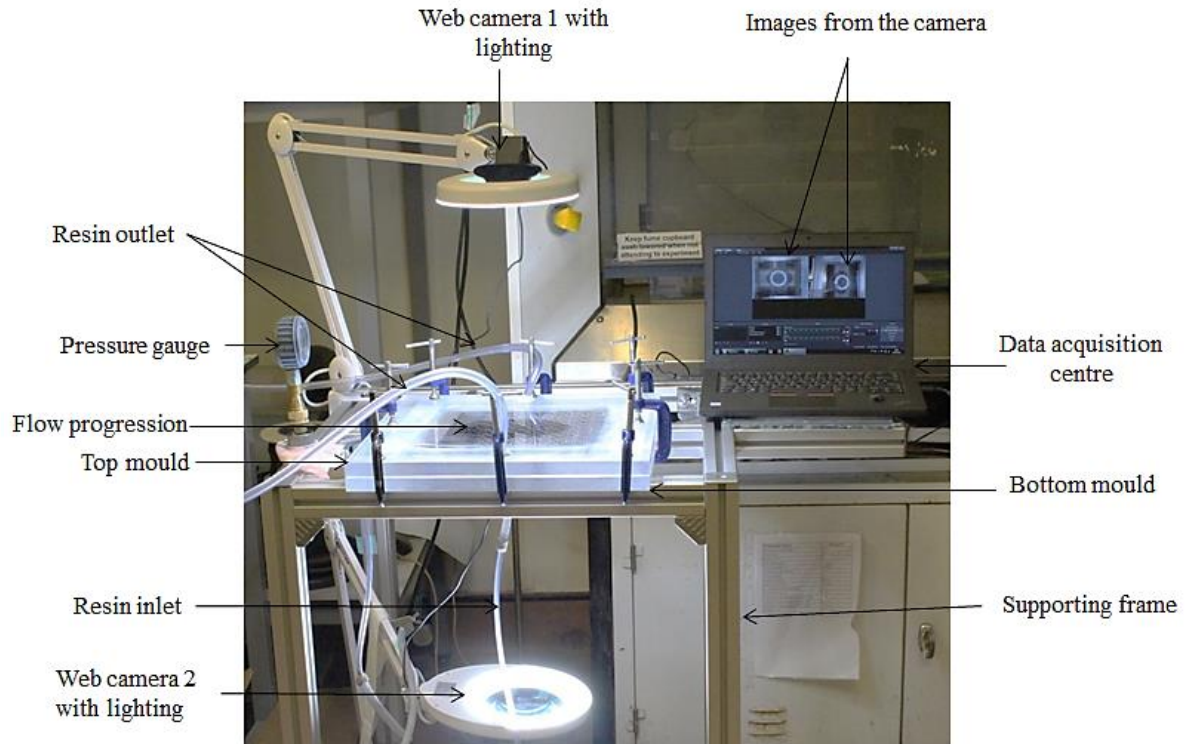
Fig. 5. 2 Permeability measurement setup.

Mould deflection can affect permeability measurement significantly [167], [168]. This issue was considered prior to the design of the set-up. To minimise the effect of mould deflection, a two-step measure was taken during the set-up design. The first step was to choose a thick mould: 20mm thick Perspex plates were chosen as top and bottom mould plates. Another important design consideration was splitting the top plate into two sections: inner and outer parts (see Fig. 5. 3). The inner part dimension was 270mm X 270mm X 20mm, and it was designed to move vertically in-ward and outer-ward. This vertical movement ensures the proper cavity thickness according to the spacer bar dimensions. 75mm long spacer bars were set on all four sides of the preforms before the inner mould compaction to reassure the uniform cavity thickness. Pressuring both plates by G-clamps was done on the outer part of the top plate. Tacky tapes were used at every permeability measurement cycle to ensure proper sealing of the inner and outer part.
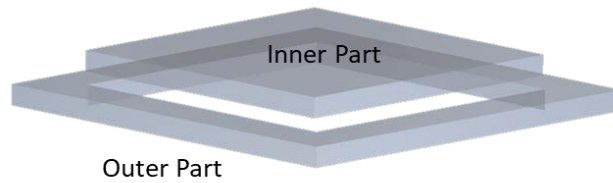
Fig. 5. 3 Parts of top plate

A measurement scale was embedded on the inner top plate for further calculation of the permeability tensors from the flow front values (see Fig. 5. 4). This scale works as a measurement reference for the flow front values.
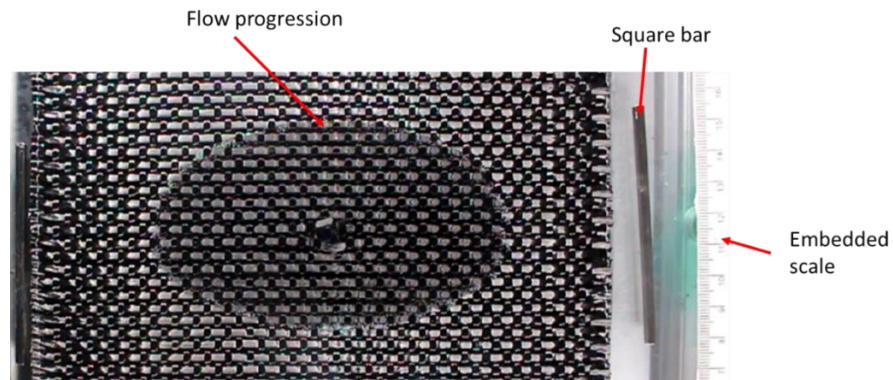
Fig. 5. 4 Embedded scale for measurement reference

5.3 Flow Analysis

From the recorded resin flow videos, flow fronts were extracted at different time intervals. By following least square fitting technique, an ellipse was fitted for every tracked flow front. The images were further processed and analysed using ImageJ software [169] to record the flow front positions in major and minor axes of the fitted ellipse. The data acquisition process sequences are shown in Fig. 5. 5.
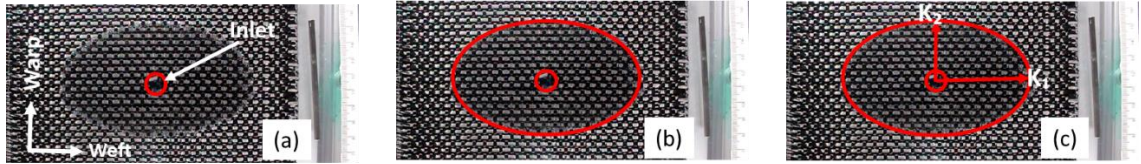
Fig. 5. 5 Sequences of image processing: (a) extracted image from video record, (b) fitted ellipse on flow front and (c) measuring major and minor axes distances.

Principle permeability were calculated using the following set of equations which were derived by Ali et al. [78] from the method described by Weitzenbock et al. [61], [62].

$$K_1 = \frac{1}{t}\frac{\mu\emptyset}{4\Delta P}\{a^2\left(2\ln\left(\frac{a}{x_0}\right)-1\right)+x_0^2\} \dots\dots\dots\dots\dots\dots\dots \ (5.1)$$

$$K_2 = \frac{1}{t}\frac{\mu\emptyset}{4\Delta P}\{b^2\left(2\ln\left(\frac{b}{y_0}\right)-1\right)+y_0^2\} \dots\dots\dots\dots\dots\dots\dots.. \ (5.2)$$

where, a and b are the ellipse axes, x_0 and y_0 are the co-ordinates of the inlet hole in their respective directions, μ is the viscosity of the resin, $\emptyset$ is the porosity of the preform and ΔP is the pressure gradient.

5.4 Materials

In-plane permeability of 3D woven preforms (both warp bound and weft bound) with different binder weave architectures was measured to investigate the role of Z binder on resin flow. Preform specifications are detailed in Chapter 3. For the warp bound preforms, cavity thickness was kept as 3mm, and for the weft bound preforms, cavity thickness was 2.5mm. Fibre volume fraction was calculated using formula (4.2) in Chapter 4. For the warp bound preforms, FVF was 37%, whereas for the weft bound, it was 33%.

A number of researches investigated the influence of test fluids on permeability [142], [143], [170]–[172]. However, the collective results are inconclusive. Naik et el. [173] the

effect of test liquid in permeability is insignificant as long as the fluid viscosity is low enough that allow the mould cavity a proper filling of. Epoxy In-2 resin was used in this current research considering availability and actual use in composite manufacturing. During all the experiments, resin temperature was kept at 20°C to get the same viscosity. As the resin datasheet [174] provides a range for the viscosity values of the resin at 20°C, it was needed to measure the actual viscosity of the resin. So the resin viscosity was measured using a HAAKE Viscometer iQ Rheometer. Average viscosity was calculated as 0.62 Pa.s. from the machine values at 20°C.

5.5 Results and Discussion

The preforms with different binder architectures, as mentioned earlier, have been subjected to in-plane permeability measurement. The newly developed permeability measurement setup was used in this case. The resin flow development in the 1x1 plain preform is shown below in Fig. 5. 6 to represent all the weaves.
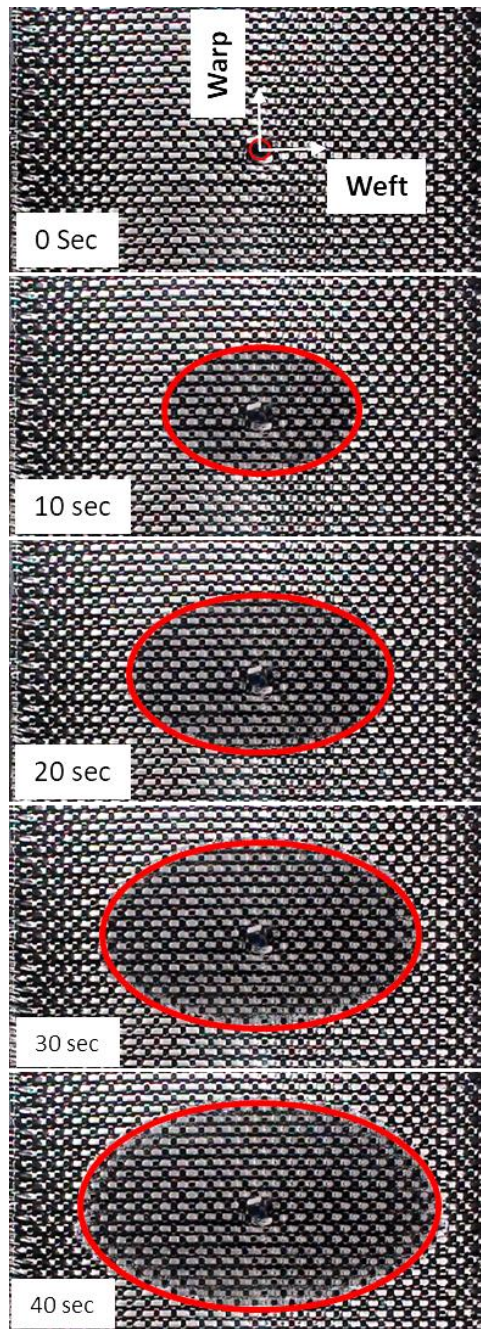
Fig. 5. 6 Resin flow development in 1x1 Plain weave

5.5.1 Permeability of the Warp Bound Preforms

The graphs for flow front progression in warp, weft and off-axis directions against time is shown for the warp bound preforms in Fig. 5. 7. The graphs show that the weft way flow rate is much higher for the orthogonal preforms with 1x1 plain, 2x1 twill and 2x2 twill binder weaves. The resin flow is in between the weft and warp way values in the

off-axis direction. All three directional flow rates are almost equal for the angle interlock preform.

(a)

(b)

(c)

(d)
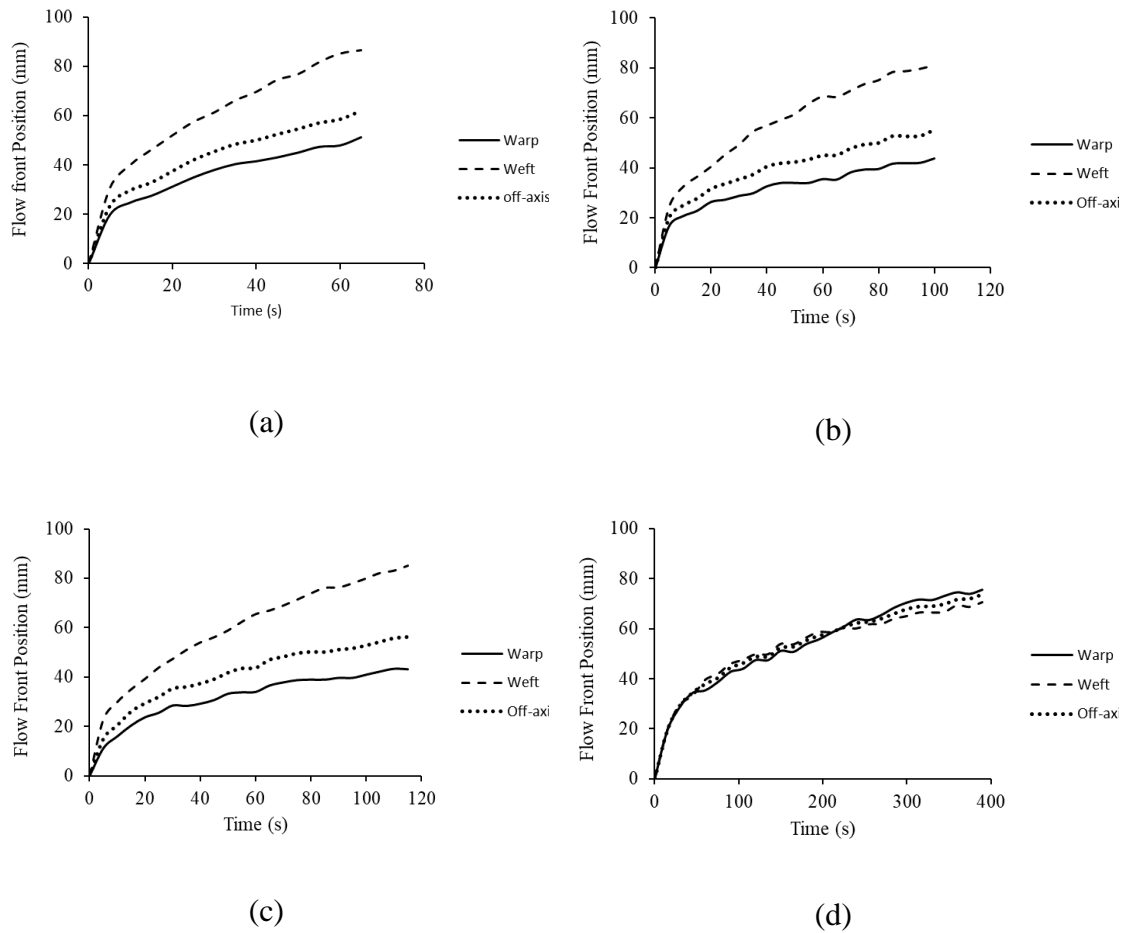
Fig. 5. 7 Flow progression diagram in warp, weft and off-axis direction for warp bound 3D woven preforms: (a) 1x1 Plain, (b) 2x1 Twill, (c) 2x2 Twill and (d) Angle Interlock (AI)

The principal in-plane permeability values warp (K_2) and weft (K_1), along with the anisotropy (i.e. the ratio K_2/K_1), are listed in the table for the warp bound preforms at 37% FVF. For all preforms, both in-plane principal permeability values are interpreted in the order of $10^{-10}m^2$.

Table 5. 1 Principle permeability and preform anisotropy of warp bound preforms

Preform Type	Principal Permeability (E-10 m²)		Anisotropy (I) K_2/K_1
	Warp (K_2)	Weft (K_1)	
1x1 Plain	1.14±0.29	6.76±1.37	0.17±0.01
2x1 Twill	0.82±0.01	3.50±0.19	0.24±0.04
2x2 Twill	0.65±0.01	3.13±0.20	0.21±0.03
Angle Interlock	0.74±0.06	0.74±0.11	1.02±0.16

As expected from the graphs in Fig. 5. 7, the weft way permeability for all the orthogonal weaved preforms is much higher than the warp way permeability except for the angle interlock weave. Among the weaves, 1x1 plain weave has the highest resin flow, which is decreased for 2x1 twill and 2x2 twill weaves, respectively. As all the weave and infusion parameters are the same in all the preforms except the number of interlacing points among these three weaves, this difference can be easily directed to the resin channels created by the binder interlacings. Previous researches also reported that the resin channels created by the binders are the most influential factor in resin flow [54]. In plain weave, the structure has the highest degree of interlacings (Table 3. 1), creating the highest number of resin channels ($705/100cm^2$). As a result, permeability is also highest among these three weaves. In 2x1 twill, the degree of interlacings is reduced by 33% to a number of $470/100cm^2$, so are the resin channels. For 2x2 twill weave degree of interlacings is reduced by 50% ($353/100cm^2$) compared to the 1x1 plain weave as well as the resin channels created by the binders. As a result of these reductions in resin channels, permeability is also decreased accordingly. For the angle interlock weave, permeability values are the lowest among all of these preforms. Due to the angular binder path, there are no significant resin channels [77]. Also, the number of interlacings are minimum ($235/100cm^2$). Both of these factors reduced the resin flow significantly for angle interlock preforms.

On the warp way, the permeability values are almost the same for all the weaves except the 1x1 Plain weave. This similarity is because of the structural similarity of the preforms in that particular direction. In the warp way direction, all the preforms have four layers of warps with the same two densities and one binder layer. The warp to binder ratio is 1:1 i.e. the binder is incorporated after every warp column. As there is no difference in the directional structures of the preforms, the resin permeation is also found almost the same. However, a higher permeability in the 1x1 plain weave may be related to the higher undulation of the warp and weft tows due to a higher degree of interlacings caused by the binder path. Several other research also reported that the orthogonal plain weave have higher warp way permeability compared to angel interlock [54] and layer to layer structures [77]. They reported that this higher permeability is due to higher waviness caused by the frequent binder interlacings.

The difference between the warp and weft way permeability can be further explained by the resin flow behaviour within the preform structures. When the resin is injected into a dry preform, flow development occurs in two ways- intra tow resin flow and inter-tow resin flow. Intra-tow permeability, also called micro-scale permeability, is the resin flow within the mono-filaments of a single tow. On the other hand, inter-tow permeability referred to as meso-scale permeability, is the resin flow between the gaps of different tows within a fibrous preform. This is also termed as gap permeability. A simple schematic illustration of intra-ow and inter-tow permeability is shown in Fig. 5. 8.
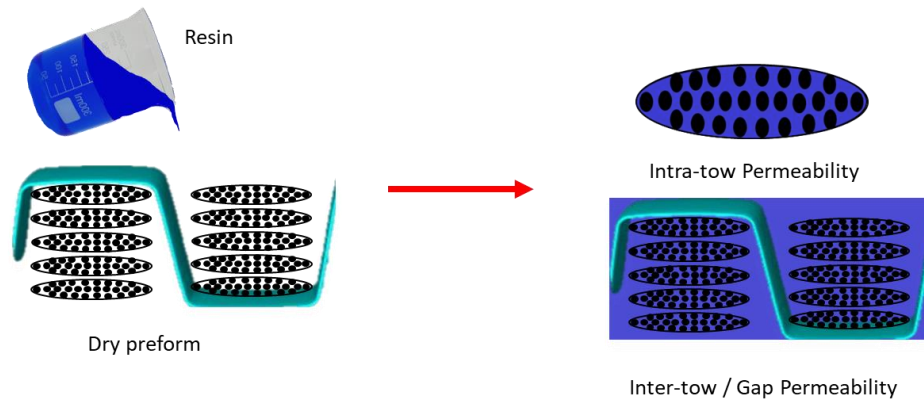
Fig. 5. 8 Schematic illustration of intra-tow and inter tow permeability.

In the warp way, ideally there is no gap in between the tows in a 3D woven preform [see Fig. 5. 9(a)]. As a result, intra-tow permeability is the dominant resin flow in that direction. In addition, binder act as flow disturbance when the resin flows towards binder direction [78]. A unit cell segmented from the X-ray micro CT images of 1x1 plain orthogonal structure is used to illustrate this event [see Fig. 5. 9(b)]. This image was segmented from a scanned 1x1 plain orthogonal woven composite with 23.5 voxel size for the illustration purpose. The image show that the z-binder surface acts as a barrier for the resin flow. Both of these reasons cause low in-plane permeability in warp direction.

(a)   (b)
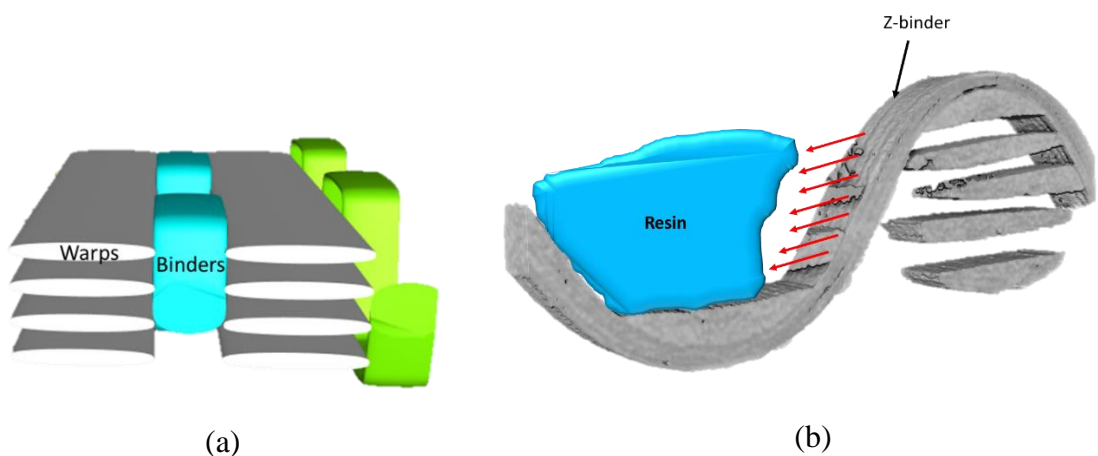
Fig. 5. 9 (a) Warp-binder positioning in ideal condition, (b) Binder surface acting as a flow barrier.

In the weft way, binders create resin channels while making interlacings with the weft yarns (see Fig. 5. 10); therefore, in addition to the intra-tow flow, resin also moves along these channels. Several published research reported that, within a preform, inter-tow /gap permeability is much more dominant than intra-tow permeability [175]–[177]. As a result, permeability in the weft direction is much higher than the warp directions due to the combination of intra-tow and inter-tow permeability.
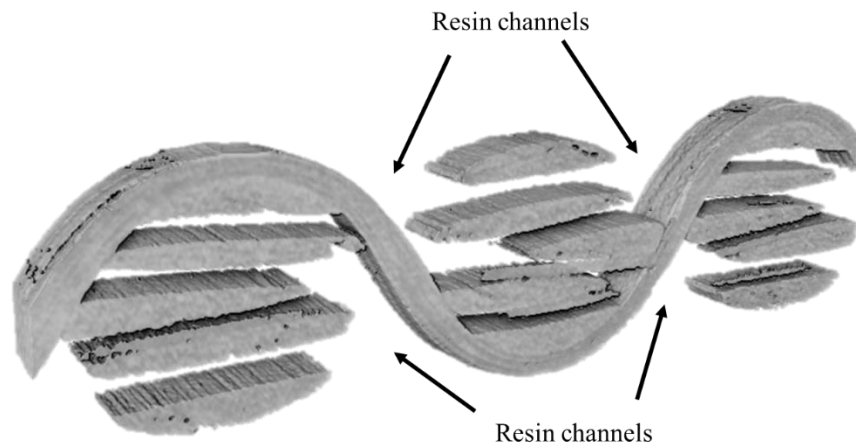
Fig. 5. 10 Resin channels created by the Z-binders

Preform anisotropy, which is the ratio between warp and weft permeability, indicates the shape of the resin flow development [77]. For the orthogonal preforms with 1x1 plain, 2x1 twill and 2x2 twill binder weave, the difference between warp and weft permeability is significantly high, suggesting that their flow front progression is in an elliptical shape. Angle interlock weave has an angular binder path which reduces the number of resin channels as well as inter tow gaps, resulting in almost equal warp and weft permeability. As a result, the resin flow development is almost in a circular shape, indicating uniform development in all directions. Fig. 5. 11 shows the development of resin flows through the warp bound preforms.
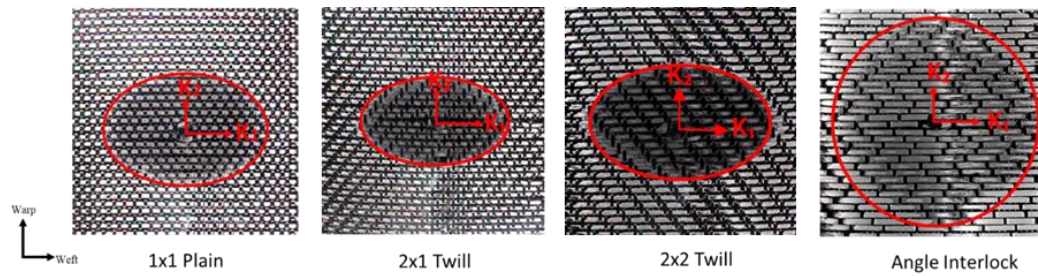
Fig. 5. 11 Flow developments in warp bound preforms with different binder weave architectures

5.5.2 Permeability of the Weft Bound Preforms

The graphs for flow front progression in warp, weft and off-axis directions against time is shown for the weft bound preforms in Fig. 5. 12. The graphs show that the warp way flow rate is significantly higher for the orthogonal preforms with 1x1 plain, 2x1 twill and 2x2 twill binder weaves. The resin flow is in between the warp and weft way values in the off-axis direction. For the angle interlock preform, all three directional flow rates are almost equal. However, the initial directional flow rates in these weft bound preforms are almost same in warp, weft and off-axis directions. This particular behaviour needs further investigation for the possible explanations.

(a)

(b)

(c)

(d)
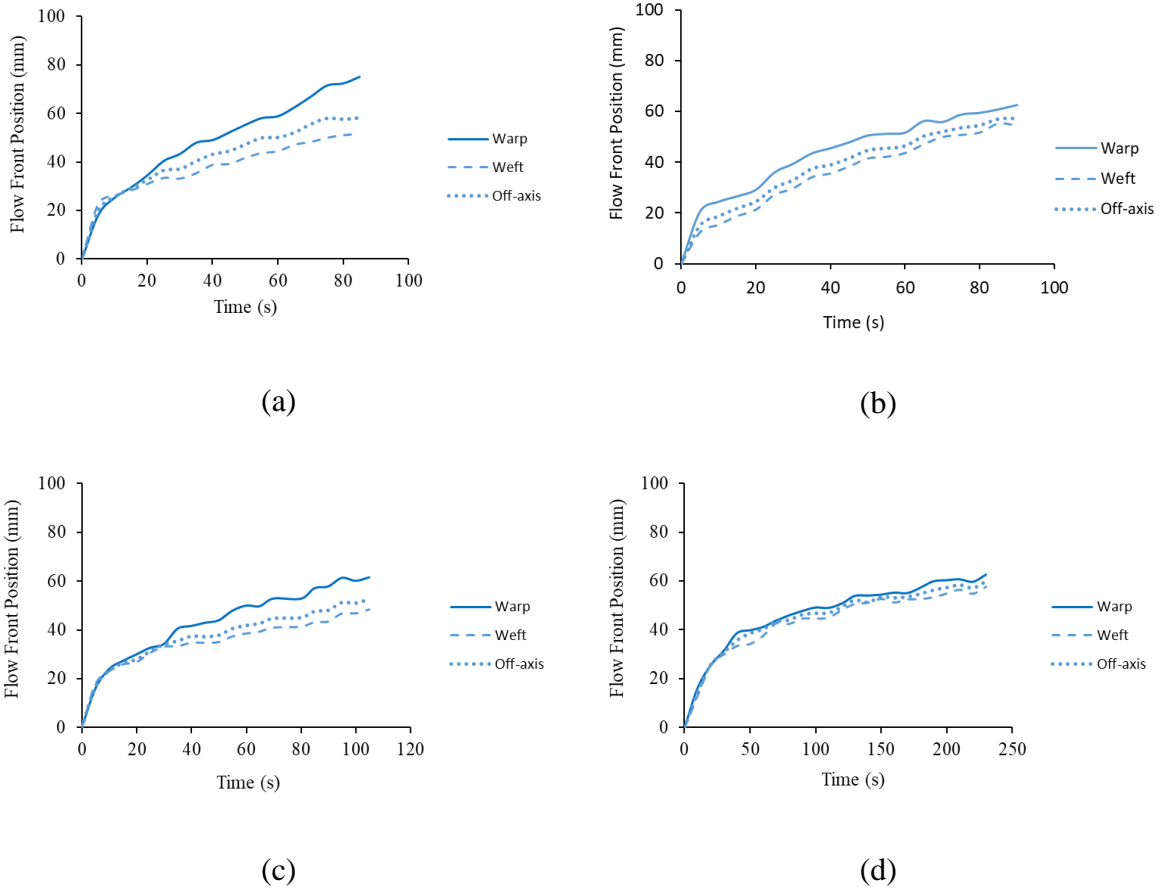
Fig. 5. 12 Flow progression diagram in warp, weft and off-axis direction for weft bound 3D woven preforms: (a) 1x1 Plain, (b) 2x1 Twill, (c) 2x2 Twill and (d) Angle Interlock.

The principal in-plane permeability values warp (K_2), and weft (K_1), along with the anisotropy (i.e. the ratio K_2/K_1), are listed in the table for the warp bound preforms at 37% FVF. For all preforms, both in-plane principal permeability values are interpreted in the order of $10^{-10}m^2$.

Table 5. 2 Principle permeability and preform anisotropy of weft bound preforms

Preform Type	Principal Permeability (E-10 m²)		Anisotropy (I) (K_2/K_1)
	Warp (K_2)	Weft (K_1)	
1x1 Plain	2.57±0.55	1.19±0.16	2.16±0.25
2x1 Twill	1.76±0.19	1.10±0.19	1.61±0.17
2x2 Twill	1.57±0.14	1.00±0.07	1.56±0.21
Angle Interlock	0.93±0.17	0.86±0.02	1.08±0.12

As expected from the graphs at Fig. 5. 12, the warp way permeability for all the orthogonal weaved preforms are much higher than the weft way permeability. This observation is almost opposite to the findings in warp bound preforms. The reason for this opposite trend is due to the incorporation of the binder in the weft way directions. As the binders are incorporated in the weft way direction, they created resin channels in the warp direction. Due to these warp way resin channels, warp way permeability is higher than the weft way [54], [77]. Like the warp bound structures, angle interlock preforms have almost equal warp and weft way permeability (as explained in section 5.5.1).

On the weft way, the permeability values are almost in the same order as the warp way for all the weaves. However, these differences in permeability values are less significant among the weaves. This similarity is because of the structural similarity of the preforms in that particular direction discussed earlier for the warp way permeability of warp bound preforms. In the weft way direction, all the preforms have three layers of weft with the same tow densities and one binder layer. Weft to binder ratio 1:1 i.e. one binder is incorporated after every weft column. As there is no difference in the directional structures of the preforms, the resin permeation is also found almost at the same level.
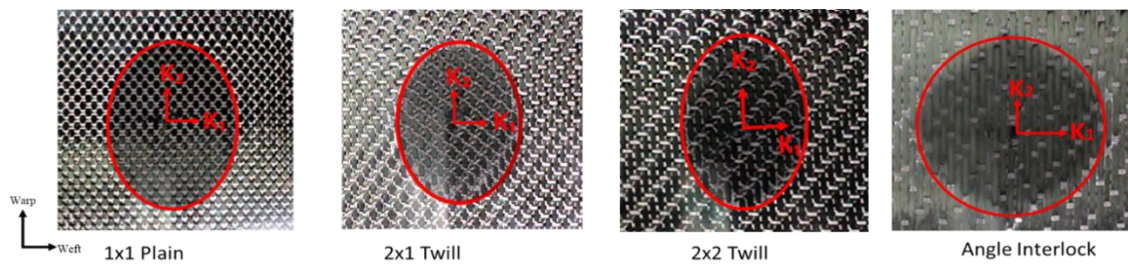
Fig. 5. 13 Flow developments in weft bound preforms with different binder weave architectures

Preform anisotropy (Fig. 5. 13) is found in the same trend of the warp bound structures. The reasons are the same as was in warp bound preforms. Orthogonal weaved preforms

121

showed higher orthotropic flow nature with more elliptical flow development [54]. Angle interlock preform has almost circular shape flow front development.

It is important to note that the difference between warp and weft way permeability in these weft bound preforms is not as high as in the warp bound preforms. The reason is the lower directional fibre volume fraction in the weft directions. As mentioned in Chapter 3, the number of weft layers and tow densities were reduced in weft bound preforms; its directional fibre volume fraction was also reduced. This reduction in FVF assisted in resin flow enhancement in weft directions.

5.5.3 Comparison of Warp and Weft Bound Preform Permeability

The main difference between warp bound and weft bound preforms is the alteration of the binder incorporation direction. In warp bound preforms, the binders are coming in warp way direction, whereas in weft bound preforms, binders are inserted in weft way direction. As a result of this alteration, the resin channels are also altered accordingly. In warp bound preforms, resin channels are created in the weft direction and in weft bound preforms, resin channels are created in warp way directions. Warp way parameters are the same for both types of preforms except the binder created resin channels. This section analyses warp way permeability of both warp bound and weft bound preforms to justify the impact of binder-created resin channels on resin flow behaviour.

The warp way permeability of both warp bound and weft bound preforms are shown in a comparative bar chart in Fig. 5. 14.
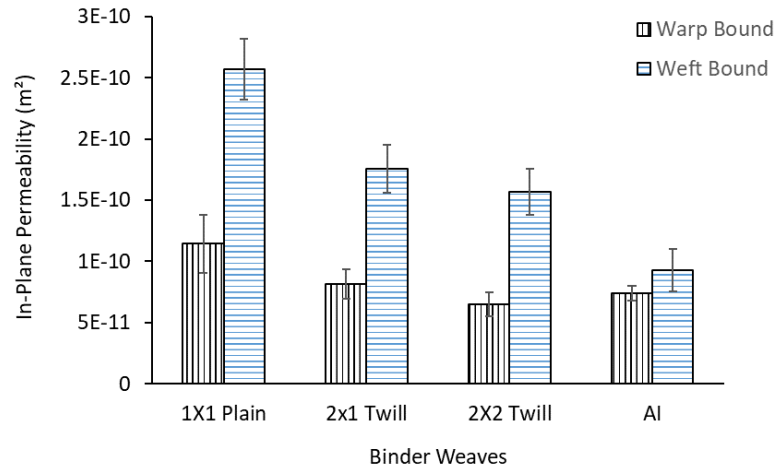
Fig. 5. 14 Warp way permeability of warp bound and weft bound preforms

The graphs show that the weft bound preforms have higher permeability compared to the warp bound preforms instead of having almost equal fibre volume fractions. For the orthogonal preforms, this difference is significantly high for all three weaves i.e. 1x1 plain, 2x1 twill and 2x2 twill binder weaves. Due to the presence of the flow enhancing resin channels in the warp direction of the weft bound preforms, they showed higher permeability [97]. For the angle interlock weave, this effect is insignificant. This is due to the geometric microstructure of the angle interlock weave where the angular binder path does not allow to form significant resin channels [54].

5.5.4 Effect of Binder Tension on Permeability

In-plane permeability of the preforms with two different binder tensions are measured following the same procedure and parameters used in measuring permeability for the warp bound preforms as discussed earlier this chapter (in section 5.5.1 Permeability of the Warp Bound Preforms). In both cases, the cavity thickness was 3mm and the fibre volume fraction was 37%. Warp and weft way permeability of the preforms with variation in binder tensions are given in Table 5. 3. The results show no significant differences in permeability values for these two structures. For both of the preforms, warp and weft way

permeability values are almost same and weft way permeability is much higher than the warp way permeability.

Table 5. 3 Principle permeability of the preforms with different binder tensions.

Preform Type	Principal Permeability (E-10 m²)		Anisotropy (I) K_2/K_1
	Warp (K_2)	Weft (K_1)	
NT	1.14±0.29	6.76±1.37	0.17±0.01
HT	1.27±0.13	6.37±0.89	0.20±0.02

As both the preforms have same internal geometrical structures in terms of tow layers, densities and the number of resin channels, the flow develops inside these structures in the similar way to each other and resulting permeability values within the same range. Although the preform with higher binder tension (HT) is reported to have manufacturing induced pre-compaction, it didn't have any significant effect on permeability. This is because of the same fibre volume fraction of both of this preforms (37%) achieved with a cavity thickness of 3mm.

5.6 Concluding Remarks

The role of Z-binder architecture and binder tension on in-plane permeability of 3D woven preforms were investigated in this chapter. A radial flow permeability measurement set-up was developed based on the flow visualisation technique. Permeability was measured for warp bound and weft bound preforms with four different binder weave architectures.

Through-thickness binders are found to create resin channels. The weave interlacings determine the frequency of resin channels. A higher degree of interlacings produced more resin channels. As a result, 1x1 plain weave has the maximum resin permeability among

all the weaves. Due to the reduction of the degree of interlacings, number of resin channels decreased for the 2x1 twill and 2x2 twill weaves so as the resin permeability. In angle interlock weave, the binder runs in an angular path which does not allow to create any significant resin channels. Also degree of interlacings in that particular weave is least among all of these preforms. As a result, angle interlock weave have the least permeability.

Binder interlacement pattern is also found to affect flow development uniformity. In orthogonal structures where the through-the-thickness binders create more and significant resin channels, the flow is more elliptical, indicating high anisotropy of the resin flow. Flow is higher in the direction of resin channels. For angle interlock weave, principle permeability is almost the same in both warp and weft directions, which indicates that due to the angular binder path, the resin flows uniformly in all directions.

Comparing the warp bound and weft bound preform permeability provides a good justification of the influence of binder created resin channels on permeability. It is found that, by altering the resin channel direction, warp way permeability can be significantly improved.

One of the major challenges of measuring the permeability was to trace the flow boundary with ease. This issue was due to the usage of transparent resin as flow liquid. In follow-up experiments, it is recommended to use flow visualisation enhancing materials (e.g. food colour) without causing any flow disturbance.

Chapter 6 Geometric Properties of 3D Woven Composites

6.1 Introduction

This chapter details the manufacturing process of the 3D woven composites and their geometrical properties. A customised vacuum bag infusion method is described to manufacture 3D woven composites in the second section. Z-binder waviness is measured in the third section in terms of crimp angle and crimp percentages. A high magnification optical microscope was used to reveal the cross-sectional images of Z-binders of different weave types. In the following section, volume fractions of fibres, matrix and voids are measured. Warp and weft directional fibre volume fractions are also calculated in that section for the 3D woven composites. The chapter finishes with concluding remarks.

6.2 Composite Manufacturing

One of the standard methods of manufacturing composite laminate is the vacuum bag infusion. However, due to the through-thickness binder interlacings, 3D composite laminates often come up with waviness on the top surface (see Fig. 6. 1). This particular cross-sectional image is taken from a carbon-epoxy composites manufactured with vacuum bag infusion with four layers of warp tows, five layers of weft tows and 1x1 Plain orthogonal Z-binder weave architecture. This unevenness of the laminate surfaces can be a potential source of crack initiation during loading.
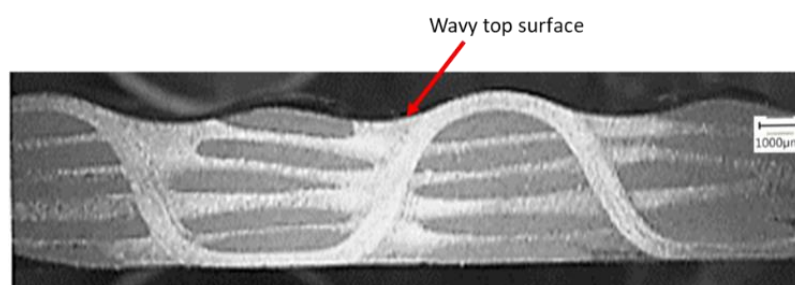
Fig. 6. 1 Surface waviness on the top side of the laminates from vacuum bag infusion.

In this current research, 3D woven composites were produced using a customised "Two plate vacuum bag infusion" method to avoid any such waviness on the laminates. Here, two metal plates were used on the top and underneath the preforms to get even surfaces and uniform thickness on the laminates. A schematic diagram of the infusion set-up is shown in Fig. 6. 2.
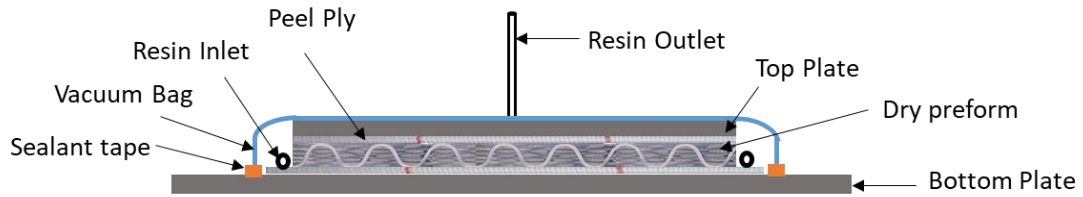
Fig. 6. 2 Schematic of the two-plate vacuum bag infusion method

Here two mirror-polished steel plates were used as the bottom (500mmX500mm) and top plates (300mmX300mm). Both plates were coated with several layers of release agents for the ease of removing the composites after curing. Peel ply was used on top and bottom of the dry preform for easy removal of the composites from the plates. In the end, the whole system was sealed by using a vacuum bag and tacky tape. After applying a vacuum level of pressure, the system was left for at least an hour to check for leakage. The resin was infused from all sides of the preform using spiral tubes, and the resin outlet was drawn from the centre of the top plate to avoid any race tracking effect. The infusion assembly is shown in Fig. 6. 3.
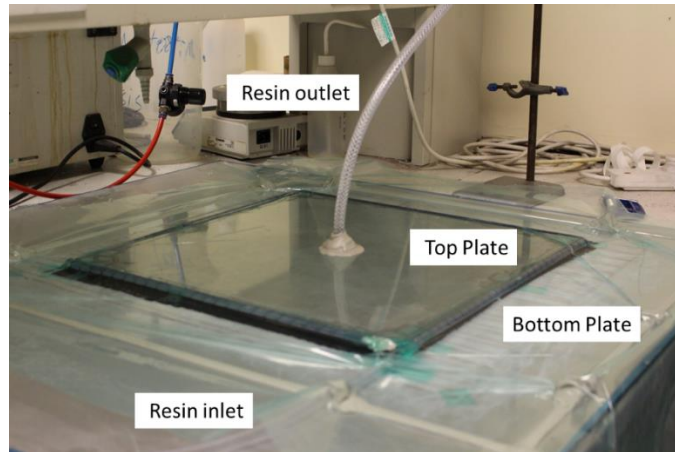
Fig. 6. 3 Vacuum bag infusion assembly using top and bottom plates.

A bi-functional, ultra-low viscosity, room temperature curing epoxy resin (Epoxy IN-2) along with the hardener (AT slow- Formulated amine) supplied by Easy Composites were used for the infusion [174]. This ultra-low viscous resin (resin-hardener mixing viscosity is ~0.2 Pa.s) was used to ensure the flow of the resin through all the intricate structures of the 3D woven preforms. The resin-hardener mixing (100:30) was stirred manually and the degassed for at least half an hour to remove any bubbles before infusion. After infusion, the set-up was left for at least 24 hours at room temperature for curing. The composite laminate was demoulded after curing and cut into test specimens for different mechanical characterisations (surface imaging, FVF, tensile and bending tests). The specimens were cut according to each testing standards using a rotary diamond cutter (SLIDERCUTTER 5600) with a blade thickness of 2.1mm and rotary speed of 700 rpm.

6.3 Measurement of Z-binder Crimp % and Crimp Angle

As part of this research, the Z-binder crimp is measured as a function of binder weave architecture and binder tension. For crimp measurement, the binder way geometry of the composites is revealed using optical microscopic images.

6.3.1 Optical Microscopy

The samples were cut by using a diamond saw for the cross-sectional images. Cut samples were ground by using grinding papers with a roughness of 120, 320, 540, 800 and 1200 grits. The samples were then polished by using diamond suspension with 6 µm and 1µm roughness. The images were obtained using a Keyence VHX-5000 Optical microscope at 200X magnification (see Fig. 6. 4).

Fig. 6. 4 A Keyence VHX-5000 optical microscope

Binder way cross-sectional images were taken for all the composites. Image stitching technique was used to get the full repeat of binder weave architecture. The binder way cross-sectional images of composites are shown in Fig. 6. 5 (warp bound composites) and Fig. 6. 6 (weft bound composites).

The images clearly show the differences among the binder weave architectures and the degree of interlacings. 1x1 plain weave have an orthogonal pattern with most interlacings in a unit area. The number of interlacings continues to decrease for the 2x1 and 2x2 twill orthogonal weaves. In angle interlock weave, the binder follows an angular path as well, as it has the minimum number of interlacings.
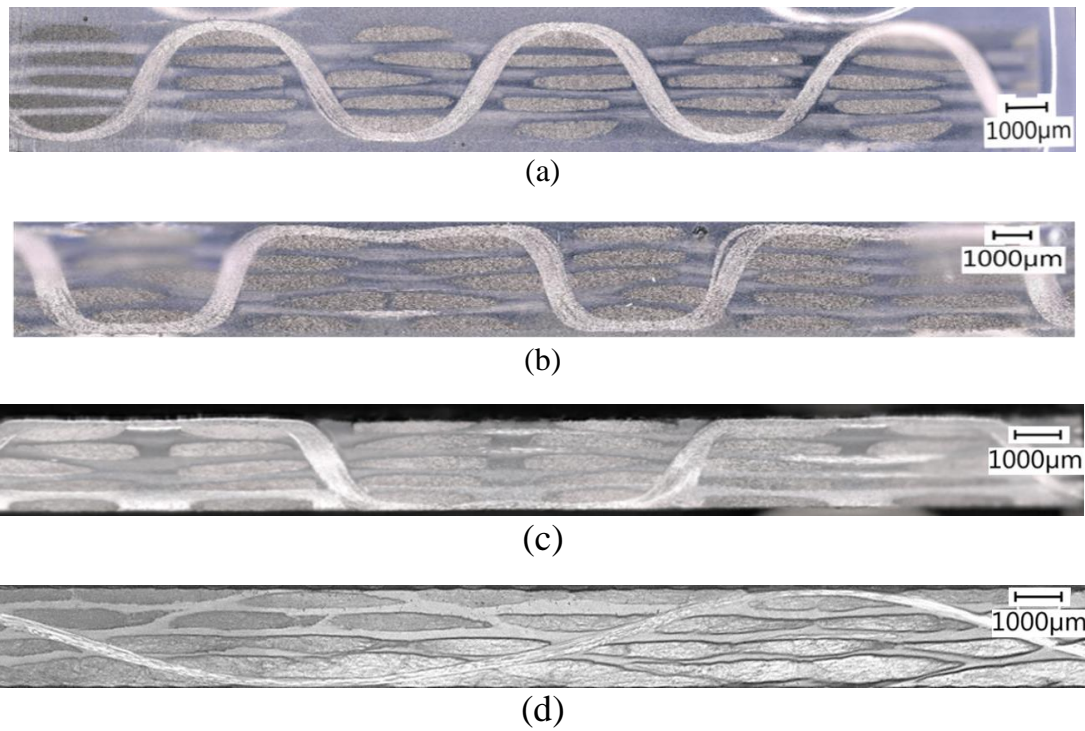
Fig. 6. 5 Cross-sectional optical images for different binder weaves (warp way binder),

a) 1x1 Plain, b) 2x1 Twill, c) 2x2 Twill and d) Angle Interlock (AI).
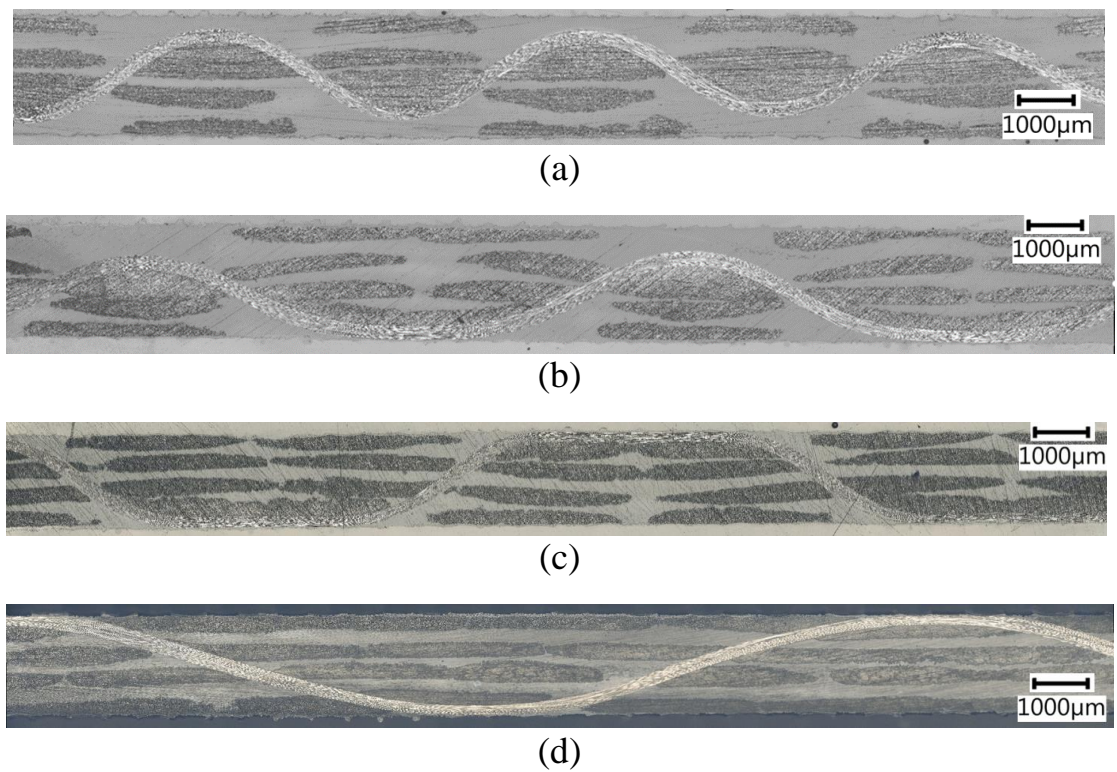
Fig. 6. 6 Cross-sectional optical images for different binder weaves (weft way binder),

a) 1x1 Plain, b) 2x1 Twill, c) 2x2 Twill and d) Angle Interlock (AI).

The cross-sectional images of 1x1 plain orthogonal composites with two different binder tensions are shown in Fig. 6. 7.

(a)

(b)
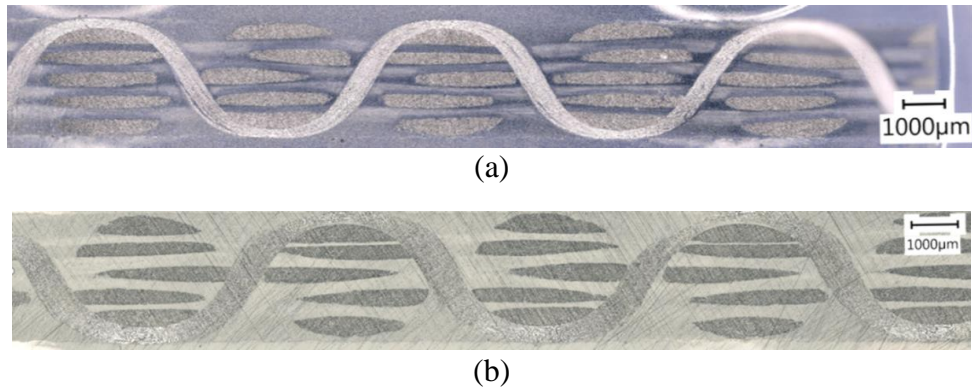
Fig. 6. 7 Cross-sectional optical images for binders for different tensions, (a) Nominal Tension (NT), (b) Higher tension (HT)

No significant differences are visible for the composites with binder tension variation in the cross-sectional images except a small degree of compaction (~6% compaction in the HT composite within the top two weft layers) exactly under the interlacement points. They both have the same orthogonal pattern with an equal degree of interlacings.

6.3.2 Binder Crimp Measurement

Cross-sectional images were taken to study the tow waviness in binders. The stitched images taken by the optical microscope were further post-processed using ImageJ software to measure the binder crimp angle and crimp %. Out-of-plane tow waviness of individual tows was studied by plotting a line along the centre of the tow. The deviation of the plotted line from a horizontal datum for each tow was measured as the crimp. A schematic diagram is shown in Fig. 6. 8 for the crimp measurement.
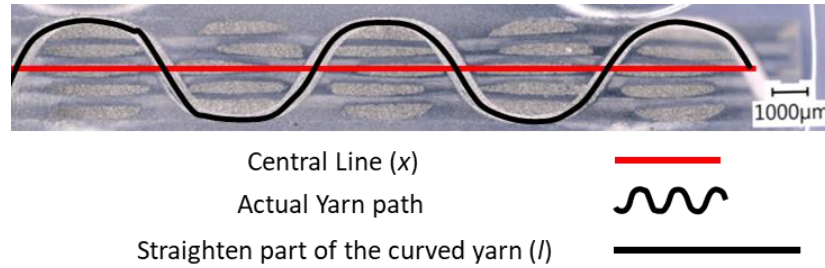
Fig. 6. 8 Schematic of yarn crimp measurement from cross-sectional images.

Crimp% was calculated by using the following equation.

$$\text{Crimp \%} = \frac{(l-x)}{x} X\ 100 \ldots\ldots\ldots\ldots\ldots\ldots\ldots\ldots (6.1)$$

Where l = Uncrimped length of the yarn

x = Crimped length of the yarn

The crimp angle and crimp percentages of Z-binders with different weave architectures and binder tension are shown in Table 6. 1 Crimp values for the Z-binders and Table 6. 2.

Table 6. 1 Crimp values for the Z-binders for different weave architectures.

Binder weave architecture	Warp bound composites			Weft bound composites		
	Laminate thickness (mm)	Crimp angle (⁰)	Crimp %	Laminate thickness (mm)	Crimp angle (⁰)	Crimp %
1x1 Plain	2.93±0.03	56.63±2.48	26.54±0.48	2.64±0.02	32.77±2.74	14.77±0.18
2x1 Twill	2.31±0.01	52.20±2.18	16.21±0.15	2.14±0.09	34.88±2.98	10.20±0.03
2x2 Twill	2.27±0.02	50.70±2.74	11.34±0.36	1.88±0.06	31.32±0.79	8.36±0.08
Angle Interlock	1.98±0.01	14.23±1.72	3.55±0.43	1.85±0.05	13.34±1.11	2.65±0.13

The tabulated values show that the Z-binder crimp is highly dependent on the degree of interlacings. For all the three orthogonal weaves, the crimp angle is in a range of 50⁰-57⁰. However, their crimp % is significantly different from each other. 1x1 plain weave have the highest crimp (26.54%) among them. Crimp is reduced by reducing the number of

interlacings for 2x1 twill (16.21%) and 2x2 twill (11.34%) weaves. This is because of the increment of the binder floating lengths due to the reduction in interlacing frequencies. The cross sectional images show that the binder follows an angular path in angle interlock weave. This angular path and the least interlacement frequencies resulted in minimum crimp % in angle interlock structure.

Both z-binder crimp angle and crimp % in weft bound structures are found much lower than the warp bound composites. In weft bound composites, the binder interlaces with four layers of warp tows. In contrast, binder interlaces with five layers of weft tows in warp bound composites. Again, when the binders are taken out to incorporate them in the weft direction in weft bound composites, there are more gaps between the warp tow stacking. The combination of these two reasons reduced the crimp angle as well as crimp %.

Both crimp angle and crimp percentages of the composites with binder tension variations are found to be at almost at similar levels. This is because of the same weave structures of these two composites.

Table 6. 2 Crimp values for the Z-binders with different tension.

Composite binder tension	1x1 plain orthogonal composites		
	Laminate thickness (mm)	Crimp angle (°)	Crimp %
NT	2.93±0.03	56.63±2.48	26.54±0.48
HT	2.75±0.01	53.71±3.11	24.21±1.15

6.4 Volume Fraction Analysis

In this research, volume fractions of the constituent parts (fibre, matrix and voids) and the directional fibre volume fractions were measured in two different methods. The

constituent volume fractions were experimentally measured using the fibre burn-off method. The directional fibre volume fractions was calculated based on the preform parameters given in Table 3. 1, Table 3. 2. Both the procedures are detailed in the following sections.

6.4.1 Fibre Burn-off Method

Fibre volume fraction (V_f) measurement was conducted based on the fibre burn-off method according to the ASTM D3171 standard (Constituent Content of Composite Materials) [178]. In this method, the specimen density was first measured according to the ASTM D792 [179]. Then the specimens were placed on crucibles, and the total weight was noted. After that, the specimens were placed on a muffle furnace and heated at 600°C for 30 minutes. The matrix is completely burnt during this heating process leaving only the fibres inside the crucibles. After heating, the furnace temperature was taken down to room temperature, and the samples were placed on the desiccator. The desiccated samples were then weighted again to find out the weight of the fibres. Following the calculations detailed in the ASTM D3I71, volume fractions for fibres, matrix and voids were measured.

6.4.2 Directional Fibre Volume Fraction

The directional fibre volume fraction is calculated based on the preform specifications to determine the contribution of warp, weft and Z-binders to the overall fibre volume fraction of the composites. The directional V_f is numerically analysed with a two-step calculation. In the first step, warp, weft and z-binder directional areal density are calculated by multiplying the tow linear density (in tex) by the warp/cm, weft/cm and binder/cm, respectively. In the next step, the directional areal density is normalised by

total areal density to calculate the contribution of warp, weft and z-binder fibres in percentages.

6.4.3 Constituent Volume Fractions

Fibre, matrix and void volume fractions of the warp bound and weft bound composites are tabulated in Table 6. 3 Volume fraction of the constituents in warp bound composites. The directional fibre volume fractions for warp, weft and Z-binders are also given in the same tables.

Table 6. 3 Volume fraction of the constituents in warp bound composites

Preforms	Laminate thickness (mm)	Fibre Volume Fraction (FVF) %	Matrix Volume Fraction (MVF) %	Void %	Directional Fibre Volume Fraction (DFVF) %		
					Warp	Weft	Binder
1x1 Plain	2.93±0.03	39.35±2.73	58.47±2.51	2.18±0.26	17.38	19.26	2.72
2x1 Twill	2.31±0.01	51.10±0.20	48.03±0.12	1.24±0.17	22.68	25.13	3.29
2x2 Twill	2.27±0.02	52.79±0.68	45.90±0.97	1.13±0.29	23.48	26.02	3.29
Angle Interlock	1.98±0.01	57.93±0.90	41.42±0.85	0.65±0.10	25.90	28.70	3.33

Table 6. 4 Volume fraction of the constituents in weft bound composites

Preforms	Laminate thickness (mm)	Fibre Volume Fraction (FVF) %	Matrix Volume Fraction (MVF) %	Void %	Directional Fibre Volume Fraction (DFVF) %		
					Warp	Weft	Binder
1x1 Plain	2.64±0.02	37.71±0.85	61.19±1.10	1.10±0.28	23.15	12.31	2.25
2x1 Twill	2.14±0.09	42.50±0.19	56.81±0.25	0.69±0.06	26.14	13.90	2.46
2x2 Twill	1.88±0.06	48.82±0.24	50.68±0.37	0.51±0.13	30.04	15.98	2.81
Angle Interlock	1.85±0.05	50.70±0.24	48.92±0.33	0.38±0.09	31.24	16.62	2.84

Following observations are found from these tabulated results.

- Fibre volume fractions are increased with the increment of the binder wavelengths. The longer binder wavelength resulting in reduced interlacings

allows more transverse compaction of the preforms during composite manufacturing. As a result, laminate thickness reduced, and FVF increased. In 1x1 plain weave, binders have the highest number of interlacings; it gives the least transverse compaction and has the lowest fibre volume fraction. On the other hand, the angle interlock (AI) weave has the highest FVF among all the weaves due to its special angular binder path. Here, the binder does not frequently move between the preform surfaces, allowing the preform to compress more in the infusion process, resulting in higher fibre volume fractions.

- Binder weave architectures are found to affect the void content of the composites. In general, 3D woven composites are reported to have more void contents than 2D woven composites due to the through-thickness binders [107]. In complex orthogonal weaving patterns, the binder frequently interlaces with other tows, creating more intricate parts in the preform structures, reducing resin contact to those areas [110], [180]. This scenario improves for the other weaves as the binder movement frequencies are reduced by increasing the floating length. This is why 1x1 plain has the highest void content among these structures and twill weaves have lower void contents. In angle interlock structure, the binder moves in an angular path which resulted in minimum interlacings. As a result, on compaction it reduces the inter tow gaps significantly resulting minimum voids.

- In the warp bound composites, weft directional fibre volume fractions is apparently looking higher than the warp directional fibre volume fractions for all the weaves. However, when the Z-binder fibre volume fractions are taken along with the warp fibres, the warp and weft directional fibre volume fractions are almost equal. In the weft bound composites, weft directional fibre volume fractions, including the Z-binder contributions, are lower than the warp directional

fibre volume fractions. This is because of the lower number of weft layers as well as the lower weft densities in that direction.

Constituent volume fractions for the composites with different binder tensions are given in Table 6. 5. The composite with higher binder tension has higher fibre volume fractions than the lower tension laminate. This is due to the inherent pre-compaction in the higher tension structure. This composite's binder way cross-sectional image (Fig. 6. 7) also shows this pre-compaction.

Table 6. 5 Constituents volume fractions of the composites with binder tension variation

Preforms	Laminate thickness (mm)	Fibre Volume Fraction (FVF) %	Matrix Volume Fraction (MVF) %	Void %	Directional Fibre Volume Fraction (DFVF) %		
					Warp	Weft	Binder
NT	2.93±0.03	39.35±2.73	58.47±2.51	2.18±0.26	17.38	19.26	2.72
HT	2.75±0.01	41.90±0.20	56.34±1.12	1.76±0.37	18.51	20.52	2.87

6.5 Concluding Remarks

3D woven composites were manufactured with a customised vacuum bag infusion method where two metal plates were used on top and bottom of the preforms to avoid any waviness in the composite surfaces. Z-binder crimp angle and crimp percentages were measured using optical imaging of the composites. Volume fractions of the fibres, matrix and voids were measured along with directional fibre volume fractions.

Orthogonal weaves have considerably much higher crimp angle and crimp % than the interlock weave. Among the orthogonal weaves, 1x1 plain weaves have the highest crimp percentages due to the highest number of interlacings. For the 2x1 twill and 2x2 twill weaves, the crimp% continues to reduce due to reduction of the degree of interlacings.

The Z-binder weave architectures highly influenced fibre volume fractions of these composites. The highest number of binder interlacings in 1x1 plain has resulted in the least compaction so as the minimum fibre volume fractions. The fibre volume fraction is seen to increase for the 2x1 twill, and 2x2 twill weaves because of the lower degree of interlacings which allowed more compaction during composite manufacturing. The binder has the longest float length in angle interlock weaves due to the minimum interlacings resulting in the highest fibre volume fraction.

Chapter 7 Tensile Properties of 3D Woven Composites

7.1 Introduction

The in-plane tensile properties of 3D woven composites and their failure mechanisms have been experimentally characterised in many studies reported in the literature [4], [98], [109], [110], [116], [118], [123], [181], [182]. One of the commonly drawn conclusions is the recommendation to improve the tensile properties by minimising the waviness of the binder and other load-bearing tows, which are directly related to the binder weave architecture.

This chapter details the tensile properties and failure mechanisms of 3D woven composites with different binder weave architectures and binder tensions. Tensile testing method along with test specimen preparation processes is described in the second section. Section 3 presents the tensile test results for the warp bound and weft bound composites as well as the composites with two different binder tensions. Composite failure mechanisms are explained in section 4. Finally, the chapter concludes with the summaries of the findings.

7.2 Tensile Testing

7.2.1 Test Specimen Preparation

Specimens for the tensile tests were prepared by cutting all the laminates in the warp and weft directions. The specimens and the tabbing materials were cut with a rotary diamond cutter (SLIDERCUTTER 5600) with a blade thickness of 2.1mm and rotary speed of 700 rpm. Cut tabs and all specimens were sandblasted at the ends in tabbing area and then cleaned thoroughly with the water. Araldite 2011 resin system was used to bond end tabs

to the cut specimens. A resin and hardener ratio of 60:40 was used. Tabs were bonded to test specimens and cured for at least 24 hours under pressure at room temperature.

The jacquard loom used in this research to weave the preforms has a limitation on weavable preform width to a maximum of 240mm. Hence maximum width of the composites was found to be 220mm. As a result, specimen size was kept as 200mm X 20mm (length X width) with a gauge length of 100mm.To keep at least one weave repeat unit within the specimen width according to the testing standard [183], for the angle interlock (AI) composites, specimen sizes were kept as 200mm X 25mm (length X width) as the width of the weave repeat for the AI is about 23mm.

7.2.2 Test Machine Set-up

An Universal Instron tensile testing machine with 100KN loadcell was used to perform the tensile tests according to the ASTM D3039 standard [183]. The tensile testing setup is shown in Fig. 7. 1. Crosshead displacement was maintained at 2mm/min. A LaVision 2D digital image correlation (DIC) system was used for live strain measurement from the surface of the test samples. These live strain values (ε_{yy}) were correlated to the Instron machine loadcell to obtain load-elongation and stress-strain diagram. The testing environment was controlled to a temperature of 21ºC and the relative humidity (RH) of 45%. Samples were tested both in warp and weft way, and at least four coupons were tested for each category.
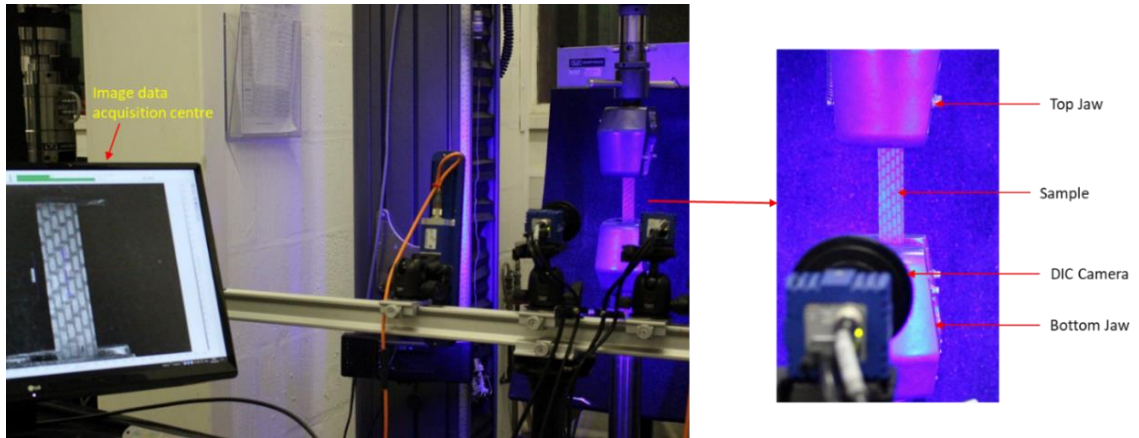
Fig. 7. 1 Experimental setup for tensile test.

Few samples were tested using both DIC and mechanical strain gauges (MTS) to verify the strain values (see Fig. 7. 2). The results from both strain sources were almost perfectly aligned. However, in most cases, slippage of the extensometer clips was noticed, which affected the stress-strain curves (see Fig. 7. 3).
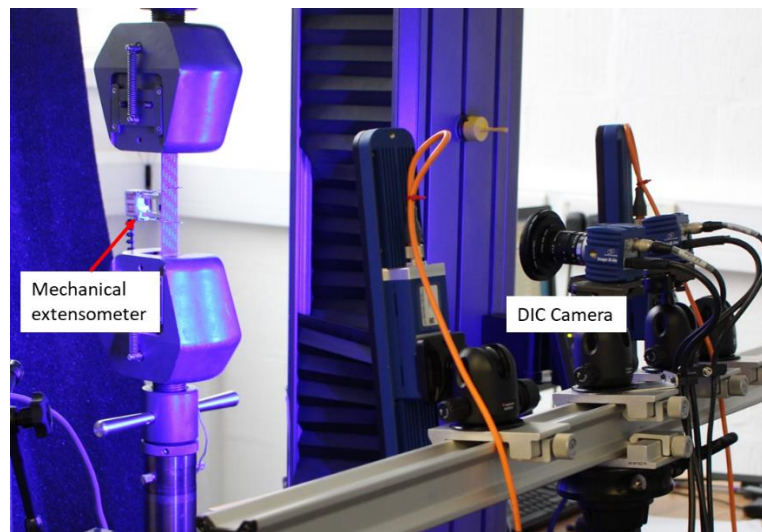
Fig. 7. 2 Experimental setup for tensile test with both mechanical extensometer and

DIC setup
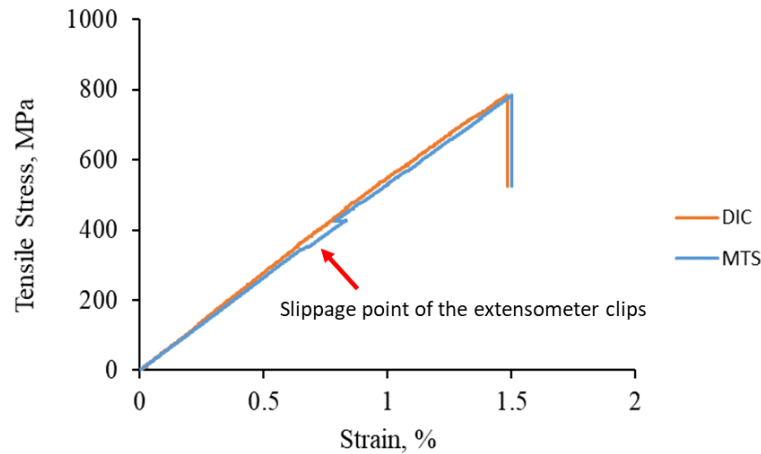
Fig. 7. 3 Stress-strain diagram of orthogonal composite (2X1 Twill binder weave) using both mechanical extensometer (MTS) and DIC

Strain measurement using DIC was preferred for the following reasons-

(i)   DIC calculates strain by analysing the entire surface of the samples. In contrast, mechanical strain gauges calculate strain from two specific points.

(ii)   DIC shows the strain localisation on the samples, which is an effective tool to predict the fracture of the composites on loading. DIC also allows clear visibility of the changes on the sample surface during the loading.

(iii)   Mechanical strain gauges often have the issue of slipping out of the samples during loading, as shown in Fig. 7. 3 which may affect the ultimate results.

No speckle patterns were used in this research as the samples had sufficient colour contrasts to yield valid strain results using the DIC. Using peel ply during the composite manufacturing helped to get this particular effect on the sample surface. The strain data was recorded at 5Hz frequency with a 10 frames/second projection rate. The DIC images were further processed with Davis 10 software.

A thickness-directional imaging system was used to track the crack initiation and propagation on the composites during loading. Two Nikon D2X cameras, which has two

sensors (12.8 MP CMOS and 32 MP CMOS), were used for this purpose. Additional warp and weft samples were mounted on the machine where laminate thickness was facing the camera. One camera captured the images of the entire gauge length area, and the other one concentrated on the highly strained areas to track the failure mechanism.

7.3 Tensile Properties

7.3.1 Warp bound Composites

Representative tensile stress-strain curves for the warp bound composites until failure are shown in Fig. 7. 4 for all the binder weave structures. The averaged tensile modulus and strengths are tabulated in Table 7. 1. Good repeatability is observed in these curves for both warp and weft way loading [Appendix III (a)]

(a)   (b)
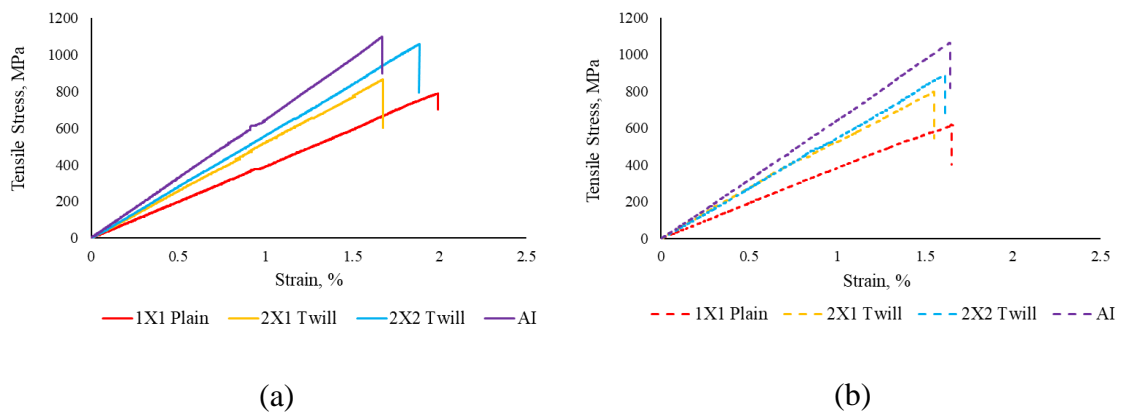
Fig. 7. 4 Representational stress-strain curves for the warp bound composites under tension: (a) Warp way loading, (b) Weft way loading.

All of these composites exhibited linear behaviour towards final failure throughout the loading process as shown in these curves. It is evident from these curves that the binder weave architectures affect the tensile performances significantly. Both tensile modulus and strength were lowest for the composite with 1x1 plain binder weave. As the degree of binder interlacings reduced subsequently for the other weaves (i.e. binder floating

lengths were increased gradually for the other structures), tensile performances were also improved significantly. This improvement can be attributed to the changes in binder path geometry and laminate fibre volume fractions.

Prior researchers have suggested that tensile properties can be enhanced by reducing the crimps in the preform structures [98], [107]. Binder crimp% is directly related to the binder degree of interlacings i.e. binder path architecture. It was discussed earlier in Chapter 3 that, the 1x1 plain weave has the highest degree of binder interlacings ($705/100cm^2$) among these four weaves. This degree of interlacings is sequentially reduced for 2x1 twill weave ($470/100cm^2$), 2x2 twill weave ($353/100cm^2$) and angle interlock weave ($235/100cm^2$). Consequently, binder crimps were measured highest for the 1x1 plain weave, which gradually decreased in 2x1 twill, 2x2 twill, and finally, the AI had the lowest crimp% (see Table 6. 1). This reduction in binder degree of interlacements and crimp % contributed to the enhancement of the tensile strength.

Another factor is the changes in the fibre volume fractions. A longer floated binder allowed the preforms to compact more in the transverse direction (discussed in section 4.3.2 Effect of Binder Weave Structure on Compressibility), resulting in higher fibre volume fractions (discussed in section 6.4.3 Constituent Volume Fractions). This increment in the fibre volume fraction contributed to the improvement of the tensile modulus. From Table 7. 1 it is found that the composite with 1x1 plain binder weave has the lowest tensile modulus and strength, which is then increased for composites with 2x1 twill, 2x2 Twill composite with AI binder weave have the highest FVF as well as the tensile stiffness and strengths.

Table 7. 1 Tensile modulus, strength and failure strain of warp bound 3D woven composites

Preforms	Modulus (GPa)		Strength (MPa)		Breaking strain %	
	Warp	Weft	Warp	Weft	Warp	Weft
1x1 Plain	40.16±2.28	38.84±1.84	787.36±15.81	653.45±20.94	1.91±0.13	1.55±0.11
2x1 Twill	52.19±2.08	52.07±0.71	876.31±59.67	809.93±27.84	1.69±0.12	1.68±0.13
2x2 Twill	56.22±1.92	55.08±3.13	1034.13±20.05	875.61±65.03	1.85±0.08	1.67±0.15
Angle Interlock	63.56±1.29	63.01±0.58	1088.86±38.60	1014.30±77.11	1.66±0.07	1.61±0.11

A comparative analysis of the composite properties in warp and weft directional loading is shown in Fig. 7. 5. The graphs indicate that the modulus is almost equal for both warp and weft directional loadings for all the weaves. This is because both warp and weft samples have almost the same directional volume fractions.
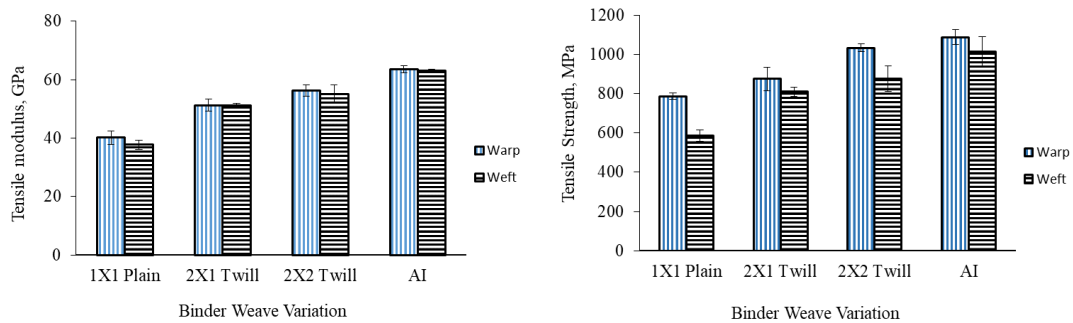
Fig. 7. 5 Comparative analysis of warp and weft way tensile properties (Warp bound composites).

However, an important observation from the strength bar charts shows that the weft directional tensile strength is always lower than the warp direction regardless of having almost equal fibre volume fractions. This is due to the pinching of the weft yarns by the binders. When the binders interlace with the weft tows in these warp-bound composites, the surface tows are pinched significantly higher than the middle ones (see Fig. 7. 6). In

these pinching areas, composites start to fail, leading to the final failure [4]. At the same time, binders also helped the structures to carry additional load [12], which resulted in higher warp way tensile strengths.
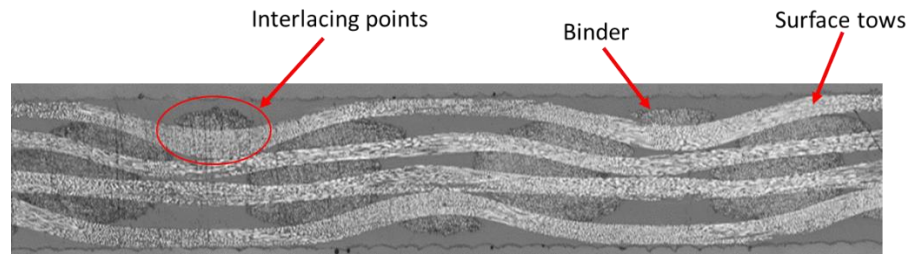
Fig. 7. 6 Surface tow pinching by the binder interlacings

7.3.2 Weft Bound composites

For the weft bound composites, representational tensile stress-strain curves until final failure are shown in Fig. 7. 7 for all the binder weave structures. The tensile property values are tabulated in Table 7. 2. Good repeatability is observed in these curves for both warp and weft way loading [Appendix III (b)]

(a)   (b)
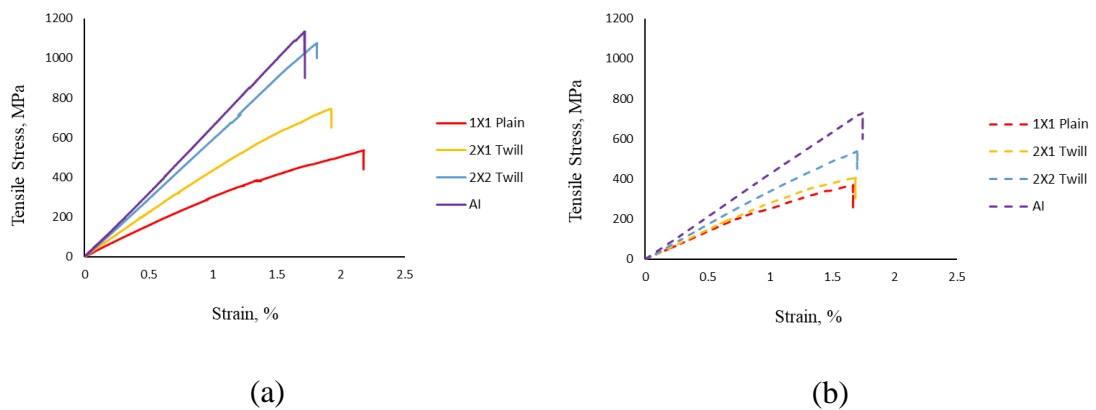
Fig. 7. 7 Representational tensile stress-strain curves for the weft bound composites:

(a) Warp way loading, (b) Weft way loading.

These curves show an almost similar trend for the tensile properties like the warp bound composites. Both tensile modulus and strength improved with the changes in the weave

146

structures. 1x1 plain weave has the least tensile values, which gradually increased for 2x1 twill, 2x2 twill and showed the highest tensile properties for the angle interlock structures. Again, this improvement can be attributed to the increase in the fibre volume fraction and reduction in the binder crimps, which are the direct implications of the binder weave architectures.

It is important to note that, the improvement of tensile modulus and strength of 2x2 Twill weave is significant in the weft bound composites when compared with the 2X1 twill weave. The primary reason is the improvement in the FVF of that particular structure. In warp bound composites, 2x1 and 2x2 twill structures have almost similar FVF (51.10% for 2x1 twill and 52.79% for 2x2 twill weave). As a result they have almost similar tensile modulus. The strength improvement in the 2x2 twill composite was due to reduced interlacing points as discussed earlier. However, in the weft bound composites, 2x2 twill (48.82%) have much higher FVF compared to 2x1 twill composites (42.50%). As a result of this higher FVF, the modulus is also significantly higher.

Table 7. 2 Tensile modulus, strength and failure strain of weft bound 3D woven composites.

Preforms	Modulus (GPa)		Strength (MPa)		Breaking strain %	
	Warp	Weft	Warp	Weft	Warp	Weft
1x1 Plain	30.44±2.00	26.46±1.64	517.86±38.37	364.33±29.24	2.26±0.20	1.64±0.08
2x1 Twill	44.21±2.53	28.85±1.84	766.75±20.01	410.48±24.82	1.85±0.10	1.84±0.27
2x2 Twill	57.34±1.74	36.10±1.62	992.82±91.68	544.99±37.71	1.73±0.11	1.62±0.08
Angle Interlock	60.01±2.34	40.17±1.70	1137.62±2.79	706.67±46.66	1.77±0.06	1.70±0.11

When the tensile properties were compared for the directional loading (Fig. 7. 8) warp way samples were found much stiffer and stronger than the weft way samples. This is because of the much higher warp directional fibre volume fractions than the weft ones

(Table 6. 3). This reduction in weft directional FVF is because of the lower number of weft layers and tow densities, as discussed in Chapter 6 (see section 6.4.2 Directional Fibre Volume Fraction).
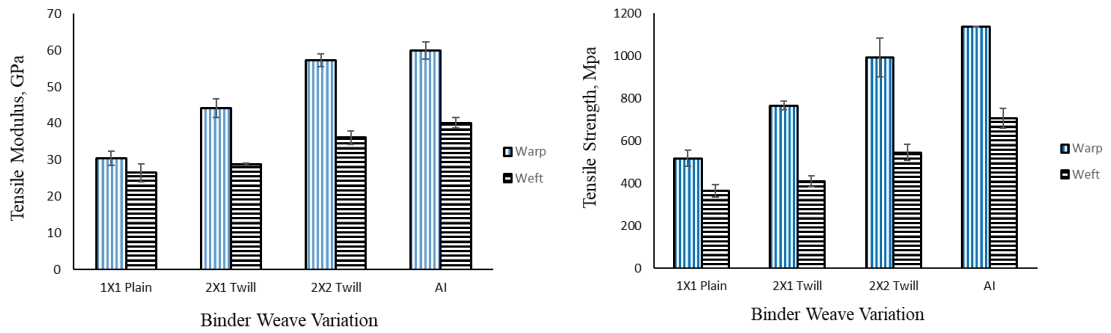
Fig. 7. 8 Comparative analysis of the warp and weft way tensile properties (Weft bound composites).

7.3.3 Comparison of Warp Bound and Weft Bound Composites

Tensile properties of warp bound and weft bound composites are compared to observe the impact of binder direction alteration. Only the warp directional loading was considered, as for both types of composites, warp directional fibre volume fractions are almost the same. The comparative bar charts are shown in Fig. 7. 9.

(a)   (b)
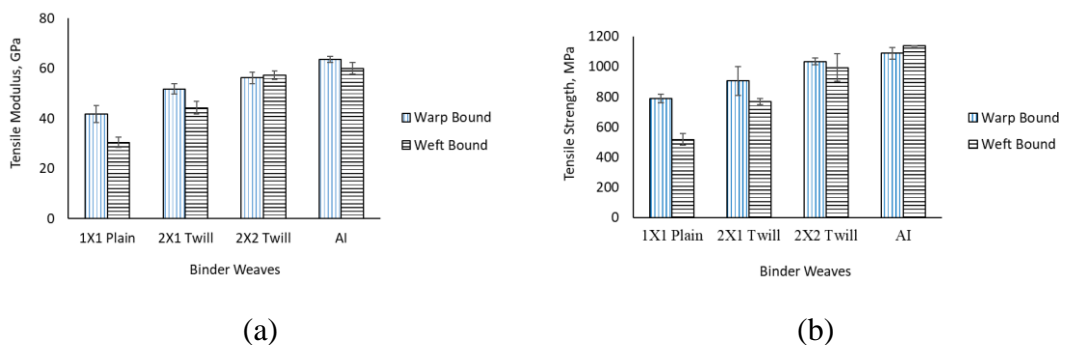
Fig. 7. 9 Tensile properties of warp bound and weft bound composites in warp directional loading. (a) Tensile Modulus, (b) Tensile Strength

148

Comparative analysis of the tensile properties of the warp and weft bound composites show a critical observation. For the 1x1 plain and 2x1 twill composites, both modulus and strength are significantly lower for the weft bound laminates. However, for the 2x2 twill weave and angle interlock (AI) weave composites, tensile properties for the weft bound composites are almost equal or slightly higher than the warp bound laminates. This improvement is due to the nature of the composite failure imposed by the binder weave architecture.

7.3.4 Composites with different Binder tensions

Fig. 7. 10 shows the warp and weft directional stress-strain curves for the 1x1 plain orthogonal composites with two different binder tensions. The averaged tensile modulus and strengths are tabulated in Table 7. 3.

(a)   (b)
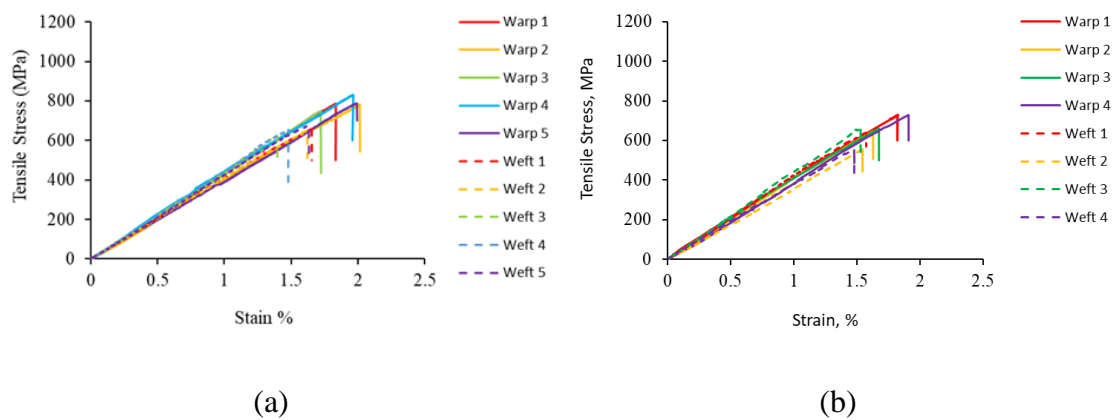
Fig. 7. 10 Stress-strain curves for the 1x1 Plain orthogonal composites with different binder tensions: (a) Nominal Tension (NT), Higher Tension (HT)

The curves from Fig. 7. 10 indicate that for both the composites (nominal binder tension and higher binder tension), warp and weft way stiffness is almost the same and likewise the other composites, warp way strengths in both cases are higher compared to the weft way.

Table 7. 3 shows the values of tensile modulus and strengths of the orthogonal composites with different binder tensions. Composite with higher binder tensions are seen to have a moderately higher modulus compared to its counterpart. This is because of the higher fibre volume fractions of that laminate. Another observation is the lower strengths for the higher binder tension (HT) composites in both warp and weft way loading. This is possibly due to the greater squashing area in the interlacement points in the HT composites which is described in the Chapter 3 (section 3.5.3 Preform Structures). A similar finding is also reported by Dhiman et al. [113] where they found composites with 6K binders failed earlier than the composites with 3K binders due to higher squashing areas. Several researchers reported that fibre matrix debonding occurs in the interlacement points, which led to the final failure [110], [184]. Due to the higher interlacement areas in HT composites, the possibility of debonding increases even more and causes early ultimate failure than the NT composites.

Table 7. 3 Tensile modulus, strength and failure strain of 3D woven composites with different binder tensions

Composites	Modulus (GPa)		Strength (MPa)		Breaking strain %	
	Warp	Weft	Warp	Weft	Warp	Weft
NT	40.16±2.28	38.84±1.84	787.36±15.81	653.45±20.94	1.91±0.13	1.55±0.11
HT	41.60±1.41	41.31±2.99	688.79±41.01	624.48±33.19	1.72±0.12	1.53±0.04

7.4 Tensile Failure Mechanisms

One of the objects of this current research is to explore the role of binder weave architectures on the directional failure behaviour of 3D woven composites. A number of researchers reported the tensile failure mechanisms of 3D woven composites, including damage initiation and progression to final failure [105], [185]–[187]. To illustrate the tensile failure of the composites, three different techniques were used in this research

including strain localisation using the DIC, tracking the crack initiation and propagation using a novel thickness directional imaging system and finally analysing the completely failed specimens. The failure mechanisms were found to be similar for all the composites (both warp bound and weft bound).

7.4.1 Warp Bound Composites

For the warp bound composites, strain mapping of the composites prior to the final failure is shown for both warp samples in Fig. 7. 11. The colour map spectrums on the right side of each DIC image represents the corresponding strain values. The composites showed a clear variation of strain depending on the binder weave architectures. The weave repeat unit is also clearly identifiable through these strain contours obtained from these DIC images.

Strain contours from the DIC strain mappings in the warp way samples show two important observations. Firstly, high strain contours are clearly visible in the transverse directions, which means that strain is more localised in the perpendicular to the loading direction.
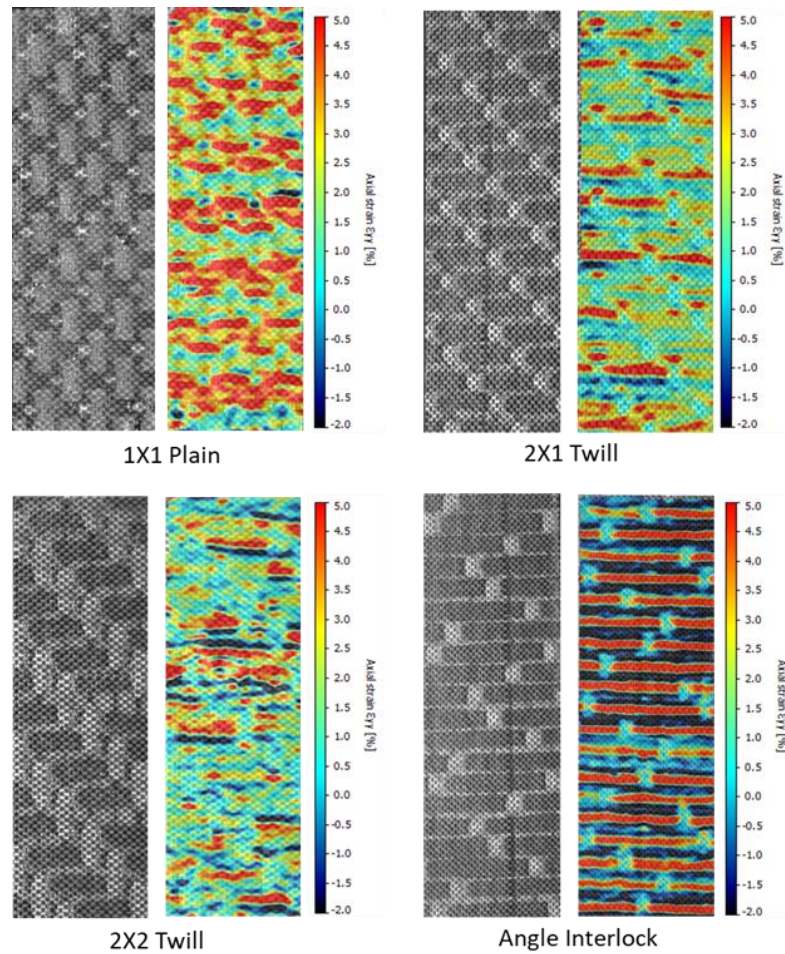
Fig. 7. 11 DIC strain mappings of the warp way samples (Warp bound composites).

The second and the most interesting observation is the lower strain in the binder interlacement to the weft tows, which is clearly visible for all the composites. This lower strain in those interlacement points indicates that the binders may tried to delay the final failure of the composites [118]. This interesting finding lead to the investigation of the tensile failure mechanism by tracking the crack initiation and propagation until final failure. To accomplish this, tensile deformations in the thickness direction while loading, was monitored using two high magnification digital cameras for the composites with 1x1 plain weave. Images were captured for three different loading values: zero loading, when the cracks are opened, and before final failure, as shown in Fig. 7. 12. It is clearly evident from these images that the binder stops the crack propagation in the thickness direction. The damage initially started from the resin-rich area created by the binder resin channels.

The cracks progressed in the transverse direction until the binders stopped them. The cracks then followed the binder way in the form of delamination for further propagation until final failure. The composites finally failed due to the fibre/tow breakage in the axial directions (Fig. 7. 13). This is consistent with the tensile failure mechanism reported by Cox et. al. [115]. This failure mechanism supports the claim for the binder to carry additional load along with the warp tows, playing an important role in delaying the final failure of the composites when loaded in the binder direction [110]. When the composites finally fail, binders are found to fail in the same way as the warp tows (Fig. 7. 13).
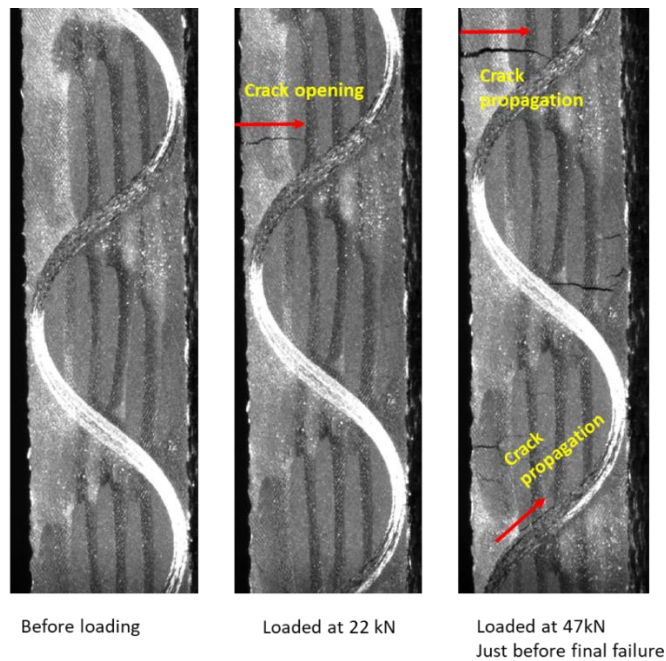
Fig. 7. 12 Damage initiation and progression when loaded in the warp/ binder way direction.
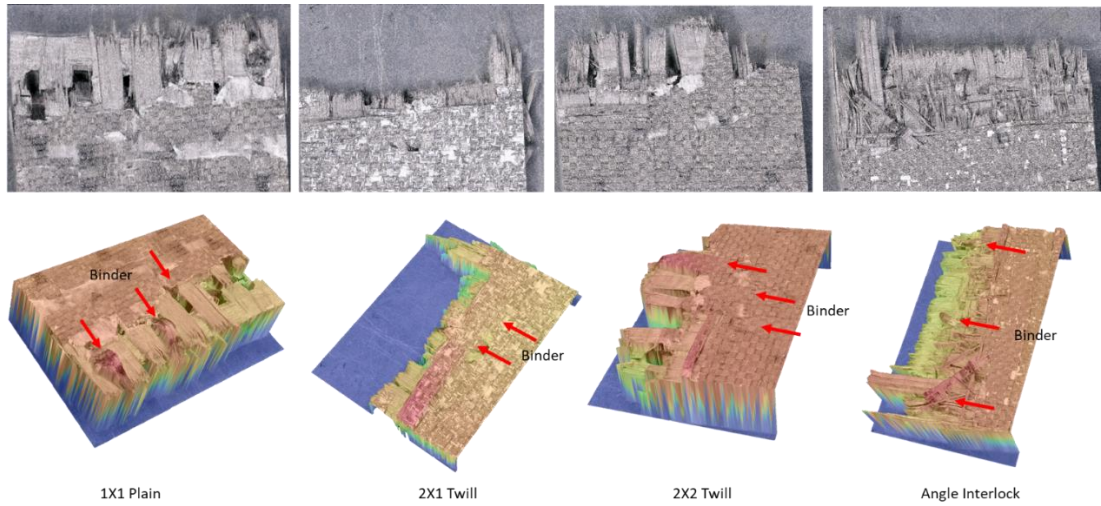
Fig. 7. 13 2D Optical microscopy (top) and 3D optical microscopy (KEYANCE VHX-5000) (bottom) showing failed specimens after loading in the warp-way direction (for warp-bound composites).
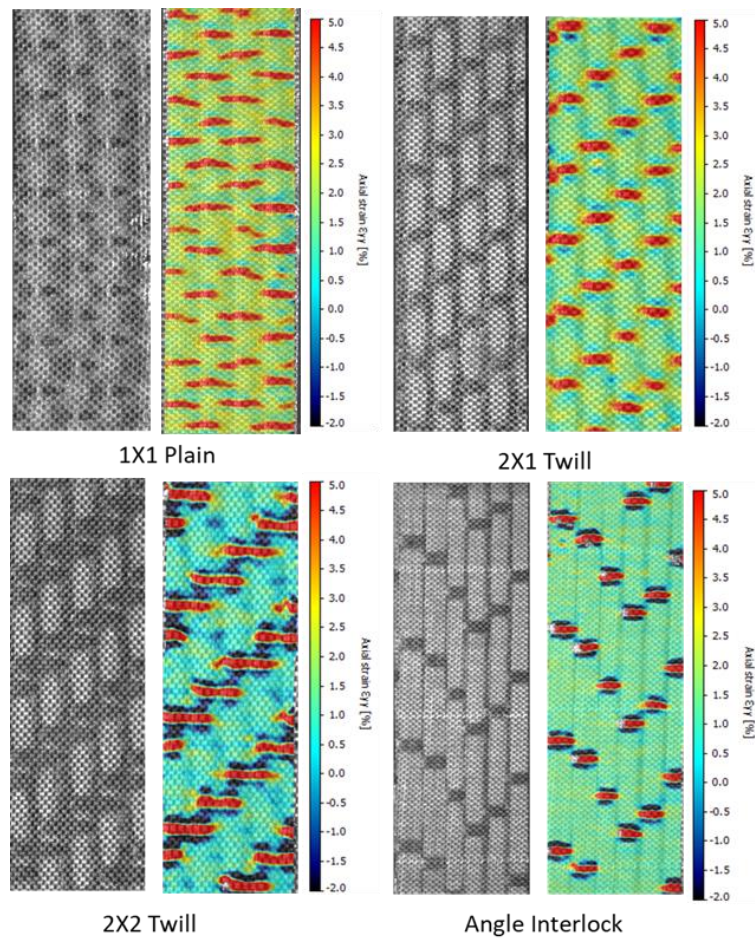
Fig. 7. 14 DIC strain mappings of the weft way samples (Warp bound composites).

Full-field strain mapping of the composites with different binder weave architectures, when loaded in the weft directions, is shown in Fig. 7. 14. Strains are found to be highly concentrated in the binder-weft interlacement points for all the weaves. These localised strains suggest a failure process starts from these interlacement interfaces. This interesting phenomenon was further investigated by the thickness directional imaging process detailed earlier this chapter (in section 7.2.2 Test Machine Set-up) for 1x1 plain samples.

These micrographs (Fig. 7. 15) show that the initial damage is the tow-matrix delamination around the binder interlacing regions in weft directional loading. Following the stress concentrations at those interlacing areas, the damage propagated perpendicular to the loading direction and finally failed in that specific region. Post failed samples shows that all the composites fail in the binder-warp interfaces, as shown in Fig. 7. 16, revealing that the tow-matrix debonding is the dominant failure mode in the weft direction for warp bound composites.
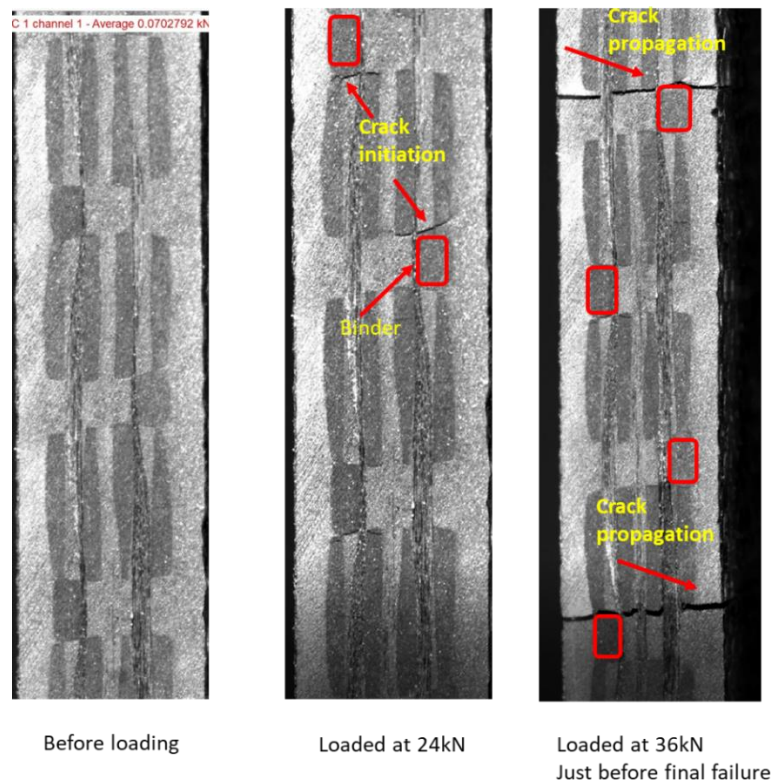
Fig. 7. 15 Damage initiation and progression when loaded in the weft way direction
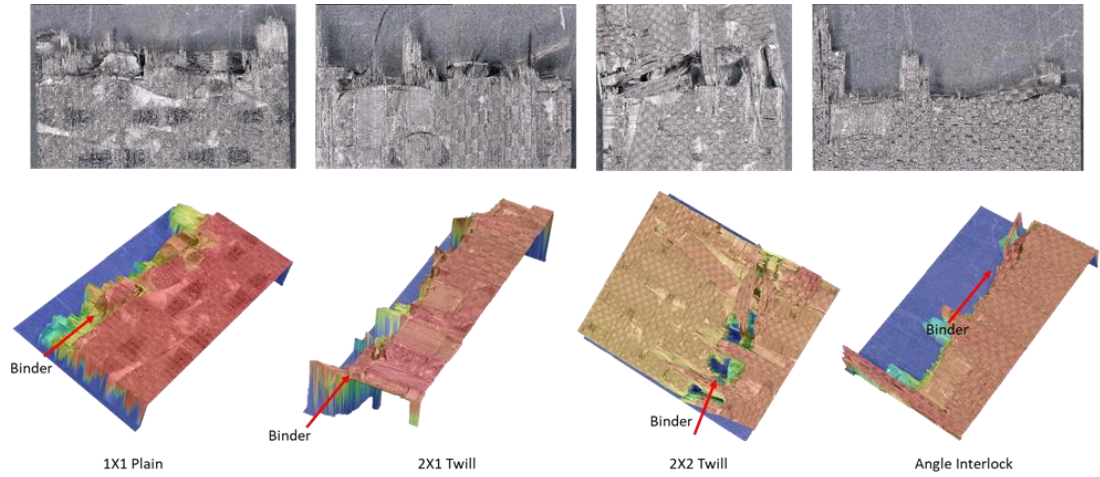
Fig. 7. 16 2D Optical microscopy (top) and 3D optical microscopy (KEYANCE VHX-5000) (bottom) showing failed specimens after loading in the weft-way direction (for warp-bound composites).

7.4.2 Weft Bound Composites

Strain mappings for the weft bound composites loaded in warp way directions are shown in Fig. 7. 17. In this case, localised strains are clearly visible for the warp way composites. As the binders were incorporated in the weft way directions, they made interlacings with the warp tows, producing the localised strains on these interlacement points on loading. Following the local strain concentrations, these composites are expected to fail in the binder and weft tows interface, which is clearly evident from the post-failure sample images Fig. 7. 18.
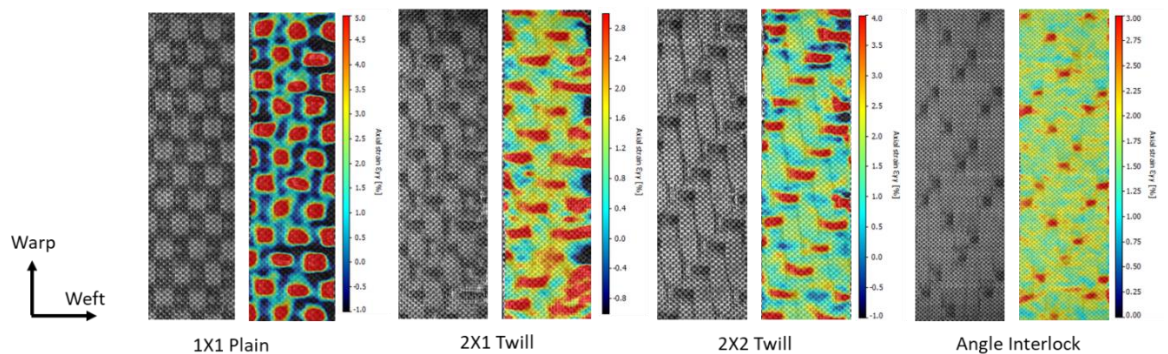
Fig. 7. 17 DIC strain mappings of the warp way samples (Weft bound composites)

156
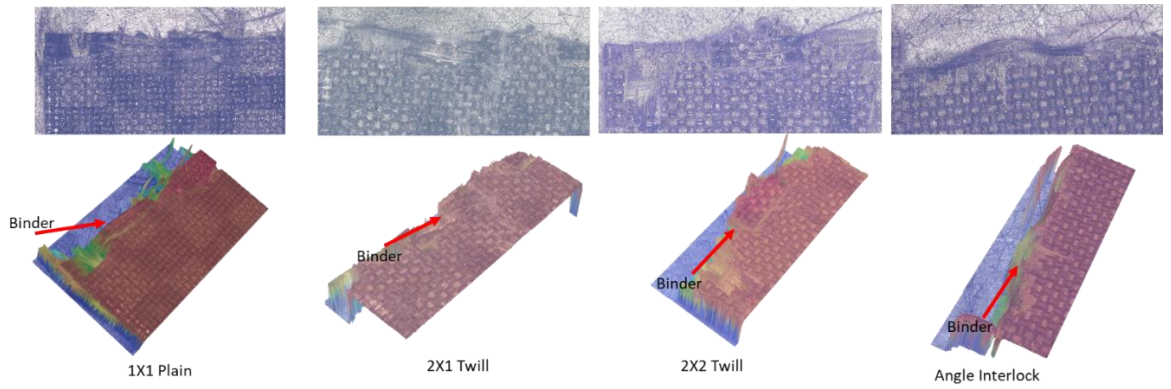
Fig. 7. 18 2D Optical microscopy (top) and 3D optical microscopy (KEYANCE VHX-5000) (bottom) showing failed specimens after loading in the warp-way direction (for weft-bound composites).

The 2D and 3D micrographs (Fig. 7. 18) of the failed warp way samples show that, all the weft bound composites failed on the interface binder and weft tows. In these cases, failure initiates as tow-matrix delamination at the binder interlacement points. Damage is further progressed through the perpendicular directions until final failure.
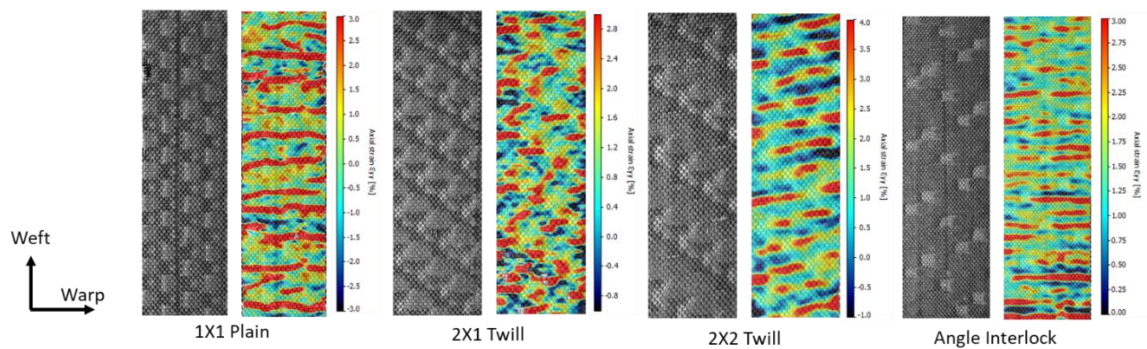
Fig. 7. 19 DIC strain mappings of the weft/binder way samples (Weft bound composites).

When the composites are loaded in the weft way direction, strain mappings (Fig. 7. 19) show lower strains in the binder interlacing points, indicating binder contribution to the tensile properties. Post failure samples show that the binders are failing at the same way as the weft tows, proving that binders also carry additional load until the final failure (Fig.

7. 20). These micrographs also show that the composites failed due to fibre/tow breakages.
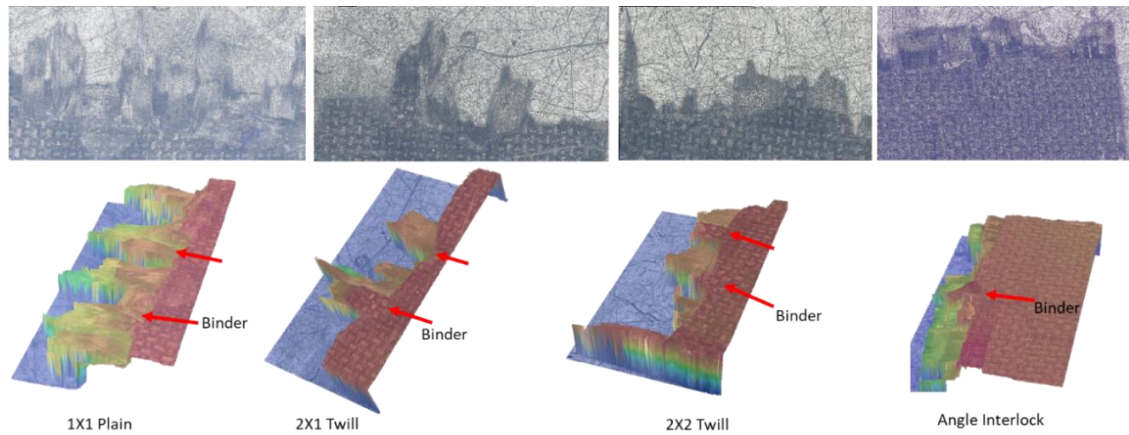
Fig. 7. 20 2D Optical microscopy (top) and 3D optical microscopy (KEYANCE VHX-5000) (bottom) showing failed specimens after loading in the weft-way direction (for weft-bound composites).

7.4.3 Composites with Different Binder Tensions

DIC strain mapping and completely failed specimens of the composites with different binder tensions on warp and weft directional tensile loading are shown in Fig. 7. 21. Images show that both type of composites are failing in the similar way.

Warp way strain maps show that the strains are localised in the transverse to the loading directions for both composites. Lowest strains are visible in the interlacing points which suggest the possible delaying of the final failure by the binders. Completely failed specimens show that both the binders and warp yarns are failing due to fibre pull-out. Weft way strain maps show that the strains are localised on the interlacing points for both composites. These localised strains suggest an initial failure starts from these interlacement interfaces. Completely failed specimens show that composites are failing in the binder-weft interlacement interfaces.
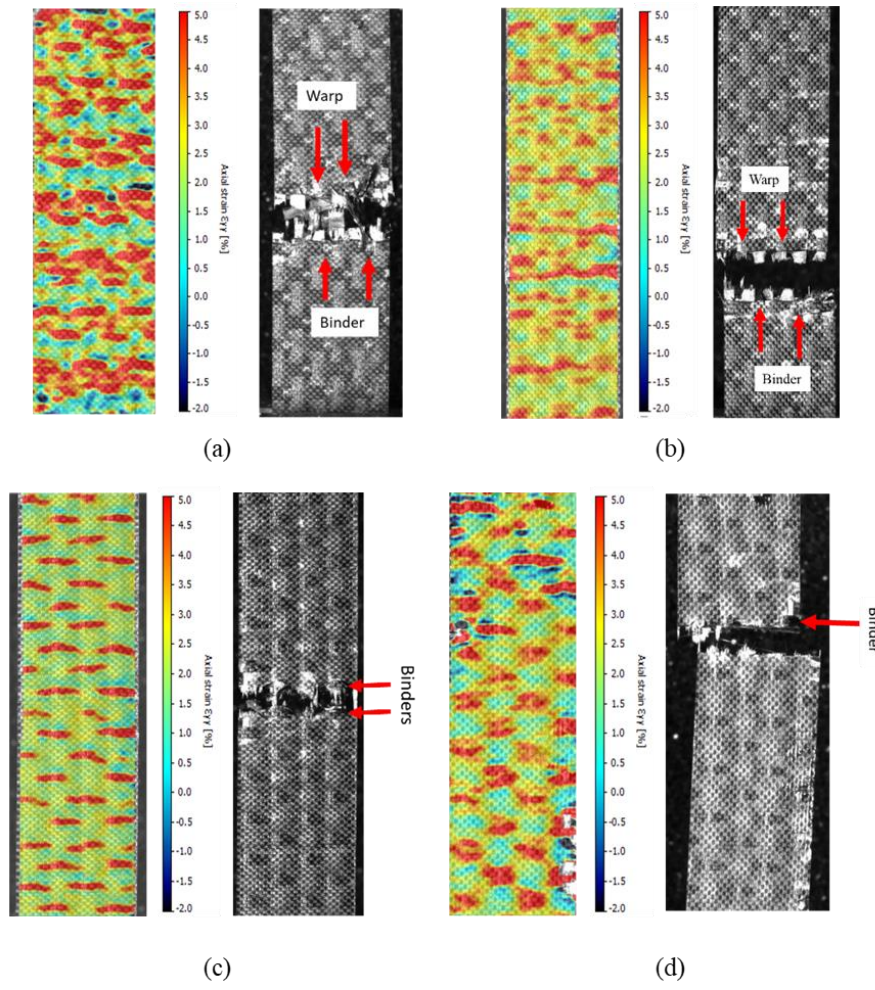
Fig. 7. 21 DIC strain maps and completely failed composites with different binders tensions: (a) Warp way NT composite, (b) Warp way HT composite, (c) Weft way NT composite and (d) Weft way HT composite

7.5 Concluding Remarks

Tensile performances for 3D woven composites with different binder weave architectures (1x1 Plain, 2x1 Twill, 2x2 Twill and AI) as well as different binder tensions were evaluated, and their failure mechanisms also investigated. Binders were inserted into the preform both in warp and weft way directions. The following conclusions can be made from the above experimental results -

(i)   Both tensile modulus and strengths for these weaves are significantly dependent on the binder weave architectures as they contribute toward the FVF and binder crimps as well as pinching on the load-bearing tows. The 1x1 plain weave has the maximum crimp% and least FVF due to more interlacings in its structure, resulting in the lowest tensile stiffness and strength among all the composites evaluated. By reducing the degree of interlacings and waviness in the binder architectures, tensile properties were improved for the 2x1 twill weave and 2x2 twill weave structures. Angle interlock has the highest modulus and strength due to the maximum FVF and minimum interlacings. Binder pinching in the load-bearing tows also contributed to the directional tensile strength. For warp bound composites, binders make the interlacings with weft tows, which ultimately pinches the surface wefts resulting in early failure and lower strengths in weft way.

(ii)   The composite failure mechanisms mainly depend on the binder weave architectures. DIC strain mapping clearly shows the impact of binder interlacings on loading. When the composites are loaded on the binder way direction (warp way for warp bound composites and weft way for weft bound composites), the binders are found to carry the load and delay the final failure. When the composites are loaded on the opposite to the binder way direction (weft way for warp bound composites and warp way for the weft bound composites), the effect of interlacings on strain development is clearly visible from the DIC images, which show the localised strains on these interlacings points. These highly strained pinching points are prone to initial failure, which then carries through the perpendicular to the loading directions until the final failure of the composites.

(iii)   No significant impact of binder tensions was seen in the composites' tensile modulus. However, a reduction in the tensile strengths was noticed for the composites with higher binder tensions. This is possibly due to these composites' higher squashing area, which led to early failure on tensile loading.

Chapter 8 Flexural Properties of 3D Woven Composites

8.1 Background

Bending properties and failure mechanisms of 3D woven composites are reported to be highly influenced by the preform weave architectures, and most importantly, the through-thickness binders were found to resist the growth of delamination cracks [89], [97]–[102]. However, in most cases, the load is applied in the three-point bending principle. As in three-point bending, load concentration is a combination of bending and shear stress; it is really difficult to isolate the actual loading effect. Four-point bending offers an attractive solution to this issue as it induces pure bending within the loading beam area [188]. Yet, the four-point bending of 3D woven composites and their failure mechanisms are rarely addressed.

Bending failure modes are commonly analysed by using optical microscopy & scanning electron microscopy (SEM) [97], [98], [100] of the fractured surfaces of the composites. In few cases, Digital Image Correlation (DIC) [102], [103] was used for mapping the strain distribution over the surfaces. However, these surface characterisations provide limited information on the complete damage scenario. X-ray micro-computed tomography (µCT) is one of the most effective means of imaging the initiation and propagation of damage modes taking place internally [185], [189], [190]. Recently, Zhang et al. [103] and Turner et al. [188] used µCT to investigate the ultimate failure behaviour of 3D woven composites under three-point bending.

This chapter details the flexural behaviour of 3D woven composites under four point bending and explains the failure mechanism using X-ray micro CT. Section 2 describes the detail of test machine setup along with test specimen. A brief discussion on the X-ray

micro CT configuration is also given in this section. Bending test results are presented in Section 3. Failure mechanisms of the composites under flexural loading are explained in section 4. The chapter finishes with some concluding remarks.

8.2 Mechanical Testing

8.2.1 Test Machine Setup

Four-point bending tests were carried out in an Instron machine (5969) with a 2KN load cell and 1mm/min testing speed following the ASTM D6272 standard [191] . The Span-to thickness ratio was kept as 40:1. This ratio was recommended for 3D woven composites by Dai et al. as it was proved to yield minimum data scattering [98]. A high magnification video camera is embedded in the system to track the composite failure under applied load. The testing environment was controlled to a temperature of 21ºC and the relative humidity (RH) of 45%. Samples were tested both in warp and weft way, and at least four coupons were tested for each category. The machine setup is shown in Fig. 8. 1.
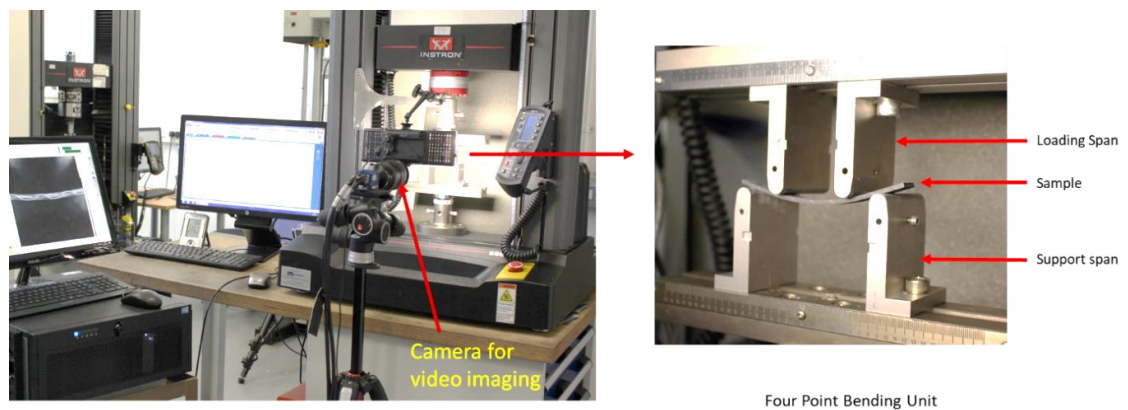
Fig. 8. 1 Machine setup for four-point bending test.

8.2.2 Test Specimen Preparation

In the four-point bending test, the dimensions of the test specimens depend on the laminate thickness. As the ultimate thickness of the composites varied according to the binder weave architectures, loading span and support span distances were also varied accordingly. A detail of the specimen dimensions is tabulated in the following Table 8. 1, Table 8. 2 and Table 8. 3 for different types of composites.

Table 8. 1 Specimen details for the warp bound composites for four-point bending tests

Composite	Thickness (mm)	Support Span length (mm) (1:40) (SS)	Loading span length (mm) (Half of SS) (LS)	Specimen length (mm) (1.20 X SS)	Width (mm)	Number of samples	
						Warp	Weft
1x1 Plain	2.95	120	60	140	17	5	4
2x1 Twill	2.31	92	46	110	17	5	4
2x2 Twill	2.27	92	46	110	17	5	4
AI	1.98	80	40	96	23	4	4

Table 8. 2 Specimen details for the weft bound composites for four-point bending tests

Composites	Thickness (mm)	Support Span length (mm) (1:40) (SS)	Loading span length (mm) (half of SS) (LS)	Specimen length (mm) (1.20 X SS)	Width (mm)	Number of samples	
						Warp	Weft
1x1 Plain	2.64	105	53	130	15	5	4
2x1 Twill	2.14	86	43	104	15	5	4
2x2 Twill	1.88	76	38	90	15	5	4
AI	1.85	74	37	90	20	4	4

Table 8. 3 Specimen details for the composites with binder tension variations

Composites	Thickness (mm)	Support Span length (mm) (1:40) (SS)	Loading span length (mm) (half of SS) (LS)	Specimen length (mm) (1.20 X SS)	Width (mm)	Number of samples	
						Warp	Weft
NT	2.95	120	60	140	17	5	4
HT	2.75	110	55	130	17	5	4

It is important to note that the weave unit size depends on the binder architecture. A wider specimen width was taken for all the composites to consider the full design weave. For the warp bound orthogonal composites, the sample width was 17mm, and for the weft bound orthogonal composites, it was 15mm. As the Angle Interlock weaves have a much wider weave design, 23mm and 20mm wide samples were taken for the warp and weft bound composites for this weave design.

8.2.3 X-ray Micro Tomography

To better understand the bending failure mechanism, composite samples were scanned with a Nikon Xtek High Flux Bay micro-CT scanner [see Fig. 8. 2(a)] at the Henry Moseley X-ray Imaging Facility, Manchester. Composites were scanned at three different loading levels- zero loading, an intermediate load where the composites start to damage and peak load. A specially designed transparent four-point rig was developed to hold the preloaded fractured composites during scans [see Fig. 8. 2(b)]. The scans were done with 145kV beam energy and 117 μA current, and four frames per projection. The total field of view was 60mm X 30mm X 30mm considering the loading span length and transparent tube diameter. The image acquisition voxel size was 23.5μm. Each radiograph exposure time was 500ms. The number of projections per frame was four, with a total of 3179 radiographs being collected over 360° rotation of the samples. The total data acquisition

time was 2 hours and 40 minutes for each sample. After scanning, the 3D images were reconstructed out of the 2D X-ray slices and analysed using Avizo visualisation software. From the reconstructed 3D images, the composite volume was extracted using the Crop tool. After cropping, the original composite structure was revealed using the colour frequency domain.

<center>(a)   (b)</center>
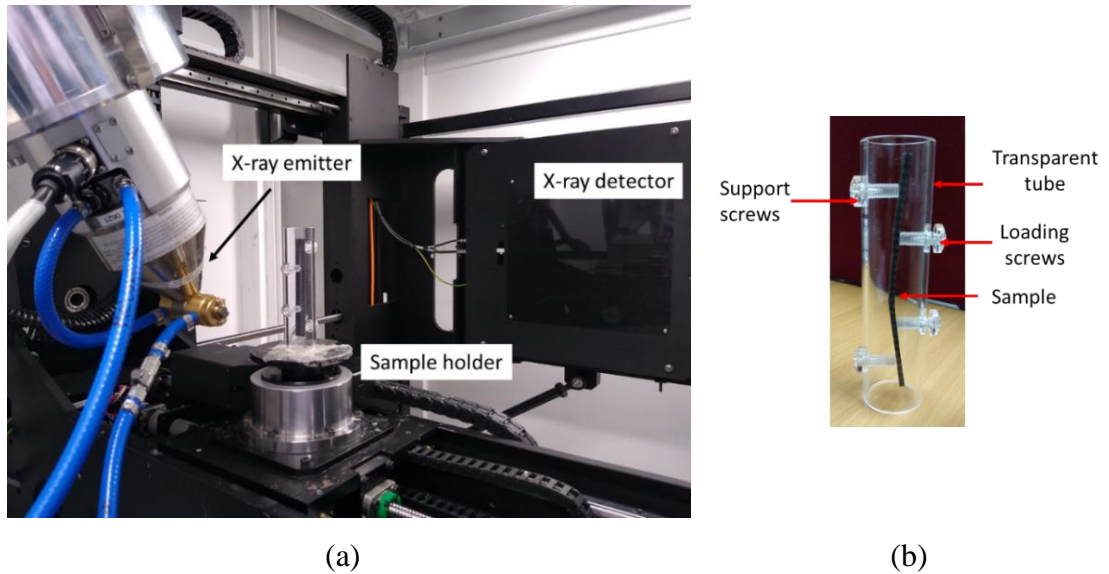
<center>Fig. 8. 2 (a) X-ray micro-CT scanner (b) Test specimen holding rig for scanning.</center>

Due to the limitation of X-ray imaging facilities, only the composites with 1x1 Plain binder weave architectures were scanned at three loading conditions. Considered specimens were: warp and weft way loaded samples for warp bound structures and warp way loaded structures for weft bound composites to compare loading directional sensitivity on bending failure mechanisms. The warp and weft way specimens from 1x1 plain orthogonal composites was chosen to explore the impact of directional loading on the failure mechanisms. On the other hand, warp way specimens from both warp and weft bound composites were chosen to investigate the impact of binder alteration in failure mechanisms.

8.3 Bending Properties

8.3.1 Warp Bound Composites

The stress-strain curves and the flexural properties for the warp bound composites tested in both warp and weft way loading are shown in Fig. 8. 3. In both ways, the stress/strain curves demonstrate good repeatability. As shown in Fig. 8. 3, all weave types exhibited a linear stress-strain behaviour until the first failure, which dropped once they reached the peak and continued to carry load even after the initial failure.
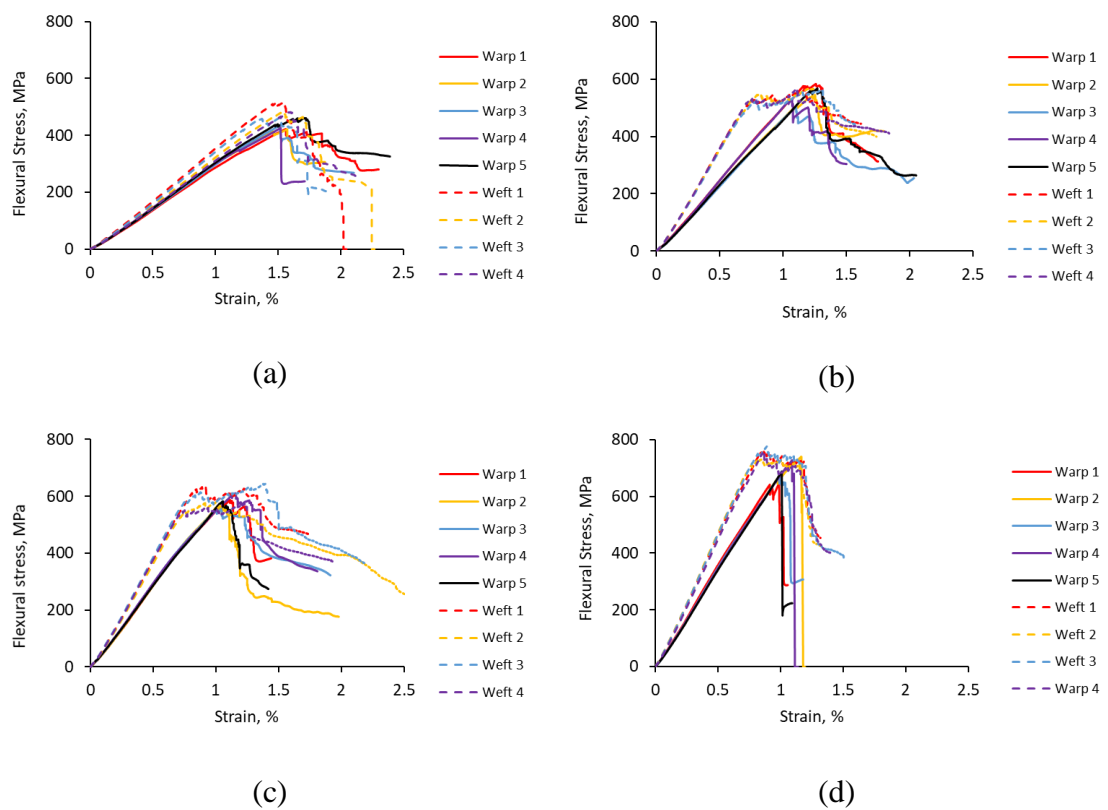
Fig. 8. 3 Flexural stress-strain diagram for the warp bound 3D woven composites with different binder weave architectures: (a) 1x1 Plain, (b) 2x1 Twill, (c) 2x2 Twill and (d) Angle Interlock (AI)

The following observations can be made from the above stress-strain curves:

(a) The stress-strain curves indicate the specimens tested in the weft direction are much stiffer than the composites tested in warp direction regardless of weave architectures and almost equal directional fibre volume fractions. This is primarily due to the extra fibre layer in the weft way. These warp bound composites have four layers of warp tows and five layers of weft tows. This additional weft layer provides the extra reinforcement for the higher modulus in the weft direction.

(b) Load dropping and further carrying is another important observation from the above stress-strain curves. A representational comparative stress-strain curves for both warp way and weft way loaded samples are shown in Fig. 8. 4. A significant load drop is visible from the curves for the warp way samples. The first load drop is almost like a catastrophic failure up to a certain point. The reason for this catastrophic failure may be related to the transverse properties of the carbon fibre bundles as detailed by Zhang et.al. [102], [103]. After this, they tend to show some forms of ductility where they continue to carry the load until final failure. On the other hand, weft way samples tend to show ductile behaviour before the first big load drop. Once they reach the peak load, they do not instantly have any significant load drops. Rather, they carry a similar quantity of load for a longer period of material extension and then gradually advance towards final failure. This ductility can be explained as result of resin matrix dominated behaviour and is consisted with the observation reported by Turner et.al. [188].
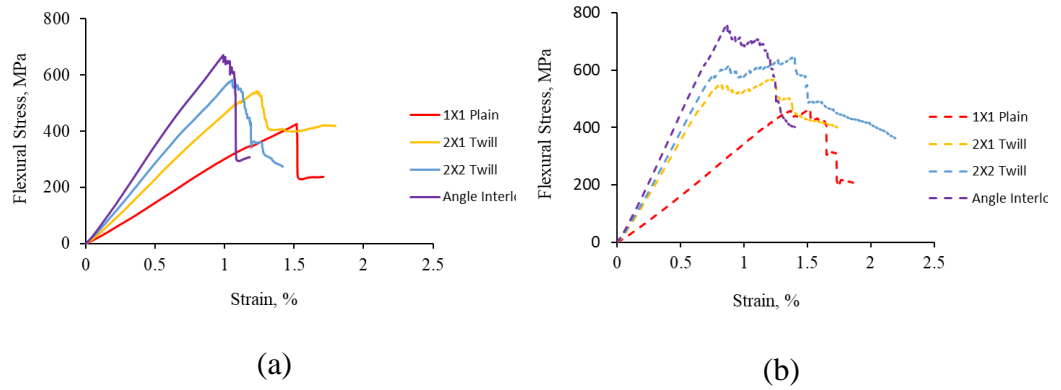
Fig. 8. 4 Representational stress-strain diagram of the warp bound composites with different weave architectures: (a) warp way, (b) weft way.

(c) The flexural modulus and strength of these 3D woven composites with different binder weave architectures are given in Table 8. 4. From the tabulated values, it is obvious that both bending stiffness and strengths are highly dependent on the degree of binder interlacings and improving for the structures with a lower number of interlacings. 1x1 plain weaves have the highest degree of interlacings among these weaves. This degree of interlacings gradually reduces for 2x1 Twill and 2x2 Twill weaves. Finally the angle Interlock (AI) has the lowest number of interlacings in its structure. This lower interlacing helps to reduce the damage initiation points, which ultimately improves the bending strengths. At the same time, a lower degree of interlacings allows the preforms to have higher binder floating lengths which ultimately increase the fibre volume fraction which ultimately improved the modulus of the less interlaced structures.

Table 8. 4 Flexural properties of warp bound composites.

Binder Weave	Warp		Weft	
	Modulus (GPa)	Strength (MPa)	Modulus (GPa)	Strength (MPa)
1x1 Plain	28.86±0.53	437.89±15.81	31.85±1.63	485.96±4.74
2x1 Twill	47.93±1.68	545.53±31.63	72.30±1.02	566.11±2.87
2x2 Twill	58.22±1.02	580.85±20.80	76.09±2.02	614.90±34.43
AI	70.45±1.27	694.51±39.42	92.98±1.91	758.02±18.58

8.3.2 Weft Bound Composites

The stress-strain curves and the flexural properties for the weft bound composites tested in both warp way and weft way loading are shown in Fig. 8. 5.
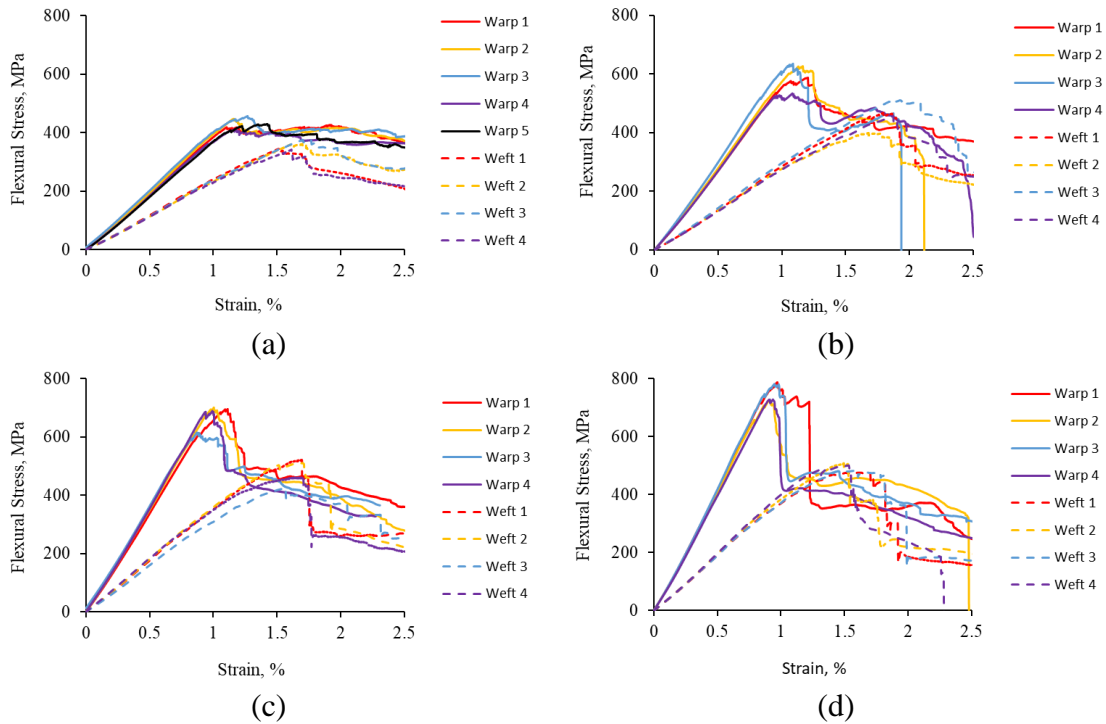
Fig. 8. 5 Flexural stress-strain diagram for the weft bound 3D woven composites with different binder weave architectures: (a) 1x1 Plain, (b) 2x1 Twill, (c) 2x2 Twill and (d) Angle Interlock (AI).

In both ways, the stress/strain curves demonstrate good repeatability. As shown in Fig. 8. 5, all weave types exhibited a linear stress-strain behaviour until the first failure, which dropped once they reached the peak load and continued to carry load even after the initial failure.

The following observations can be made from the above stress-strain curves:

(a) The stress-strain curves indicate the specimens tested in the warp direction are much stiffer than the composites tested in the weft direction regardless of weave architectures. This is primarily because of the higher directional fibre volume fractions in the warp way samples. As in the weft way, both the number of weft

170

layers and weft tow densities were reduced significantly due to manufacturing constraints (as discussed in Chapter 3), weft way directional fibre volume fractions were far lower than the warp way FVF (as reported in Chapter 6). For this very reason, weft way bending properties are significantly lower than the warp way properties.

(b) In the warp way, the initial load dropping phenomenon is not as prominent as was in warp bound composites. The composites tend to show some forms of ductility after the first load drop where they continued to carry similar levels of loads before the big second load drops. This is possibly due to changes in the preform geometry which is explained in the next section. For the weft way samples, big load drops were noticed for 2x2 twill and angle interlock weaves. The representational curves are shown in Fig. 8. 6.

(a)   (b)
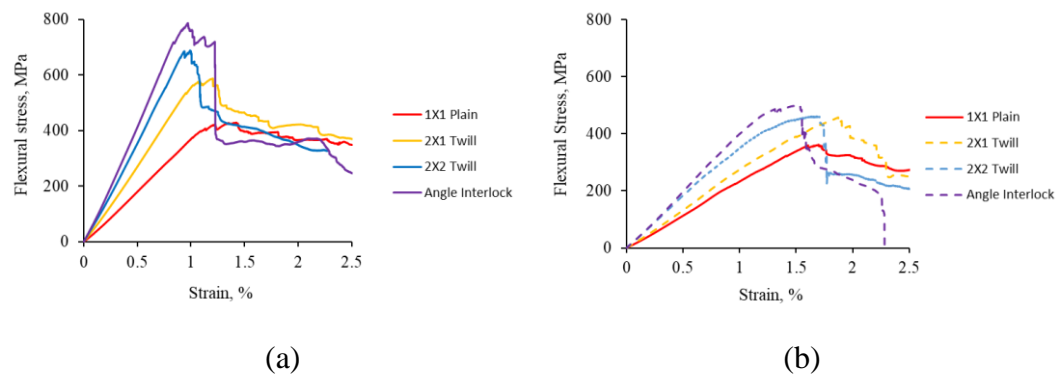
Fig. 8. 6 Representational stress-strain diagram of the weft bound composites with different weave architectures: (a) Warp way, (b) Weft way.

(c) Likewise, the warp bound composites, a significant impact of binder weave architectures are seen in these weft bound structures. The flexural modulus and strength of these weft bound composites are shown in the Table 8. 5. The tabulated results show that both bending modulus and strengths were improved by lowering

the degree of binder interlacings. 1x1 plain weave with the highest degree of interlacings has the lowest modulus and strength among all weave types. Bending properties are improved for 2x1 twill, and 2x2 twill weaves due to the reduced number of binder interlacings. Angle interlock weave have the lowest interlacings among all of these structures and hence the highest bending stiffness and strength.

(d) Another important observation is the ductile behaviour of the 1x1 plain woven structure. In both warp and weft directional loading this particular structure is seen to show significant ductility i.e. carrying load for considerable amount of strain%. This is probably because of the frequent resin rich areas in their structure created by the binder movement. During loading, the cracks develop in the resin rich areas on the tensile surface of the composites. With the continuous loading, these cracks are arrested by the binders and tend to delay the further failure.

Table 8. 5 Flexural properties of weft bound composites

Binder Weave	Warp		Weft	
	Modulus (GPa)	Strength (MPa)	Modulus (GPa)	Strength (MPa)
1x1 Plain	37.75±1.21	432.39±15.81	21.94±1.41	356.13±15.73
2x1 Twill	55.41±3.08	605.22±46.41	26.57±0.90	459.41±47.12
2x2 Twill	68.77±1.19	682.84±45.49	34.15±1.98	479.61±44.25
AI	82.24±1.87	761.90±36.07	37.35±1.29	496.04±10.49

8.3.3 Comparing Warp Bound and Weft Bound Composites

Bending modulus and strength for the weft bound composites are higher than the warp bound composites regardless of binder weave variations, except for the ultimate strength of the 1x1 Plain weave. In this particular structure, bending strength is almost equal for both warp bound and weft bound composites. For the other weaves, weft bound properties are significantly higher than the warp bound composites (see Fig. 8. 7).
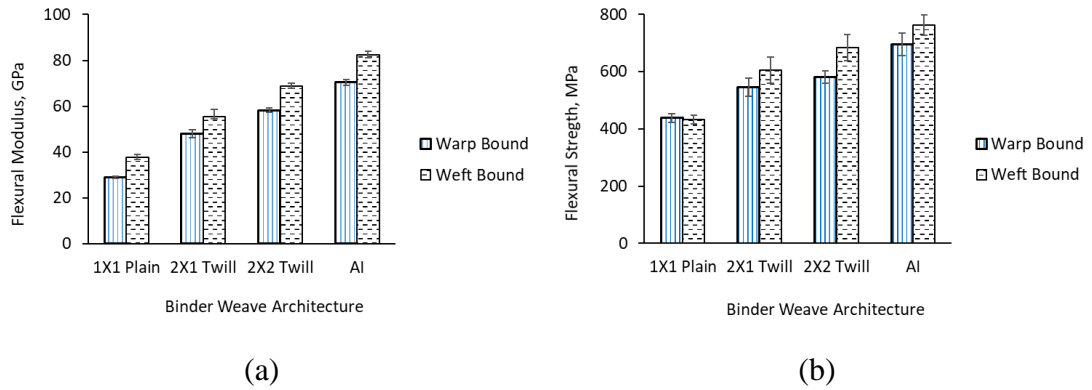
Fig. 8. 7 Bending properties for warp bound and weft bound composites in warp directional loading. (a) Bending Modulus (b) Bending Strength

This improvement in the weft bound structures is due to the changes in the structural geometry of the composites. In warp bound composites, warp layers are positioned in between the weft layers. Additionally, the warp way binders create resin channels along their way [110]. As a result, they have a high amount of damage initiating resin-rich areas in warp ways. On the other side, in weft bound composites, warp layers are positioned on both the top and bottom surfaces of the preforms. These top and bottom layers acted as reinforcement during loading [94]. Also, due to these surface tow layers, crack initiating resin rich areas were significantly reduced. As a result, they have the least resin-rich areas in that direction, leading to better bending properties.

8.3.4 Composites with Binder Tension Variation

The stress-strain curves for the composites with two different binder tensions (NT & HT) tested in both warp way and weft way loading, are shown in Fig. 8. 8. All the weave types exhibited a linear stress-strain behaviour until the first failure, which dropped once they reached the peak and continued to carry load even after the initial failure.
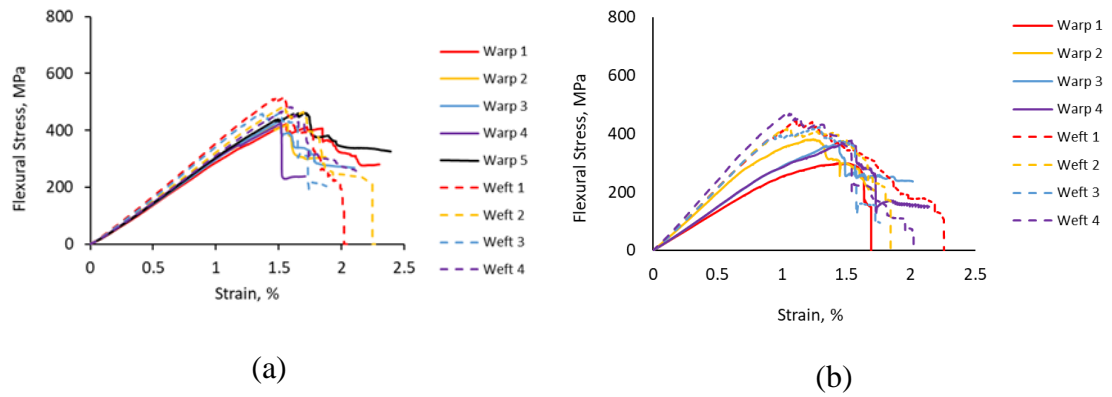
Fig. 8. 8 Flexural stress-strain diagram for the 3D woven composites with different binder tension: (a) Nominal tension (NT), (b) Higher Tension (HT).

In both cases, weft way specimens show higher stiffness and ductile behaviour during composite failing. On the other hand, the warp samples show a noticeable load drop during the first damage. Bending modulus and strengths are tabulated in Table 8. 6 for both composites.

Table 8. 6 Flexural properties of composites with binder tension variation

Binder Tension	Warp		Weft	
	Modulus (GPa)	Strength (MPa)	Modulus (GPa)	Strength (MPa)
NT	28.86±0.53	437.89±15.81	31.85±1.63	485.96±4.74
HT	31.41±5.58	355.26±38.41	44.34±2.97	440.2±24.68

The tabulated values show that the composite with higher binder tension has a higher bending modulus in both warp and weft ways. This is primarily because of the higher fibre volume fraction of this composite (mentioned in Chapter 6). Due to higher fibre volume fractions the composite with higher tension (HT), yield higher bending modulus. However, in both warp and weft ways, bending strengths are lower for the composites with higher binder tension. This is possibly due to the larger interlacement squashing areas, as discussed in Chapter 3. Because of the higher squashing areas, more stress concentration occurs surrounding these interlacing areas of the higher bender tension

composites (HT), resulting early failure compared with the composite with lower binder tension (NT) [113].

8.4 Bending Failure Mechanisms

8.4.1 Warp Bound Composites

Bending failure shows a distinctive pattern of damages for warp bound composites in warp and weft directional loading. In bending load, the upper part of the composites goes through compression, whereas the lower part goes through a tensile load. In warp way samples (Fig. 8. 9), initial cracks are observed in the tension side of the composites, which further leads to the final failure of the specimen.
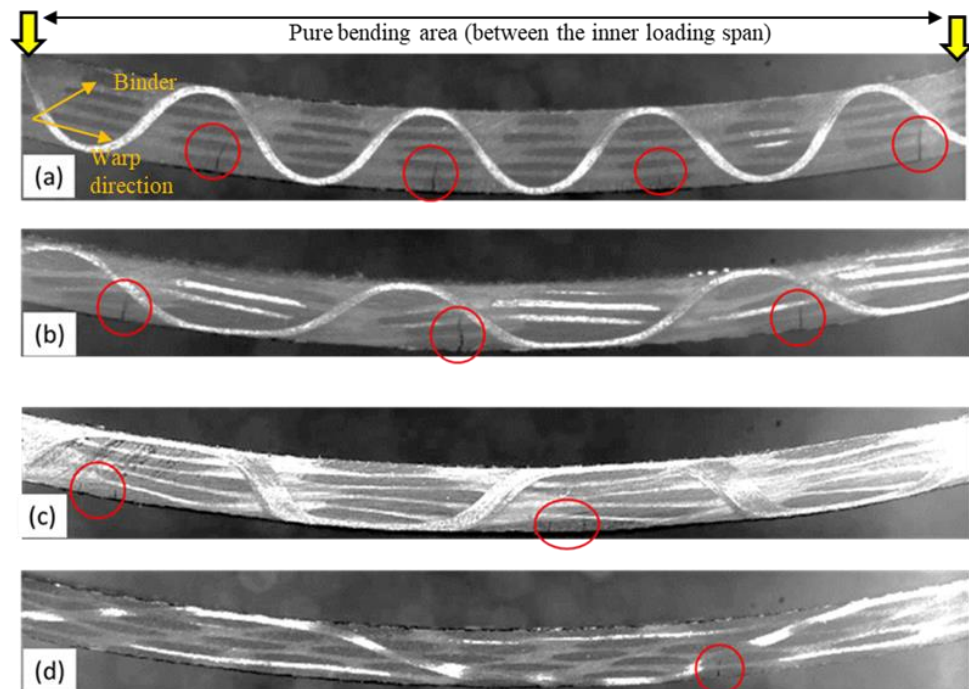
Fig. 8. 9 Crack opening in warp directional loading for warp bound composites: (a) 1x1 Plain, (b) 2x1 Twill, (c) 2x1 Twill and (d) Angle Interlock.

With initial loading, the cracks are opened in the resin-rich areas on the tensile side of the specimens. These cracks progress further until stopped by the binder. However, the cracks

can be transferred to the next layer of stuffer-matrix interfaces until final failure. As we cannot see this internal crack propagation, X-situ micro CT has been employed. Composites were scanned at zero loading, an intermittent load where the cracks are seen to be started (using a high magnification video camera), and at peak loads.
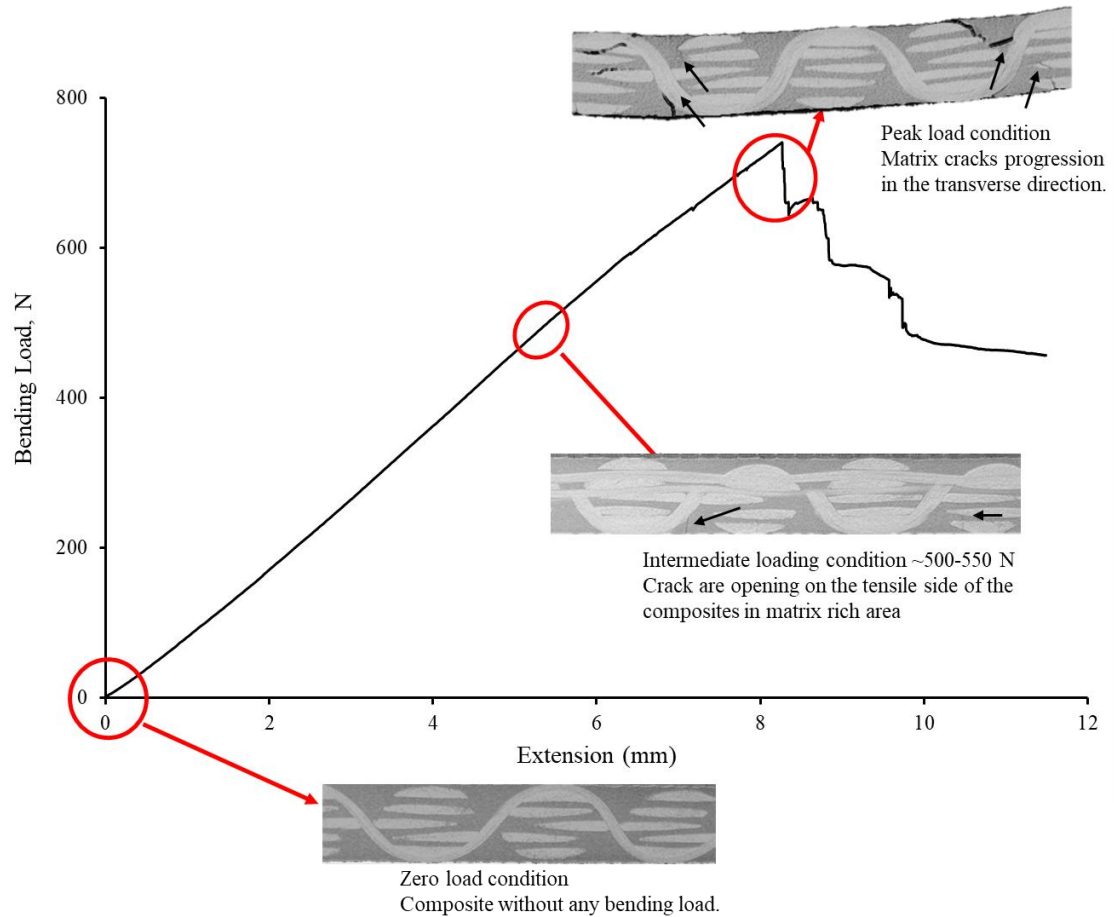
Fig. 8. 10 Typical warp way load extension diagram with X-ray CT images (insets) of the warp bound composite (1x1 Plain binder weave) at different load stages showing respective failure modes.

The scanned images (Fig. 8. 10) show that the cracks are initially started in the resin-rich areas on the channels created by the binder path and then progress through the thickness direction until they reach the binder. When hindered by the binders, the cracks start to follow them until transferring to the neighbouring warp-matrix layer interfaces (see Fig.

8. 11). Due to the pure bending, the cracks are spaced uniformly throughout the tensile layer of the composites, and the composite failed within the loading area (see Fig. 8. 11).
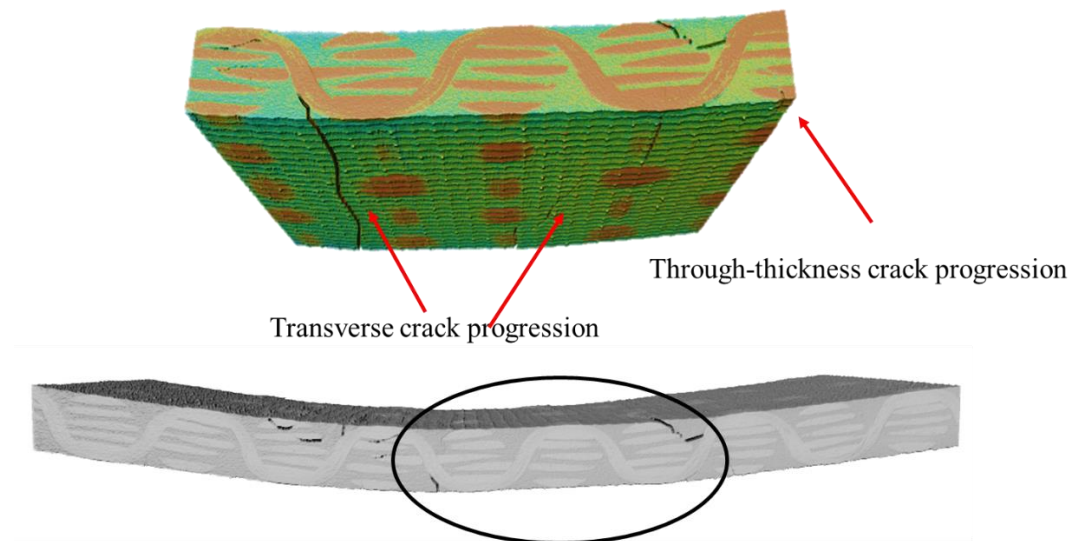
Fig. 8. 11 X-ray micro CT images of warp bound composites when loaded in warp way direction at peak load.

Another important observation from Fig. 8. 9 is the frequency of the matrix cracking on the composites. In the 1x1 plain structure, there are more binder interlacings, creating more resin-rich areas and more matrix cracks [115]. As a result, these composites fail much earlier. With the change in the weave architectures, this interlacement frequency goes down, reducing the possibility of matrix cracking and improving flexural performances. This is why 2x1 twill has higher modulus and strength than plain weave, 2x2 twill has even higher, and angle interlock structure has the highest among all four weaves.

For the weft way specimens, tow-matrix delamination is found as the dominant initial failure mode (see Fig. 8. 12). In initial loading, the composites are found to develop delamination between the matrix and the weft fibre. On the progression, the delamination

is found to be stopped by the binder interlacement points. As a reason, the length of the delamination is determined by the binder weave architectures.
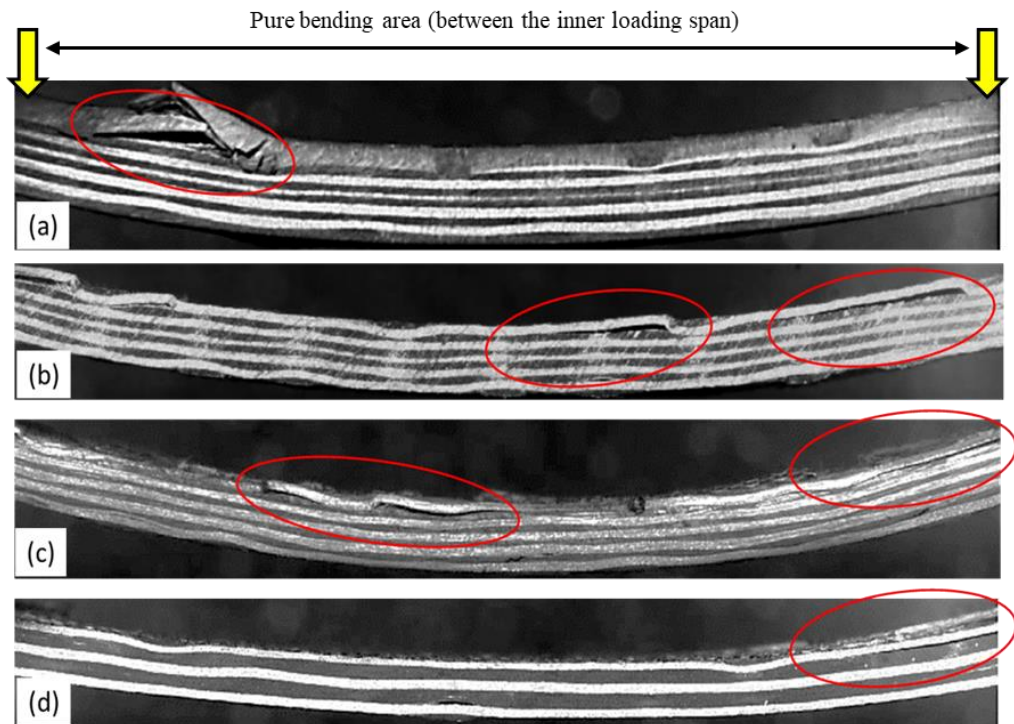
Fig. 8. 12 Crack opening in weft directional loading for warp bound composites: (a) 1x1 Plain, (b) 2x1 Twill, (c) 2x1 Twill and (d) Angle Interlock.

To better understand the damage development of the weft way specimens until final failure, X-situ micro CT was employed to the 1x1 plain orthogonal composite. Scans were done at three different loading levels: zero loading, an intermittent load where the cracks are seen to be started (using a high magnification video camera), and at peak loads. Load-extension diagram with corresponding failure modes at loading levels is shown in Fig. 8. 13.
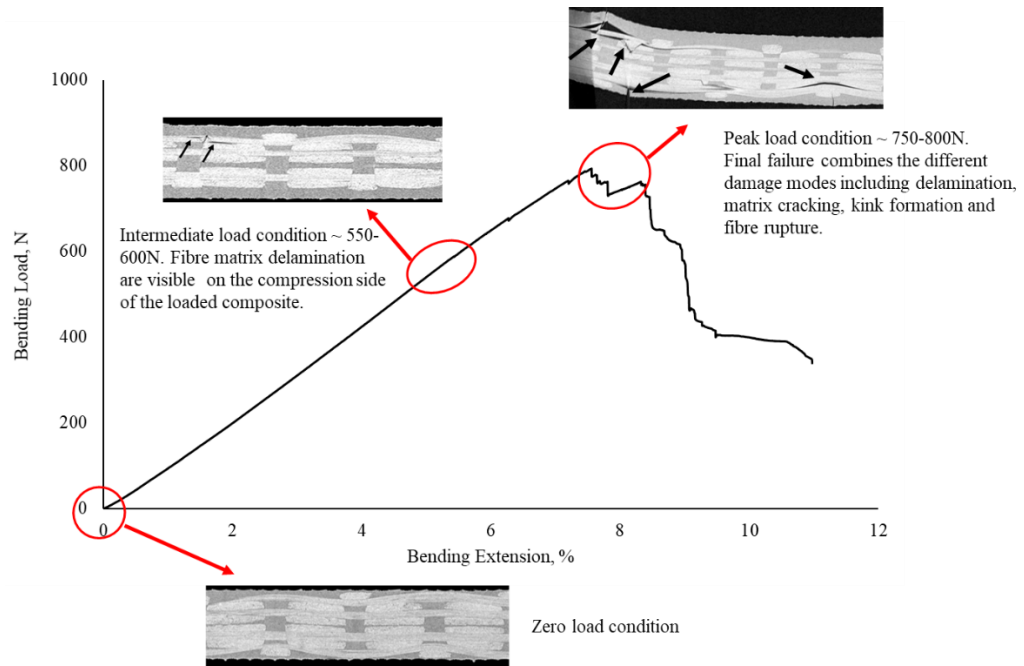
Fig. 8. 13 Typical weft way load extension diagram with X-ray CT images (insets) of the warp bound composite (1x1 Plain binder weave) at different load stages showing respective failure modes.

The longitudinal mid-section cross-sectional CT slice at 550-600N (Fig. 8. 13) confirms that the initial failure mode is ply delamination. However, the ultimate failure sequence constitutes a combination of failure modes including ply delamination, tow kinking and tow rupture (see Fig. 8. 14). In essence upon increasing the bending load to the peak load, matrix-tow and tow-tow delamination continue to develop. The development of the kink band results in the region of higher shear strain near the loading span, causes the surrounding fibre-matrix interface to crack. Further loading then leads to the cracking of the load-bearing fibres [103]. As a result, for the weft-bound composites, it was common for the composites to fail near the point of loading rather than within the gauge section.
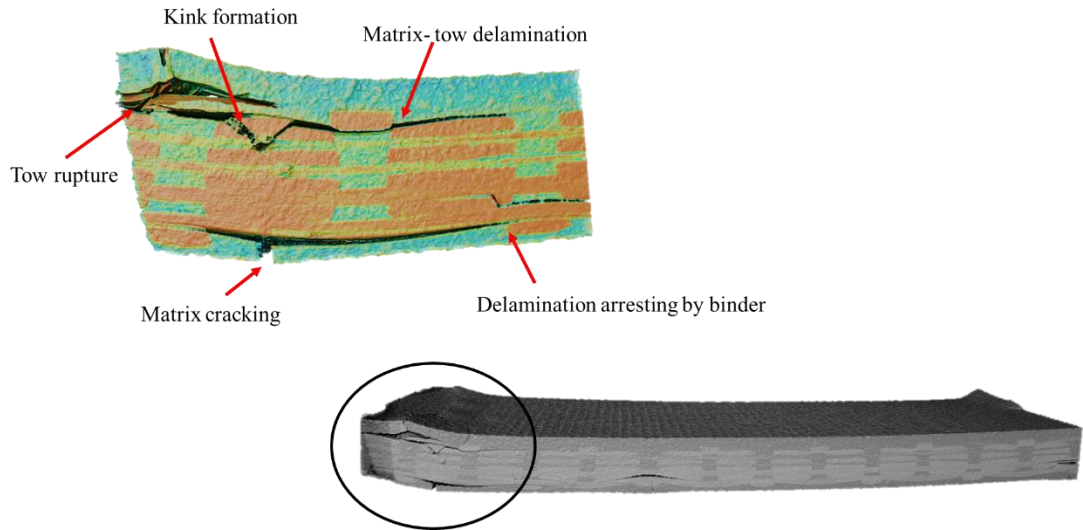
Fig. 8. 14 X-ray micro-CT image showing damage modes of weft way samples of warp bound composites at peak load.

8.4.2 Weft Bound Composites

Weft-bound composites' failure modes were also analysed using high magnification video imaging and X-ray micro CT. Distinctive failure modes were found for both warp way and weft way specimens.

For the warp directional loaded composites, tow layer delamination was observed as the dominant initial failure type (Fig. 8. 15). On initial loading, all the composites are found to develop inter-ply delamination between warps, wefts and binders. These initial delamination patterns were found same for all the weaves. Another important observation was the area of the initial delamination occurring. For all the weaves, delamination occurred near the loading points rather than the gauge area except for the 1x1 Plain weave where few delamination points were found in the gauge areas.
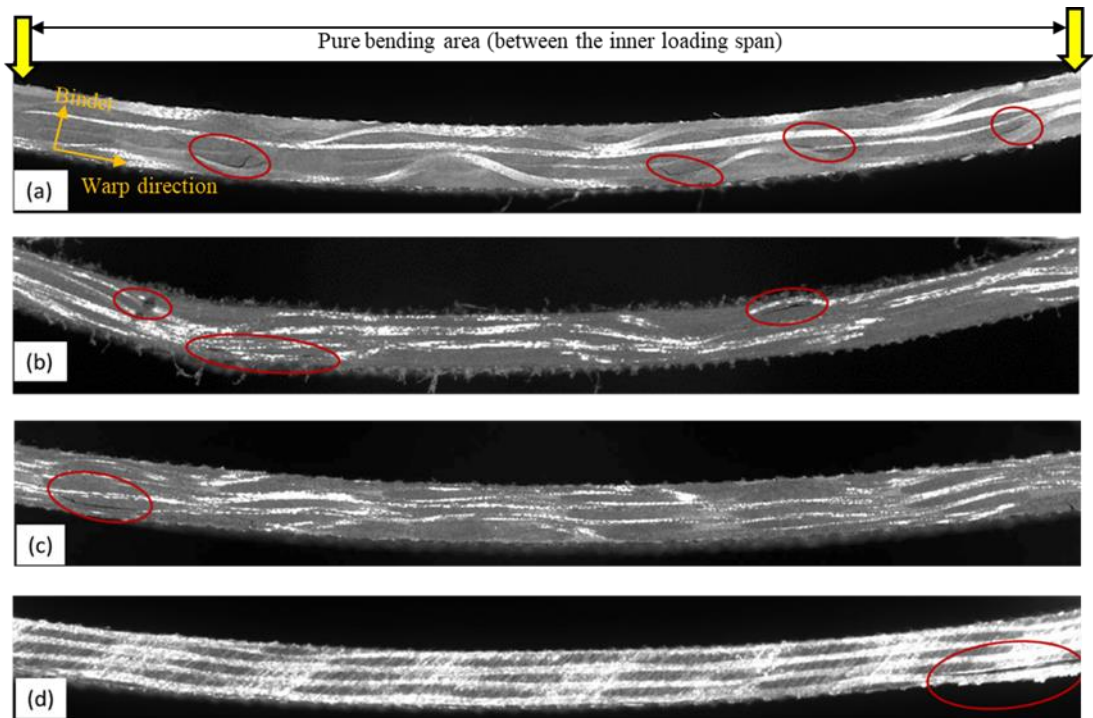
Fig. 8. 15 Crack openings in warp directional loading for weft bound composites: (a) 1x1 Plain, (b) 2x1 Twill, (c) 2x1 Twill and (d) Angle Interlock

For the sake of comparing the damage mechanisms of the warp bound and weft bound composites, warp directional preloaded weft bound composites were scanned using X-situ micro CT. Composites were scanned at zero loading, an intermittent load where the cracks are seen to be started (using a high magnification video camera), and peak loaded state. Load-extension diagram with failure modes at corresponding loading levels is shown in Fig. 8. 16.
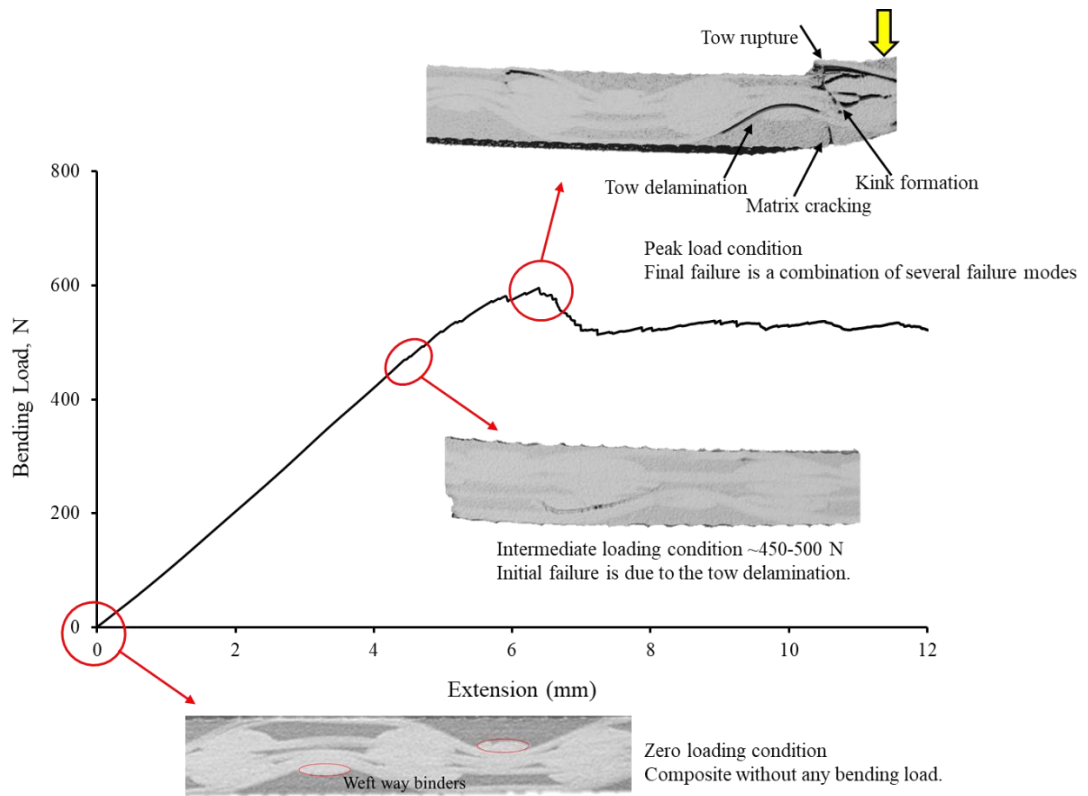
Fig. 8. 16 Typical warp way load extension diagram with X-ray CT images of the weft bound composite (1x1 Plain binder weave) with different load stages and respective failure modes.

The scanned images (Fig. 8. 16) show that the initial failure mode is the ply delamination. However, the ultimate failure constitutes a combination of different failure modes such as ply delamination, tow kinking and tow rupture. Matrix tow and tow-tow delamination continue to develop with further application of bending loads. The development of the kink band results in the localisation of higher shear strain near the loading span, which causes the surrounding fibre-matrix interface to crack [102]. Further continuous loading leads to the cracking of the load-bearing fibres. For the weft bound composites, it was common to fail near the point of loading rather than in the gauge section (see Fig. 8. 17).
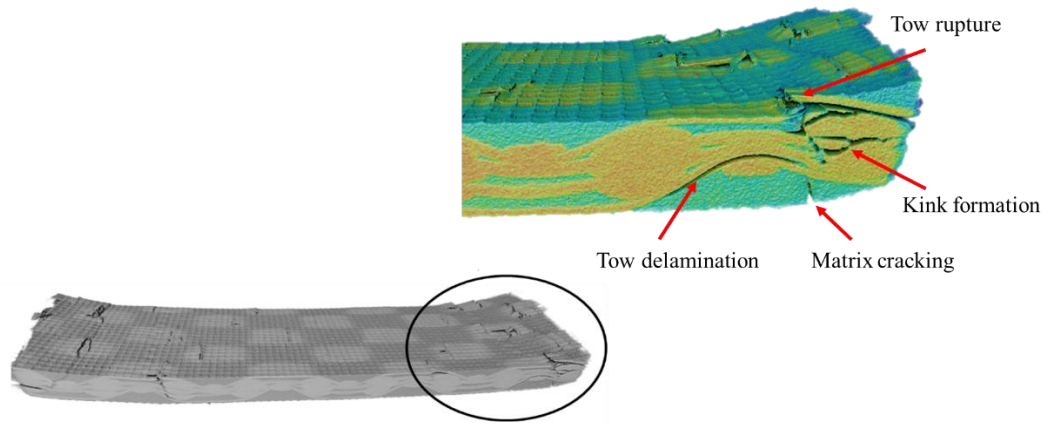
Fig. 8. 17 X-ray micro-CT image showing damage modes of warp way samples of weft bound composites at peak load (inset).

For the weft way samples, damage modes were found that of similar to the warp way samples of the warp bound composites. Initial failure mode in the form of matrix cracking was found in the loaded samples' tensile side (see Fig. 8. 18). These crack openings are highly dependent on the matrix channels created by the binder weave architectures [119]. As the initial mode of failure is almost the same as the warp bound warp way samples, it is expected that the final failure will also follow a similar pattern i.e. damage progression through the transverse direction.
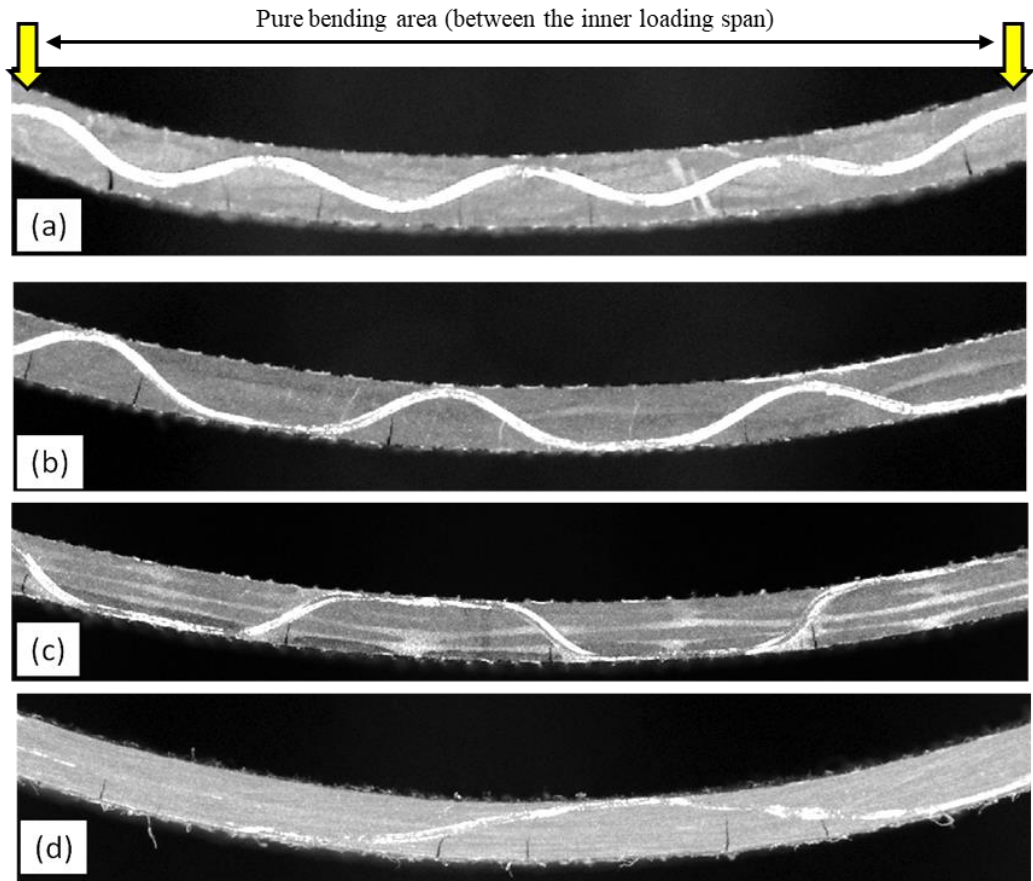
Fig. 8. 18 Crack opening in weft directional loading for weft bound composites: (a) 1x1 Plain, (b) 2x1 Twill, (c) 2x1 Twill and (d) Angle Interlock.

8.4.3 Composites with Binder Tension Variation

Damage mechanisms of the composites with two different binder tensions (NT and HT) on four point bending load are shown in Fig. 8. 19 and Fig. 8. 20. Images show that the damage modes are similar for both the composites. In the warp way, matrix cracking is the dominant failure mode and in the weft way, fibre-matrix delamination is the dominant failure type. The ultimate failure follow the same mechanisms of warp bond composites (detailed in section 8.4.1 Warp Bound Composites).
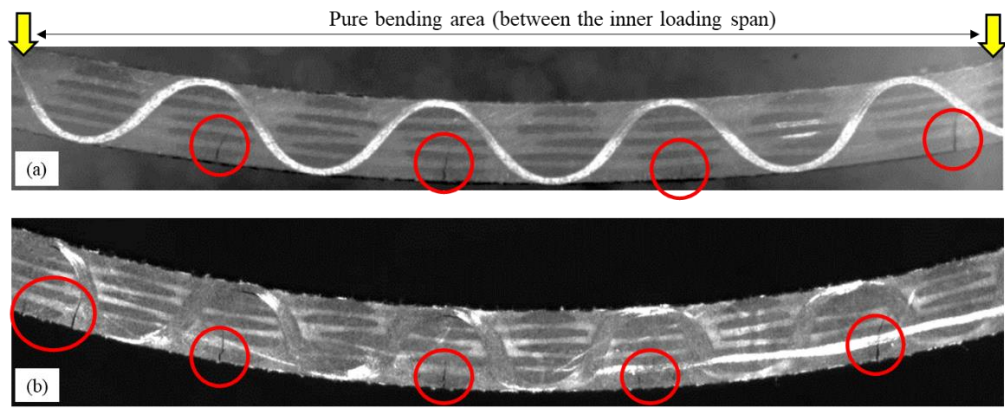
Fig. 8. 19 Warp way damage modes for the composites with different binder tensions: (a) Nominal tension and (b) Higher tension. (Red circles show the matrix cracking in the tensile side of the loaded samples).
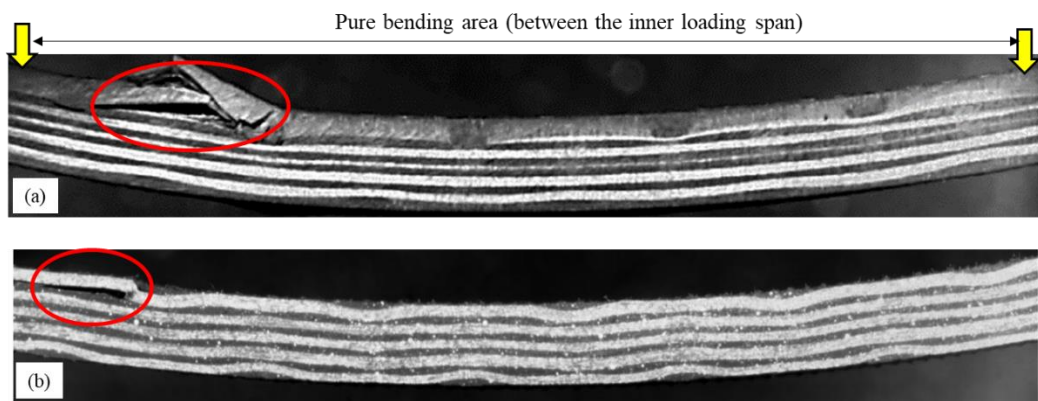
Fig. 8. 20 Weft way damage modes for the composites with different binder tensions: (a) Nominal tension and (b) Higher tension. (Red circles show the fibre-matrix delamination in the compressive sides of the loaded samples)

8.5 Concluding Remarks

Flexural properties for 3D woven composites with different binder weave architectures (1x1 Plain, 2x1 Twill, 2x2 Twill and Angle Interlock) and different binder tensions were evaluated, and their failure mechanisms were also investigated. Both warp bound and weft bound structures were considered for the investigation. The following conclusions can be made from the experimental results.

- Both flexural modulus and strengths significantly depend on the binder weave architectures as they determine the degree of interlacings and FVF. Due to higher binder interlacings in the 1x1 plain composites, more matrix cracks developed on the tensile face, resulting in inferior bending performance. This situation improves with the changes in weave architectures as they have increasingly fewer binder crossing points in the 2x1 twill, 2x2 twill and angle interlock composites, respectively.

- Bending properties are also found to be sensitive to the loading direction. In the warp bound composites, where the directional fibre volume fraction is almost same for warp and weft ways, weft way stiffness and strength are found much higher than the warp way. This is due to the additional weft layer in that structure and weft tow lay-up geometry.

- The composite failure mechanism mainly depends on the loading direction. On the binder way direction (warp way in warp bound and weft way in weft bound composites), matrix cracking in the tensile side is the dominant initial failure mode. These cracks are then progressed to the thickness direction until final failure. On the opposite direction (weft way for warp bound and warp way for weft bound), tow-matrix delamination was found to be the dominant initial failure mode. However, the ultimate failure combines different other damage types, including tow delamination, matrix cracking, kink formation and tow rupture.

- No significant impact of binder tensions was seen on the stiffness of the orthogonal composites with a 1x1 plain binder weave. However, a reduction in the flexural strengths was noticed for the composites with higher binder tensions. This is possibly due to the higher squashing area in those composites, which led to early failure on four-point bending load.

Chapter 9 Conclusions and Future Works

9.1 Introduction

Due to excellent delamination resistance and superior through-thickness properties, 3D woven composites are attracting greater interest from academicians and industries. Although extensive research interest has been carried out on the structures of the 3D woven preforms, specific concentration on Z-binder parameters was rarely addressed. Therefore the current research focused on two main parameters of Z-binders: binder weave architectures and binder tension. 3D woven preforms were developed with four different Z-binder weave architectures and two samples with different binder tensions. The role of Z-binder weave architectures was investigated for preform compressibility and permeability. Tensile and bending properties of the 3D woven composites with different Z-binder weave architectures and tensions were characterised to explore the impact of Z-binders on the mechanical properties.

All the key findings of this research are summarised in the next section. Recommendations for future work, based on the current research, are made following the conclusions.

9.2 Conclusions

9.2.1 Manufacturing of 3D Woven Preforms

3D woven preforms were manufactured considering two binder parameters: binder weave architectures and binder tension. Warp bound, and weft bound preforms were developed with four different binder weave structures. Necessary modification on the existing loom set-up was done to accommodate weft way binders and to change the binder tension. The considered weave architectures were 1x1 plain, 2x1 twill and 2x2 twill with orthogonal

structures and an angle interlock weave structure. The weave structures were chosen to reduce the degree of binder interlacings sequentially, which directly affects the crimp percentages of the binders. The weave architectures were chosen based on the recommendation of the previous literatures where it is reported that the in-plane properties can be improved by reducing binder waviness [98]. The sequential reduction in binder interlacings were chosen to explain the impact of Z-binder architectures on the failure mechanisms of 3D woven composites. Another set of 3D woven preforms was developed where the Z-binder tension was varied. Two orthogonal preforms were developed with 1x1 plain weave, where the binders were drawn in two different tensions. They were named nominal tension (NT) structures and high tension (HT) structures. The surface images of the preform structures revealed that the binders are more spread in the interlacing positions with the high tension binders than in the nominal tension structures.

9.2.2 Compressibility of the 3D Woven Preforms

The compaction behaviour of the 3D woven preforms with different binder weave structures was studied with cyclic transverse compaction tests. Preform compressibility was measured from the thickness-pressure curve. The fibre volume fractions were also predicted for different compaction levels.

The major changes in the preform thicknesses were found to occur during the first cycle of loading for all the preforms. Thickness changes were less significant in the following cycles, which suggests that the internal fibre structures were reordered during the first cycles. However, the degree of structural reordering was highly dependent on the binder weave architectures. 1x1 plain weave has the least compressibility due to the highest degree of interlacings. The frequently occupied through-thickness Z-binders prevent the transverse compression of the preforms. With the reduction of the binder interlacement

points, compressibility increased for 2x1 twill and 2x2 twill. Among all the weaves, the angle interlock (AI) has the highest compressibility due to the angular binder path and few interlacings. There are some forms of plastic deformations in the preforms that are observed in every compaction cycle. This is why the highest fibre volume fraction was found after multiple cyclic loads. Due to the highest compressibility among all the structures, the angle interlock had the maximum fibre volume fraction.

9.2.3 In-Permeability of the 3D Woven Preforms

The role of Z-binder architecture on in-plane permeability was studied using both warp bound and weft bound structures. A permeability measurement setup was developed based on the flow visualisation principle.

The through-thickness binders created resin channels. The frequency of these channels is determined by the degree of binder interlacings. 1x1 plain weave have the highest number of interlacings, so has the highest number of resin channels. As a result, it has the maximum permeability among all the structures. For the other weaves, the resin channels continue to decrease as a function of interlacement numbers and permeability. Angle interlock has the lowest permeability among all the structures. Flow development was also related to the binder architectures. The flow developed in an elliptical shape for all the orthogonal preforms. For the angle interlock weave, where the binder moves in an angular way, the flow shape was almost circular, indicating a uniform directional flow development in the warp and weft ways.

9.2.4 Composite Manufacturing and Geometric Properties

3D woven composites were manufactured using a customised vacuum bag infusion method to avoid surface unevenness. Volume fractions of the composite constituents were

experimentally measured. Z-binder crimp percentages were also calculated from the cross-sectional images of the composites.

Fibre volume fractions of the 1x1 plain woven composite were the lowest due to its least compression. The binder float length was increased for 2x1 twill and 2x2 twill by reducing the number of interlacings. These higher float lengths assisted in more compaction of the structure and increased the fibre volume fraction. Angle interlock has the maximum fibre volume fraction among all the weaves due to its highest compressibility. For the same reason, Z- binder in the 1x1 plain weave has the highest crimp%, and the angle interlock weave has the lowest crimp.

9.2.5 Tensile Properties of the 3D Woven Composites

Tensile properties for 3D woven composites with different binder weave architectures (1x1 Plain, 2x1 Twill, 2x2 Twill and Angle Interlock), as well as different binder tensions, were evaluated. Their failure mechanisms were investigated using online video imaging DIC for strain mapping and analysing the post failed samples.

Both tensile modulus and strengths for these composites were significantly dependent on the binder weave architectures, as they contribute toward the FVF and binder crimp %. 1x1 plain weave had the lowest tensile modulus and strength among all the weaves because of the lowest fibre volume fraction and highest crimp %. Both stiffness and strengths were improved for the 2x1, and 2x2 twill weaves by reducing the degree of binder interlacings. The tensile properties were also found to be highly sensitive to loading directions. DIC strain mapping showed that the strains are localised at the interlacing points. Z-binders were seen to assist in carrying loads when the composites were loaded in the binder direction. In the other direction, Z-binders were found to have initiated the damage in the interlacing areas. Due to the higher squashing area in the

interlacings of the composites with higher binder tensions, they failed early compared to the low binder tension composites.

9.2.6 Flexural Properties of the 3D Woven Composites

Flexural performances for 3D woven composites with different binder weave architectures (1x1 Plain, 2x1 Twill, 2x2 Twill and Angle Interlock), as well as different binder tensions were evaluated using four-point bending tests. Their failure mechanisms were investigated using X-ray micro-CT and online video imaging during testing.

The binder weave architectures and the binder tension were found to influence the properties and failure of 3D woven composites under bending loads. Due to higher binder interlacings in the 1x1 plain composites, more matrix cracks developed on the tensile face, resulting in inferior bending performance. This situation improves with the changes in weave architectures as they have fewer binder crossing points in the 2x1 twill, 2x2 twill and angle interlock composites respectively. Both flexural modulus and strength were found to be highly sensitive to the loading directions. Weft way stiffness and strength in the warp bound composites were much higher than in the warp way specimens, despite having similar FVF. This is due to the additional weft layer and the surface positioning of the weft layers. Composites with higher binder tension were found to have lower strength than the nominal binder tension specimen. This is probably because of the high tension specimen's higher squashing area, which led to early failure. Weft bound composites were found to have significantly higher bending properties compared to the warp bound structures due to the nature of the failure. Using Micro CT, distinctive failure modes were found for the warp bound and weft bound composites. For warp bound composites, in the warp direction, the cracks initiated in resin-rich areas along the tensile face of the laminates advanced through the thickness direction until final failure. In the

weft way, the final failure is a combination of tow-matrix delamination, tow rupture and kink band formation. By contrast, weft bound composites have a combination of different failure modes in the warp way. In the weft way, matrix delamination is the dominant failure mode.

9.3 Summary

3D woven structures were developed with customised binder weave architectures to investigate the mechanical properties of the composites. Binder were incorporated in both warp yarn direction as well as weft way directions. Binder tension was also changed to investigate the impact of tension on composite structures. It is found that the reduction in the degree of binder interlacements improve the level of compaction and gives higher FVF. By altering the direction of resin channels, directional permeability of the weft bound preforms were significantly improved. This particular finding may offer a solution to the existing problems of infusing large scale preforms such as wind turbine blades. Reduction in binder degree of interlacements improved the in-plane tensile and flexural properties significantly. For high load application, orthogonal structures with less interlacements such as 2x2 twill binder interlacings can be used to get higher performances. On flexural loading, it is found that the plain weave shoed more ductility. As a result, applications where ductile failure is needed such as leaf springs, plain 3Dwoven composites can be used. Overall, angle interlock weave showed the best mechanical performances among all the structures in both tensile and flexural loading. With the increase of binder tension, interlacing squashing areas also increased which actually reduced the mechanical strengths of the composites significantly. It is indicative from these findings that the tensile and bending strength can be improved by reducing binder tension. This needs to be further investigated.

9.4 Future Work Recommendations

The following recommendations are made for future research:

- One of the current research limitations was the variation in binder tension. Manufacturing 3D woven structures with more variation in binder tension will help to understand the impact of binder tension on mechanical properties more clearly. Impact of other binder parameters such as binder density, twist, binder size etc. can also be explored.

- Using X-ray micro CT technique to reveal the internal geometry of 3D woven preforms at different compaction levels. This can be an effective investigation tool to model the compaction behaviour of 3D woven preforms under different compaction loading conditions. These models can be further used to predict the resin flow behaviour of the preforms.

- The permeability study can be further continued to investigate the through-thickness resin flow behaviour of these preforms. This investigation will probably help to explore the role of Z-binder parameters on through-thickness permeability.

- The Current research showed directional loading sensitivity in both tensile and flexural properties when specimens were tested in warp and weft directions. The mechanical characterisation can continue to explore the off-axis loading conditions. Also, the in-situ X-ray tomography technique will be the most effective tool to explore the time-lapse damage mechanisms in both tensile and bending loading conditions.

- Other mechanical properties such as compressive, impact damage, interlinear shear etc. can be studied varying binder parameters. An optimisation network can be developed based mechanical property database to predict the optimum geometrical structures of the 3D woven preforms for specific applications.

References

[1] P. Potluri and J. Atkinson, "Automated manufacture of composites: handling, measurement of properties and lay-up simulations," *Compos. Part A Appl. Sci. Manuf.*, vol. 34, no. 6, pp. 493–501, Jun. 2003, doi: 10.1016/S1359-835X(03)00056-3.

[2] L. Tong, A. P. Mouritz, and M. K. Bannister, "Chapter 1- 3D fibre reinforced polymer composites," Elsevier, 2002, p. 241.

[3] A. P. Mouritz, M. K. Bannister, P. J. Falzon, and K. H. Leong, "Review of applications for advanced three-dimensional fibre textile composites," *Compos. Part A Appl. Sci. Manuf.*, 1999, doi: 10.1016/S1359-835X(99)00034-2.

[4] B. N. Cox, M. S. Dadkhah, and W. L. Morris, "On the tensile failure of 3D woven composites," *Compos. Part A Appl. Sci. Manuf.*, 1996, doi: 10.1016/1359-835X(95)00053-5.

[5] M. Ansar, W. Xinwei, and Z. Chouwei, "Modeling strategies of 3D woven composites: A review," *Compos. Struct.*, vol. 93, no. 8, pp. 1947–1963, Jul. 2011, doi: 10.1016/J.COMPSTRUCT.2011.03.010.

[6] F. Boussu, I. Cristian, and S. Nauman, "General definition of 3D warp interlock fabric architecture," *Compos. Part B Eng.*, 2015, doi: 10.1016/j.compositesb.2015.07.013.

[7] P. R. (Peter R. Lord and M. H. Mohamed, *Weaving : conversion of yarn to fabric*. Woodhead Publishing Limited, 2010.

[8] M. H. Mohamed and A. E. Bogdanovich, "Comparative Analysis Of Different 3D

Weaving Processes, Machines and Products," *17th International Conference on Composite Materials (ICCM)*, 2009.

[9] S. Rudov-Clark, A. P. Mouritz, L. Lee, and M. K. Bannister, "Weaving damage to three-dimensional glass-polymer composites," *44th AIAA/ASME/ASCE/AHS/ASC Struct. Struct. Dyn. Mater. Conf.*, 2003, doi: 10.2514/6.2003-1878.

[10] S. Rudov-Clark, A. P. Mouritz, L. Lee, and M. K. Bannister, "Fibre damage in the manufacture of advanced three-dimensional woven composites," *Compos. Part A Appl. Sci. Manuf.*, vol. 34, no. 10, pp. 963–970, Oct. 2003, doi: 10.1016/S1359-835X(03)00213-6.

[11] C. H. Chiu and C. C. Cheng, "Weaving Method of 3D Woven Preforms for Advanced Composite Materials," *Text. Res. J.*, vol. 73, no. 1, pp. 37–41, Jul. 2016, doi: 10.1177/004051750307300107.

[12] D. Patel, V. Koncherry, Z. Yousaf, and P. Potluri, "Influence of 3D Weaving Parameters on Preform Compression and Laminate Mechanical Properties," *21st International Conference on Composite Materials (ICCM21), 2017.*

[13] L. Lee, S. Rudov-Clark, A. . Mouritz, M. . Bannister, and I. Herszberg, "Effect of weaving damage on the tensile properties of three-dimensional woven composites," *Compos. Struct.*, vol. 57, no. 1–4, pp. 405–413, Jul. 2002, doi: 10.1016/S0263-8223(02)00108-3.

[14] Mohamed, Mansour H., Mohmoud M. Salama, "High speed three-dimensional weaving method and machine," US Patent No. 6315007B1, 2001.

[15] K. Fukuta, R Miyashita, J Sekiguti, Y Nagatsuka, S Tsuburaya, E Aoki, "Three-dimensional fabric, and method and loom construction for the production thereof,"

US Patent No. 3834424A, 1974.

[16] Mohamed, M. H., Zhang Z. H., "Method of forming variable cross-sectional shaped three-dimensional fabrics," US Patent No. 5085252A, 1990.

[17] Prasad Potluri, Dhavalsinh Jetavat, Sandeep Sharma, "Method and apparatus for weaving a three-dimensional fabric," US Patent No. 9598798B2, 2013.

[18] M. Matveev, V. Koncherry, S. S. Roy, P. Potluri, and A. Long, "Novel textile preforming for optimised fibre architectures," doi: 10.1088/1757-899X/406/1/012050.

[19] R. A. Naik, "TEXCAD – Textile composite analysis for Design. Version 1.0: User's manual," 1994.

[20] TexEng, "Textile Industry Software available from TexEng – TexEng." https://texeng.net/software.

[21] J. W. S. Hearle and X. Chen, "3D Woven Preforms and Properties for Textile Composites," *17th International Conference on Composite Materials (ICCM17),* 2009.

[22] X. Chen, "Mathematical modelling of 3D woven fabrics for CAD/CAM software:," *Text. Res. J.*, vol. 81, no. 1, pp. 42–50, Nov. 2010, doi: 10.1177/0040517510385168.

[23] I. Verpoest and S. V. Lomov, "Virtual textile composites software WiseTex: Integration with micro-mechanical, permeability and structural analysis," *Compos. Sci. Technol.*, vol. 65, no. 15–16, pp. 2563–2574, Dec. 2005, doi: 10.1016/J.COMPSCITECH.2005.05.031.

[24] L. P. Brown and M. Sherburn, "louisepb/TexGen: TexGen v3.10.0," Dec. 2017, doi: 10.5281/ZENODO.1115604.

[25] A. C. Long and L. P. Brown, "Modelling the geometry of textile reinforcements for composites: TexGen," *Compos. Reinf. Optim. Perform.*, pp. 239–264, Jan. 2011, doi: 10.1533/9780857093714.2.239.

[26] Carlson and C. H., "Preliminary scramjet design for hypersonic airbreathing missile application," Nov. 1983, Accessed: Jun. 11, 2018. [Online]. Available: https://ntrs.nasa.gov/search.jsp?R=19840005127.

[27] Jewell J, Kennedy R, and Menard A, "Full-scale LEAP fan blade-out rig test yields outstanding results; advanced LEAP fan endurance test complete," *CFM Power Flight*, 2011.

[28] G. Marsh, "Aero engines lose weight thanks to composites," *Reinf. Plast.*, vol. 56, no. 6, pp. 32–35, Nov. 2012, doi: 10.1016/S0034-3617(12)70146-7.

[29] T. Huang, Y. Wang, and G. Wang, "Review of the Mechanical Properties of a 3D Woven Composite and Its Applications," *Polym. Plast. Technol. Eng.*, vol. 57, no. 8, pp. 740–756, May 2017, doi: 10.1080/03602559.2017.1344857.

[30] M. H. Mohamed and K. K. Wetzel, "3D Woven Carbon/Glass Hybrid Spar Cap for Wind Turbine Rotor Blade," *J. Sol. Energy Eng.*, vol. 128, no. 4, pp. 562–573, Nov. 2006, doi: 10.1115/1.2349543.

[31] K. Sharp, A. Bogdanovich, R. Boyle, J. Brown, and D. Mungalov, "Wind blade joints based on non-crimp 3D orthogonal woven Pi shaped preforms," *Compos. Part A Appl. Sci. Manuf.*, vol. 49, pp. 9–17, Jun. 2013, doi: 10.1016/J.COMPOSITESA.2013.01.012.

[32] J. G. Hemrick, E. Lara-Curzio, E. R. Loveland, K. W. Sharp, and R. Schartow, "Woven graphite fiber structures for use in ultra-light weight heat exchangers," *Carbon N. Y.*, vol. 49, no. 14, pp. 4820–4829, Nov. 2011, doi: 10.1016/J.CARBON.2011.06.094.

[33] E. Vitug, "First 3D woven composite for NASA thermal protection systems," 2016, Accessed: Jun. 11, 2018. [Online]. Available: https://www.nasa.gov/feature/first-3d-woven-composite-for-nasa-thermal-protection-systems.

[34] M. N. Saleh and C. Soutis, "Recent advancements in mechanical characterisation of 3D woven composites," *Mech. Adv. Mater. Mod. Process. 2017 31*, vol. 3, no. 1, pp. 1–17, Jul. 2017, doi: 10.1186/S40759-017-0027-Z.

[35] Redman C, Bayraktar H, and Mcclain M, "Curved beam test behavior of 3D woven composites," *SAMPE Conference J 45*, 2014.

[36] H. Bayraktar, D. Ehrlich, J. Goering, and M. Mcclain, "3D Woven Composites for Energy Absorbing Applications," Accessed: Jan. 22, 2022. [Online]. Available: http://www.albint.com/aec.

[37] Mcclain M, Senior R, and Organic TE, "Overview of recent developments in 3D structures," *lbany Eng Compos* , 2012.

[38] M. K. Bannister, "Development and application of advanced textile composites," *Proc. Inst. Mech. Eng. Part L J. Mater. Des. Appl.*, vol. 218, no. 3, pp. 253–260, Jul. 2004, doi: 10.1177/146442070421800310.

[39] L. Limmer, G. Weissenbach, D. Brown, R. McIlhagger, and E. Wallace, "The potential of 3-D woven composites exemplified in a composite component for a

lower-leg prosthesis," *Compos. Part A Appl. Sci. Manuf.*, vol. 27, no. 4, pp. 271–277, Jan. 1996, doi: 10.1016/1359-835X(95)00040-9.

[40] F. Robitaille and R. Gauvin, "Compaction of textile reinforcements for composites manufacturing," *Polym Compos*, vol. 19, no. 2, pp. 198–216, 1998, doi: 10.1002/pc.10091.

[41] A. Hammami, "Effect of reinforcement structure on compaction behavior in the vacuum infusion process," *Polym. Compos.*, vol. 22, no. 3, pp. 337–348, Jun. 2001, doi: 10.1002/PC.10542.

[42] J. Hu and A. Newton, "Low-load Lateral-compression Behaviour of Woven Fabrics," *J. Text. Inst.*, vol. 88, no. 3, pp. 242–254, 2009, doi: 10.1080/00405009708658548.

[43] C. M. van Wyk, "Note on the compressibility of wool," *J Text Inst Trans*, vol. 37, no. 12, pp. T285–T292, Dec. 1946, doi: 10.1080/19447024608659279.

[44] R. J. Harwood, S. A. Grishanov, S. V. Lomov, and T. Cassidy, "Modelling of Two-component Yarns Part I: The Compressibility of Yarns," *J. Text. Inst.*, vol. 88, no. 4, pp. 373–384, 2015, doi: 10.1080/00405000.1997.11090890.

[45] T. G. Gutowski, "Resin flow/fiber deformation model for composites," *SAMPE Q.*, vol. 16, no. 4, pp. 58–64, 1985.

[46] S. De Jong, J. W. Snaith, and N. A. Michie, "A Mechanical Model for the Lateral Compression of Woven Fabrics," *Text. Res. J.*, vol. 56, no. 12, pp. 759–767, 1986, doi: 10.1177/004051758605601208.

[47] M. Maisudaira and H. Qin, "Features and Mechanical Parameters of a Fabric's

Compressional Property," *J. Text. Inst.*, vol. 86, no. 3, pp. 476–486, 2008, doi: 10.1080/00405009508658774.

[48] B. Chen and T. W. Chou, "Compaction of woven-fabric preforms in liquid composite molding processes: single-layer deformation," *Compos. Sci. Technol.*, vol. 59, no. 10, pp. 1519–1526, Aug. 1999, doi: 10.1016/S0266-3538(99)00002-0.

[49] P. Potluri and T. V. Sagar, "Compaction modelling of textile preforms for composite structures," *Compos. Struct.*, vol. 86, no. 1–3, pp. 177–185, Nov. 2008, doi: 10.1016/J.COMPSTRUCT.2008.03.019.

[50] B. Chen and T. W. Chou, "Compaction of woven-fabric preforms: nesting and multi-layer deformation," *Compos. Sci. Technol.*, vol. 60, no. 12–13, pp. 2223–2231, Sep. 2000, doi: 10.1016/S0266-3538(00)00017-8.

[51] Z. Yousaf, & P. Potluri, and P. J. Withers, "Influence of Tow Architecture on Compaction and Nesting in Textile Preforms," doi: 10.1007/s10443-016-9554-8.

[52] R. A. Saunders, C. Lekakou, and M. G. Bader, "Compression and microstructure of fibre plain woven cloths in the processing of polymer composites," *Compos. Part A Appl. Sci. Manuf.*, vol. 29, no. 4, pp. 443–454, Jan. 1998, doi: 10.1016/S1359-835X(97)00092-4.

[53] R. S. Parnas, K. M. Flynn, and M. E. Dal-Favero, "A permeability database for composites manufacturing," *Polym. Compos.*, vol. 18, no. 5, pp. 623–633, Oct. 1997, doi: 10.1002/PC.10313.

[54] A. Endruweit and A. C. Long, "Analysis of Compressibility and Permeability of Selected 3D Woven Reinforcements," *J. Compos. Mater.*, vol. 44, no. 24, pp. 2833–2862, Nov. 2010, doi: 10.1177/0021998310369586.

[55]   Y. Mahadik, K. A. R. Brown, and S. R. Hallett, "Characterisation of 3D woven composite internal architecture and effect of compaction," *Compos. Part A Appl. Sci. Manuf.*, vol. 41, no. 7, pp. 872–880, Jul. 2010, doi: 10.1016/J.COMPOSITESA.2010.02.019.

[56]   N. Vernet and F. Trochu, "Analysis and modeling of 3D Interlock fabric compaction behavior," *Compos. Part A Appl. Sci. Manuf.*, vol. 80, pp. 182–193, Jan. 2016, doi: 10.1016/J.COMPOSITESA.2015.10.024.

[57]   G. Stewart, A. T. McIlhagger, J. P. Quinn, and S. King, "An Investigation into the Effect of Compaction on the Mechanical Performance of a 3D Reinforced Advanced Composite:," *Polym. Compos.*, vol. 15, no. 7, pp. 535–543, Oct. 2007, doi: 10.1177/096739110701500703.

[58]   E. Swery, S. Rao, H. Alhussein, R. Umer, W. Cantwell, and S. Bickerton, "In-plane and Through Thickness Permeability Characterization of 3D Woven Reinforcements,"*19th International Conference on Composite Materials (ICCM19)*, 2015.

[59]   H. Alhussein, R. Umer, S. Rao, and W. J. Cantwell, "Through Thickness Compaction Response of 3D Woven Reinforcements,"*19th International Conference on Composite Materials (ICCM19)*, 2015.

[60]   J. R. Weitzenböck, R. A. Shenoi, and P. A. Wilson, "Measurement of principal permeability with the channel flow experiment," *Polym. Compos.*, vol. 20, no. 2, pp. 321–335, Apr. 1999, doi: 10.1002/pc.10359.

[61]   J. R. Weitzenböck, R. A. Shenoi, and P. A. Wilson, "Radial flow permeability measurement. Part A: Theory," *Compos. Part A Appl. Sci. Manuf.*, vol. 30, no. 6,

pp. 781–796, Jun. 1999, doi: 10.1016/S1359-835X(98)00183-3.

[62] J. Weitzenböck, R. . Shenoi, and P. . Wilson, "Radial flow permeability measurement. Part B: Application," *Compos. Part A Appl. Sci. Manuf.*, vol. 30, no. 6, pp. 797–813, Jun. 1999, doi: 10.1016/S1359-835X(98)00184-5.

[63] N. Vernet *et al.*, "Experimental determination of the permeability of engineering textiles: Benchmark II," *Compos. Part A Appl. Sci. Manuf.*, vol. 61, pp. 172–184, Jun. 2014, doi: 10.1016/J.COMPOSITESA.2014.02.010.

[64] E. R. J.B. Alms, N. Correia, S.G. Advani, "Experimental procedures to run longitudinal injections to measure unsaturated permeability of LCM reinforcements," *FPCM Collaboration 1 (2010)*, 2010.

[65] A. W. Chan, D. E. Larive, and R. J. Morgan, "Anisotropic Permeability of Fiber Preforms: Constant Flow Rate Measurement:," *J. Compos. Mater.*, vol. 27, no. 10, pp. 996–1008, Jul. 2016, doi: 10.1177/002199839302701003.

[66] R. Gauvin, A. Kerachni, and B. Fisa, "Variation of Mat Surface Density and Its Effect on Permeability Evaluation for RTM Modelling:," *J. Reinf. Plast. Compos.*, vol. 13, no. 4, pp. 371–383, Aug. 2016, doi: 10.1177/073168449401300408.

[67] R. Umer, S. Bickerton, and A. Fernyhough, "The effect of yarn length and diameter on permeability and compaction response of flax fibre mats," *Compos. Part A Appl. Sci. Manuf.*, vol. 42, no. 7, pp. 723–732, Jul. 2011, doi: 10.1016/J.COMPOSITESA.2011.02.010.

[68] S. A. Ariadurai, P. Potluri, and I. L. Whyte, "Modeling the In-Plane Permeability of Woven Geotextiles1:," *Text. Res. J.*, vol. 69, no. 5, pp. 345–351, Jul. 2016, doi: 10.1177/004051759906900507.

[69] W. B. Young and S. F. Wu, "Permeability Measurement of Bidirectional Woven Glass Fibers:," *J. Reinf. Plast. Compos.*, vol. 14, no. 10, pp. 1108–1120, Aug. 2016, doi: 10.1177/073168449501401006.

[70] T. L. Luce, S. G. Advani, J. G. Howard, and R. S. Parnas, "Permeability characterization. Part 2: Flow behavior in multiple-layer preforms," *Polym. Compos.*, vol. 16, no. 6, pp. 446–458, Dec. 1995, doi: 10.1002/PC.750160603.

[71] V. ˆnica M. A. Calado and S. G. Advani, "Effective average permeability of multi-layer preforms in resin transfer molding," *Compos. Sci. Technol.*, vol. 56, no. 5, pp. 519–531, Jan. 1996, doi: 10.1016/0266-3538(96)00037-1.

[72] K. M. Pillai and S. G. Advani, "A Model for Unsaturated Flow in Woven Fiber Preforms during Mold Filling in Resin Transfer Molding:," *J. Compos. Mater.*, vol. 32, no. 19, pp. 1753–1783, Jul. 2016, doi: 10.1177/002199839803201902.

[73] S. Bickerton, E. M. Sozer, P. J. Graham, and S. G. Advani, "Fabric structure and mold curvature effects on preform permeability and mold filling in the RTM process. Part I. Experiments," *Compos. Part A Appl. Sci. Manuf.*, vol. 31, no. 5, pp. 423–438, May 2000, doi: 10.1016/S1359-835X(99)00087-1.

[74] K. K. Han, C. W. Lee, and B. P. Rice, "Measurements of the permeability of fiber preforms and applications," *Compos. Sci. Technol.*, vol. 60, no. 12–13, pp. 2435–2441, Sep. 2000, doi: 10.1016/S0266-3538(00)00037-3.

[75] G. Rieber and P. Mitschang, "2D Permeability changes due to stitching seams," *Compos. Part A Appl. Sci. Manuf.*, vol. 41, no. 1, pp. 2–7, Jan. 2010, doi: 10.1016/J.COMPOSITESA.2009.09.006.

[76] N. Vernet and F. Trochu, "In-plane and through-thickness permeability models for

three-dimensional Interlock fabrics," *J. Compos. Mater.*, vol. 50, no. 14, pp. 1951–1969, Jun. 2016, doi: 10.1177/0021998315597989.

[77]   R. Umer, E. Swery, S. Rao, H. Alhussein, W. Cantwell, and S. Bickerton, "In-plane and Through Thickness Permeability Characterization of 3D Woven Reinforcements," *19ᵗʰ International Conference on Composite Materials (ICCM19)* 2015.

[78]   M. A. Ali, R. Umer, K. A. Khan, and W. J. Cantwell, "In-plane virtual permeability characterization of 3D woven fabrics using a hybrid experimental and numerical approach," *Compos. Sci. Technol.*, vol. 173, pp. 99–109, Mar. 2019, doi: 10.1016/J.COMPSCITECH.2019.01.030.

[79]   F. Stig, M. W. Tahir, M. Åkermo, and S. Hallström, "An experimental study of the influence from fibre architecture on the permeability of 3D-woven textiles:," *J. Reinf. Plast. Compos.*, vol. 34, no. 17, pp. 1444–1453, Aug. 2015, doi: 10.1177/0731684415593351.

[80]   X. Xiao, A. Endruweit, X. Zeng, J. Hu, and A. Long, "Through-thickness permeability study of orthogonal and angle-interlock woven fabrics," *J. Mater. Sci.*, vol. 50, no. 3, pp. 1257–1266, Feb. 2015, doi: 10.1007/s10853-014-8683-4.

[81]   K. Reifsnider *et al.*, "Additional Comparisons of Interlocked Fabric and Laminated Fabric Kevlar 49/Epoxy Composites," *J. Compos. Technol. Res.*, vol. 8, no. 4, p. 163, 1986, doi: 10.1520/CTR10338J.

[82]   J. Arendts, F.J. ; Drechsler, K.; Brandt, *Advanced textile structural composites -- status and outlook*. The Society, 1993.

[83]   O. B. Billaut, F ; Roussel, "Impact resistance of 3-D graphite/epoxy composites,"

Tenth International Conference on Composite Materials Society, 1995.

[84]   J. Brandt, K. Drechsler, and F.-J. Arendts, "Mechanical performance of composites based on various three-dimensional woven-fibre preforms," *Compos. Sci. Technol.*, vol. 56, no. 3, pp. 381–386, Jan. 1996, doi: 10.1016/0266-3538(95)00135-2.

[85]   J. W. Herrick, "Advanced Impact Resistant Multidimensional Composites." *Fibre Materials Inc.*, 1979,

[86]   S. Chou, H.-C. Chen, and H.-E. Chen, "Effect of weave structure on mechanical fracture behavior of three-dimensional carbon fiber fabric reinforced epoxy resin composites," *Compos. Sci. Technol.*, vol. 45, no. 1, pp. 23–35, Jan. 1992, doi: 10.1016/0266-3538(92)90119-N.

[87]   Wayne E. Lundblad, Carl Dixon, Harold C. Ohler, "Ballistic resistant article comprising a three dimensional interlocking woven fabric," US Patent No. 545694, Feb. 1994.

[88]   J. N. Baucom and M. A. Zikry, "Low-velocity impact damage progression in woven E-glass composite systems," *Compos. Part A Appl. Sci. Manuf.*, vol. 36, no. 5, pp. 658–664, May 2005, doi: 10.1016/J.COMPOSITESA.2004.07.008.

[89]   R. Gerlach, C. R. Siviour, J. Wiegand, and N. Petrinic, "In-plane and through-thickness properties, failure modes, damage and delamination in 3D woven carbon fibre composites subjected to impact loading," *Compos. Sci. Technol.*, vol. 72, no. 3, pp. 397–411, Feb. 2012, doi: 10.1016/J.COMPSCITECH.2011.11.032.

[90]   V. A. Guenon, T.-W. Chou, and J. W. Gillespie, "Toughness properties of a three-dimensional carbon-epoxy composite," *J. Mater. Sci.*, vol. 24, no. 11, pp. 4168–

4175, Nov. 1989, doi: 10.1007/BF01168991.

[91]   A. Mouritz, C. Baini, and I. Herszberg, "Mode I interlaminar fracture toughness properties of advanced textile fibreglass composites," *Compos. Part A Appl. Sci. Manuf.*, vol. 30, no. 7, pp. 859–870, Jul. 1999, doi: 10.1016/S1359-835X(98)00197-3.

[92]   Y. Tanzawa, N. Watanabe, and T. Ishikawa, "Interlaminar fracture toughness of 3-D orthogonal interlocked fabric composites," *Compos. Sci. Technol.*, vol. 59, no. 8, pp. 1261–1270, Jun. 1999, doi: 10.1016/S0266-3538(98)00167-5.

[93]   R. Umer, H. Alhussein, J. Zhou, and W. Cantwell, "The mechanical properties of 3D woven composites," *J. Compos. Mater.*, 2017, doi: 10.1177/0021998316681187.

[94]   P. Potluri, P. Hogg, M. Arshad, D. Jetavat, and P. Jamshidi, "Influence of fibre architecture on impact damage tolerance in 3D woven composites," *Appl. Compos. Mater.*, vol. 19, no. 5, pp. 799–812, Oct. 2012, doi: 10.1007/S10443-012-9256-9/FIGURES/13.

[95]   Y. Luo, L. Lv, B. Sun, Y. Qiu, and B. Gu, "Transverse impact behavior and energy absorption of three-dimensional orthogonal hybrid woven composites," *Compos. Struct.*, vol. 81, no. 2, pp. 202–209, Nov. 2007, doi: 10.1016/J.COMPSTRUCT.2006.08.011.

[96]   R. Seltzer, C. González, R. Muñoz, J. LLorca, and T. Blanco-Varela, "X-ray microtomography analysis of the damage micromechanisms in 3D woven composites under low-velocity impact," *Compos. Part A Appl. Sci. Manuf.*, vol. 45, pp. 49–60, Feb. 2013, doi: 10.1016/J.COMPOSITESA.2012.09.017.

[97]   R. Umer, H. Alhussein, J. Zhou, and W. Cantwell, "The mechanical properties of 3D woven composites," *J. Compos. Mater.*, vol. 51, no. 12, pp. 1703–1716, May 2017, doi: 10.1177/0021998316681187.

[98]   S. Dai, P. R. Cunningham, S. Marshall, and C. Silva, "Influence of fibre architecture on the tensile, compressive and flexural behaviour of 3D woven composites," *Compos. Part A Appl. Sci. Manuf.*, vol. 69, pp. 195–207, Feb. 2015, doi: 10.1016/J.COMPOSITESA.2014.11.012.

[99]   W. S. Kuo, T. H. Ko, K. B. Cheng, and K. Y. Hsieh, "Flexural behavior of three-axis woven carbon/carbon composites," *J. Mater. Sci. 2001 3611*, vol. 36, no. 11, pp. 2743–2752, Jun. 2001, doi: 10.1023/A:1017968914529.

[100]   L. Jin, H. Hu, B. Sun, and B. Gu, "Three-point bending fatigue behavior of 3D angle-interlock woven composite:," *J. Compos. Mater.*, vol. 46, no. 8, pp. 883–894, Aug. 2011, doi: 10.1177/0021998311412218.

[101]   M. Pankow, A. Salvi, A. M. Waas, C. F. Yen, and S. Ghiorse, "Resistance to delamination of 3D woven textile composites evaluated using End Notch Flexure (ENF) tests: Experimental results," *Compos. Part A Appl. Sci. Manuf.*, vol. 42, no. 10, pp. 1463–1476, Oct. 2011, doi: 10.1016/J.COMPOSITESA.2011.06.013.

[102]   D. Zhang, A. M. Waas, and C. F. Yen, "Progressive damage and failure response of hybrid 3D textile composites subjected to flexural loading, part I: Experimental studies," *Int. J. Solids Struct.*, vol. 75–76, pp. 309–320, Dec. 2015, doi: 10.1016/J.IJSOLSTR.2015.06.034.

[103]   D. Zhang, M. Sun, X. Liu, X. Xiao, and K. Qian, "Off-axis bending behaviors and failure characterization of 3D woven composites," *Compos. Struct.*, vol. 208, pp.

45–55, Jan. 2019, doi: 10.1016/J.COMPSTRUCT.2018.10.009.

[104] L. Tong, A. P. Mouritz, M. K. Bannister, L. Tong, A. P. Mouritz, and M. K. Bannister, "Chapter 5 – 3D Woven Composites," in *3D Fibre Reinforced Polymer Composites*, 2002.

[105] J. P. Quinn, A. T. McIlhagger, and R. McIlhagger, "Examination of the failure of 3D woven composites," *Compos. Part A Appl. Sci. Manuf.*, vol. 39, no. 2, pp. 273–283, Feb. 2008, doi: 10.1016/J.COMPOSITESA.2007.10.012.

[106] F. Stig and S. Hallström, "Assessment of the mechanical properties of a new 3D woven fibre composite material," *Compos. Sci. Technol.*, vol. 69, no. 11–12, pp. 1686–1692, Sep. 2009, doi: 10.1016/J.COMPSCITECH.2008.04.047.

[107] F. Stig and S. Hallström, "Influence of crimp on 3D-woven fibre reinforced composites," *Compos. Struct.*, vol. 95, pp. 114–122, Jan. 2013, doi: 10.1016/J.COMPSTRUCT.2012.07.022.

[108] T. A. Bogetti, C. P. R. Hoppel, V. M. Harik, J. F. Newill, and B. P. Burns, "Predicting the nonlinear response and failure of composite laminates," in *Failure Criteria in Fibre-Reinforced-Polymer Composites*, Elsevier, 2004, pp. 961–975.

[109] P. J. Callus, A. P. Mouritz, M. K. Bannister, and K. H. Leong, "Tensile properties and failure mechanisms of 3D woven GRP composites," *Compos. Part A Appl. Sci. Manuf.*, vol. 30, no. 11, pp. 1277–1287, Nov. 1999, doi: 10.1016/S1359-835X(99)00033-0.

[110] M. N. Saleh, A. Yudhanto, P. Potluri, G. Lubineau, and C. Soutis, "Characterising the loading direction sensitivity of 3D woven composites: Effect of z-binder architecture," Elsevier, Nov. 2016. doi: 10.1016/J.COMPOSITESA.2016.08.028.

[111] E. Archer, S. Buchanan, A. McIlhagger, and J. Quinn, "The effect of 3D weaving and consolidation on carbon fiber tows, fabrics, and composites," *J. Reinf. Plast. Compos.*, vol. 29, no. 20, pp. 3162–3170, Oct. 2010, doi: 10.1177/0731684410371405.

[112] M. Lefebvre, B. Francois, and C. Daniel, "Influence of high-performance yarns degradation inside three-dimensional warp interlock fabric," *J. Ind. Text.*, vol. 42, no. 4, pp. 475–488, Apr. 2013, doi: 10.1177/1528083712444298.

[113] S. Dhiman, P. Potluri, and C. Silva, "Influence of binder configuration on 3D woven composites," *Compos. Struct.*, vol. 134, pp. 862–868, Dec. 2015, doi: 10.1016/J.COMPSTRUCT.2015.08.126.

[114] K. H. Leong, B. Lee, I. Herszberg, and M. K. Bannister, "The effect of binder path on the tensile properties and failure of multilayer woven CFRP composites," *Compos. Sci. Technol.*, vol. 60, no. 1, pp. 149–156, 2000, doi: 10.1016/S0266-3538(99)00108-6.

[115] B. N. Cox, M. S. Dadkhah, W. L. Morris, and J. G. Flintoff, "Failure mechanisms of 3D woven composites in tension, compression, and bending," *Acta Metall. Mater.*, vol. 42, no. 12, pp. 3967–3984, Dec. 1994, doi: 10.1016/0956-7151(94)90174-0.

[116] N. Castaneda, B. Wisner, J. Cuadra, S. Amini, and A. Kontsos, "Investigation of the Z-binder role in progressive damage of 3D woven composites," *Compos. Part A Appl. Sci. Manuf.*, vol. 98, pp. 76–89, Jul. 2017, doi: 10.1016/J.COMPOSITESA.2016.11.022.

[117] S. V. Lomov, A. E. Bogdanovich, D. S. Ivanov, D. Mungalov, M. Karahan, and I.

Verpoest, "A comparative study of tensile properties of non-crimp 3D orthogonal weave and multi-layer plain weave E-glass composites. Part 1: Materials, methods and principal results," *Compos. Part A Appl. Sci. Manuf.*, vol. 40, no. 8, pp. 1134–1143, Aug. 2009, doi: 10.1016/J.COMPOSITESA.2009.03.012.

[118] M. Pankow, B. Justusson, M. Riosbaas, A. M. Waas, and C. F. Yen, "Effect of fiber architecture on tensile fracture of 3D woven textile composites," *Compos. Struct.*, vol. 225, p. 111139, Oct. 2019, doi: 10.1016/j.compstruct.2019.111139.

[119] K. Sawrov, A. Fernando, V. Koncherry, P. Withers, and P. Potluri, "Damage Evaluation in 3D Woven Composites with Warp-way and Weft-way Binders," *AIAA SCITECH 2022 Forum*, Jan. 2022, doi: 10.2514/6.2022-1421.

[120] Y. Mahadik and S. R. Hallett, "Effect of fabric compaction and yarn waviness on 3D woven composite compressive properties," *Compos. Part A Appl. Sci. Manuf.*, vol. 42, no. 11, pp. 1592–1600, Nov. 2011, doi: 10.1016/J.COMPOSITESA.2011.07.006.

[121] W. Johnson, J. Masters, N. Fleck, P. Jelf, and P. Curtis, "Compressive Failure of Laminated and Woven Composites," *J. Compos. Technol. Res.*, vol. 17, no. 3, p. 212, 1995, doi: 10.1520/CTR10485J.

[122] L. Wang, M. Bannister, I. Herszberg, S. John," Prediction of binder yarn crimp factor in 3D orthogonal woven composite preform,*" ACUN-2: International Conferenec on Composites in the Transport Industry, 2000.*

[123] B. N. Cox, M. S. Dadkhah, R. V. Inman, W. L. Morris, and J. Zupon, "Mechanisms of compressive failure in 3D composites," *Acta Metall. Mater.*, vol. 40, no. 12, pp. 3285–3298, Dec. 1992, doi: 10.1016/0956-7151(92)90042-D.

[124] W. S. Kuo, T.-H. Ko, and C.-P. Chen, "Effect of weaving processes on compressive behavior of 3D woven composites," *Compos. Part A Appl. Sci. Manuf.*, vol. 38, no. 2, pp. 555–565, Feb. 2007, doi: 10.1016/J.COMPOSITESA.2006.02.025.

[125] G. L. Farley, B. T. Smith, and J. Maiden, "Compression Response of Thick Layer Composite Laminates with Through-the-Thickness Reinforcement," *J. Reinf. Plast. Compos.*, vol. 11, no. 7, pp. 787–810, Jul. 1992, doi: 10.1177/073168449201100705.

[126] K. C. Warren, R. A. Lopez-Anido, and J. Goering, "Experimental investigation of three-dimensional woven composites," *Compos. Part A Appl. Sci. Manuf.*, vol. 73, pp. 242–259, Jun. 2015, doi: 10.1016/J.COMPOSITESA.2015.03.011.

[127] H. L. Yi and X. Ding, "Conventional Approach on Manufacturing 3D Woven Preforms Used for Composites:," *J. Ind. Text.*, vol. 34, no. 1, pp. 39–50, Jul. 2016, doi: 10.1177/1528083704045847.

[128] B. J. Hill, R. McIlhagger, C. M. Harper, B. HiU, R. Mcllhagger, and C. Harper, "Weaving of Three-dimensional Fabrics for Preform Construction: Part I: Use of Texturised Glass Yarn," *J. Text. Inst.*, vol. 86, no. 1, pp. 96–103, Jan. 2008, doi: 10.1080/00405009508631312.

[129] B. J. Hill, R. McIlhagger, C. M. Harper, B. Hill, R. Mcllhagger, and C. Harper, "Weaving of Three-dimensional Fabrics for Preform Construction. Part II: Use of Flat Continuous Glass Filament Yarn," *J. Text. Inst.*, vol. 86, no. 1, pp. 104–109, Jan. 2008, doi: 10.1080/00405009508631313.

[130] J. A. Soden and B. J. Hill, "Conventional weaving of shaped preforms for

engineering composites," *Compos. Part A Appl. Sci. Manuf.*, vol. 29, no. 7, pp. 757–762, Jul. 1998, doi: 10.1016/S1359-835X(98)00053-0.

[131] Dhavalsinh Jetavat, Sandeep Sharma, and Prasad Potluri, "3D Weaving of Near Net Preforms," *15th European Conference on Composite Materials (ECCM15)*, 2012.

[132] A. Rawal, "A correction to van Wyk's model of the compressibility of fibrous materials:," *Text. Res. J.*, vol. 91, no. 13–14, pp. 1682–1684, Jun. 2021, doi: 10.1177/00405175211017402.

[133] K. A. Khan and R. Umer, "Modeling the viscoelastic compaction response of 3D woven fabrics for liquid composite molding processes:," *J. Reinf. Plast. Compos.*, vol. 36, no. 18, pp. 1299–1315, Apr. 2017, doi: 10.1177/0731684417707263.

[134] A. X. H. Yong *et al.*, "Experimental characterisation of textile compaction response: A benchmark exercise," *Compos. Part A Appl. Sci. Manuf.*, vol. 142, p. 106243, Mar. 2021, doi: 10.1016/J.COMPOSITESA.2020.106243.

[135] L. Tong, A. P. Mouritz, and M. K. Bannister, "3D fibre reinforced polymer composites," Elsevier, 2002, p. 241.

[136] P. P. V. Koncherry, J.S. Park, K. Sowrov, M. Matveev, L.P. Brown, A.C. Long, "Novel manufacturing techniques for optimized 3D multiaxial orthogonal preform," 22nd International Conferenec on Composite Materials (ICCM22), 2019.

[137] Toray, "https://www.toraycma.com/wp-content/uploads/T700S-Technical-Data-Sheet-1.pdf ."

[138] R. S. Parnas, J. G. Howard, T. L. Luce, and S. G. Advani, "Permeability

characterization. Part 1: A proposed standard reference fabric for permeability," *Polym. Compos.*, vol. 16, no. 6, pp. 429–445, Dec. 1995, doi: 10.1002/PC.750160602.

[139] C. Lekakou, M. A. K. Johari, D. Norman, and M. G. Bader, "Measurement techniques and effects on in-plane permeability of woven cloths in resin transfer moulding," *Compos. Part A Appl. Sci. Manuf.*, vol. 27, no. 5, pp. 401–408, Jan. 1996, doi: 10.1016/1359-835X(95)00028-Z.

[140] M. L. Diallo, R. Gauvin, and F. Trochu, "Experimental analysis and simulation of flow through multi-layer fiber reinforcements in liquid composite molding," *Polym. Compos.*, vol. 19, no. 3, pp. 246–256, Jun. 1998, doi: 10.1002/PC.10097.

[141] B. R. Gebart and P. Lidström, "Measurement of in-plane permeability of anisotropic fiber reinforcements," *Polym. Compos.*, vol. 17, no. 1, pp. 43–51, Feb. 1996, doi: 10.1002/PC.10589.

[142] V. H. Hammond and A. C. Loos, "The Effects of Fluid Type and Viscosity on the Steady-State and Advancing Front Permeability Behavior of Textile Preforms:," *J. Reinf. Plast. Compos.*, vol. 16, no. 1, pp. 50–72, Aug. 2016, doi: 10.1177/073168449701600105.

[143] T. S. Lundström, R. Stenberg, R. Bergström, H. Partanen, and P. A. Birkeland, "In-plane permeability measurements: a nordic round-robin study," *Compos. Part A Appl. Sci. Manuf.*, vol. 31, no. 1, pp. 29–43, Jan. 2000, doi: 10.1016/S1359-835X(99)00058-5.

[144] R. S. Parnas and A. J. Salem, "A comparison of the unidirectional and radial in-plane flow of fluids through woven composite reinforcements," *Polym. Compos.*,

vol. 14, no. 5, pp. 383–394, Oct. 1993, doi: 10.1002/PC.750140504.

[145] S. Bickerton, S. G. Advani, R. V. Mohan, and D. R. Shires, "Experimental analysis and numerical modeling of flow channel effects in resin transfer molding," *Polym. Compos.*, vol. 21, no. 1, pp. 134–153, Feb. 2000, doi: 10.1002/pc.10172.

[146] D. Modi, N. Correia, M. Johnson, A. Long, C. Rudd, and F. Robitaille, "Active control of the vacuum infusion process," *Compos. Part A Appl. Sci. Manuf.*, vol. 38, no. 5, pp. 1271–1287, May 2007, doi: 10.1016/J.COMPOSITESA.2006.11.012.

[147] A. A. Skordos, P. I. Karkanas, and I. K. Partridge, "A dielectric sensor for measuring flow in resin transfer moulding," *Meas. Sci. Technol.*, vol. 11, no. 1, pp. 25–31, Jan. 2000, doi: 10.1088/0957-0233/11/1/304.

[148] A. Dominauskas, D. Heider, and J. W. Gillespie, "Electric time-domain reflectometry sensor for online flow sensing in liquid composite molding processing," *Compos. Part A Appl. Sci. Manuf.*, vol. 34, no. 1, pp. 67–74, Jan. 2003, doi: 10.1016/S1359-835X(02)00232-4.

[149] M. K. Kang, J. J. Jung, and W. Il Lee, "Analysis of resin transfer moulding process with controlled multiple gates resin injection," *Compos. Part A Appl. Sci. Manuf.*, vol. 31, no. 5, pp. 407–422, May 2000, doi: 10.1016/S1359-835X(99)00086-X.

[150] Y. H. Lai, B. Khomami, and J. L. Kardos, "Accurate permeability characterization of preforms used in polymer matrix composite fabrication processes," *Polym. Compos.*, vol. 18, no. 3, pp. 368–377, Jun. 1997, doi: 10.1002/pc.10288.

[151] K. Lynch, P. Hubert, and A. Poursartip, "Use of a simple, inexpensive pressure sensor to measure hydrostatic resin pressure during processing of composite laminates," *Polym. Compos.*, vol. 20, no. 4, pp. 581–593, Aug. 1999, doi:

10.1002/pc.10381.

[152] S. Amico and C. Lekakou, "An experimental study of the permeability and capillary pressure in resin-transfer moulding," *Compos. Sci. Technol.*, vol. 61, no. 13, pp. 1945–1959, Oct. 2001, doi: 10.1016/S0266-3538(01)00104-X.

[153] S. H. Ahn, W. Il Lee, and G. S. Springer, "Measurement of the Three-Dimensional Permeability of Fiber Preforms Using Embedded Fiber Optic Sensors," *J. Compos. Mater.*, vol. 29, no. 6, pp. 714–733, Apr. 1995, doi: 10.1177/002199839502900602.

[154] J. R. Bernstein and J. W. Wagner, "Fiber optic sensors for use in monitoring flow front in vacuum resin transfer molding processes," *Rev. Sci. Instrum.*, vol. 68, no. 5, p. 2156, Jun. 1998, doi: 10.1063/1.1148065.

[155] S. R. M. Kueh, R. S. Parnas, and S. G. Advani, "A methodology for using long-period gratings and mold-filling simulations to minimize the intrusiveness of flow sensors in liquid composite molding," *Compos. Sci. Technol.*, vol. 62, no. 2, pp. 311–327, Feb. 2002, doi: 10.1016/S0266-3538(01)00217-2.

[156] S. R. M. Kueh *et al.*, "Long-period gratings as flow sensors for liquid-composite molding," in *5th Annual International Symposium on Nondestructive Evaluation and Health Monitoring of Aging Infrastructure*, May 2000, vol. 3993, pp. 240–250, doi: 10.1117/12.385495.

[157] Shawn M. Walsh, "In-situ sensor method and device," US Patent No. 5210499A, 1990.

[158] U. K. Vaidya, N. C. Jadhav, M. V Hosur, J. W. Gillespie, and B. K. Fink, "Assessment of flow and cure monitoring using direct current and alternating

current sensing in vacuum-assisted resin transfer molding," *Smart Mater. Struct.*, vol. 9, no. 6, pp. 727–736, Dec. 2000, doi: 10.1088/0964-1726/9/6/301.

[159] R. Mathur, S. G. Advani, D. Heider, C. Hoffmann, J. W. Gillespie, and B. K. Fink, "Flow front measurements and model validation in the vacuum assisted resin transfer molding process," *Polym. Compos.*, vol. 22, no. 4, pp. 477–490, Aug. 2001, doi: 10.1002/pc.10553.

[160] William H. GreenShawn M. WalshDale R. Shires, "Surveillant concurrent engineering process tool for environment rendering (SCEPTER) for resin flow monitoring in composites," US Patent No. 6577958B1, 2000.

[161] P. B. Nedanov and S. G. Advani, "A Method to Determine 3D Permeability of Fibrous Reinforcements," *J. Compos. Mater.*, vol. 36, no. 2, pp. 241–254, Jan. 2002, doi: 10.1177/0021998302036002462.

[162] D. Nielsen and R. Pitchumani, "Intelligent model-based control of preform permeation in liquid composite molding processes, with online optimization," *Compos. Part A Appl. Sci. Manuf.*, vol. 32, no. 12, pp. 1789–1803, Dec. 2001, doi: 10.1016/S1359-835X(01)00013-6.

[163] D. Nielsen and R. Pitchumani, "Closed-loop flow control in resin transfer molding using real-time numerical process simulations," *Compos. Sci. Technol.*, vol. 62, no. 2, pp. 283–298, Feb. 2002, doi: 10.1016/S0266-3538(01)00213-5.

[164] D. R. Nielsen and R. Pitchumani, "Control of flow in resin transfer molding with real-time preform permeability estimation," *Polym. Compos.*, vol. 23, no. 6, pp. 1087–1110, Dec. 2002, doi: 10.1002/pc.10504.

[165] B. W. Grimsley, P. Hubert, X.-L. Song, R. J. Cano, A. C. Loos, and R. B. Pipes,

"Flow and Compaction During the Vacuum Assisted Resin Transfer Molding Process," Jan, 2001. [Online]. Available: https://ntrs.nasa.gov/search.jsp?R=20040086021.

[166] J. R. Sayre and A. C. Loos, "Resin infusion of triaxially braided preforms with through-the-thickness reinforcement," *Polym. Compos.*, vol. 24, no. 2, pp. 229–236, Apr. 2003, doi: 10.1002/pc.10024.

[167] M. Bodaghi and N. Correia, "On The Effect of Mould Deflection on Flow Charactrisation in RTM," Accessed: Jan. 03, 2022. [Online]. Available: http://cchp.meca.polymtl.ca//fichiers/permeabilityBenchmarkII/PermBenchmark _letter.pdf.

[168] A. Endruweit, P. McGregor, A. C. Long, and M. S. Johnson, "Influence of the fabric architecture on the variations in experimentally determined in-plane permeability values," *Compos. Sci. Technol.*, vol. 66, no. 11–12, pp. 1778–1792, Sep. 2006, doi: 10.1016/J.COMPSCITECH.2005.10.031.

[169] M. D. Abramoff, P. J. Magalhães, and S. J. Ram, "Image processing with ImageJ," *Biophotonics Int.*, vol. 11, no. 7, pp. 36–42, 2004,

[170] D. A. Steenkamer, S. H. McKnight, D. J. Wilkins, and V. M. Karbhari, "Experimental characterization of permeability and fibre wetting for liquid moulding," *J. Mater. Sci. 1995 3012*, vol. 30, no. 12, pp. 3207–3215, Jun. 1995, doi: 10.1007/BF01209239.

[171] J. G. Williams, C. E. M. Morris, and B. C. Ennis, "Liquid flow through aligned fiber beds," *Polym. Eng. Sci.*, vol. 14, no. 6, pp. 413–419, Jun. 1974, doi: 10.1002/PEN.760140603.

[172] Y. Luo, I. Verpoest, K. Hoes, M. Vanheule, H. Sol, and A. Cardon, "Permeability

measurement of textile reinforcements with several test fluids," *Compos. Part A Appl. Sci. Manuf.*, vol. 32, no. 10, pp. 1497–1504, Oct. 2001, doi: 10.1016/S1359-835X(01)00049-5.

[173] N. K. Naik, M. Sirisha, and A. Inani, "Permeability characterization of polymer matrix composites by RTM/VARTM," *Prog. Aerosp. Sci.*, vol. 65, pp. 22–40, Feb. 2014, doi: 10.1016/J.PAEROSCI.2013.09.002.

[174] "IN-2 Epoxy Infusion Resin - Technical Datasheet," www.easycomposites.co.uk.

[175] M. W. Tahir, S. Hallström, and M. Åkermo, "Effect of dual scale porosity on the overall permeability of fibrous structures," *Compos. Sci. Technol.*, vol. 103, pp. 56–62, Oct. 2014, doi: 10.1016/J.COMPSCITECH.2014.08.008.

[176] S. Ranganathan, F. R. Phelan, and S. G. Advani, "A generalized model for the transverse fluid permeability in unidirectional fibrous media," *Polym. Compos.*, vol. 17, no. 2, pp. 222–230, Apr. 1996, doi: 10.1002/PC.10607.

[177] H. Gooijer, M. m. c. g. Warmoeskerken, and J. Groot Wassink, "Flow Resistance of Textile Materials: Part II: Multifilament Fabrics," *Text. Res. J.*, vol. 73, no. 6, pp. 480–484, Jul. 2016, doi: 10.1177/004051750307300603.

[178] ASTM, "Standard Test Methods for Constituent Content of Composite Materials," *ASTM Int.*, no. May 2009, pp. 1–6, 2010, doi: 10.1520/D3529M-10.2.

[179] ASTM, "ASTM D792 - 00 Standard Test Methods for Density and Specific Gravity (Relative Density) of Plastics by Displacement." https://compass.astm.org/Standards/HISTORICAL/D792-00.htm (accessed Aug. 24, 2018).

[180] R. Umer, S. Bickerton, and A. Fernyhough, "The effect of yarn length and diameter on permeability and compaction response of flax fibre mats," *Compos. Part A Appl. Sci. Manuf.*, vol. 42, no. 7, pp. 723–732, Jul. 2011, doi: 10.1016/J.COMPOSITESA.2011.02.010.

[181] Lomov S.V., Bogdanovich A.E., Karahan M., Mungalov D., and Verpoest I., "Mechanical Behaviour Of Non-Crimp 3d Wovencarbon/Epoxy Composite Under In-Plane Tensileloading," In *18th International Conference On Composite Materials (ICCM18)*, pp. 1–5 , 2011.

[182] K. Leong, B. Lee, I. Herszberg, and M. . Bannister, "The effect of binder path on the tensile properties and failure of multilayer woven CFRP composites," *Compos. Sci. Technol.*, vol. 60, no. 1, pp. 149–156, Jan. 2000, doi: 10.1016/S0266-3538(99)00108-6.

[183] ASTM International, "ASTM D3039 / D3039M-17, Standard Test Method for Tensile Properties of Polymer Matrix Composite Materials," *Stand. Test Method Tensile Prop. Polym. Matrix Compos. Mater.*, vol. 03, 2017, doi: 10.1520/D3039_D3039M-17.

[184] M. N. Saleh *et al.*, "Investigating the Potential of Using Off-Axis 3D Woven Composites in Composite Joints' Applications," *Appl. Compos. Mater.*, vol. 24, no. 2, pp. 377–396, Apr. 2017, doi: 10.1007/s10443-016-9529-9.

[185] B. Yu, R. S. Bradley, C. Soutis, P. J. Hogg, and P. J. Withers, "2D and 3D imaging of fatigue failure mechanisms of 3D woven composites," *Compos. Part A Appl. Sci. Manuf.*, vol. 77, pp. 37–49, Oct. 2015, doi: 10.1016/J.COMPOSITESA.2015.06.013.

[186] E. Obert, F. Daghia, P. Ladevèze, and L. Ballere, "Micro and meso modeling of

woven composites: Transverse cracking kinetics and homogenization," *Compos. Struct.*, vol. 117, no. 1, pp. 212–221, Nov. 2014, doi: 10.1016/J.COMPSTRUCT.2014.06.035.

[187] K. M. M. D. V. I. Lomov S.V. Bogdanovich A.E., "Mechanical Behaviour of Non-Crimp 3D Woven Carbon/Epoxy Composite Under In-Plane Tensile Loading," n *18th International Conference On Composite Materials (ICCM18),* Feb, 2011.

[188] P. Turner, T. Liu, and X. Zeng, "Collapse of 3D orthogonal woven carbon fibre composites under in-plane tension/compression and out-of-plane bending," *Compos. Struct.*, vol. 142, pp. 286–297, May 2016, doi: 10.1016/J.COMPSTRUCT.2016.01.100.

[189] S. C. Garcea, Y. Wang, and P. J. Withers, "X-ray computed tomography of polymer composites," *Compos. Sci. Technol.*, vol. 156, pp. 305–319, Mar. 2018, doi: 10.1016/J.COMPSCITECH.2017.10.023.

[190] P. J. Withers *et al.*, "X-ray computed tomography," *Nat. Rev. Methods Prim. 2021 11*, vol. 1, no. 1, pp. 1–21, Feb. 2021, doi: 10.1038/s43586-021-00015-4.

[191] ASTM D6272, "Standard Test Method for Flexural Properties of Unreinforced and Reinforced Plastics and Electrical Insulating Materials by Four-Point Bending." https://www.astm.org/d6272-17.html (accessed Jan. 19, 2022).

Appendix

List of appendices

1. Appendix I (a): Compressibility Data for Warp Bound Preforms at 1 Bar Pressure.
2. Appendix I (b): Compressibility Data for Weft Bound Preforms at 1 Bar Pressure.
3. Appendix II (a): Flow Front Progression and Permeability Data Table for Warp Bound Preforms.
4. Appendix II (b): Flow Front Progression and Permeability Data Table for Weft Bound Preforms.
5. Appendix III (a): Tensile Stress-Strain Curves for the Warp Bound Composites.
6. Appendix III (b): Tensile Stress-Strain Curves for the Weft Bound Composites.

Appendix I (a)

Compressibility Data For Warp Bound Preforms at 1 bar Pressure.

Table 1: Compressibility data for 1X1 Plain weave

Preforms	Initial thickness (mm)	Thickness at 1 bar (mm)	Fibre volume fraction (FVF) at 1 bar	Compressibility ($10^{-6}Pa^{-1}$)				
				Cycle 1	Cycle 2	Cycle 3	Cycle 4	Cycle 5
Sample 1	3.43	2.66	0.43	2.85	2.61	2.40	2.35	2.28
Sample 2	3.43	2.46	0.47	2.83	2.48	2.45	2.36	2.31
Sample 3	3.43	2.51	0.46	2.66	2.53	2.34	2.24	2.15
Average	3.43	2.54	0.45	2.78	2.54	2.40	2.32	2.25
Stdv	0	0.10	0.02	0.10	0.06	0.05	0.07	0.09
CV%	0	4.12	4.05	3.74	2.43	2.22	2.82	3.95

Table 2: Compressibility data for 2X1 Twill weave

Preforms	Initial thickness (mm)	Thickness at 1 bar (mm)	Fibre volume fraction (FVF) at 1 bar	Compressibility ($10^{-6}Pa^{-1}$)				
				Cycle 1	Cycle 2	Cycle 3	Cycle 4	Cycle 5
Sample 1	3.21	2.20	0.52	3.10	2.34	2.31	2.32	2.30
Sample 2	3.21	2.17	0.52	3.18	2.40	2.32	2.26	2.19
Sample 3	3.21	2.21	0.51	3.12	2.16	2.15	2.05	2.03
Average	3.21	2.19	0.52	3.13	2.30	2.26	2.21	2.17
Stdv	0	0.02	0.00	0.04	0.13	0.10	0.14	0.14
CV%	0	0.89	0.91	1.37	5.50	4.41	6.39	6.25

Table 3: Compressibility data for 2X2 Twill weave

Preforms	Initial thickness (mm)	Thickness at 1 bar (mm)	Fibre volume fraction (FVF) at 1 bar	Compressibility ($10^{-6}Pa^{-1}$)				
				Cycle 1	Cycle 2	Cycle 3	Cycle 4	Cycle 5
Sample 1	3.16	2.12	0.53	3.23	2.46	2.38	2.32	2.25
Sample 2	3.16	2.16	0.53	3.16	2.21	2.20	2.10	2.08
Sample 3	3.16	2.13	0.53	3.21	2.38	2.32	2.25	2.19
Average	3.16	2.14	0.53	3.20	2.35	2.30	2.22	2.18
Stdv	0	0.02	0.00	0.03	0.13	0.09	0.11	0.09
CV%	0	0.89	0.89	1.07	5.39	4.01	4.98	3.93

Table 4: Compressibility data for Angle Interlock (AI) weave

Preforms	Initial thickness (mm)	Thickness at 1 bar (mm)	Fibre volume fraction (FVF) at 1 bar	Compressibility ($10^{-6}Pa^{-1}$)				
				Cycle 1	Cycle 2	Cycle 3	Cycle 4	Cycle 5
Sample 1	3.07	1.76	0.64	4.24	1.72	1.57	1.48	1.41
Sample 2	3.07	1.95	0.58	3.81	1.54	1.49	1.38	1.35
Sample 3	3.07	1.86	0.61	3.92	1.53	1.38	1.38	1.30
Average	3.07	1.86	0.61	3.99	1.60	1.48	1.41	1.35
Stdv	0	0.09	0.03	0.23	0.11	0.09	0.05	0.06
CV%	0	5.07	5.07	5.64	6.73	6.36	3.89	4.16

Table 5: Compressibility data for 1X1 Plain weave with higher binder tension

Prefoms	Initial Thickness (mm)	Thickness at 1 bar (mm)	Fibre Volume Fraction (FVF) at 1 bar	Compressibility ($10^{-6}Pa^{-1}$)				
				Cycle 1	Cycle 2	Cycle 3	Cycle 4	Cycle 5
Sample 1	3.33	2.49	0.46	2.51	2.10	2.12	2.10	2.02
Sample 2	3.33	2.56	0.45	2.31	1.97	1.99	2.00	1.96
Sample 3	3.33	2.47	0.46	2.54	1.95	2.02	2.01	2.02
Average	3.33	2.50	0.46	2.45	2.00	2.05	2.04	2.00
Stdv	0	0.05	0.01	0.12	0.08	0.07	0.06	0.04
CV%	0	1.86	1.84	5.03	4.01	3.30	2.75	1.86

Appendix I (b)

Compressibility Data for Weft Bound Preforms at 1 bar Pressure

Table 6: Compressibility data for 1X1 Plain weave

Preforms	Initial thickness (mm)	Thickness at 1 bar (mm)	Fibre volume fraction (FVF) at 1 bar	Compressibility ($10^{-6}Pa^{-1}$)				
				Cycle 1	Cycle 2	Cycle 3	Cycle 4	Cycle 5
Sample 1	3.16	2.19	0.39	3.08	2.75	2.72	2.63	2.59
Sample 2	3.16	2.19	0.39	3.12	2.77	2.75	2.69	2.57
Sample 3	3.16	2.24	0.38	2.89	2.79	2.61	2.42	2.33
Average	3.16	2.20	0.39	3.03	2.77	2.69	2.58	2.50
Stdv	0	0.03	0.01	0.12	0.02	0.08	0.14	0.14
CV%	0	1.33	1.32	4.11	0.77	2.79	5.39	5.71

Table 7: Compressibility data for 2X1 Twill weave

Preforms	Initial thickness (mm)	Thickness at 1 bar (mm)	Fibre volume fraction (FVF) at 1 bar	Compressibility ($10^{-6}Pa^{-1}$)				
				Cycle 1	Cycle 2	Cycle 3	Cycle 4	Cycle 5
Sample 1	2.97	1.95	0.42	3.40	2.45	2.41	2.34	2.32
Sample 2	2.97	1.93	0.43	3.44	2.69	2.61	2.56	2.49
Sample 3	2.97	1.97	0.42	3.37	2.42	2.42	2.32	2.30
Average	2.97	1.95	0.42	3.40	2.52	2.48	2.40	2.37
Stdv	0	0.02	0.00	0.04	0.15	0.11	0.13	0.10
CV%	0	0.96	0.96	1.05	5.81	4.61	5.51	4.37

Table 8: Compressibility data for 2X2 Twill weave

Preforms	Initial thickness (mm)	Thickness at 1 bar (mm)	Fibre volume fraction (FVF) at 1 bar	Compressibility ($10^{-6}Pa^{-1}$)				
				Cycle 1	Cycle 2	Cycle 3	Cycle 4	Cycle 5
Sample 1	2.91	1.87	0.44	3.51	2.77	2.70	2.64	2.58
Sample 2	2.91	1.91	0.43	3.44	2.49	2.49	2.40	2.39
Sample 3	2.91	1.83	0.46	3.65	2.67	2.52	2.48	2.43
Average	2.91	1.87	0.44	3.53	2.64	2.57	2.51	2.46
Stdv	0.00	0.04	0.02	0.11	0.14	0.11	0.13	0.10
CV%	0.00	2.07	3.80	3.10	5.30	4.31	5.00	4.08

Table 9: Compressibility data for Angle Interlock (AI) weave

Preforms	Initial thickness (mm)	Thickness at 1 bar (mm)	Fibre volume fraction (FVF) at 1 bar	Compressibility ($10^{-6}Pa^{-1}$)				
				Cycle 1	Cycle 2	Cycle 3	Cycle 4	Cycle 5
Sample 1	2.82	1.49	0.55	4.65	1.72	1.57	1.48	1.31
Sample 2	2.82	1.68	0.49	4.24	1.56	1.40	1.32	1.24
Sample 3	2.82	1.60	0.55	4.30	1.64	1.48	1.38	1.33
Average	2.82	1.59	0.53	4.40	1.64	1.48	1.39	1.29
Stdv	0	0.09	0.03	0.22	0.08	0.08	0.08	0.04
CV%	0	5.93	6.56	5.00	4.90	5.53	5.61	3.47

Appendix II (a)

Flow Front Progression and Permeability Data Table for Warp Bound Preforms.

Flow Front and permeability data table for 1X1 Plain orthogonal preform

Sl No	Time	Flow Front Progression (mm)			Effective Permeability (m²)			Principal Permeability (m²)		Anisotropy
		Warp	Off-axis	Weft	KI	KII	KIII	k1	K2	I
1	0	0	0	0	0	0	0	0	0	0
2	5	15.181	19.083	28.042	8.0872E-11	1.5801E-10	4.632E-10	8.08517E-11	4.63186E-10	0.175
3	10	20.000	25.185	38.117	9.1277E-11	1.6735E-10	5.166E-10	9.12544E-11	5.16645E-10	0.177
4	15	22.602	28.725	45.234	8.5829E-11	1.5743E-10	5.317E-10	8.58074E-11	5.31793E-10	0.161
5	20	25.766	32.616	51.561	9.22E-11	1.6799E-10	5.531E-10	9.21769E-11	5.5316E-10	0.167
6	25	29.728	37.727	58.822	1.0819E-10	1.968E-10	6.125E-10	1.08167E-10	6.12562E-10	0.177
7	30	32.156	40.817	64.341	1.1086E-10	2.0115E-10	6.356E-10	1.10835E-10	6.35668E-10	0.174
8	35	36.126	45.726	74.029	1.2859E-10	2.2767E-10	7.655E-10	1.28562E-10	7.65521E-10	0.168
9	40	35.963	46.387	79.727	1.1121E-10	2.08E-10	8.006E-10	1.11185E-10	8.00722E-10	0.139
10	45	40.666	51.690	85.053	1.3542E-10	2.4188E-10	8.308E-10	1.35388E-10	8.30918E-10	0.163
11	50	41.763	53.388	87.386	1.3041E-10	2.3496E-10	7.977E-10	1.30372E-10	7.97748E-10	0.163
12	55	45.861	58.064	91.329	1.5013E-10	2.6347E-10	8.056E-10	1.50092E-10	8.05617E-10	0.186
13	60	47.043	59.673	94.665	1.4668E-10	2.5788E-10	8.042E-10	1.46647E-10	8.04215E-10	0.182
Average					1.1431E-10	2.0688E-10	6.764E-10	1.14278E-10	6.7648E-10	0.169
Stdv					2.3832E-11	3.8487E-11	1.374E-10	2.38256E-11	1.3746E-10	0.012

226

Flow Front and permeability data table for 2X1 Twill orthogonal preform

Sl no	Time (s)	Flow front Progression (mm)			Effective Permeability (m²)			Principal Permeability (m²)		Anisotropy
		Warp	Off-axis	Weft	KII	KIII	k1	K2	I	0
1	0	0	0	0	0	0	0	0	0	0
2	5	16.842	19.758	24.689	1.131E-10	1.847E-10	3.3549E-10	1.13092E-10	3.35528E-10	0.337
3	10	20.67	24.901	32.536	1.024E-10	1.663E-10	3.5041E-10	1.02398E-10	3.5046E-10	0.292
4	15	22.775	27.472	36.555	8.9567E-11	1.4761E-10	3.1601E-10	8.95636E-11	3.16059E-10	0.283
5	20	26.316	31.126	40.574	9.974E-11	1.5731E-10	3.0952E-10	9.97366E-11	3.09559E-10	0.322
6	25	27.177	33.021	45.359	8.7018E-11	1.4731E-10	3.2824E-10	8.70147E-11	3.28291E-10	0.265
7	30	28.708	35.186	49.378	8.396E-11	1.4107E-10	3.3829E-10	8.39561E-11	3.38351E-10	0.248
8	35	29.761	37.216	54.641	7.9188E-11	1.3828E-10	3.728E-10	7.91846E-11	3.72878E-10	0.212
9	40	32.536	40.464	57.033	8.7603E-11	1.497E-10	3.6254E-10	8.75992E-11	3.62605E-10	0.242
10	45	33.876	41.953	59.33	8.6509E-11	1.4418E-10	3.5508E-10	8.65056E-11	3.55146E-10	0.244
11	50	33.876	42.494	61.627	7.7858E-11	1.3357E-10	3.5073E-10	7.78549E-11	3.50799E-10	0.222
12	55	33.876	43.171	65.837	7.078E-11	1.2918E-10	3.746E-10	7.07771E-11	3.74695E-10	0.189
13	60	35.407	44.659	68.708	7.276E-11	1.2988E-10	3.809E-10	7.27567E-11	3.80987E-10	0.191
14	65	35.215	45.066	68.517	6.6225E-11	1.2066E-10	3.4923E-10	6.62223E-11	3.49315E-10	0.190
15	70	38.086	47.637	71.005	7.5243E-11	1.2958E-10	3.5355E-10	7.52398E-11	3.53624E-10	0.213
16	75	39.234	49.261	73.684	7.5769E-11	1.3159E-10	3.6087E-10	7.57656E-11	3.60944E-10	0.210
17	80	39.426	49.396	75.215	7.1924E-11	1.2679E-10	3.5551E-10	7.19209E-11	3.5559E-10	0.202
18	85	41.531	52.238	78.469	7.7272E-11	1.3653E-10	3.7049E-10	7.72687E-11	3.70571E-10	0.209
19	90	41.722	52.373	78.852	7.3834E-11	1.2839E-10	3.5403E-10	7.38303E-11	3.54102E-10	0.209
20	95	41.914	52.509	79.809	7.0767E-11	1.2269E-10	3.4525E-10	7.07634E-11	3.45324E-10	0.205
21	100	43.636	55.08	81.148	7.4434E-11	1.3045E-10	3.4134E-10	7.44311E-11	3.41409E-10	0.218
Average					8.1798E-11	1.3979E-10	3.5024E-10	8.17941E-11	3.50312E-10	0.235
Stdv					1.2093E-11	1.5798E-11	1.8599E-11	1.20932E-11	1.86122E-11	0.044

Flow Front and permeability data table for 2X2 Twill orthogonal preform

Sl no	Time (s)	Flow front Progression (mm)			Effective Permeability (m²)			Principal Permeability (m²)		Anisotropy
		Warp	Off-axis	Weft	KI	KII	KIII	k1	K2	I
1	0	0	0	0	0	0	0	0	0	0
2	5	11.193	14.272	22.936	3.0137E-11	7.373E-11	2.693E-10	3.0136E-11	2.69418E-10	0.112
3	10	15.963	20.24	29.908	4.7322E-11	9.2797E-11	2.7598E-10	4.73202E-11	2.76056E-10	0.171
4	15	20.367	25.17	35.046	6.4347E-11	1.2149E-10	2.7857E-10	6.43445E-11	2.78617E-10	0.231
5	20	23.67	28.803	39.266	7.344E-11	1.2605E-10	2.7984E-10	7.3437E-11	2.79887E-10	0.262
6	25	25.505	31.398	43.853	7.2052E-11	1.265E-10	2.9632E-10	7.20486E-11	2.96369E-10	0.243
7	30	28.44	34.512	47.339	8.0483E-11	1.3706E-10	2.9925E-10	8.048E-11	2.99298E-10	0.269
8	35	28.257	35.031	51.009	6.7808E-11	1.2331E-10	3.09E-10	6.7805E-11	3.09063E-10	0.219
9	40	29.174	36.328	54.037	6.4597E-11	1.1888E-10	3.1192E-10	6.45944E-11	3.11987E-10	0.207
10	45	30.642	38.404	56.147	6.5385E-11	1.1908E-10	3.0475E-10	6.53818E-11	3.04816E-10	0.214
11	50	33.211	40.999	58.899	7.2674E-11	1.2645E-10	3.0853E-10	7.26704E-11	3.08583E-10	0.235
12	55	33.761	42.297	62.385	6.8954E-11	1.2778E-10	3.2288E-10	6.89509E-11	3.22948E-10	0.214
13	60	33.945	42.946	65.505	6.4107E-11	1.1835E-10	3.3337E-10	6.41045E-11	3.33451E-10	0.192
14	65	36.514	45.67	66.972	7.1469E-11	1.3147E-10	3.2476E-10	7.14657E-11	3.2482E-10	0.220
15	70	37.798	47.227	68.991	7.2528E-11	1.2974E-10	3.241E-10	7.25246E-11	3.24161E-10	0.224
16	75	38.716	48.395	71.376	7.1983E-11	1.3052E-10	3.2844E-10	7.19798E-11	3.28501E-10	0.219
17	80	38.899	48.784	73.945	6.8303E-11	1.2594E-10	3.3536E-10	6.82995E-11	3.35434E-10	0.204
18	85	38.899	49.043	76.147	6.4285E-11	1.1801E-10	3.3876E-10	6.42818E-11	3.38842E-10	0.190
19	90	39.633	49.822	76.33	6.3681E-11	1.1695E-10	3.2179E-10	6.36784E-11	3.21868E-10	0.198
20	95	39.633	50.6	77.982	6.033E-11	1.137E-10	3.2097E-10	6.03269E-11	3.21048E-10	0.188
21	100	40.917	51.768	80	6.2159E-11	1.1435E-10	3.2422E-10	6.21563E-11	3.24293E-10	0.192
22	105	42.202	53.195	82.202	6.403E-11	1.1655E-10	3.2955E-10	6.40272E-11	3.29623E-10	0.194
23	110	43.303	54.882	83.119	6.5233E-11	1.1883E-10	3.2303E-10	6.52303E-11	3.23106E-10	0.202
24	115	43.119	55.401	85.138	6.1729E-11	1.1614E-10	3.2724E-10	6.17266E-11	3.27324E-10	0.189
Average					6.5089E-11	1.1929E-10	3.1252E-10	6.50857E-11	3.12588E-10	0.208
Stdv					9.9415E-12	1.322E-11	2.0397E-11	9.94116E-12	2.0398E-11	0.032

Flow Front and permeability data table for Angle Interlock preform

Sl no	Time (s)	Flow front Progression (mm)			Effective Permeability (m²)			Principal Permeability (m²)		Anisotropy
		Warp	Off-axis	Weft	KI	KII	KIII	k1	K2	I
1	0	0	0	0	0	0	0	0	0	0
2	15	19.315	19.615	19.521	5.5468E-11	5.33E-11	5.7183E-11	5.5468E-11	5.71828E-11	0.970
3	30	28.767	29.059	29.589	8.3217E-11	8.466E-11	8.9683E-11	8.32171E-11	8.96831E-11	0.928
4	45	34.315	34.145	33.082	8.8178E-11	8.579E-11	8.0169E-11	8.81783E-11	8.01691E-11	1.100
5	60	35.342	37.051	39.452	7.1384E-11	8.269E-11	9.4692E-11	7.13828E-11	9.46939E-11	0.754
6	75	38.63	40.102	41.815	7.1786E-11	7.758E-11	8.7833E-11	7.17856E-11	8.78339E-11	0.817
7	90	42.74	44.025	45.822	7.7364E-11	8.272E-11	9.2202E-11	7.7363E-11	9.22027E-11	0.839
8	105	43.973	45.768	47.466	7.125E-11	7.846E-11	8.633E-11	7.12489E-11	8.63314E-11	0.825
9	120	47.466	48.819	49.726	7.5539E-11	7.866E-11	8.4841E-11	7.55386E-11	8.48413E-11	0.890
10	135	47.466	48.529	49.726	6.7146E-11	7.027E-11	7.5414E-11	6.71454E-11	7.54144E-11	0.890
11	150	51.164	52.307	53.836	7.2861E-11	7.548E-11	8.266E-11	7.28603E-11	8.26602E-11	0.881
12	165	50.753	52.161	53.63	6.4923E-11	6.957E-11	7.4436E-11	6.49221E-11	7.44365E-11	0.872
13	180	53.836	55.358	56.301	6.8883E-11	7.161E-11	7.6931E-11	6.88826E-11	7.69316E-11	0.895
14	195	55.685	56.811	58.562	6.9114E-11	7.183E-11	7.8234E-11	6.91132E-11	7.82343E-11	0.883
15	210	58.356	58.554	58.562	7.202E-11	7.068E-11	7.2646E-11	7.20196E-11	7.26456E-11	0.991
16	225	60.822	60.298	60.205	7.4398E-11	7.19E-11	7.2563E-11	7.43979E-11	7.25632E-11	1.025
17	240	63.699	62.332	60	7.8086E-11	7.2E-11	6.7462E-11	7.80865E-11	6.74614E-11	1.157
18	255	63.493	62.913	61.644	7.2914E-11	6.92E-11	6.7837E-11	7.29145E-11	6.78365E-11	1.075
19	270	65.548	63.494	61.849	7.4421E-11	6.874E-11	6.459E-11	7.44212E-11	6.45898E-11	1.152
20	285	68.425	65.819	63.904	7.8259E-11	7.004E-11	6.6274E-11	7.82601E-11	6.62731E-11	1.181
21	300	70.479	68.144	64.932	7.987E-11	7.116E-11	6.5457E-11	7.9871E-11	6.54559E-11	1.220
22	315	71.712	69.016	66.37	7.9326E-11	7.027E-11	6.5752E-11	7.93267E-11	6.57517E-11	1.206
23	330	71.507	69.016	66.37	7.5198E-11	6.73E-11	6.2764E-11	7.51987E-11	6.2763E-11	1.198
24	345	73.151	69.887	66.575	7.5989E-11	6.638E-11	6.0486E-11	7.599E-11	6.04858E-11	1.256
25	360	74.589	71.631	69.247	7.6324E-11	6.776E-11	6.3775E-11	7.63252E-11	6.37748E-11	1.197
26	375	73.973	71.631	68.63	7.1821E-11	6.57E-11	5.991E-11	7.18214E-11	5.99097E-11	1.199
27	390	75.616	73.229	70.479	7.2813E-11	6.694E-11	6.1438E-11	7.28142E-11	6.1438E-11	1.185
Average					7.379E-11	7.233E-11	7.3522E-11	7.37905E-11	7.35217E-11	1.023
Stdv					6.2033E-12	7.013E-12	1.1006E-11	6.2036E-12	1.10071E-11	0.158

Appendix II (b)

Flow Front Progression and Permeability Data Table for Weft Bound Preforms.

Flow Front and permeability data table for 1X1 Plain orthogonal preform

Sl no	Time (s)	Flow front Progression (mm)			Effective Permeability (m²)			Principal Permeability (m²)		Anisotropy
		Warp	Off-axis	Weft	K_I	K_{II}	K_{III}	k1	K2	I
1	0	0	0	0	0	0	0	0	0	0
2	5	18.246	20.097	22.778	1.5177E-10	1.91256E-10	2.84957E-10	1.42866E-10	2.68259E-10	0.533
3	10	25.355	25.618	26.212	1.912E-10	1.89877E-10	2.09218E-10	1.79984E-10	1.9695E-10	0.914
4	15	29.561	29.144	28.294	1.9241E-10	1.80009E-10	1.71256E-10	1.8113E-10	1.61212E-10	1.124
5	20	34.564	32.587	31.012	2.1741E-10	1.80286E-10	1.63785E-10	2.0466E-10	1.54178E-10	1.327
6	25	40.472	36.468	33.479	2.6083E-10	1.95235E-10	1.60094E-10	2.45546E-10	1.50702E-10	1.629
7	30	43.403	37.115	33.189	2.595E-10	1.69273E-10	1.30418E-10	2.44296E-10	1.22766E-10	1.990
8	35	48.057	40.353	35.424	2.8728E-10	1.79434E-10	1.32397E-10	2.7045E-10	1.24629E-10	2.170
9	40	49.144	43.145	38.841	2.6581E-10	1.86673E-10	1.46789E-10	2.50232E-10	1.38177E-10	1.811
10	45	52.226	44.477	39.241	2.7486E-10	1.78813E-10	1.33936E-10	2.58756E-10	1.26077E-10	2.052
11	50	55.415	47.238	41.753	2.8643E-10	1.8737E-10	1.41158E-10	2.69644E-10	1.32876E-10	2.029
12	55	58.178	49.944	43.729	2.9353E-10	1.959E-10	1.44245E-10	2.7633E-10	1.35782E-10	2.035
13	60	58.966	50.190	44.455	2.781E-10	1.75044E-10	1.37828E-10	2.61805E-10	1.29742E-10	2.018
14	65	62.587	52.107	47.161	2.9703E-10	1.67116E-10	1.47581E-10	2.79628E-10	1.38922E-10	2.013
15	70	67.003	55.434	48.288	3.2564E-10	2.00631E-10	1.45378E-10	3.06566E-10	1.36848E-10	2.240
16	75	71.626	58.232	50.029	3.5727E-10	2.08214E-10	1.48212E-10	3.36348E-10	1.39515E-10	2.411
17	80	72.500	57.511	51.119	3.449E-10	1.91915E-10	1.466E-10	3.247E-10	1.37998E-10	2.353
18	85	75.215	58.227	51.546	3.5472E-10	1.85597E-10	1.4086E-10	3.33945E-10	1.32595E-10	2.519
Average					2.7286E-10	1.86038E-10	1.57924E-10	2.56876E-10	1.18661E-10	2.16
Stdv					5.8357E-11	1.08705E-11	3.7702E-11	5.49438E-11	3.54951E-11	0.55

Flow Front and permeability data table for 2X1 Twill orthogonal preform

Sl no	Time (s)	Flow front Progression (mm)			Effective Permeability (m²)			Principal Permeability (m²)		Anisotropy
		Warp	Off-axis	Weft	KI	KII	KIII	k1	K2	I
1	0	0	0	0	0	0	0	0	0	0.000
2	5	20.529	15.054	12.409	2.13169E-10	8.1917E-11	4.61452E-11	2.0051E-10	4.33942E-11	4.621
3	10	24.371	18.695	15.378	1.71801E-10	7.6791E-11	4.56071E-11	1.61591E-10	4.28883E-11	3.768
4	15	26.510	21.777	18.780	1.43944E-10	8.02647E-11	5.5069E-11	1.35381E-10	5.17865E-11	2.614
5	20	29.091	24.427	21.333	1.38439E-10	8.29962E-11	5.93943E-11	1.30201E-10	5.5854E-11	2.331
6	25	33.929	29.926	27.202	1.65912E-10	1.14759E-10	9.25744E-11	1.56034E-10	8.70571E-11	1.792
7	30	37.304	32.888	29.723	1.76659E-10	1.23256E-10	9.77097E-11	1.66142E-10	9.18863E-11	1.808
8	35	41.405	37.367	34.146	1.97618E-10	1.46966E-10	1.20495E-10	1.85851E-10	1.13314E-10	1.640
9	40	43.421	38.891	35.614	1.95025E-10	1.42376E-10	1.17576E-10	1.83414E-10	1.10569E-10	1.659
10	45	45.747	41.493	38.368	1.97694E-10	1.50022E-10	1.26576E-10	1.85922E-10	1.19033E-10	1.562
11	50	48.420	44.621	41.543	2.05121E-10	1.62421E-10	1.395E-10	1.92906E-10	1.31187E-10	1.470
12	55	49.094	45.411	42.210	1.9302E-10	1.55459E-10	1.32047E-10	1.81526E-10	1.24178E-10	1.462
13	60	49.559	46.340	43.659	1.81142E-10	1.49434E-10	1.31825E-10	1.70354E-10	1.23969E-10	1.374
14	65	54.122	50.224	47.133	2.08055E-10	1.7291E-10	1.47502E-10	1.95665E-10	1.38713E-10	1.411
15	70	53.724	51.889	50.000	1.89702E-10	1.68098E-10	1.58727E-10	1.78402E-10	1.4927E-10	1.195
16	75	56.649	53.472	50.798	2.01801E-10	1.69004E-10	1.54097E-10	1.89782E-10	1.44915E-10	1.310
17	80	57.343	54.455	51.748	1.94941E-10	1.66764E-10	1.51273E-10	1.8333E-10	1.42259E-10	1.289
18	85	58.712	56.938	55.307	1.94432E-10	1.75785E-10	1.67847E-10	1.8285E-10	1.57847E-10	1.158
19	90	60.432	57.166	54.496	1.97095E-10	1.69057E-10	1.52845E-10	1.85356E-10	1.43737E-10	1.290
Average					1.86976E-10	1.38238E-10	1.16489E-10	1.75845E-10	1.09548E-10	1.875
Stdv					2.06651E-11	3.56359E-11	4.08618E-11	1.94339E-11	3.84275E-11	0.935

231

Flow Front and permeability data table for 2X2 Twill orthogonal preform

Sl no	Time (s)	Flow front Progression (mm)			Effective Permeability (m²)			Principal Permeability (m²)		Anisotropy
		Warp	Off-axis	Weft	KI	KII	KIII	k1	K2	I
1	0	0	0	0	0	0	0	0	0	0.000
2	5	16.009	16.769	17.823	1.0307E-10	6.9437E-11	1.4187E-10	9.6932E-11	1.33421E-10	0.727
3	10	24.007	23.235	23.068	1.6487E-10	1.0414E-10	1.477E-10	1.55046E-10	1.389E-10	1.116
4	15	27.318	26.368	25.856	1.5605E-10	1.034E-10	1.3455E-10	1.46757E-10	1.2653E-10	1.160
5	20	30.001	27.875	26.762	1.5022E-10	8.2503E-11	1.1075E-10	1.41273E-10	1.04152E-10	1.356
6	25	32.699	31.109	30.569	1.507E-10	7.6945E-11	1.2627E-10	1.41719E-10	1.18748E-10	1.193
7	30	34.250	33.927	33.075	1.4169E-10	1.085E-10	1.2939E-10	1.33251E-10	1.21679E-10	1.095
8	35	40.525	35.430	33.256	1.8711E-10	1.0529E-10	1.1249E-10	1.75971E-10	1.05789E-10	1.663
9	40	41.602	37.304	34.657	1.7501E-10	1.0689E-10	1.0957E-10	1.64586E-10	1.03044E-10	1.597
10	45	42.922	37.157	34.630	1.6837E-10	9.485E-11	9.7198E-11	1.58344E-10	9.14056E-11	1.732
11	50	43.917	37.733	34.935	1.6055E-10	8.883E-11	8.9493E-11	1.50995E-10	8.41597E-11	1.794
12	55	47.865	40.451	37.227	1.8118E-10	9.79E-11	9.5849E-11	1.70394E-10	9.01364E-11	1.890
13	60	49.939	41.712	38.424	1.8462E-10	9.68E-11	9.5288E-11	1.73634E-10	8.96089E-11	1.938
14	65	49.717	42.603	39.213	1.6854E-10	9.5191E-11	9.2651E-11	1.58505E-10	8.71289E-11	1.819
15	70	52.848	44.643	40.834	1.8214E-10	1.0007E-10	9.5384E-11	1.71295E-10	8.96994E-11	1.910
16	75	52.747	44.890	41.208	1.5862E-10	8.7808E-11	8.5414E-11	1.49177E-10	8.03229E-11	1.857
17	80	57.061	47.521	43.050	1.8127E-10	9.7721E-11	8.981E-11	1.70477E-10	8.44575E-11	2.018
18	85	57.781	47.902	43.320	1.7655E-10	9.4284E-11	8.617E-11	1.66045E-10	8.10343E-11	2.049
19	90	61.308	51.114	46.580	1.9342E-10	1.068E-10	9.7983E-11	1.81905E-10	9.21428E-11	1.974
20	95	60.085	50.802	46.669	1.749E-10	9.8859E-11	9.3532E-11	1.64488E-10	8.79571E-11	1.870
21	100	61.523	52.597	48.238	1.7651E-10	1.035E-10	9.6763E-11	1.65998E-10	9.0996E-11	1.824
Average					1.6677E-10	9.5986E-11	1.0641E-10	1.5684E-10	1.00066E-10	1.629
Stdv					2.035E-11	1.0416E-11	1.9352E-11	1.91411E-11	1.82E-11	0.381

Flow Front and permeability data table for Angle Interlock preform

Sl no	Time (s)	Flow front Progression (mm)			Effective Permeability (m²)			Principal Permeability (m²)		Anisotropy
		Warp	Weft	Off-axis	KI	KII	KIII	k1	K2	I
1	0	0	0	0	0	0	0	0	0	0.000
2	10	16.302	13.078	14.581	5.44683E-11	3.41765E-10	2.7419E-11	5.11924E-11	2.57682E-11	1.987
3	20	25.590	25.711	25.837	9.81879E-11	5.73147E-10	9.9452E-11	9.22774E-11	9.34656E-11	0.987
4	30	31.508	29.976	30.733	1.14023E-10	5.59101E-10	9.9994E-11	1.0716E-10	9.39742E-11	1.140
5	40	38.695	33.456	35.810	1.45618E-10	5.78606E-10	1.0004E-10	1.36856E-10	9.40199E-11	1.456
6	50	39.876	34.281	38.674	1.25786E-10	4.83358E-10	8.5267E-11	1.18218E-10	8.01327E-11	1.475
7	60	41.233	37.629	40.393	1.14135E-10	4.43693E-10	9.0374E-11	1.07266E-10	8.49332E-11	1.263
8	70	43.874	42.793	43.509	1.14475E-10	4.97919E-10	1.0748E-10	1.07584E-10	1.01014E-10	1.065
9	80	46.039	42.518	44.194	1.13069E-10	4.50251E-10	9.2526E-11	1.06264E-10	8.69558E-11	1.222
10	90	47.784	44.681	46.326	1.10323E-10	4.40931E-10	9.322E-11	1.03683E-10	8.76081E-11	1.183
11	100	49.141	44.588	46.897	1.06483E-10	4.08579E-10	8.3458E-11	1.00075E-10	7.84335E-11	1.276
12	110	49.042	45.122	46.997	9.63168E-11	3.72818E-10	7.818E-11	9.05202E-11	7.34731E-11	1.232
13	120	50.789	48.158	49.497	9.63345E-11	3.82517E-10	8.4371E-11	9.05364E-11	7.92919E-11	1.142
14	130	53.947	50.702	52.227	1.03269E-10	3.92591E-10	8.8543E-11	9.70532E-11	8.32123E-11	1.166
15	140	54.024	51.144	51.398	9.62292E-11	3.55086E-10	8.4012E-11	9.04374E-11	7.8954E-11	1.145
16	150	54.446	52.722	53.643	9.15598E-11	3.60044E-10	8.4553E-11	8.60488E-11	7.9463E-11	1.083
17	160	55.245	51.269	53.183	8.89806E-11	3.33924E-10	7.3958E-11	8.36253E-11	6.95055E-11	1.203
18	170	55.060	52.487	53.609	8.30549E-11	3.24655E-10	7.3784E-11	7.80559E-11	6.93418E-11	1.126
19	180	57.317	52.642	54.819	8.66025E-11	3.1528E-10	7.0196E-11	8.13906E-11	6.59699E-11	1.234
20	190	59.914	53.448	56.386	9.14732E-11	3.17434E-10	6.9051E-11	8.59686E-11	6.4894E-11	1.325
21	200	60.325	54.934	57.420	8.83687E-11	3.13377E-10	7.02E-11	8.30505E-11	6.59733E-11	1.259
22	210	60.720	56.461	58.461	8.55173E-11	3.1086E-10	7.1531E-11	8.03705E-11	6.72247E-11	1.196
23	220	59.695	54.847	57.254	7.82937E-11	2.84591E-10	6.3569E-11	7.35818E-11	5.97415E-11	1.232
24	230	62.627	57.712	59.924	8.42126E-11	2.99615E-10	6.893E-11	7.91444E-11	6.47797E-11	1.222
Average					9.85557E-11	3.97398E-10	8.0875E-11	9.26243E-11	8.60057E-11	1.084
Stdv					1.8524E-11	9.06405E-11	1.6713E-11	1.74092E-11	1.57069E-11	0.196

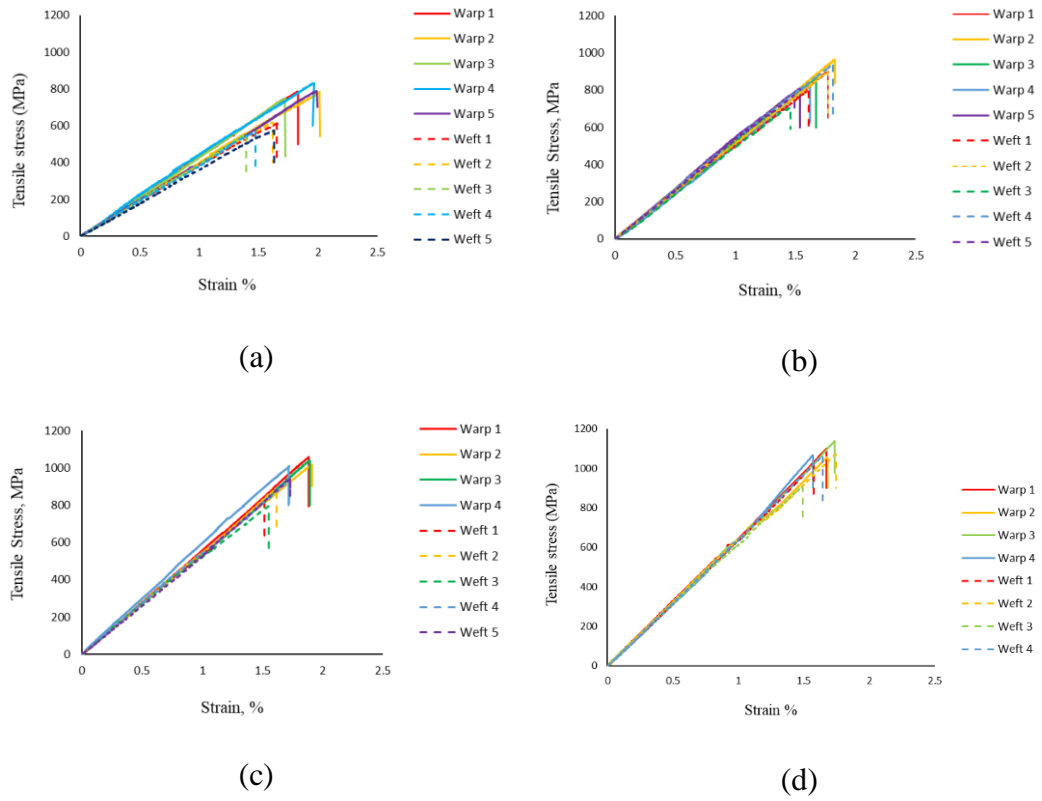**Tensile stress-strain curves for the warp bound composites.**

Fig. 1 Stress-strain curves for warp bound composites with different binder weave architectures loaded in both warp and weft directions- (a) 1X1 Plain, (b) 2X1 Twill, (c) 2X2 Twill and (d) Angle Interlock (AI).

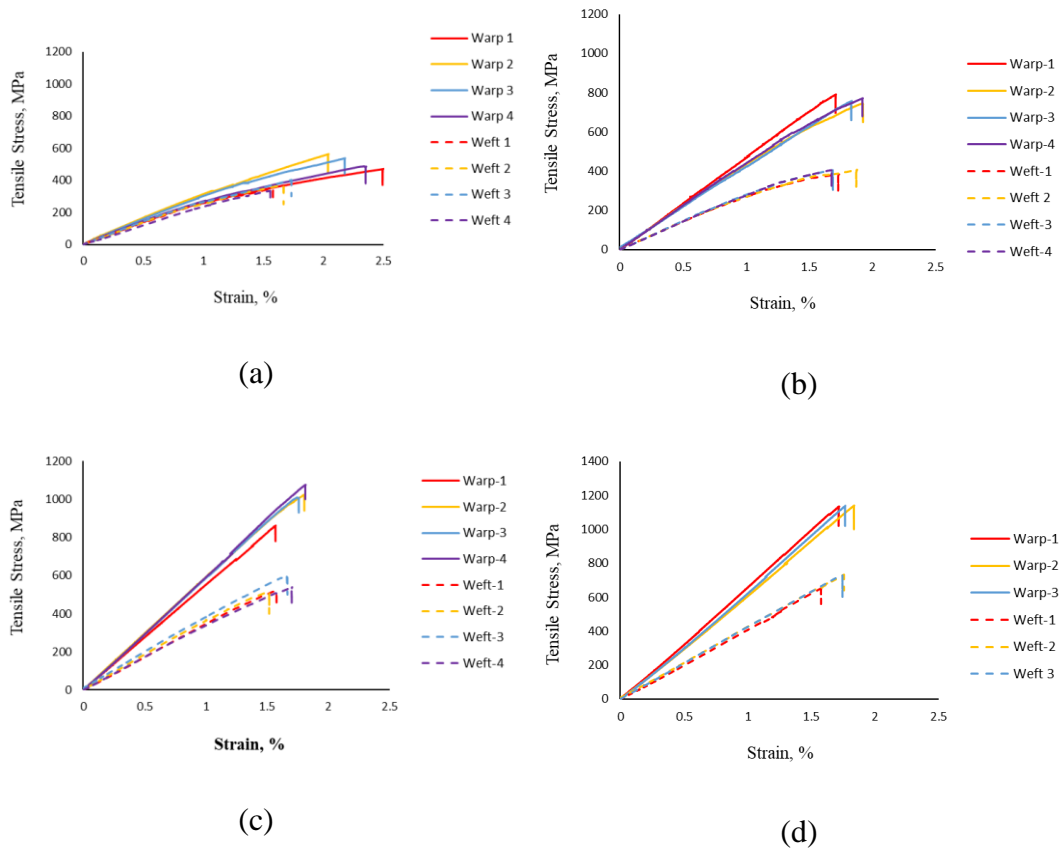**Tensile Stress-strain Curves for the Weft Bound Composites**

Fig. 2 Stress-strain curves for weft bound composites with different binder weave architectures loaded in both warp and weft directions- (a) 1X1 Plain, (b) 2X1 Twill, (c) 2X2 Twill and (d) angle Interlock (AI).